Astronomy Unit
School of Physics and Astronomy
Queen Mary, University of London

Baroclinic Jets on "Other" Jupiters and Earths

Inna Polichtchouk

January 27, 2015

Submitted in partial fulfilment of the requirements for the degree of
Doctor of Philosophy in Physics and Astronomy of the University of London

Declaration

I, Inna Polichtchouk, confirm that the research included within this thesis is my own work or that where it has been carried out in collaboration with, or supported by others, that this is duly acknowledged below and my contribution indicated. Previously published material is also acknowledged below.

I attest that I have exercised reasonable care to ensure that the work is original, and does not to the best of my knowledge break any UK law, infringe any third party's copyright or other Intellectual Property Right, or contain any confidential material.

I accept that the College has the right to use plagiarism detection software to check the electronic version of the thesis.

I confirm that this thesis has not been previously submitted for the award of a degree by this or any other university.

Signature:

Date:

Details of collaboration and publications:

The results presented in Chapter 3 and 4 contain original material that has been published in peer review journals in the following articles:

- Polichtchouk, I., and Cho, J. Y-K. (2012). Baroclinic instability on hot extra-solar planets. *MNRAS*, 424(2), 1307–1326.
- Polichtchouk, I., Cho, J. Y-K., Watkins, C., Thrastarson, H. Th, Umurhan, O.M., and de la Torre Juarez, M. (2014). Intercomparison of general circulation models for hot extrasolar planets. *Icarus* 229, 355-377.

Parts of Chapter 5 is material that is currently being prepared for submission:

- Polichtchouk, I., and Cho, J. Y-K. Superrotation in Held & Suarez-like flows with weak surface temperature gradient. *QJRMS*

Other works submitted or currently being prepared, which have not been included are:

- Cho, J. Y-K., Polichtchouk, I., Thrastarson, H. Th. Sensitivity and Variability Redux in Hot-Jupiter Flow Simulations. *MNRAS*, submitted.
- Polichtchouk, I., Cho, J. Y-K. Global Axial Angular Momentum Conservation in General Circulation Models of (Exo)Planetary Atmospheres. *Phys. Rev. E*, in prep.

Abstract

Dynamics of baroclinic jets on extrasolar planets is studied using three-dimensional general circulation models (GCMs) which solve the traditional hydrostatic primitive equations. The focus is on: *i*) baroclinic flow and instability on hot-Jupiters; *ii*) detailed GCM intercomparison in a commonly used extrasolar planet setup; and, *iii*) equatorial superrotation on Earth-like planets.

Stability, non-linear evolution and equilibration of high-speed ageostrophic jets are studied under adiabatic condition relevant to hot-Jupiters. It is found that zonal jets can be baroclinically unstable, despite the planetary size of the Rossby deformation scale, and that high resolution is necessary to capture the process. Non-linear jet evolution is then used as a test case to assess model convergence in five GCMs used in current hot-Jupiter simulations. The GCMs are also tested under a diabatic condition (thermal relaxation on a short timescale) similar to that used in many hot-Jupiter studies. In the latter case, in particular, the models show significant inter- and intra-model variability, limiting their quantitative prediction capability. Some models severely violate global angular momentum conservation.

The generation of equatorial superrotation in Earth-like atmospheres, subject to "Held & Suarez-like" zonally-symmetric thermal forcing is also studied. It is shown that transition to superrotation occurs when the meridional gradient of the equilibrium surface entropy is weak in this setup. Two factors contribute to the onset of superrotation — suppression of breaking Rossby waves (generated by mid-latitude baroclinic instability) that decelerate the equatorial flow, and, generation of inertial and barotropic instabilities in the equatorial region that provide the stirring to accelerate the equatorial flow.

In summary, forcing condition and physical setup used in current hot-Jupiter simulations severely stretch model performance and predictive capability. Superrotation in Earth-like conditions may be common, but its strength decreases with resolution. Broadly, numerical convergence must be assessed in GCM experiments for each problem or setup considered.

Acknowledgments

My deepest gratitude goes to my supervisor James Y-K. Cho, for all his support and encouragement. It has been a privilege to benefit from his knowledge, guidance and generosity and from the numerous enlightening and stimulating discussions with him.

Many thanks to the members of the Planetary Atmosphere and Dynamics Group (PAD) for many hours of productive discussions, support, and for the feedback on the work in this thesis: Heidar Thor Thrastarson, Christopher Watkins, Orkan Umurhan, Stephen Thomson, Zoe Gumm, and, James Y-K. Cho. Special thanks goes to Stephen Thomson and Christopher Watkins for reading this thesis.

I thank my husband, Martin, for supporting and helping me in so many ways.

Thanks to my parents, for their understanding and encouragement.

Thanks to my friends and colleagues in the Astronomy Unit for making my time at Queen Mary a very enjoyable experience.

Many thanks to my examiners Prof. Peter Read and Prof. David Dritschel for a very enjoyable viva and for their many useful and inspiring comments, which have greatly improved this thesis.

This work is supported by a research studentship from the Westfield Trust Fund and from the Science and Technology Facilities Council (STFC).

Contents

List of Figures

List of Tables

1 Introduction

1.1 Extrasolar Planets and Their Atmospheres

Following the discovery of the first extrasolar planets in 1992, around 1800 planets, orbiting a star other than the Sun, have been detected to date (http://exoplanet.eu). The first planets were of several Earth-mass and were detected orbiting a pulsar PSR B1257+12 by the pulsar timing method (Wolszczan and Frail, 1992). In 1995, the first Jupiter-mass planet orbiting a main-sequence star, 51 Pegasi, was detected using the radial velocity technique (Mayor and Queloz, 1995). Since these early discoveries, the rate of detection has been rising due to improved observation techniques and dedicated ground- and space-based telescopes and spacecrafts (e.g., HATNet, SuperWASP, CoRoT, Kepler, etc.). To date, the majority of the confirmed extrasolar planets (henceforth exoplanets) have been discovered by the radial velocity and transit methods. The former measures the variation in the speed with which the star moves toward or away from the observer as a response to the orbiting planet's gravitational pull. The latter detects planets by measuring a small dip in the star's brightness as the planet transits between the star and the observer's line of sight. Both methods are biased towards finding more massive planets on small orbits. Other detection methods include direct imaging, gravitational microlensing, and transit timing variation techniques. At present, the majority of the confirmed exoplanets are between the size of the Earth and Neptune. This observation followed the recent NASA Kepler mission announcement of over 700 new exoplanets validated by a statistical method (Lissauer et al., 2014; Rowe et al., 2014). However, prior to the announcement, Jupiter size planets on close-in orbits ($a \lesssim 0.05$ AU, where a is semi-major axis, and 1 AU=1.496$\times$ 10^{11} m) — the so-called "hot-Jupiters" — were the most common exoplanets.

The diverse range of physical and orbital characteristics (e.g., masses, radii, temperatures, orbital periods, semi-major axes, surface properties, eccentricities, etc.) of the exoplanets motivate the study of their atmospheres and provide an opportunity to apply and extend theories of atmospheric dynamics, beyond the parameter

regimes applicable to the Solar System planets. Moreover, since dynamics affects temperature distributions and the observed spectra, understanding general circulation is crucial for guiding and interpreting observations of exoplanet atmospheres.

The transit method makes it possible to observe some properties of extrasolar planet atmospheres. Due to the larger probability of hot-Jupiters transiting their host stars (the probability of transit is R_*/a, where R_* is the stellar radius), these planets are by far the best characterized exoplanets and have received the most attention in exoplanet atmospheric studies. Due to their close proximity to the star, tidal forces are believed to maintain a rotation rate synchronous with the circular orbit (e.g., Goldreich and Soter, 1966), leading to permanent day and night sides on the planet. This situation presents a new regime of atmospheric circulation not encountered in our Solar System: moderately rotating (rotation periods of few days) giant planets, which are continuously exposed to intense stellar heating on the same side. In the first part of this thesis, baroclinic jet dynamics is studied under conditions relevant to not only spin-orbit synchronized but also more distant unsynchronized hot-Jupiters. The atmospheres of smaller, terrestrial planets are also becoming amenable to observations, and it is equally important to study the range of circulations permitted under Earth-like parameter regimes. In the second part of this thesis, the focus is therefore shifted from hot-Jupiter to Earth-like conditions.

All planets with atmospheres, independent of their proximity to the host star, are expected to possess stably stratified (i.e., entropy increases with height), dynamically active layers in which advective and radiative transport is important. Dynamics and dissipation processes govern the energy distribution in these layers. Incoming stellar radiation provides forcing. Part of this incoming radiation is scattered or reflected and part is absorbed by the deeper atmosphere or the ground on terrestrial planets. The atmosphere itself, radiates at much longer wavelengths (mostly in infrared for planets orbiting Sun-like stars). Part of this outgoing radiation is absorbed by trace constituents elsewhere in the atmosphere and part is lost to space. Clouds, if present, can either reflect the incoming stellar radiation or trap the outgoing radiation. If radiative cooling timescales are long compared to dynamic timescales, an adiabatic description can be valid.

The stably stratified well-mixed layers are bounded at the top by a layer in which molecular diffusion and ion drag dominate the advection. On gas giants, convection becomes the dominant energy transport mechanism in the optically thick layers underlying the dynamically active radiative layers. The gas giants in our Solar System are expected to have heat fluxes emanating from their convective interiors. These fluxes can stir the stably stratified dynamic layers from below and hence drive

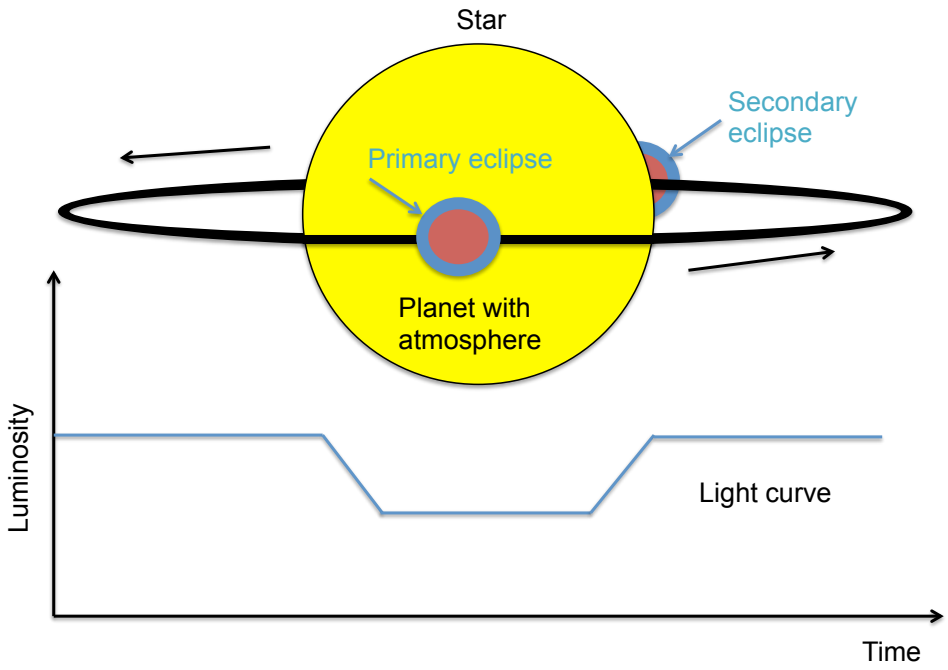

Figure 1.1: Transit method of detection. During the transit (or primary eclipse), the planet blocks a small fraction of star's flux. During occultation (or secondary eclipse) all planetary flux is blocked. The graph below shows the light curve of a star during transit.

vigorous atmospheric motions. For the gas giants in our Solar System, the radiative-convective boundary is situated in the region 0.1-1 bar. For highly irradiated hot-Jupiters the radiative-convective boundary may extend down to as deep as 1000 bars (Guillot and Showman, 2002). However, the location of this boundary on tidally synchronized hot-Jupiters is likely to vary substantially between the day and night sides.

1.2 Observations

As discussed above, most observations of exoplanet atmospheres are of close-in giant planets. In particular, HD 209458b and HD 189733b are the two most studied and observed hot-Jupiters. Both radial velocity and transit methods give the orbital period of a planet — and, by invoking the tidal locking assumption, rotation rate. By combining light curves of stars with transiting planets together with the radial velocity observations, the planet's mass can be obtained. As the planet passes in front of the star, the starlight drops by the amount of the planet-to-star cross-sectional area ratio. Thus, the shape of the light curve can also reveal the size

of the planet, provided the stellar radius is known. This information, combined with the mass gives the bulk density of the planet, and hence some insight into the composition.

Measurements of both the transit (or primary eclipse) and the occultation (or secondary eclipse) can give information about the composition and temperature structure of the planetary atmosphere. The former occurs when the planet passes in front of the star (from the observer's view point), and the latter when the planet passes behind the star (see Figure 1.1). During a transit, a small portion of the starlight is filtered through the upper atmosphere of the planet where it is partially absorbed at certain wavelengths. This gives a transmission spectrum of the planetary atmosphere. If the star's flux spectrum during the secondary eclipse, when the planetary flux is blocked, is subtracted from its flux spectrum just before or after (when both the star and planet contribute to the total flux), only the signal from the planet remains. This gives an emission spectrum for the day-side of the planet and it is possible to infer the brightness temperature of the planet at different wavelengths.

Hot-Jupiter atmospheres are expected to be composed mostly of hydrogen and helium. From the transmission and emission spectra of both HD 209458b and HD 189733b a presence of trace species such as sodium, water, methane, carbon monoxide and carbon dioxide has been inferred (e.g., Charbonneau et al., 2005; Tinetti et al., 2007; Grillmair et al., 2008; Swain et al., 2008). Somewhat inconclusive constraints have also been placed on the horizontal temperature contrasts between day and night sides of HD 209458b and HD 189733b. In some observations (Knutson et al., 2007, 2009; Cowan et al., 2007), light curves of both these planets exhibit 20–30% differences between the day and night side brightness temperatures, which might suggest redistribution of thermal energy by atmospheric circulation. In other observations (e.g., Crossfield et al., 2012), the day-night contrast in brightness temperature is considerably larger, which might suggest low energy redistribution by atmospheric circulation. In addition, pressure-temperature profiles can be indirectly inferred from comparison of models and observations. But, such profiles contain significant assumptions.

Some insight into atmospheric time variability can be obtained by measuring absorption and emission features at different epochs. For example, Grillmair et al. (2008) report discrepancies in emission features between two epochs and Charbonneau et al. (2005) find spectral features in secondary eclipse that are inconsistent with measurements in e.g., Knutson et al. (2007). This indicates that vigorous atmospheric motions in the stably stratified layers will strongly influence observable

properties. Hence, a good understanding of atmospheric dynamics on extrasolar planets is needed (e.g., Cho et al., 2003, 2008; Cho, 2008; Showman et al., 2008, 2009; Menou and Rauscher, 2009; Showman et al., 2011; Thrastarson and Cho, 2010; Watkins and Cho, 2010; Polichtchouk et al., 2014; Cho et al., 2014). Because it is yet not possible to obtain observational constraints on two- or three-dimensional (2D and 3D, respectively) flow structure, hydrodynamic models can be used to gain an understanding into mechanisms that govern circulation and climate on an exoplanet. Such models are also useful for determining the sensitivity of a planet's circulation and climate to changes in physical and dynamical parameters.

1.3 Previous Modelling Work

Large-scale atmospheric circulation of hot-Jupiters has been investigated using both, 2D and 3D hydrodynamic models. Using the one-layer, equivalent barotropic equations, which are a vertically integrated version of the primitive equations solved in this thesis and introduced in Section 2.1, Cho et al. (2003) and Cho (2008) performed global 2D simulations with small-scale turbulent forcing and large-scale deflection of the bottom boundary to represent day-night differential heating experienced by the synchronously rotating planet. Their simulations generally exhibited significant time variability and led to several (one to three), broad zonal jets with flow speeds of $\sim 10^3$ m s^{-1}, and, coherent polar vortices. At large deformation radii (see Chapter 2) or with added angular momentum forcing, the equilibrated equatorial flow was either eastward or westward — depending on the initial condition and forcing details. Global, 2D simulations of hot-Jupiters with the shallow water model with a mass source on the day-side and a sink on the night-side have also been performed by e.g., Langton and Laughlin (2007); Showman and Polvani (2011). Both studies exhibited relatively steady flows; but in the former study, retrograde jets were always produced at the equator whereas, in the latter study, a superrotating jet formed as a consequence of the applied angular momentum source which represents the effect on the upper layer of momentum advection from the lower layer.

Using a 3D general circulation model (GCM), which solves the primitive equations, Cooper and Showman (2006); Cooper and Showman (2005); Showman et al. (2008); Menou and Rauscher (2009); Rauscher and Menou (2010); Thrastarson and Cho (2010, 2011); Heng et al. (2011) performed global simulations, in which the day-side heating and night-side cooling was parametrized with a simple Newtonian cooling scheme. Studies by e.g., Showman et al. (2009); Lewis et al. (2010); Heng and Vogt

(2011); Kataria et al. (2013) also use a primitive equation model, but represent the thermal forcing by a non-gray, cloud-free radiative transfer scheme with opacities calculated assuming local chemical equilibrium. An alternative modeling approach was taken by Dobbs-Dixon and Lin (2008); Dobbs-Dixon et al. (2010), who solve the full compressible Navier-Stokes equations.

With the exception of a few large-scale fast zonal jets, the consensus has not been reached among different simulation results. Some studies show considerable variability and sensitivity to initial conditions (e.g., Cho et al., 2003; Cho, 2008; Thrastarson and Cho, 2010, 2011), while others produce supersonic jets and essentially no time variability or sensitivity to initial conditions (e.g., Cooper and Showman, 2005; Showman et al., 2009; Liu and Showman, 2013). Furthermore, it is not clear whether GCMs, originally tested and developed for the Earth conditions (i.e., ~ 50 m s^{-1} flow speeds, ~ 60 K temperature differences, and, $\sim 10-40$ days thermal relaxation times), can fruitfully simulate markedly different conditions relevant to hot-Jupiters (i.e., fast ~ 1000 m s^{-1} flow speeds, large ~ 1000 K temperature differences, and, short $\sim 0.1-5$ days thermal relaxation times), which are much more exacting on a numerical model.

Due to their ease of observability, a considerable effort has been given to modelling atmospheres of hot-Jupiters. However, the atmospheres of Earth-like exoplanets are also beginning to be accessible to characterization. Terrestrial exoplanet atmospheric modelling has, thus far, received little attention and to date, the focus has mainly been on characterizing general circulation of spin-orbit synchronized Earth-like planets (e.g., Merlis and Schneider, 2010; Heng and Vogt, 2011) rather than unsynchronized Earth-like planets forced by zonally-symmetric thermal forcing. Partly motivated by the terrestrial bodies in our Solar System, there are, however, many theoretical studies characterizing the range of global circulations on terrestrial unsynchronized planets at different rotation rates and radii [e.g.,Williams (2003); Lee et al. (2007); Mitchell and Vallis (2010)].

1.4 Outline of the Thesis

In this thesis, dynamics of large-scale baroclinic jets (i.e., height-dependent jets) in synchronized and unsynchronized hot-Jupiter, and, Earth-like atmospheres is studied using GCMs that solve the traditional hydrostatic primitive equations. The hydrostatic approximation is appropriate for statically stable large-scale flows with horizontal scale of motion greatly exceeding the vertical scale of motion. The hori-

zontal to vertical aspect ratio of global scale flows on hot-Jupiter and the Earth-like planets is large ($\sim$ 100), and therefore the hydrostatic approximation is reasonable. In particular, throughout this thesis a careful attention is paid to the ability of a GCM to accurately simulate large-scale baroclinic jets. In Chapter 2, the traditional hydrostatic primitive equations and the numerical model used in this thesis are reviewed. Chapter 3 investigates stability and equilibration properties of large-scale baroclinic jets in a dynamical parameter regime relevant to hot-Jupiters. Both, linear normal mode analysis and non-linear initial-value calculations are carried out in an adiabatic situation and the focus is placed on baroclinic instability resulting from ageostrophic, high speed (1000 m s^{-1}) prograde equatorial and high latitude retrograde jets. Here, the ability of GCMs to capture baroclinic instability in hot-Jupiter conditions is also discussed. Motivated by the variability in published results of hot-Jupiters by others and the findings in Chapter 3, an extensive intercomparison of five GCMs, which have recently been used to study hot-Jupiter atmospheres, is presented in Chapter 4. Here, the goal is to identify each model's ability to accurately simulate dynamical response to the extreme conditions relevant to hot-Jupiters. Many non-zonally-symmetrically forced simulations of planetary atmospheres, including those of synchronized hot-Jupiters, have been carried out to study equatorial superrotation. However, few studies exist of equatorial superrotation in Earth-like atmospheres under zonally-symmetric thermal forcing. In Chapter 5 transition and dynamical mechanisms leading to superrotation under such conditions are investigated. Finally, conclusions and outlook for future work are given in Chapter 6.

2 Governing Equations and Numerical Model

2.1 The Primitive Equations

The hydrostatic primitive equations govern the large-scale dynamics of planetary atmospheres (e.g., Holton, 1992). In this thesis, the primitive equations with different vertical coordinates are considered. Therefore, it is convenient to present the equations in the generalized coordinate s. In the generalized vertical coordinate s, the "dry" primitive equations in vector form read (e.g., Kasahara, 1974):

$$\frac{\mathrm{D}\mathbf{v}}{\mathrm{D}t} = -\frac{1}{\rho}\boldsymbol{\nabla}_s p - g\boldsymbol{\nabla}_s z - f\mathbf{k}\times\mathbf{v} + \boldsymbol{\mathcal{F}}_\mathbf{v} + \boldsymbol{\mathcal{D}}_\mathbf{v} \tag{2.1a}$$

$$\frac{\mathrm{D}\theta}{\mathrm{D}t} = \frac{\theta}{c_p T}\,\dot{q}_{\mathrm{net}} + \mathcal{D}_\theta \tag{2.1b}$$

$$\frac{\partial p}{\partial s} = -\rho g\,\frac{\partial z}{\partial s} \tag{2.1c}$$

$$0 = \frac{\partial}{\partial s}\left(\frac{\partial p}{\partial t}\right)_s + \boldsymbol{\nabla}_s\cdot\left(\mathbf{v}\frac{\partial p}{\partial s}\right) + \frac{\partial}{\partial s}\left(\dot{s}\frac{\partial p}{\partial s}\right), \tag{2.1d}$$

where

$$\frac{\mathrm{D}}{\mathrm{D}t} \equiv \left(\frac{\partial}{\partial t}\right)_s + \mathbf{v}\cdot\boldsymbol{\nabla}_s + \dot{s}\frac{\partial}{\partial s}\,.$$

Here, $\mathbf{v}(\mathbf{x}, s, t) = (u, v)$ is the (zonal, meridional) velocity in the frame rotating with $\boldsymbol{\Omega}$, the planetary rotation vector, and $\mathbf{x} \in \mathbb{R}^2$; $\dot{s} \equiv \mathrm{D}s/\mathrm{D}t$ is the generalized vertical velocity; $z = z(\mathbf{x}, s, t)$ is the physical height, directed locally upward (in the direction of the unit vector $\mathbf{k}$); $\boldsymbol{\nabla}_s$ is the 2D gradient operator, operating along constant surfaces of $s = s(\mathbf{x}, z, t)$; $\rho(\mathbf{x}, s, t)$ is the density; $p(\mathbf{x}, s, t)$ is the pressure; $f = 2\Omega\sin\phi = 2\boldsymbol{\Omega}\cdot\mathbf{k}$ is the Coriolis parameter, where ϕ is the latitude; $\boldsymbol{\mathcal{F}}_\mathbf{v}(\mathbf{x}, s, t)$ represents momentum sources; $\boldsymbol{\mathcal{D}}_\mathbf{v}(\mathbf{x}, s, t)$ and $\mathcal{D}_\theta(\mathbf{x}, s, t)$ represent momentum and potential temperature sinks, respectively; g is the gravitational acceleration, assumed to be constant and to include the centrifugal acceleration con-

tribution; $\theta(\mathbf{x}, s, t) = T(p_\mathrm{r}/p)^\kappa$ is the potential temperature, where $T(\mathbf{x}, s, t)$ is the temperature, p_r is a constant reference pressure, and $\kappa = \mathcal{R}/c_p$, with $\mathcal{R}$ the specific gas constant and c_p the constant specific heat at constant pressure; and, $\dot{q}_\mathrm{net}(\mathbf{x}, s, t)$ is the *net* diabatic heating rate (i.e., heating minus cooling). The above equation set is closed with the ideal gas equation of state, $p = \rho\mathcal{R}T$. The equation set (2.1) assumes spherical geopotential approximation. This is a valid approximation for the Earth because the rotation rate is not large enough to result in significant oblateness. The oblateness is also expected to be insignificant on hot-Jupiters which are characterized by moderate rotation rates (rotation period of ~ 3 days). However, non-spherical effects due to the tides raised on hot-Jupiters by their host star might be important. Nevertheless, non-spherical effects are not considered in this thesis.

The equation set (2.1a)–(2.1d) is supplemented with the boundary conditions,

$$\dot{s} \;=\; 0 \qquad \text{at} \qquad s = s_\mathrm{T} \tag{2.2a}$$

$$\dot{s} \;=\; \frac{\partial s_\mathrm{B}}{\partial t} + \mathbf{v}_\mathrm{B}\cdot\boldsymbol{\nabla} s_\mathrm{B} \qquad \text{at} \qquad s = s_\mathrm{B}. \tag{2.2b}$$

Here, s_T is the boundary surface at the top of the modelled domain; s_B is the boundary surface at the bottom, at a fixed altitude above the reference height ($z = 0$); and, $\mathbf{v}_\mathrm{B}$ is horizontal velocity at the bottom surface. Boundary conditions (2.2) imply no mass transport through the upper and lower boundary surfaces. Note, if the lower boundary coincides with a constant s-surface (i.e., $s_\mathrm{B} \not\equiv s_\mathrm{B}(\mathbf{x}, t)$), then the boundary condition (2.2b) simply reduces to

$$\dot{s} \;=\; 0 \qquad \text{at} \qquad s = s_\mathrm{B}\,. \tag{2.3}$$

While letting $s \to z$ might be an intuitive choice for a vertical coordinate, in practice it is common to use pressure or other, pressure-based, coordinates: for example, $s \to p$, $s \to \sigma(p)$, or $s \to \eta(p, p_s)$. The σ-coordinate is a surface pressure based coordinate such that $\sigma(p) \equiv p/p_s(\mathbf{x}, t)$, where $p_s(\mathbf{x}, t)$ is a deformable surface pressure. The hybrid η-coordinate is a monotonic function of p, which reduces to a pure p-coordinate at the top, and a pure σ-coordinate at the bottom of the domain. It is defined implicitly through the relation $p(\mathbf{x}, \eta, t) = A_\eta p_r + B_\eta p_s(\mathbf{x}, t)$, where $A_\eta, B_\eta \in [0, 1]$. In the p-coordinate, the continuity equation (2.1d) takes on a simple diagnostic form. However, the p-coordinate system poses a computational disadvantage when modelling a planetary atmosphere with a solid surface, if topography is present. In this case, the boundary condition (2.2b) becomes difficult to handle. The σ-coordinate or the η-coordinate circumvents this problem because the planet's

surface does not cross a vertical coordinate surface in either coordinate systems.

The momentum equation (2.1a), the heat equation (2.1b) and the continuity equation (2.1d) are derived from the full Navier-Stokes equations, together with the energy equation, equation of state, and boundary conditions in spherical geometry. Two approximations are made to the Navier-Stokes equations: 1) the "shallow atmosphere" and 2) the "traditional" approximations. The first assumes that the height of the atmosphere $z_{\rm T}$ is small compared to the planetary radius $R_{\rm p}$ (i.e., $z_{\rm T} \ll R_{\rm p}$). The second is formally valid in the limit of strong stratification, when the Prandtl ratio $(N/\Omega)^2 >> 1$, where N is the Brunt-Väisälä frequency (see equation (2.16)). In the traditional approximation, the Coriolis and metric terms involving vertical velocity are omitted. Metric terms arise from representing the equations (2.1a – 2.1d) in spherical coordinates as the directions of the coordinate axes change with position on the sphere. In the next section, the validity of the above approximations is discussed.

As can be seen from equation (2.1c), the vertical momentum equation describes the atmosphere in hydrostatic balance. This approximation restricts the vertical motions to be slow compared to the horizontal motions. This restriction is equivalent to assuming the vertical length scale of motion to be small compared to the horizontal length scale. The hydrostatic primitive equations with the boundary conditions (2.2), filter vertically propagating sound waves and horizontally propagating waves that travel faster than the speed of sound. The only waves that remain are the large-scale slowly evolving Rossby, or planetary, waves and smaller-scale faster evolving gravity waves. The horizontally propagating external gravity, or Lamb, wave travels at the speed of sound and is the fastest wave permitted.

2.2 Parameter Regime

Because HD 209458b is one of the most studied and observed hot-Jupiters, primarily, physical parameters appropriate for HD 209458b are chosen in Chapters 3 and 4. In Chapter 5, physical parameters for the Earth are adopted. Typical parameter values for both are listed in Table 2.1. To appreciate how different the hot-Jupiter parameter regime is compared to the gas giant planets in our Solar System, physical parameters for Jupiter are also listed in Table 2.1 for convenience. Two of the most obvious differences between hot-Jupiters and the Solar System giant planets are: 1) the equilibrium temperature, and 2) the rotation rate. These differences and their implications are discussed further below.

Table 2.1: Measured and estimated parameter values for hot-Jupiter HD 209458b, Jupiter and the Earth. Here, g is gravity; R_p is equatorial radius; M_p is the planetary mass; a is the semi-major axis; P is period; Ω is rotation rate; $\mathcal{R}$ is gas constant; c_p is specific heat at constant pressure; H_p is pressure scale height; $T_{\rm eq}$ is equilibrium temperature; and, N is Brunt-Väisälä frequency. For HD 209458b, g, R_p, M_p, a, and P are measured from radial velocity and transit observations. To obtain Ω for HD 209458b, spin-orbit synchronization is assumed. An estimate of H_p is obtained from $H_p = \mathcal{R}T_{\rm eq}/g$, where $\mathcal{R}$ for HD 209458b is estimated assuming same composition as for Jupiter (i.e., 90% H_2, 10% He), and, $T_{\rm eq}$ is calculated from equation (2.4).

Parameter	HD 209458b	Jupiter	Earth	Units
g	9.0	25.9	9.8	m s^{-2}
R_p	10^8	7.0×10^7	6.37×10^6	m
M_p	1.35×10^{27}	1.90×10^{27}	5.97×10^{24}	kg
a	0.05	5.2	1.0	AU
P	3.5	4333	365	days
Ω	2.1×10^{-5}	1.6×10^{-4}	7.3×10^{-5}	s^{-1}
$\mathcal{R}$	3.5×10^3	3.5×10^3	287	J kg^{-1} K^{-1}
c_p	1.23×10^4	1.23×10^4	1004	J kg^{-1} K^{-1}
H_p	6×10^5	2.7×10^4	10^4	m
$T_{\rm eq}$	1500	110	288	K
N	2×10^{-3}	2×10^{-2}	10^{-2}	s^{-1}

The equilibrium temperature $T_{\rm eq}$ of a planet can be estimated, in a crude way, as the black-body "effective" temperature

$$T_{\rm eq} \approx T_{\rm eff} = \sqrt{\frac{R_*}{2a}}(1-\alpha)^{1/4}T_* = \left\{\frac{(1-\alpha)S}{4\sigma}\right\}^{1/4}. \tag{2.4}$$

Here, α is the bond albedo, i.e., the fraction of reflected to total intercepted stellar radiation, integrated over all wavelengths and directions; R_* is the radius of a star; a is the orbital semi-major axis; T_* is the effective temperature of a star; $S \equiv \sigma T_*^4 (R_*/a)^2$ is the stellar radiation flux incident upon the planet; and, $\sigma = 5.67 \times 10^{-8}$ W m^{-2} K^{-4} is the Stefan-Boltzmann constant. Recall that hot-Jupiters are found to orbit their host star on close-in orbits (i.e., $a \lesssim 0.05$ AU). Assuming that hot-Jupiters orbit Sun-like stars with $R_* \sim 7\times10^8$ m, and, $T_* \sim 6000$ K, and taking $\alpha \approx 0.25$ (upper limit obtained for HD 209458b in Rowe et al., 2006), equation (2.4) gives 1000 K $< T_{\rm eq} <$ 2000 K. Similar estimates for the Earth and Jupiter give

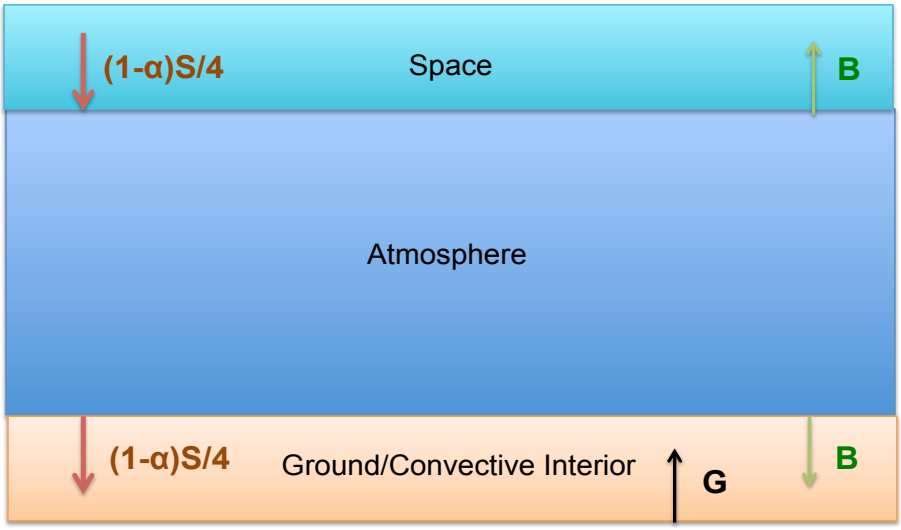

Figure 2.1: Slab model of the stably stratified radiative atmosphere lying above the ground or the convective layer. $(1-\alpha)S/4$ is the net solar radiation, B is the energy flux in and out of the atmosphere, and G is the energy flux out of the "ground".

$T_{\rm eq} \sim 255$ K and $T_{\rm eq} \sim 100$ K, respectively. However, unlike a black body, a real atmosphere is not completely transparent to the outgoing infrared radiation and the lower layers of the atmosphere can have significantly warmer temperatures. For the Earth, surface equilibrium temperature is warmer, $T_{\rm eq} \sim 288$ K, and $T_{\rm eq} \sim 255$ K is more characteristic of a temperature in the upper troposphere.

Due to the expected high equilibrium temperatures, the radiative relaxation timescales in the stably stratified radiative layers of hot-Jupiter atmospheres can be very short—much shorter than for the Solar System bodies. The time taken to establish a radiative equilibrium can be estimated by considering fluxes in and out of the ground (or, for gas giants, the convective layer opaque to the incoming stellar radiation) and the stably stratified atmosphere above (e.g., James, 1995). For simplicity, the atmosphere here is crudely represented as a single slab of gas (see Figure 2.1). Let G be the energy flux out of the ground, and B be the energy flux in and out of the atmosphere and assume that the atmosphere is totally opaque to the outgoing radiation (mostly infrared for planets orbiting Sun-like stars) and transparent to the incoming radiation (mostly visible for planets orbiting Sun-like stars). In radiative equilibrium fluxes in and out of the ground must balance:

$$(1-\alpha)\frac{S}{4} + B = G, \tag{2.5}$$

as must the fluxes in and out of the atmosphere:

$$2B = G. \tag{2.6}$$

If the atmospheric temperature T_a is disturbed away from the equilibrium, equation (2.6) no longer holds. Instead

$$\frac{c_p p}{g}\frac{dT_a}{dt} = G - 2B, \tag{2.7}$$

where $c_p p/g$ is the thermal capacity of an atmospheric column of unit cross sectional area. With the aid of equations (2.5) and (2.4), equation (2.7) can be rewritten as

$$\frac{c_p p}{g}\frac{dT_a}{dt} = -B + \sigma T_{\rm eq}^4, \tag{2.8}$$

and the flux in and out of the atmosphere B can be approximated using Stefan's law as $B = \sigma T_a^4$. Assuming small departures of temperature $\triangle T$ from the equilibrium $T_{\rm eq}$, such that $T_{\rm eq} = T_a - \triangle T$ and $|\triangle T| << T_{\rm eq}$, equation (2.9) can be linearized about $T_{\rm eq}$, to give

$$\frac{d(\triangle T)}{dt} = -\frac{4\sigma T_{\rm eq}^3 g}{p c_p}\triangle T. \tag{2.9}$$

The solution to this equation yields the estimate of the radiative time scale

$$\tau_{\rm th} \sim \frac{c_p\ p}{4\sigma\ g\ T_{\rm eq}^3}. \tag{2.10}$$

Equation (2.10) can be used to estimate radiative time scales on an extrasolar planet. However, in deriving equation (2.10), a single slab model of an atmosphere completely transparent to the incoming stellar radiation and totally opaque to the outgoing radiation is assumed. A more realistic model of an atmosphere would account for a more complicated vertical structure, have depth-dependent opacities, and include other processes such as scattering of the incoming radiation by atmospheric particles. More importantly, large temperature contrasts ($\sim 100 - 1000$ K) are often observed in simulations of spin-orbit synchronized hot-Jupiters. Therefore, departures from the equilibrium $T_{\rm eq}$ are not typically small (i.e., $|\triangle T| \sim T_{\rm eq}$) and the application of equation (2.10) in estimating radiative timescales on spin-orbit synchronized hot-Jupiters is somewhat questionable. Bearing in mind these caveats, substitution of estimated values of parameters for HD 209458b (see Table 2.1) into equation (2.10) yields $\tau_{\rm th} \sim 45$ h at $p = 1$ bar level. Similar estimates for the Earth

and Jupiter result in considerably longer radiative time scales: $\tau_{\rm th} \sim 450$ h and $\tau_{\rm th} \sim 4.5{\times}10^4$ h, respectively. Equation (2.10) will be used to crudely estimate radiative time scales when considering diabatic condition in Chapters 4 and 5.

Assuming spin-orbit synchronization, the implied rotation periods for hot-Jupiters are typically 2-5 Earth days ($50 - 120$ h)—much slower than for Jupiter (10 h) or other gas giants in our Solar System. The importance of rotation can be estimated by performing a scale analysis on the horizontal equations of motion (equation (2.1a)). If the horizontal length scale of motion scales as L and a typical flow speed scales as U, then the advective term scales as U^2/L, and the Coriolis term scales as $f\ U$. The ratio of the advective to the Coriolis term is the Rossby number,

$$Ro \equiv \frac{U}{fL}. \tag{2.11}$$

For $Ro << 1$, the Coriolis terms dominate the advective terms in the horizontal direction. In the absence of momentum sources/sinks, the only terms that can balance the horizontal Coriolis force are the first two terms on the right hand side of equation (2.1a). This balance is the geostrophic balance. If pressure (p) is taken as a vertical coordinate, the first term on the right hand side of equation (2.1a) vanishes on isobaric surfaces and the geostrophic balance becomes

$$f\mathbf{k}\times\mathbf{v} \approx -g\boldsymbol{\nabla}_p z \tag{2.12}$$

or in spherical polar coordinates

$$f\ u \ \approx \ -\frac{1}{R_{\rm p}}\frac{\partial\Phi}{\partial\phi}, \qquad\qquad f\ v \ \approx \ \frac{1}{R_{\rm p}\cos\phi}\frac{\partial\Phi}{\partial\lambda}, \tag{2.13}$$

where $\Phi = gz$ is the specific geopotential above R_p and λ is longitude. Differentiating these equations with respect to p and making use of the hydrostatic balance and the definition of potential temperature, leads to the thermal wind balance (Pedlosky, 1986, e.g.,) that relates the vertical shear of the horizontal wind to the horizontal temperature gradients:

$$\frac{\partial u}{\partial p} = \frac{\mathcal{R}}{fpR_{\rm p}}\left(\frac{\partial T}{\partial\phi}\right)_p, \qquad \frac{\partial v}{\partial p} = -\frac{\mathcal{R}}{fpR_{\rm p}\cos\phi}\left(\frac{\partial T}{\partial\lambda}\right)_p. \tag{2.14}$$

On large scales (i.e., $L \sim R_p$) and away from the equator, geostrophic balance holds reasonably well for both the Earth and Jupiter as both lie in low Rossby number regime $Ro \ \sim \ 0.001 - 0.1$. Typical value for U for hot-Jupiters is unknown and

can only be crudely estimated from simulations. If U is taken as 200 – 2000 m s^{-1}, global scale Rossby number for HD 209458b is $Ro \sim 1 - 0.1$. Bearing in mind the caveats of such simple scaling analysis, the above estimates of Ro imply that the Coriolis force is less important on hot-Jupiters than on the Earth or Jupiter.

A typical length scale of the most unstable baroclinic mode is the Rossby deformation length scale

$$L_{\rm D} \equiv \frac{NH}{f}, \tag{2.15}$$

where H is the vertical scale of the flow and N is the Brunt-Väisälä frequency (see equation (2.16)). Coherent vortices often have horizontal scales close to or larger than $L_{\rm D}$. $L_{\rm D}$ also sets the range over which flow structures can effectively interact. In a stably stratified atmosphere, an adiabatically displaced fluid parcel oscillates at the Brunt-Väisälä frequency

$$N = \sqrt{\frac{g}{T}\left(\frac{\partial T}{\partial z} + \frac{g}{c_p}\right)}. \tag{2.16}$$

For HD 209458b, N is estimated to be $\sim 2 \times 10^{-3}$ s^{-1} corresponding to the buoyancy oscillation period of under one hour. This estimate is obtained from equation (2.16) by assuming that the vertical temperature gradient $\partial T/\partial z$ is negligible[1] compared to the dry adiabatic lapse rate g/c_p, and that $T \approx T_{\rm eq}$. Equation (2.16) would yield stronger stratification (i.e., higher N) for $\partial T/\partial z > 0$ and weaker stratification (i.e., lower N) for $\partial T/\partial z < 0$ and static instability (i.e., $N < 0$) if $\partial T/\partial z < -g/c_p$. For the Earth and Jupiter (in the stratosphere) the stratification is stronger: $N \sim 10^{-2}$ s^{-1} (this estimate is for the Earth in the troposphere) corresponding to shorter buoyancy oscillation periods of ∼10 min.

If the vertical scale H is taken to be the pressure scale height $H_p = \mathcal{R}T/g$, the estimate of $L_{\rm D}$ for HD 209458b at mid-latitudes is $L_{\rm D} \sim 4{\times}10^7$ m, giving $L_{\rm D}/R_p \sim O(1)$. This implies that the dominant flow structures on hot-Jupiters can be planetary in scale (e.g., Cho et al., 2003). In comparison, the dominant structures on the Earth and Jupiter are much smaller with $L_{\rm D}/R_p \sim 0.01$ for Jupiter, and $L_{\rm D}/R_p \sim 0.1$ for the Earth.

In a stratified rotating fluid, the motion is predominantly layer-wise and quasi-2D. In this regime, turbulent flow exhibits inverse cascade of energy to larger scales as a consequence of successive vortex mergers, and, forward cascade of enstrophy to smaller scales (e.g., Vallis, 2006). On a rotating sphere, the meridional gradient of

[1]Based on radiative-transfer model calculations (e.g., Iro et al., 2004) assuming $\partial T/\partial z = 0$ in dynamically active radiative layers is reasonable.

the Coriolis parameter $\beta \equiv \partial f/\partial y$ provides a restoring force on the growing eddies in the meridional (north-south) direction but none in the zonal (east-west) direction. As a consequence of this anisotropy, vortices grow to the largest available scale in the zonal direction, forming zonal bands and jets (Rhines, 1975). The meridional width of the jets is roughly characterized by the Rhines scale

$$L_\beta = \pi\sqrt{\frac{U}{\beta}}, \tag{2.17}$$

where $\beta \equiv R_\mathrm{p}^{-1}(\partial f/\partial\phi) = 2\Omega\cos\phi/R_\mathrm{p}$ is the meridional gradient of the Coriolis parameter. Thus, the expected number of bands on a sphere can be estimated to be

$$N_\mathrm{jets} \sim \pi R_\mathrm{p}/L_\beta \sim \sqrt{2\Omega R_\mathrm{p}/U}. \tag{2.18}$$

This "β mechanism" has been relatively successful in explaining the number, size, and amplitudes of zonal jets on Solar System planets (e.g., Williams, 1978; Cho and Polvani, 1996). Taking $U \sim 50$ m s^{-1} for both Jupiter and the Earth, equation (2.18) gives an estimate of ~ 20 and ~ 4 jets, respectively—similar to the number observed. For hot-Jupiters, for $200 < U < 2000$ m s^{-1}, the estimate is 1–3 jets and hence the dynamical structures are expected to be more global in scale than on Solar System giant planets and the Earth. Consistent with these estimates, 2D simulations of hot-Jupiter atmospheres forced at small scales obtain 1–3 jets (Cho et al., 2003; Cho, 2008). Published 3D simulations of hot-Jupiter atmospheres forced by day-night heating contrast (e.g., Cooper and Showman, 2005; Showman et al., 2008; Menou and Rauscher, 2009; Rauscher and Menou, 2010; Thrastarson and Cho, 2010, 2011) also produce 1–3 jets. However, in this case the mechanism is unlikely to be the "β mechanism" as such simulations are forced at scales comparable to or larger than the jet scales and hence lack the inverse cascade.

Before describing the numerical model used in this thesis, a brief discussion about the validity of the primitive equation model is needed. In this thesis, baroclinic jet dynamics is studied in the atmospheres extending in height over less than five scale heights. This implies that for hot-Jupiters $z_\mathrm{T}/R_\mathrm{p} < 0.03$ and for the Earth $z_\mathrm{T}/R_\mathrm{p} < 0.01$, and hence, the shallow atmosphere assumption is well met. Because for large scales $(N/\Omega)^2 >> 1$ for both hot-Jupiters and the Earth (see Table 2.1 for the values of N and Ω), the traditional approximation is also valid. The condition for neglect of the Coriolis terms involving vertical velocities from the zonal momentum equation is $2\Omega H_\mathrm{p}\cos\phi/U << 1$. This condition is well met, as the quantity

$2\Omega H_{\rm p}\cos\phi/U$ takes a value of $\sim 0.03\cos\phi$ for both the Earth and hot-Jupiters (assuming $U \sim 50$ m s^{-1} for the Earth and $U \sim 1000$ m s^{-1} for hot-Jupiters). Furthermore, the hydrostatic description is justified since non-hydrostatic effects are important for scales much smaller than considered in this thesis. Non-hydrostatic effects are expected to become important for horizontal resolutions exceeding 400 total wavenumbers retained in the spherical harmonic expansion (e.g., Daley, 1988).

2.3 Numerical Model

To solve the dry, non-linear primitive equations in spherical "domain", the parallel dynamical core BOB (Scott et al., 2003) is used in most of the simulations in this thesis. Other models are also used in the GCM intercomparison study in Chapter 4 and will be described there. The dynamical core is essentially the engine of a comprehensive GCM, which is what remains when all the sophisticated physical parametrizations (e.g., convection, radiation, wave-drag, etc.) have been stripped away. In this thesis, none of the sophisticated physical parametrizations are included in the model. Only Newtonian relaxation to the prescribed "equilibrium" temperature is used to represent diabatic heating/cooling in Chapters 4 and 5 and linear momentum (Rayleigh) drag is used to represent surface boundary layer friction in Chapter 5.

The BOB core uses the pseudospectral algorithm (Orszag, 1970; Eliasen et al., 1970; Canuto et al., 2007) for the horizontal direction. Equations (2.1) in the vorticity-divergence form are transformed with triangular truncation (i.e., $M = N$, where M is the maximum zonal wavenumber and N is the maximum total wavenumber retained in the spherical harmonic expansion). Given M and N, all the nonlinear products in the full set of equations (2.1) are first evaluated in physical space on a Gaussian grid with enough points, in principle, to eliminate aliasing errors and then transformed to spectral space. The linear terms are directly transformed.

For the vertical direction, a standard second-order finite difference scheme is used. In this direction, the grid is equally spaced in p-coordinates. Note that BOB and all other cores used in this thesis use the Lorenz grid (Lorenz, 1960), in which the vertical velocity is defined at the boundary of the layers and the prognostic variables (e.g., vorticity, divergence, and temperature/potential temperature) are defined at the centres of the layers. The grid allows boundary conditions of no flux at the top and bottom of the domain to be easily fulfilled. However, a spurious computational mode is admitted, arising from an extra degree of freedom introduced in the potential

temperature (Arakawa and Moorthi, 1988). In the simulations in this thesis, this can lead to small-amplitude oscillations in the temperature field on the timescale of a timestep.

As for the time integration, BOB uses a semi-implicit leap-frog scheme. In the semi-implicit formulation, terms associated with gravity waves are treated implicitly whereas other terms are treated explicitly. A small Robert-Asselin time filter coefficient ϵ (Robert, 1966; Asselin, 1972) is applied at every timestep in each layer to filter the computational mode arising from using the second-order time-marching scheme (see, e.g., Thrastarson and Cho, 2010). To integrate the equations over long simulation durations, explicit dissipation is applied to the prognostic variables so that artificial accumulation of energy at small scales is prevented (e.g., Cho and Polvani, 1996; Thrastarson and Cho, 2011). The dissipations, $\mathcal{D}_{\mathbf{v},\theta}$ in equations (2.1), are in the form of a "hyperdissipation" operator (see equation (2.20) below).

2.3.1 The BOB Equations in Continuous Form

BOB solves equations (2.1) in the Eulerian framework in the p-coordinate:

$$\frac{\partial \zeta}{\partial t} = \mathbf{k}\cdot\boldsymbol{\nabla}\times\mathbf{n}_{\mathrm{p}} + \mathcal{D}_{\zeta} \tag{2.19a}$$

$$\frac{\partial \delta}{\partial t} = \boldsymbol{\nabla}\cdot\mathbf{n}_{\mathrm{p}} - \nabla^2\big(E+\Phi\big) + \mathcal{D}_{\delta} \tag{2.19b}$$

$$\frac{\partial \theta}{\partial t} = -\boldsymbol{\nabla}\cdot\big(\theta\,\mathbf{v}\big) - \frac{\partial(\omega\theta)}{\partial p} + \frac{\theta}{c_p T}\dot{q}_{\mathrm{net}} + \mathcal{D}_{\theta} \tag{2.19c}$$

$$\frac{\partial \Phi}{\partial \xi} = -c_p\,\theta \tag{2.19d}$$

$$\frac{\partial \omega}{\partial p} = -\delta, \tag{2.19e}$$

where $\zeta = \mathbf{k}\cdot(\boldsymbol{\nabla}\times\mathbf{v})$ is the relative vorticity in the vertical direction;

$$\mathbf{n}_{\mathrm{p}} = -\big(\zeta+f\big)\mathbf{k}\times\mathbf{v} - \delta\mathbf{v} - \frac{\partial(\omega\mathbf{v})}{\partial p}\,;$$

$\delta = \boldsymbol{\nabla}\cdot\mathbf{v}$ is the divergence; $E = (\mathbf{v}\cdot\mathbf{v})/2$ is the specific kinetic energy; $\xi = (p/p_{\mathrm{r}})^{\kappa}$; $\omega = \mathrm{D}p/\mathrm{D}t$ is the vertical velocity, where

$$\frac{\mathrm{D}}{\mathrm{D}t} \equiv \frac{\partial}{\partial t} + \mathbf{v}\cdot\boldsymbol{\nabla} + \omega\frac{\partial}{\partial p}$$

is the material derivative with $\boldsymbol{\nabla}$ operating along constant surfaces of p; and the diffusion terms $\mathcal{D}_\chi$, where $\chi = \{\zeta, \delta, \theta\}$, are given by:

$$\mathcal{D}_\chi \;=\; \nu_{2\mathfrak{p}} \left[\nabla^2 + \mathcal{C}\right]^p \chi \,, \tag{2.20}$$

where $\mathfrak{p}$ (different from p, the pressure) is the order of the hyperdissipation operator; $\nu_{2\mathfrak{p}}$ is the hyperdissipation coefficient; and, $\mathcal{C} = (2/R_p^2)^{\mathfrak{p}}$ is a correction term added to the vorticity and divergence equations to prevent damping of uniform rotations for angular momentum conservation.

BOB has an additional constraint of no vertically integrated divergence over the whole atmosphere. This constraint excludes the divergent "shallow-water mode" (i.e., the Lamb mode), which has a barotropic vertical structure, and increases the computationally stability of the model. With this additional constraint, the boundary conditions (2.2) become

$$\omega = 0 \qquad \text{at} \qquad p = 0,\ p_{\text{B}}, \tag{2.21}$$

and the lower boundary always coincides with a constant p-surface. The above boundary conditions entail zero flux of any quantity through the upper and lower pressure surfaces.

As already discussed, using the p-coordinate system with the boundary conditions (2.21) means that the continuity equation (2.1c) simplifies to a simple diagnostic form (equation (2.19d)). Thus, BOB only integrates three equations—that is, only three variables are prognostic. In the absence of sources and sinks (including hyperdissipation), the vertical discretization scheme preserves the global conservation properties of absolute angular momentum, potential temperature and total energy.

Appendix 2.A Numerical Methods

2.A.1 Finite Difference Method

The derivative of a function $\psi(x)$ at point x_0 can be approximated as forward, backward or centered difference:

$$\frac{d\psi}{dx}(x_0) = \lim_{\Delta x \to 0} \frac{\psi(x_0 + \Delta x) - \psi(x_0)}{\Delta x} \tag{2.22}$$

$$\frac{d\psi}{dx}(x_0) = \lim_{\Delta x \to 0} \frac{\psi(x_0) - \psi(\Delta x - x_0)}{\Delta x} \tag{2.23}$$

$$\frac{d\psi}{dx}(x_0) = \lim_{\Delta x \to 0} \frac{\psi(x_0 + \Delta x) - \psi(x_0 - \Delta x)}{2\Delta x} \tag{2.24}$$

where Δx is the grid spacing in the x-direction. Provided $\psi(x)$ is sufficiently smooth, the accuracy of the finite difference methods can be determined by expanding $\psi(x_0 \pm \Delta x)$ terms in Taylor series about x_0. For example, substituting

$$\psi(x_0+\Delta x) = \psi(x_0)+\Delta x\frac{d\psi}{dx}(x_0)+\frac{(\Delta x)^2}{2}\frac{d^2\psi}{dx^2}(x_0)+\frac{(\Delta x)^3}{6}\frac{d^3\psi}{dx^3}(x_0)+O[(\Delta x)^4] \tag{2.25}$$

into equation (2.22) gives

$$\frac{\psi(x_0 + \Delta x) - \psi(x_0)}{\Delta x} - \frac{d\psi}{dx}(x_0) = \frac{\Delta x}{2}\frac{d^2\psi}{dx^2}(x_0) + \frac{(\Delta x)^2}{6}\frac{d^3\psi}{dx^3}(x_0) + O[(\Delta x)^3]. \tag{2.26}$$

The right hand side of equation (2.26) is the truncation error. The lowest power of Δx determines the order of accuracy of the scheme—hence the forward scheme is first-order accurate. Similar treatment reveals that while the backward differencing is also first-order accurate, the centered difference is second-order accurate.

2.A.2 Leapfrog Time-Differencing

The differential equation of form

$$\frac{d\psi}{dt} = F(\psi) \tag{2.27}$$

can be solved using the three-time-level leapfrog scheme. If ζ^n is the numerical approximation to $\psi(n\Delta t)$, where Δt is the timestep size, and $n = 1, 2, ..., T$, where T is the total number of timesteps, the general form of the leapfrog scheme is

$$\zeta^{n+1} = \zeta^{n-1} + 2\Delta t F(\zeta^n), \tag{2.28}$$

where superscript denotes the timestep. The numerical error introduced by the leapfrog time-differencing scheme in wave-propagation problems can be examined by considering the solution to the oscillation equation

$$\frac{d\psi}{dt} = i\varpi\psi, \tag{2.29}$$

where ϖ is a real constant representing frequency. If the leapfrog scheme is applied to equation (2.29), the result is

$$\zeta^{n+1} = \zeta^{n-1} + 2i\varpi\Delta t\zeta^n. \tag{2.30}$$

The exact amplification factor A_e arising from the application of the leapfrog scheme on equation (2.29) over one timestep is $A_\mathrm{e} \equiv e^{i\varpi\Delta t}$. A numerical amplification factor may be defined as $\zeta^{n+1} = A\zeta^n$, such that equation (2.30) satisfies quadratic equation

$$A^2 - 2i\varpi\Delta tA - 1 = 0, \tag{2.31}$$

whose roots are

$$A_\pm = i\varpi\Delta t \pm \sqrt{1-\varpi^2\Delta t^2} \approx i\varpi\Delta t \pm (1 - \frac{1}{2}\varpi^2\Delta t^2 - \frac{1}{16}\varpi^4\Delta t^4 + O[(\varpi\Delta t)^6]) \tag{2.32}$$

In the limit of good numerical resolution $\varpi\Delta t \to 0$, $A_+ \to 1$ and $A_+ \to -1$. Hence, the numerical solution behaves in two different ways. The mode associated with A_+ is "physical" and the mode associated with A_- is "numerical" as it arises as an artifact of the numerical computation. A comparison of the expression for the physical mode with the asymptotic behaviour of the exact amplification factor

$$A_\mathrm{e} = e^{i\varpi\Delta t} = 1 + i\varpi\Delta t - \frac{(\varpi\Delta t)^2}{2} - i\frac{(\varpi\Delta t)^3}{6} + O[(\varpi\Delta t)^4] \tag{2.33}$$

reveals that the local truncation error (i.e., arising from taking one time step only) of the leapfrog scheme is $O[(\varpi\Delta t)^3]$.

For $\varpi^2\Delta t^2 < 1$, $|A_\pm| = 1$ and both the physical and computational modes are stable. In the case $\varpi^2\Delta t^2 > 1$,

$$A_\pm = |i\varpi\Delta t \pm i\sqrt{\varpi^2\Delta t^2 - 1}| > |i\varpi\Delta t| > 1, \tag{2.34}$$

and the leapfrog scheme is unstable. For $\varpi^2\Delta t^2 = 1$, $A_+ = A_-$ and the general

solution to ζ^n is

$$\zeta^n = C_1(i\varpi\Delta t)^n + C_2 n(i\varpi\Delta t)^n. \tag{2.35}$$

The magnitude of this solution grows as a function of timestep and hence, the scheme is unstable for $\varpi^2\Delta t^2 = 1$. The relative phase change is defined as

$$R = (\varpi\Delta t)^{-1} \arctan\left(\mathfrak{Im}[A]/\mathfrak{R}[A]\right), \tag{2.36}$$

which is the ratio of the phase advance produced by one timestep of the scheme to the change is phase experienced by the true solution. For leapfrog scheme

$$R_{\pm} = \frac{1}{\varpi\Delta t} \arctan\left(\frac{\pm\varpi\Delta t}{\sqrt{1-\varpi^2\Delta t^2}}\right) \tag{2.37}$$

and the computational and physical modes oscillate in opposite directions. In the limit of good time-resolution the leapfrog time-differencing is accelerating as

$$R_{+} \approx 1 + \frac{(\varpi\Delta t)^2}{6}. \tag{2.38}$$

The leapfrog computational mode can be controlled by incorporating a second-derivative time filter, the Robert-Asselin filter (Robert, 1966; Asselin, 1972), to the time integration cycle, such that each leapfrog step

$$\zeta^{n+1} = \overline{\zeta^{n-1}} + 2i\varpi\Delta t\zeta^n \tag{2.39}$$

is followed by the filtering operation

$$\overline{\zeta^n} = \zeta^n + \epsilon(\overline{\zeta^{n-1}} - 2\zeta^n + \zeta^{n+1}). \tag{2.40}$$

Similarly, it can be shown that the amplification factor for the filtered physical mode is

$$A_{+\text{filter}} = 1 + i\varpi\Delta t - \frac{1}{2(1-\epsilon)}\varpi^2\Delta t^2 + O[(\varpi\Delta t)^4]. \tag{2.41}$$

Therefore the filtering degrades the global truncation error from second-order to first-order. It can also be shown that Robert-Asselin filter increases the phase error as

$$R_{+\text{filter}} \approx 1 + \frac{1+2\epsilon}{6(1-\epsilon)}(\varpi\Delta t)^2. \tag{2.42}$$

2.A.3 Spectral Method

Suppose that a function $\psi(x)$ is periodic on the domain $-\pi < x < \pi$ and that its first derivative is continuous. Then ψ and $\partial\psi/\partial x$ can be represented by the convergent Fourier series (or any other series whose expansion functions form and orthogonal set)

$$\psi(x) = \sum_{k=-\infty}^{\infty} a_k e^{ikx}, \tag{2.43}$$

and

$$\frac{d\psi}{dx} = \sum_{k=-\infty}^{\infty} ika_k e^{ikx}, \tag{2.44}$$

where k is the wavenumber and a_k are Fourier coefficients. In spectral method, the series (2.43) will be truncated at a wavenumber N, but a_k for $|k| \leq N$ are identical as in the infinite series (2.43). Therefore, the error in the spectral representation of $d\psi/dx$ is

$$E = \sum_{|k|>N} ika_k e^{ikx}. \tag{2.45}$$

If the sth derivative of ψ is piece-wise continuous and all lower derivatives are continuous, then the Fourier coefficients satisfy the inequality

$$|a_k| \leq \frac{C}{|k|^s}, \tag{2.46}$$

where C is a constant. Hence,

$$|E| \;\leq\; 2\sum_{k=N+1}^{\infty} \frac{C}{|k|^{p-1}} \;\leq\; 2C\int_N^{\infty} \frac{dp}{p^{s-1}} = \frac{2C}{s-2}\left(\frac{1}{N^{s-2}}\right). \tag{2.47}$$

The spectral computation is equivalent to a finite difference computation with grid spacing $\Delta x = 2\pi/(2N+1)$ and therefore $\Delta x \propto N^{-1}$ and

$$|E| \leq C_2(\Delta x)^{s-2}, \tag{2.48}$$

where C_2 is another constant. Thus, if ψ is infinitely differentiable the truncation error goes to zero faster than any finite power of Δx and hence in this case the spectral method is "infinite-order" accurate. Note however, that in turbulent flows, such as those considered in the most part of this thesis, ψ is not infinitely differentiable and the statement of infinite-order accuracy does not apply.

For the horizontal discretization in spherical geometry, instead of equation (2.43),

the prognostic variable $\psi(\mu, \lambda)$, where $\mu \equiv \sin\phi$, is represented as the truncated series of spherical harmonics

$$\psi(\mu, \lambda) = \sum_{m=0}^{M} \sum_{n=|m|}^{N(m)} \psi_n^m Y_n^m(\mu, \lambda), \tag{2.49}$$

where M and N determine the order of zonal and meridional truncation respectively and

$$Y_n^m(\mu, \lambda) = P_n^m(\mu) e^{im\lambda} \tag{2.50}$$

are the spherical harmonics (the eigenfunctions of the Laplacian operator in spherical geometry), where $P_n^m(\mu)$ are the associated Legendre polynomials with normalization conditions

$$\frac{1}{2} \int_1^{-1} d\mu P_n^m P_{n'}^m = \delta_{n,n'} \tag{2.51}$$

$$\frac{1}{4\pi} \int_1^{-1} d\mu \int_0^{2\pi} d\lambda Y_n^{*m} Y_{n'}^{m'} = \delta_{m,m'} \delta_{n,n'}. \tag{2.52}$$

The coefficients ψ_n^m are given by

$$\psi_n^m = \frac{1}{4\pi} \int_{-1}^{1} d\mu \int_0^{2\pi} d\lambda Y_n^{*m}(\mu, \lambda) \psi(\mu, \lambda). \tag{2.53}$$

The integral over λ is performed via the Fast Fourier Transform (FFT) and the integral over μ is performed via Gaussian quadrature on a Gaussian grid

$$\psi_n^m = \sum_{i=1}^{I} \psi^m(\mu_i) P_n^m(\mu_i) w_i, \tag{2.54}$$

where I is the number of meridional grid points, μ_i are the Gaussian grid points in the meridional direction, and w_i are the Gaussian weights.

3 Baroclinic Instability on Hot-Jupiters

Baroclinic instability is investigated in flow conditions relevant to hot-Jupiters. The instability is important for transporting and mixing heat, as well as for influencing large-scale variability on the planets. Both linear normal mode analysis and non-linear initial value simulations are carried out – focusing on the freely-evolving, adiabatic situation. Using a high-resolution GCM which solves the traditional primitive equations, it is shown that large-scale jets similar to those observed in current simulations of hot-Jupiters are likely to be baroclinically unstable on a timescale of few to few tens of planetary rotations, generating cyclones and anticyclones that drive weather systems. The growth rate and scale of the most unstable mode obtained in the linear analysis are in qualitative, good agreement with the full non-linear simulations. In general, unstable jets evolve differently depending on their signs (eastward or westward), due to the change in sign of the jet curvature. For jets located at or near the equator, instability is strong at the flanks – but not at the core. Crucially, the instability is either poorly or not at all captured in simulations with low resolution and/or high artificial viscosity. Hence, the instability has not been observed or emphasized in past circulation studies of hot-Jupiters.

3.1 Introduction

Baroclinic instability is a generic flow instability that occurs in rotating, stably-stratified fluids subject to a meridional (north-south) temperature gradient. Examples of such a fluid are planetary atmospheres and oceans. The temperature gradient induces a vertical (altitudinal) shear in the mean flow by thermal wind balance (see Chapter 2); hence, baroclinic flows are those that nominally vary in the vertical direction. The instability itself is important because it gives rise to large- and meso-scale weather systems on planets. It also serves as a source of turbulence, which has been invoked as the initial condition in some simulations of extrasolar

planets to generate plausible initial jet profiles (e.g., Cho et al., 2003, 2008). More importantly, the instability is a source of spatio-temporal variability which could be observed remotely.

Baroclinic instability on extrasolar planets has not been studied thus far. In this work a simple linear analysis of a horizontally uniform jet in vertical shear is performed. A highly-accurate pseudospectral GCM BOB (section 2.3) which solves the hydrostatic primitive equations is used to study the non-linear evolution of a non-uniform, gradient-wind balanced jet on an extrasolar planet. Here the main focus is on close-in gaseous planets, as they remain the best studied type of extrasolar planet thus far. However, many of the findings and much of the discussion apply to hot extrasolar planets in general – regardless of whether a solid boundary is present or the radiatively stable layer extends deeply into the planet.

For concreteness, calculations for a model planet with physical parameters appropriate for the extrasolar giant planet HD209458b (Table 2.1) are presented. The focus is on the stability of broad, high-speed zonal jets – positive (eastward) at the equator and negative (westward) at high latitude – under adiabatic (i.e., radiative timescale much longer than the dynamic timescale) situation. Here "broad" means width of $\sim L_{\rm D}$, where $L_{\rm D}$ is the Rossby deformation length (sections 2.2), and "high-speed" means the speed is ~ 1000 m s^{-1} at the core of the jet. Such jets are commonly produced in diabatically-forced GCM simulations of synchronized hot-Jupiters (e.g., Showman et al., 2008; Rauscher and Menou, 2010; Thrastarson and Cho, 2010). A study of adiabatic behaviour is needed because it provides the necessary baseline for comparing the instability under forced conditions and because, in many circumstances, the produced jets are not maintained by the applied thermal forcing (but some flow-modified version, away from the specified radiative equilibrium).

The basic approach in this work is to carefully study baroclinic instability in sufficient generality, without complicating the fundamental process with details which are still uncertain for extrasolar planets. The primary aim here is three-fold: 1) to ascertain the importance of baroclinic instability as a generic process operating on extrasolar planets; 2) to gain a better understanding of the outputs from current extrasolar planet GCM simulations, made difficult by the complexity of solving the primitive equations accurately; and, 3) to explore fundamental issues in baroclinic instability that have received less emphasis in traditional geophysical fluid dynamics studies, due to the markedly different parameter regime of many extrasolar planets compared to that of the Earth.

The overall plan of the chapter is as follows. Section 3.2 presents linear stability

analysis. Linear growth rates and phase speeds are calculated for the traditional primitive equations on the "β-plane", a differentially rotating plane tangent to the surface of the planet at a given latitude. In section 3.3 the non-linear evolution of the instability, obtained from full numerical simulations is presented. This section also presents the description of the setup, as well as the non-convergence of under-resolved and/or over-dissipated simulations. The foundation for baroclinic life-cycle study is also laid in this section; a detailed discussion of the phenomenon is presented elsewhere, as are of forced evolution and transient growth. Recapitulation and discussion are given in section 4.4.

3.2 Linear Theory

3.2.1 Charney-Stern-Pedlosky Criteria

Necessary conditions for instability exist. These may be derived directly from global conservation of pseudoenergy and are given in Charney and Stern (1962) and Pedlosky (1964). Hence, the conditions shall not be derived here but simply listed for the reader's convenience. The conditions play an important role in this work, particularly in understanding the setup of the nonlinear initial value problem (section 3.3).

Let $q = \rho^{-1}(\boldsymbol{\omega} + 2\boldsymbol{\Omega}) \cdot \nabla^{\mathrm{L}}\varphi$ be the potential vorticity, where $\boldsymbol{\omega}$ is the relative vorticity, $\boldsymbol{\Omega}$ is the planetary vorticity, and ∇^{L} is a gradient operator acting on a materially conserved field φ, which may be a function of temperature and pressure (e.g., potential temperature or entropy). Additionally, let x, y and z be the zonal ($\mathbf{i}$), meridional ($\mathbf{j}$) and vertical ($\mathbf{k}$) directions, respectively. Given the zonal flow, $\mathbf{U} = U(y, z)\,\mathbf{i}$, and the basic state potential vorticity $Q(y, z)$ such that $q(x, y, z) = Q + q'(x, y, z)$, one of the following necessary criteria must be met for the onset of instability:

(i) $\partial Q/\partial y$ and $\partial U/\partial z$ are opposite signs at the upper boundary

(ii) $\partial Q/\partial y$ and $\partial U/\partial z$ are same signs at the lower boundary

(iii) $\partial U/\partial z$ is the same sign at the upper *and* lower boundaries – a condition that is distinct from condition (i) or (ii), if $\partial Q/\partial y = 0$

(iv) $\partial Q/\partial y$ changes sign somewhere in the interior.

Note that $Q = Q(\mathbf{U})$ and the prime denotes deviation from the basic state.

For realistic flow profiles studied in section 3.3, the instability criterion is normally satisfied through criterion (iv). In addition, criteria (i) and (ii) are also satisfied in

most cases. These conditions are useful for assessing stability of any basic flow configuration. However, they do not provide quantitative information, such as the growth rates of unstable modes and phase speeds of waves/eddies generated by the instability.

For the Earth, the stability analysis is typically based on the quasi-geostrophic (QG) theory, in which small Rossby number Ro and order unity Burger number Bu are assumed (Charney, 1947; Eady, 1949; Phillips, 1951). Given the horizontal length scale L, and the Rossby deformation length scale $L_{\rm D}$ (section 2.2), Bu is defined as $Bu = (L_{\rm D}/L)^2$. Note that both Ro and Bu vary with latitude. For example, formally, $Ro \to \infty$ as $\phi \to 0$.

In QG theory, adiabatic dynamics is governed by the material advection of potential vorticity by geostrophic wind:

$$\frac{{\rm D}q_{\rm QG}}{{\rm D}t} \;=\; 0\,,$$

where ${\rm D}/{\rm D}t$ is the rate of change following the geostrophic wind

$$q_{\rm QG} \;=\; f + \nabla^2\psi + \frac{1}{\rho}f_0^2\frac{\partial}{\partial z}\left(\frac{\rho}{N^2}\frac{\partial\psi}{\partial z}\right)$$

is the QG potential vorticity in the "β-plane approximation" (see section 3.2.3). Here $f = f_0 + \beta y$, where $f_0 = f(\phi_0)$ and $\beta = ({\rm d}f/{\rm d}y)|_{\phi=\phi_0}$ for a specific latitude ϕ_0; ψ is the streamfunction; and, ∇^2 is the horizontal Laplacian operator. Note that $q_{\rm QG}$ can be inverted – as with the full primitive equation q, under the QG balance condition – to obtain all other dynamical variables (Hoskins et al., 1985).

The QG equations (the above advection equation for $q_{\rm QG}$ plus boundary conditions) derive from the more complete primitive equations. The standard QG equations are appropriate for large-scale motions on many planets, away from the low latitudes. However, they are not broadly[1] appropriate for a large number of extrasolar planets, which are characterized by Ro of order unity (see section 2.2) – even away from the equatorial region. More importantly, much dynamics of interest on extrasolar planets occur in the equatorial region (section 3.3.4), where the traditional QG theory does formally break down. Therefore, stability analysis is performed using the full primitive equations.

[1] QG theory may still be valid locally on hot-Jupiters.

3.2.2 Governing Equations

In this chapter linear analysis is performed on the hydrostatic primitive equations (2.1) in pressure (p) coordinates. In Eulerian frame of reference these equations read:

$$\frac{\partial \mathbf{v}}{\partial t} + \mathbf{v}\cdot\nabla\,\mathbf{v} + \omega\frac{\partial \mathbf{v}}{\partial p} + f\mathbf{k}\times\mathbf{v} + \nabla\Phi \;=\; \boldsymbol{\mathcal{F}}_{\mathrm{v}} + \boldsymbol{\mathcal{D}}_{\mathrm{v}} \tag{3.1a}$$

$$\frac{\partial \theta}{\partial t} + \mathbf{v}\cdot\nabla\,\theta + \omega\frac{\partial \theta}{\partial p} \;=\; \frac{\theta}{c_pT}\,\dot{q}_{\mathrm{net}} + \mathcal{D}_\theta \tag{3.1b}$$

$$\nabla\cdot\mathbf{v} + \frac{\partial \omega}{\partial p} \;=\; 0 \tag{3.1c}$$

$$\frac{\partial \Phi}{\partial p} + h\theta \;=\; 0\,. \tag{3.1d}$$

Here ∇ operates along constant surfaces of p (which in general is not materially conserved); and $h(p) = \mathcal{R}\,(p/p_{\mathrm{r}})^{\kappa}/\,p$. Otherwise the notation is same to that in Chapter 2. As before, the above set of equations is closed with the ideal gas law, $p = \rho\mathcal{R}T$. The equations are also supplemented with the boundary conditions (2.21).

3.2.3 Two-Layer, Beta-Plane Analysis

In this section, linearization of equations (3.1) on the β-plane is performed. Here $f(\phi)$ is represented by $f(y) = f_0 + \beta y$, where f_0 and β are constants, $y = R_p(\phi - \phi_0)$ and the motion is assumed to be periodic in the zonal direction with no meridional component at the latitudinal boundaries. The β-plane is a tangent plane located at ϕ_0, and the setup is only formally justified for scales that are small compared to R_p. However, in practice the β-plane approximation mainly results in small distortion of planetary waves and captures the essential qualitative behaviour. For the analysis in this section, source and dissipation terms in equations (3.1) are neglected – i.e., $\boldsymbol{\mathcal{F}}_{\mathrm{v}} = \boldsymbol{\mathcal{D}}_{\mathrm{v}} = \dot{q}_{\mathrm{net}} = \mathcal{D}_\theta = 0$. This is because, as discussed in section 3.1, interest is placed in the dynamics of jets that result from conditions e.g., when the net heating is not large or the effective thermal relaxation time is not small.

A standard normal mode analysis of the baroclinic instability admitted by a two-layer representation of equations (3.1) is performed. Similar work has been carried out by Wiin-Nielsen (1963) and Fraedrich and Frisius (2001) for the Earth. As in these studies, the equation set (3.1) is simplified to that appropriate for a discretised model with two equally-spaced, stacked layers in the p-coordinate. In this model $\mathbf{v}$, θ and Φ are defined at odd levels and ω is defined at even levels. The structure is illustrated in Figure 3.1. The equations for the interior levels are:

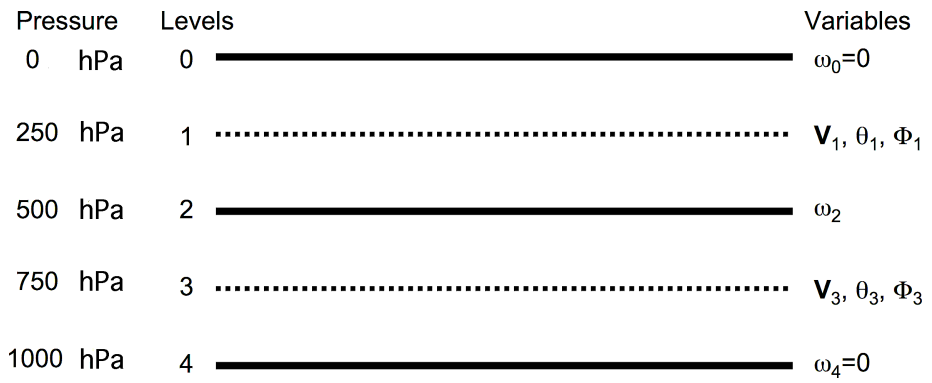

Figure 3.1: Vertical structure of the two-layer primitive equations model. Different field variables are defined on different levels; 1 hPa = 10^2 Pa = 1 mbar. Bold lines are the layer boundaries.

$$\frac{\partial \mathbf{v}_1}{\partial t} + \mathbf{v}_1 \cdot \nabla \mathbf{v}_1 + \omega_2 \left(\frac{\mathbf{v}_3 - \mathbf{v}_1}{2 \triangle p} \right) + f \mathbf{k} \times \mathbf{v}_1 \;=\; -\nabla \Phi_1 \tag{3.2a}$$

$$\frac{\partial \mathbf{v}_3}{\partial t} + \mathbf{v}_3 \cdot \nabla \mathbf{v}_3 + \omega_2 \left(\frac{\mathbf{v}_3 - \mathbf{v}_1}{2 \triangle p} \right) + f \mathbf{k} \times \mathbf{v}_3 \;=\; -\nabla \Phi_3 \tag{3.2b}$$

$$\frac{\partial \theta_1}{\partial t} + \nabla \cdot (\theta_1 \, \mathbf{v}_1) + \frac{\omega_2 \theta_2}{\triangle p} \;=\; 0 \tag{3.2c}$$

$$\frac{\partial \theta_3}{\partial t} + \nabla \cdot (\theta_3 \, \mathbf{v}_3) - \frac{\omega_2 \theta_2}{\triangle p} \;=\; 0 \tag{3.2d}$$

$$\nabla \cdot \mathbf{v}_1 + \frac{\omega_2}{\triangle p} \;=\; 0 \tag{3.2e}$$

$$\nabla \cdot \mathbf{v}_3 - \frac{\omega_2}{\triangle p} \;=\; 0 \tag{3.2f}$$

$$\Phi_1 - \Phi_3 \;=\; h_2 \triangle p \, \theta_2 \,, \tag{3.2g}$$

where $\triangle p = p_\mathrm{r}/2$ denotes the pressure difference between odd or even numbered levels and $\theta_2 = \theta = (\theta_1 + \theta_3)/2$. It follows from equations (3.2e) and (3.2f) that barotropic (vertically averaged) wind is non-divergent. In the present analysis, the Brunt-Väisälä frequency N is taken to be uniform. This is consistent with GCM simulations by Thrastarson and Cho (2010), which show static stability to be fairly constant over one or two scale heights for a wide range of conditions.

Baroclinic instability in the two-level primitive equations system is obtained from

perturbations of an unstable basic flow with uniform vertical shear and stratification:

$$\begin{aligned}
\bar{u}_1 &= -\bar{u}_3 = U_0 \\
\bar{v}_1 &= \bar{v}_3 = 0 \\
\bar{\omega}_1 &= \bar{\omega}_3 = 0 \\
\bar{\theta}_1 &= -\frac{2f_0}{h_2 \triangle p} U_0\, y + \sigma_0 \\
\bar{\theta}_3 &= -\frac{2f_0}{h_2 \triangle p} U_0\, y - \sigma_0 \\
\bar{\theta}_2 &= \bar{\theta} = -\frac{2f_0}{h_2 \triangle p} U_0\, y\,.
\end{aligned}$$

Here U_0 $(= U/2)$ characterizes the strength of the thermal wind and its shear; and, $\sigma_0 = (\theta_1 - \theta_3)/2$ is related to the reference static stability, $S = -\rho^{-1}\, \partial \ln\theta/\partial p$, through

$$S = \frac{\sigma_0 h_2}{\triangle p}\,.$$

For simplicity meridionally-independent perturbations applied to the above basic flow are considered. The equations (3.2) are now linearized about this basic state to arrive at the following:

$$\frac{\partial \mathbf{v}_1'}{\partial t} + U_0 \frac{\partial \mathbf{v}_1'}{\partial x} - \frac{U_0}{\triangle p}\omega_2' \mathbf{i} + f\mathbf{k}\times\mathbf{v}_1' = -\frac{\partial \Phi_1'}{\partial x} \tag{3.3a}$$

$$\frac{\partial \mathbf{v}_3'}{\partial t} - U_0 \frac{\partial \mathbf{v}_3'}{\partial x} - \frac{U_0}{\triangle p}\omega_2' \mathbf{i} + f\mathbf{k}\times\mathbf{v}_3' = -\frac{\partial \Phi_3'}{\partial x} \tag{3.3b}$$

$$\frac{\partial \theta'}{\partial t} - \frac{f_0\, U_0}{h_2 \triangle p}(v_1' + v_3') - \sigma_0 \frac{\omega_2'}{\triangle p} = 0 \tag{3.3c}$$

$$\nabla\cdot\mathbf{v}_1' + \frac{\omega_2'}{\triangle p} = 0 \tag{3.3d}$$

$$\nabla\cdot\mathbf{v}_3' - \frac{\omega_2'}{\triangle p} = 0 \tag{3.3e}$$

$$\Phi_1' - \Phi_3' = h_2 \triangle p\, \theta'\,. \tag{3.3f}$$

The temperature equation (3.3c) is obtained by summing equations (3.2c) and (3.2d) and linearising. Further, if the vertical average of a variable ξ is denoted by

$$\xi_+ \equiv \frac{1}{2}(\xi_1 + \xi_3)$$

and the half vertical difference by

$$\xi_- \equiv \frac{1}{2}(\xi_1 - \xi_3)\,,$$

summing and subtracting equations (3.3a) and (3.3b) give:

$$\frac{\partial \mathbf{v}'_+}{\partial t} + U_0 \frac{\partial \mathbf{v}'_-}{\partial x} - \frac{U_0}{\triangle p}\omega'_2\,\mathbf{i} + f\mathbf{k}\times\mathbf{v}'_+ \;=\; -\frac{\partial \Phi'_+}{\partial x} \tag{3.4a}$$

$$\frac{\partial \mathbf{v}'_-}{\partial t} + U_0 \frac{\partial \mathbf{v}'_+}{\partial x} + f\mathbf{k}\times\mathbf{v}'_- \;=\; -\frac{\partial \Phi'_-}{\partial x}. \tag{3.4b}$$

By applying curl and divergence, vorticity and divergence forms, respectively, of the above equations are obtained. The equations set is closed when potential temperature and pressure velocity ω are eliminated using the hydrostatic and continuity equations. By introducing the streamfunctions, ψ_1 and ψ_3, and the velocity potentials, χ_1 and χ_3, for levels 1 and 3 such that

$$\frac{\partial^2}{\partial x^2}\left(\chi_1 + \chi_3\right) \;=\; 0$$

four evolution equations for the barotropic vorticity, baroclinic vorticity, baroclinic divergence, and geopotential (i.e., potential temperature) are obtained:

$$\begin{aligned}
\frac{\partial^2 \psi'_+}{\partial x^2} &= \frac{\partial^2}{\partial x^2}\left(\frac{\psi'_1 + \psi'_3}{2}\right), \\
\frac{\partial^2 \psi'_-}{\partial x^2} &= \frac{\partial^2}{\partial x^2}\left(\frac{\psi'_1 - \psi'_3}{2}\right), \\
\frac{\partial^2 \chi'_-}{\partial x^2} &= \frac{\partial^2}{\partial x^2}\left(\frac{\chi'_1 - \chi'_3}{2}\right) \;=\; -\frac{\omega'_2}{\triangle p}, \\
\Phi'_- &= \frac{h_2 \triangle p\, \theta'}{2},
\end{aligned}$$

respectively. The evolution equations for these quantities are:

$$\frac{\partial}{\partial t}\left(\frac{\partial^2 \psi'_+}{\partial x^2}\right) = -U_0 \frac{\partial}{\partial x}\left(\frac{\partial^2 \psi'_-}{\partial x^2}\right) - \beta \frac{\partial \psi'_+}{\partial x} \tag{3.5a}$$

$$\frac{\partial}{\partial t}\left(\frac{\partial^2 \psi'_-}{\partial x^2}\right) = -U_0 \frac{\partial}{\partial x}\left(\frac{\partial^2 \psi'_+}{\partial x^2}\right) - f_0 \frac{\partial^2 \chi'_-}{\partial x^2} - \beta \frac{\partial \psi'_-}{\partial x} \tag{3.5b}$$

$$\frac{\partial}{\partial t}\left(\frac{\partial^2 \chi'_-}{\partial x^2}\right) = -\frac{\partial^2 \Phi'_-}{\partial x^2} + f_0 \frac{\partial^2 \psi'_-}{\partial x^2} - \beta \frac{\partial \chi'_-}{\partial x} \tag{3.5c}$$

$$\frac{\partial \Phi'_-}{\partial t} \;=\; U_0 f_0 \frac{\partial \psi'_+}{\partial x} - \frac{\mathcal{R}\,\sigma_0}{2^{\kappa+1}} \frac{\partial^2 \chi'_-}{\partial x^2}\,. \tag{3.5d}$$

At this point, the foregoing system of equations can be made non-dimensional for a more "generalized" treatment, as is typical in instability studies. However, the analysis of the equations presented in the dimensional form shall be described. It is felt that this facilitates a more lucid interpretation of the results in some ways. For the interested reader, the non-dimensional account is included in the Appendix 3.A and the reader is referred to that section, especially for the dependence of the results on non-dimensional parameters.

Denoting disturbances by

$$\mathbf{\Psi} \;=\; \hat{\mathbf{\Psi}} \exp\{ik\,(x - c\,t)\}\,,$$

where $\mathbf{\Psi} = (\psi'_+, \psi'_-, \chi'_-, \Phi'_-)^{\mathrm{T}}$, $\hat{\mathbf{\Psi}} = (\hat{\Psi}_+, \hat{\Psi}_-, \hat{\chi}_-, \hat{\Phi}_-)^{\mathrm{T}}$ and $c \in \mathbb{C}$, equations (3.5) reduce to

$$\mathbf{M}\,\hat{\mathbf{\Psi}} \;=\; 0$$

with

$$\mathbf{M} \;=\; \begin{bmatrix} -c - \beta/k^2 & U_0 & 0 & 0 \\ U_0 & -c - \beta/k^2 & -i\,f_0/k & 0 \\ 0 & i\,f_0/k & -c - \beta/k^2 & -i/k \\ f_0\,U_0 & 0 & -i\,k\,\mathcal{R}\,\sigma_0/2^{\kappa+1} & c \end{bmatrix}.$$

For a non-trivial solution, $\det(\mathbf{M}) = 0$. This leads to a fourth-order characteristic equation for c:

$$\begin{aligned} c^4 \;+\; c^3\left(\frac{3\beta}{k^2}\right) \;+\; c^2\left(\frac{3\beta^2}{k^4} \;-\; \frac{f_0^2}{k^2} - \frac{\mathcal{R}\,\sigma_0}{2^{\kappa+1}} - U_0^2\right) \;+ \\ c\left(\frac{\beta^3}{k^6} \;-\; \frac{\beta\,f_0^2}{k^4} \;-\; \frac{\beta\,\mathcal{R}\,\sigma_0}{2^{\kappa}\,k^2} \;-\; \frac{\beta\,U_0^2}{k^2}\right) \;+ \\ \left(\frac{\mathcal{R}\,\sigma_0\,U_0^2}{2^{\kappa+1}} - \frac{f_0^2\,U_0^2}{k^2} \;-\; \frac{\beta^2\,\mathcal{R}\,\sigma_0}{2^{\kappa+1}\,k^4}\right) \;=\; 0\,. \end{aligned} \tag{3.6}$$

Equation (3.6) is solved numerically for c as a function of k, while keeping the values of $f_0\,, \beta\,, U_0\,, \mathcal{R}\,, \sigma_0$ and κ constant. If $\Im\mathfrak{m}\{c\} \neq 0$, the disturbances grow or decay exponentially since they are proportional to $\exp\{-i\,k\,c\,t\}$. Two of the roots of equation (3.6) are stable eastward- and westward-traveling inertia-gravity waves. The other two roots are baroclinic waves. These waves propagate neutrally

(i.e., without growing or decaying) eastward and westward, if $\Im\mathfrak{m}\{c\} = 0$ (provided $\Re\mathfrak{e}\{c\} \neq 0$).

The baroclinic wave solutions to equation (3.6) are presented in Figure 3.2 for a planet with HD209458b parameters given in Table 2.1. The top panel shows the growth rate, $k \cdot \Im\mathfrak{m}\{c\}$, as a function of wavelength $2\pi\, k^{-1}$ at several different latitudes: $\phi = (60°, 45°, 35°, 25°)$. Note that the latitudinal dependence comes from f_0 and β. The growth rates are labelled "HD60" (red), "HD45" (green), "HD35" (yellow) and "HD25" (blue), respectively. The bottom panel shows the corresponding phase speeds $\Re\mathfrak{e}\{c\}$. Note here that unstable baroclinic waves travel westward relative to the mean flow ($\Re\mathfrak{e}\{c\} < 0$).

From Figure 3.2 it can be seen that the wavelength of the most unstable mode at $\phi = 60°$ is 1.7×10^8 m, corresponding to 1.8 undulations (i.e., ~ 2 crests and troughs each) at this latitude. The growth rate of the instability is $3.1\,\tau^{-1}$, where $\tau = 2\pi\,\Omega^{-1}$ is the planetary rotation time. At $\phi = 45°$ and $\phi = 35°$, the most unstable modes correspond to 2.2 and 2.3 undulations around their respective latitude circles with growth rates $2.3\,\tau^{-1}$ and $1.5\,\tau^{-1}$, respectively. Hence, jets centred at lower latitudes have increased growth times with modestly increased wavelengths of the most unstable mode. Significantly, linear analysis predicts stability for jets located at or equator-ward of $\phi = 28°$ (see e.g., the flat, blue curve labelled "HD25").

To illustrate the dependence of the growth rate and phase speed on the characteristic flow speed (or, equivalently, shear strength), in Figure 3.2 result obtained for the case with $U_0 = 200$ m s^{-1} at $\phi = 45°$ (black curve labelled "HD45L") are presented. Comparing the "HD45" (green) and "HD45L" (black) curves, it can be seen immediately that the growth rate of the most unstable mode decreases significantly for the smaller U_0 case. The instability takes ~ 4 times longer to develop in the weaker speed/shear case. Also note that the wavelength of the most unstable mode decreases slightly. Hence, as U_0 decreases, the number of undulations increases for a jet located at a given latitude.

The qualitative behaviour described above is not restricted to HD209458b. It applies to any planet that has a meridional temperature gradient. To illustrate the general applicability of the results, presented in Figure 3.3 are the growth rates and phase speeds at $\phi = 45°$ for several planets: Earth, Jupiter and GJ436b (red, green and black curves, respectively). For the Earth, the wavelength of the most unstable mode is 4100 km, corresponding to ~ 7 undulations at midlatitude, with growth rate of $1.6\,\tau^{-1}$ (i.e., growth time of 15 hours). This is consistent with many studies of baroclinic instability on the Earth (e.g., Thorncroft et al., 1993; Polvani et al., 2004). The corresponding values of undulations for Jupiter and GJ436b are

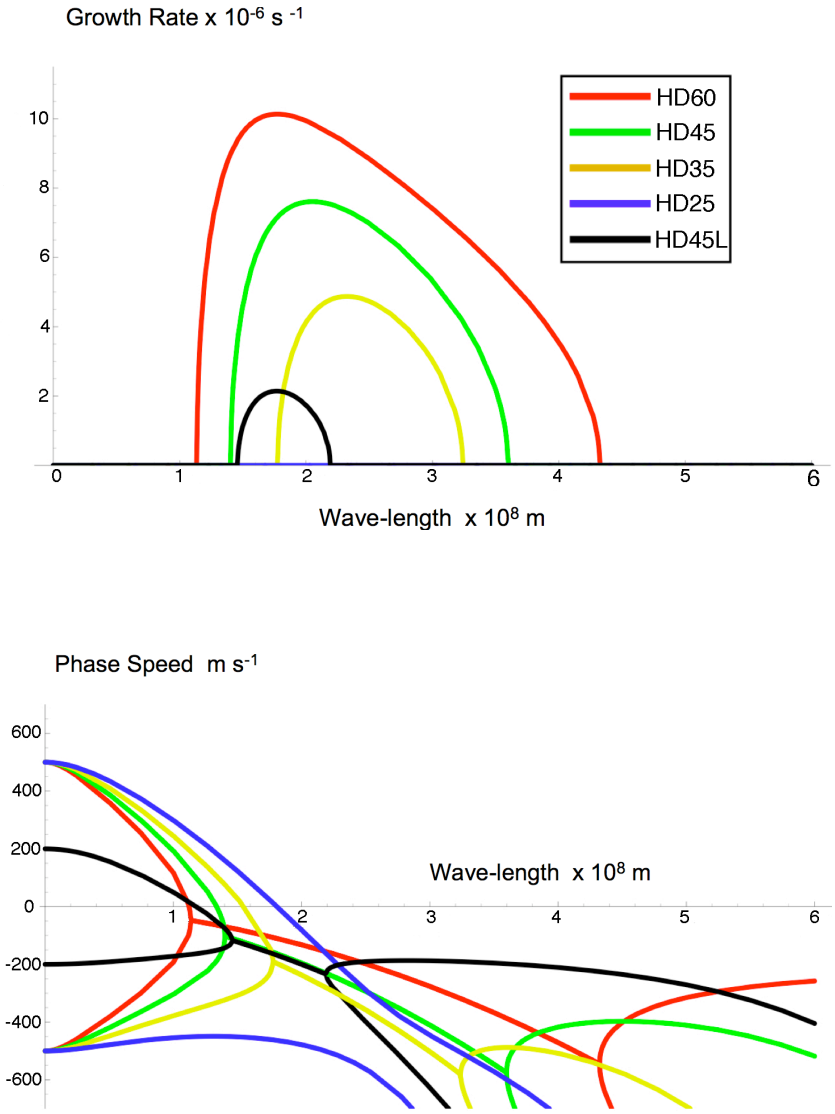

Figure 3.2: Growth rate $[k \cdot \Im\mathfrak{m}\{c\}]$ (top) and phase speed $[\Re\mathfrak{e}\{c\}]$ (bottom) for HD209458b, as a function of wavelength $2\pi\, k^{-1}$. Curves "HD60", "HD45", "HD35" and "HD25" represent growth rates and phase speeds at $\phi = (60°, 45°, 35°, 25°)$; $f_0 = 4.2 \times 10^{-5} \sin\phi$ s^{-1}, $\beta = 4.2 \times 10^{-13} \cos\phi$ m^{-1} s^{-1}, $U_0 = 500$ m s^{-1}, $\mathcal{R} = 3500$ J kg^{-1} K^{-1}, $\sigma_0 = 300$ K and $\kappa = 0.286$. Curve "HD45L" has been computed for HD209458b parameters at $\phi = 45°$, but with $U_0 = 200$ m s^{-1}.

~ 43 and ~ 1 with growth rates $0.48\,\tau^{-1}$ and $0.56\,\tau^{-1}$, respectively. Accordingly, if baroclinic instability occurs on these planets, it appears Jupiter simulations must be of very high resolution ($\sim$ T682, or 682 sectoral modes and 682 total modes in the spectral expansion—this estimate is based on the ensuing discussion and has not been explicitly verified in non-linear simulation experiments) to capture the instability. On the other hand, the instability at the midlatitude of GJ436b would clearly be of planetary scale and thus may lead to a possible observable variability signal for this planet on a timescale of ~ 1.8 planetary rotations. Note that the phase speeds of the unstable baroclinic waves on Earth and Jupiter are very small (close to zero) compared to those on the extrasolar planets, HD209458b and GJ436b.

A linear growth rate analysis with the two-layer QG model for HD209458b has also been carried out. The QG results were compared with those from the primitive equations model, presented above. In the two models, the growth rates at high latitudes and midlatitudes are equivalent to within 5 per cent. However, at low latitudes, the QG model overestimates the growth rates by approximately 25 per cent. Moreover, the QG model predicts instability down to $\phi = 23°$, whereas the primitive equations model predicts instability only down to $\phi = 28°$. Below these latitudes, both models predict stability. Thus, ageostrophy appears to provide a stabilizing factor in this case. Given that inertia-gravity waves are not filtered in the primitive equations model (as they are in the QG model), the enhanced stability may be due to the gravity waves "leaking away" some of the energy that drive the instability.

3.2.4 Limitations

The preceding analysis is highly idealised. Therefore, it has limitations. For example, in general, planetary jets possess a three-dimensional structure (i.e., $(\bar{u}, \bar{v}) = (\bar{u}(x, y, p), \bar{v}(x, y, p))$) – with concurrent vertical and meridional shears, as well as zonal asymmetry. Also, the atmosphere is continuously stratified. One effect of a two-layer discretisation with uniform zonal flow in each layer is the inability to capture the symmetry breaking between eastward and westward jets. These limitations are discussed more in detail below.

In flows with both vertical and horizontal shears, the growth of unstable baroclinic waves may be suppressed by the "barotropic governor" effect (e.g., James, 1987; Nakamura, 1993a; Pedlosky, 1964). The effect is not fundamentally related to the sign of the jet, but a key ingredient is a counter-gradient eddy momentum flux $\overline{u'v'}$ generated under a horizontally sheared flow; here the overbar indicates a zonal

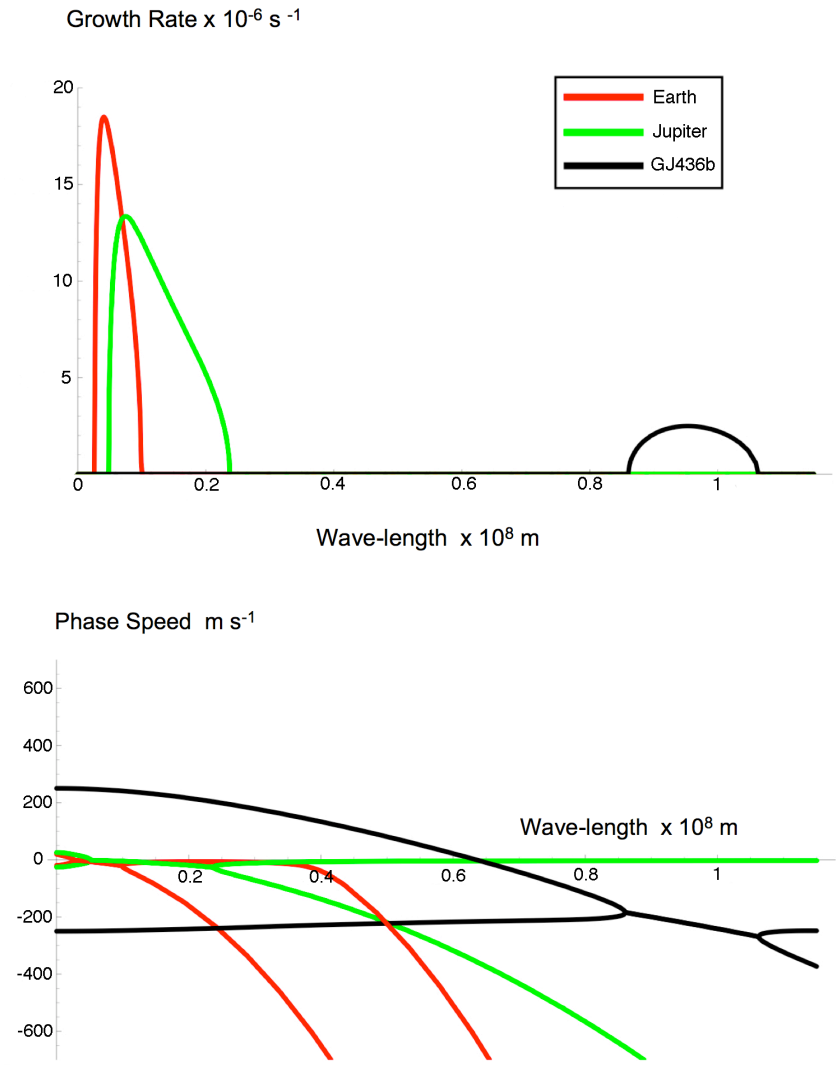

Figure 3.3: Growth rate $[k \cdot \Im\mathfrak{m}\{c\}]$ (top) and phase speed $[\Re\mathfrak{e}\{c\}]$ (bottom) at $\phi = 45°$ for Earth, Jupiter and GJ436b as a function of wavelength $2\pi\, k^{-1}$. For the Earth, $f_0 = 10^{-4}$ s^{-1}, $\beta = 1.6 \times 10^{-11}$ m^{-1} s^{-1}, $U_0 = 20$ m s^{-1}, $\mathcal{R} = 287$ J kg^{-1} K^{-1}, $\sigma_0 = 15$ K, $\kappa = 0.286$. For Jupiter, $f_0 = 2.5 \times 10^{-4}$ s^{-1}, $\beta = 3.5 \times 10^{-12}$ m^{-1} s^{-1}, $U_0 = 25$ m s^{-1}, $\mathcal{R} = 3779$ J kg^{-1} K^{-1}, $\sigma_0 = 24$ K, $\kappa = 0.286$. For GJ436b, $f_0 = 3.9 \times 10^{-5}$ s^{-1}, $\beta = 1.4 \times 10^{-12}$ m^{-1} s^{-1}, $U_0 = 250$ m s^{-1}, $\mathcal{R} = 3500$ J kg^{-1} K^{-1}, $\sigma_0 = 150$ K, $\kappa = 0.286$. Note, σ_0 values for Jupiter and GJ436b have been computed assuming constant temperatures of 120 K and 750 K, respectively. Note the change in scales, compared with Figure 3.2.

average. The shear and the momentum flux reinforce each other to distort the meridional structure of the wave, suppressing the growth rate and shortening the wavelength of the most unstable mode. Thus, the full non-linear evolution of the instability exhibits lower growth rates and shorter wavelengths, compared with those indicated by the linear analysis presented in this section (see section 3.3).

The atmosphere is also continuously stratified. A representation more realistic than a two-layer model changes the instability properties described in this section. The main change is that the short-wave and long-wave cut-offs in the two-layer representation (see Figures 3.2 and 3.3) no longer exist in the continuum of unstable modes (e.g., Charney, 1947; Green, 1960; Kuo, 1979). The retained modes (Charney and Green modes, discussed below) are not expected to change qualitatively the asymptotic behaviour of the instability. However, they do provide additional modes for wave-wave interaction during the non-linear growth phase – hence, affect the details of the evolution; this may be significant for finite-time variability.

Another limitation of the linear model presented is that it does not distinguish between the signs of the jet (or shear). This is because symmetry is preserved under the interchange of the shear sign, given the laterally uniform flow; hence, distinction between the two signs is not expected. This is in contrast to the flow used in the non-linear simulation (section 3.3), in which the growth rate for an unstable westward (negative shear) jet is smaller than that for the unstable eastward (positive shear) jet at the same latitude. The two signed flows behave differently in this case because of the change in the sign of the jet curvature. Furthermore, a westward jet has only one unstable mode (Charney mode) as opposed to an eastward jet, which has an infinite number of unstable modes (Green modes).

A similar observation has been made by Wang (1990), who observed a difference between eastward- and westward-sheared baroclinic flows in the Charney model (continuously stratified QG model on the β-plane). He has pointed out that the maximum growth rate for the absolute value of non-dimensional shear is substantially smaller for a flow with westward shear than a flow with eastward shear. Moreover, while the eastward jet is baroclinically unstable for any value of vertical shear Λ, the westward jet is unstable only if

$$\Lambda \; < \; -\frac{\beta\, N^2\, H}{f_0^2}\,. \tag{3.7}$$

Note that, at $\phi = 45°$, the critical shear for HD209458b parameters used in this work is: $\Lambda_c = -7.9 \times 10^{-4}$ s^{-1}. The shear of the unstable westward jet described in section 3.3.3 is $\Lambda = -1.7 \times 10^{-3}$ s^{-1}, consistent with (3.7).

Table 3.1: Summary of jet configurations discussed: b is a parameter that controls the jet width [see equation (3.8)]. Note, in run E45N2b the bottom boundary is set at $p = 2$ bar and the vertical structure function $F(z^*)$ in equation (3.8) is specified as $F(z^{**}) = \{\,1 - \tanh^8[\,(z^{**} - z_{2b})\,/\,\Delta z_0\,]\,\}\,\sin^4(\pi\, z^{**}/z_1)$, where $z^{**} = -H\log[(p + p_0)/p_r]$, with $p_0 = 60$ hPa and $z_{2b} = 900$ km.

Run	Width (b)	Latitude	Direction
E45N	3.0	45° N	East
E45N2b	3.0	45° N	East
W60N	3.0	60° N	West
EEQ	0.5	0°	East

3.3 Non-Linear Evolution

3.3.1 Model and Setup

To study the full non-linear evolution in spherical geometry, the pseudospectral model, BOB is used. As described in Chapter 2, this model solves equations (2.19), subject to the boundary conditions (2.21). To control the small-scale noise inherent in the non-linear simulations, superdissipation (i.e., $\mathfrak{p}$=2 in equation (2.20)) is applied to the prognostic variables, $\{\zeta, \delta, \theta\}$, and the superdissipation coefficient ν_4 is taken to be constant.

The non-linear evolution of baroclinic instability is studied by initializing the model with an idealized jet that satisfies the necessary condition for baroclinic instability, the Charney-Stern-Pedlosky condition described in section 3.2. The jet is initially set to be either eastward or westward, and centred at a latitude between 0° to 60° N. A large number of simulations have been performed for this study, carefully varying each parameter (jet location, strength, shear, profile, direction as well as domain size, etc.) in an independent series of simulations. A very small subset of these runs, which are used for discussions in sections 3.3.1 to 3.3.4, is given in Table 3.1. The set illustrates the basic points of this study.

All the jets are initially non-linearly balanced so that a self-consistent background temperature structure is generated (Figure 3.4). The jets are then perturbed at the beginning of the simulation by an infinitesimal temperature disturbance which is

independent of altitude, a barotropic "heat bump", and allowed to evolve freely thereafter. The setup is chosen to be similar to that in Polvani et al. (2004) for validation and comparison purposes. For example, following that work, the initial zonal flow u_0 in the runs here is, in general,

$$u_0(\phi, p) \;=\; \begin{cases} U\,\sin^b[\pi \sin^2(\phi - \phi_0)]\,F(z^*), & \phi_0 < \phi < \phi_{\rm T} \\ 0\,, & \text{otherwise}\,. \end{cases} \tag{3.8}$$

Here

$$F(z^*) \;=\; \frac{1}{2}\left[1 - \tanh^3\left(\frac{z^* - z_0}{\Delta z_0}\right)\right] \sin\left(\frac{\pi z^*}{z_1}\right) \tag{3.9}$$

with $z^* = -H\log(p/p_{\rm r})$, and ϕ_0 and $\phi_{\rm T}$ are taken to be the following: $\phi_0 = 0$ and $\phi_{\rm T} = \pi/2$ for jets centred at midlatitude (E45N and E45N2b), $\phi_0 = \pi/12$ and $\phi_{\rm T} = \pi/2$ for jets centred at 60°N (W60N) and $\phi_0 = -\pi/4$ and $\phi_{\rm T} = \pi/4$ for jets centred on the equator (EEQ). The typical values of the parameters are: $U = \pm 1000$ m s^{-1}, $z_0 = 1823$ km, $z_1 = 2486$ km, $\Delta z_0 = 414$ km, $H = 580$ km, and $p_{\rm r} = 10^5$ Pa (= 1 bar). The latitudinal width of the jet is determined by b in (3.8), where $b = 3$ corresponds to a jet width of $\sim 40°$ (Figure 3.4a and Figure 3.4b) and $b = 1/2$ to a width of $\sim 85°$ (Figure 3.4c). To discuss jets that closely match those produced in current GCM simulations of extrasolar giant planets, runs which are initialized with wider ($b = 1/2$) jets in the equatorial region and narrower jets ($b = 3$) poleward of 45° N are presented.

The basic state temperature, $T_0 = T_0(\phi, p)$, is obtained by combining meridional momentum and hydrostatic balance equations:

$$\frac{\partial T_0}{\partial \phi} \;=\; -\frac{H}{\mathcal{R}}\left(R_p f + 2u_0 \tan\phi\right)\frac{\partial u_0}{\partial z^*}\,. \tag{3.10}$$

Integrating (3.10) results in a temperature distribution that is in non-linear, gradient wind balance with the specified jet. Here a reference temperature of 1500 K is used as the constant of integration. The value is consistent with the initial conditions and results of many GCM simulations. The basic state flow $u_0(\phi, p)$ and potential temperature $\theta_0(\phi, p)$ for runs E45N (eastward midlatitude jet), W60N (westward high latitude jet) and EEQ (wide eastward equatorial jet) are shown in Figure 3.4. Recall that θ_0 is related to T_0 by $\theta_0 = T_0(p_{\rm r}/p)^{\kappa}$. To catalyse the instability, T_0 is given a small perturbation T' in the form of a localized bump at all pressure levels such that

$$T'(\lambda, \phi) \;=\; \mathcal{A}\,\mathrm{sech}^2\left[3\left(\lambda - \lambda_0\right)\right]\,\mathrm{sech}^2\left[6(\phi - \phi_0)\right]\,, \tag{3.11}$$

for $-\pi < \lambda < \pi$. Here $\mathcal{A} = 1$ K and (ϕ_0, λ_0) represents the jet centre (latitude, longitude).

The vertical domain, which typically extends from 1 to 10^{-3} bar, is resolved by 20 equally spaced pressure levels — as in Polvani et al. (2004). The horizontal resolution of results presented in section 3.3.2 to section 3.3.4 is T170, or 170 sectoral modes and 170 total modes in the spectral expansion (see e.g., Thrastarson and Cho, 2011). The resolution is designated "T170L20". The inverse transformation is performed on to a 512×256 Gaussian grid covering the entire globe. The grid size is chosen for de-aliasing (Canuto et al., 2007, and references therein). Equations (3.1) are integrated for up to $60\,\tau$ (i.e., 60 planetary rotations) with $\nu_4 = 6 \times 10^{19}$ m^4 s^{-1}. A timestep size, $\Delta t = 30$ s, and a Robert-Asselin coefficient, $\epsilon = 0.01$, are used for the time integration.

As already mentioned, the choice of the initial conditions is partly motivated by current GCM results of hot-Jupiter atmospheres. These studies suggest typical flow speeds of $O(100 - 3000$ m s$^{-1})$ and zonal flow consisting of up to ~ 3 jets – often a broad equatorial eastward jet and a smaller amplitude narrower westward jet at a higher latitude on both northern and southern hemispheres (e.g., Showman et al., 2008; Rauscher and Menou, 2010; Thrastarson and Cho, 2010; Heng et al., 2011). The altitudinal and latitudinal profiles used here roughly mimic those presented in figure 9 of Showman et al. (2008) and figure 3 of Rauscher and Menou (2010).

In what follows, the evolution of the midlatitude *eastward* jet (run E45N) is first described. Although such a jet is not commonly observed in current simulations of hot-Jupiters, reviewing this case is useful because it allows the present work to be compared with analogous studies – and observations – of the Earth and because it allows a baseline to be constructed for other initial conditions presented here, namely the high-latitude westward and equatorial eastward jets that match more closely with aforementioned extrasolar planet simulations.

3.3.2 Paradigm Case

Run E45N is the "paradigm case". It illustrates a typical non-linear evolution of a perturbed baroclinic jet on a hot-Jupiter in numerical simulations with high resolution. Note that while the jets satisfy the (necessary) condition for instability, they require an initial perturbation to evolve: without the perturbation no conversion of the potential energy into eddy kinetic energy occurs and the flow remains zonally symmetric (and stable) at all times. The jet is zonally symmetric and eastward with speed 1000 m s^{-1} at the jet core and decaying to zero at the periphery (see

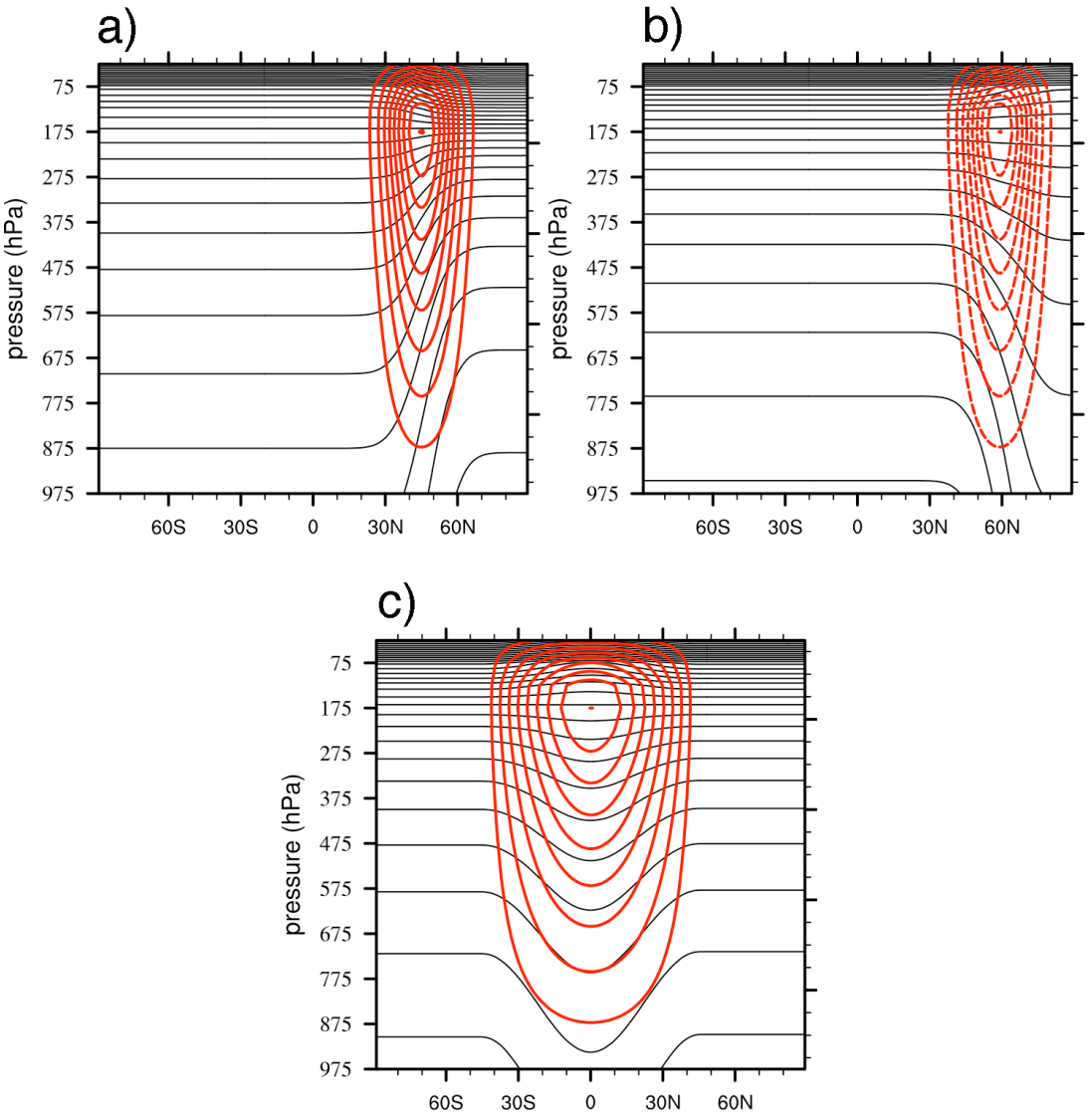

Figure 3.4: The basic state zonal wind u_0 [m s^{-1}] (red) and potential temperature θ_0 [K] (black) as a function of latitude and pressure for runs (see Table 3.1): a) E45N, b) W60N, and c) EEQ. Contour interval for the zonal wind is 100 m s^{-1} and for the potential temperature 100 K. Negative contours are dashed.

Figure 3.4a). It meets the necessary conditions (i), (ii) and (iv) for baroclinic instability. This can be seen from Figure 3.5, which shows $(\partial q_0/\partial y)_\theta$ evaluated on an isentrope as a function of ϕ and p. Note, here q_0 is the potential vorticity defined on isobars,

$$q_0(\phi, p) \;=\; -g(f\mathbf{k} + \nabla\times\mathbf{v}_0)\cdot\nabla\theta_0 \;,$$

where ∇ is the three-dimensional gradient operator in (λ, ϕ, p) space; and, $(\partial q_0/\partial y)_\theta$ is a derivative taken along an isentrope such that

$$\left(\frac{\partial q_0}{\partial y}\right)_\theta \;=\; \left(\frac{\partial q_0}{\partial y}\right)_p - \left(\frac{\partial \theta_0}{\partial y}\right)_p \left(\frac{\partial \theta_0}{\partial p}\right)^{-1} \frac{\partial q_0}{\partial p} \;,$$

where $y = R_p\phi$ and $(\partial(\,\cdot\,)/\partial y)_p$ is the derivative taken on an isobar. Other cases, with jets of different sign or location, are to be compared with this one. In Figure 3.5 $(\partial q_0/\partial y)_\theta$ also changes sign in the horizontal direction. Thus the necessary condition for barotropic instability is also satisfied. However, by considering dominant energy conversions, in what follows it will be shown that the instability is predominantly baroclinic rather than barotropic (cf. Figure 3.8).

Figure 3.6 presents the evolution of T (left column) and ζ (right column) fields at the $p = 975$ hPa surface from run E45N, for $t = 0\ \tau$ to $t = 8\ \tau$. The fields near the reference pressure level (i.e., $p_\mathrm{r} = 1000$ hPa) are shown since the kinetic energy is the maximum at the lower boundary for jet profiles shown in Figure 3.4, similar to Gall (1976) and Simons (1972). Note that for these jets $T \approx \theta$ at this pressure level.

In Figure 3.6, the perturbed jet undergoes initially a period of linear growth $(t \ll 4\tau)$, when the most unstable mode emerges. At this early stage, the T field shows a small-amplitude perturbation from zonal symmetry. The ζ field, on the other hand, is much more dynamic. At $t = 4\ \tau$, finite-amplitude wave breaking in the ζ field is already clearly evident, and the perturbation in this field is characterized by a distinct northwest–southeast tilt on the poleward side of the jet and southwest–northeast tilt on the equatorward side of the jet. The enhancement of the tilt proceeds concomitantly with the barotropic component of the flow, which generates negative meridional flux of the eddy zonal momentum (i.e., $\overline{u'v'} < 0$) on the poleward flank of the jet and positive meridional flux of the eddy zonal momentum (i.e., $\overline{u'v'} > 0$) on the equatorward flank of the jet (see e.g., Nakamura, 1993b).

During this early stage of the evolution, conversion of available potential energy (APE) into eddy kinetic energy (EKE) slowly begins, as can be seen from Figures 3.7

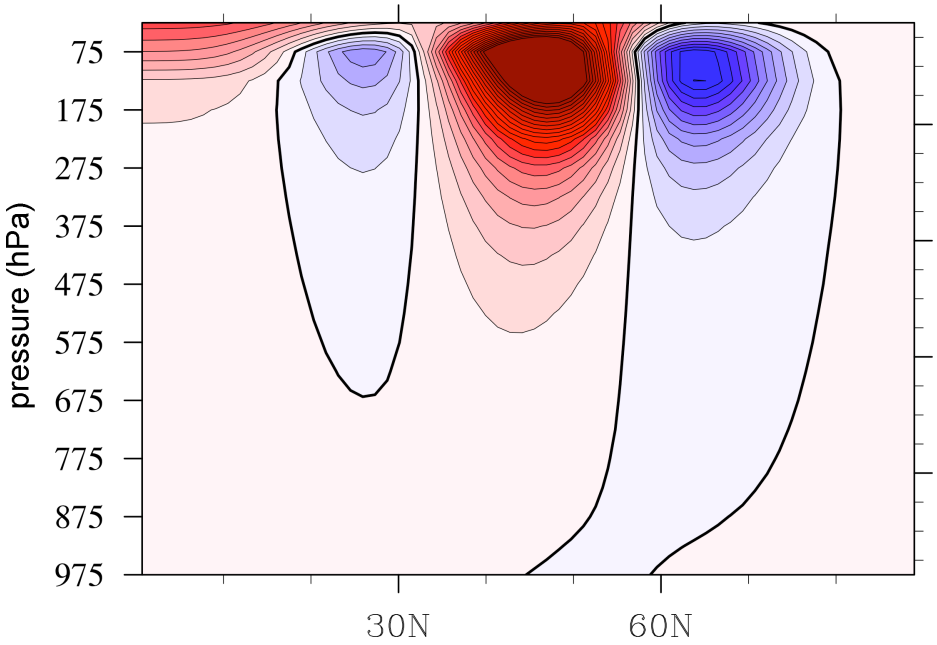

Figure 3.5: Meridional cross-section of the meridional potential vorticity gradient $(\partial q_0/\partial y)_\theta$ for run E45N (northern hemisphere). Maximum and minimum values are $\pm 3 \times 10^{-12}$ K m kg^{-1} s^{-1} with contour interval 2×10^{-13} K m kg^{-1} s^{-1}. Negative values are in blue and positive are in red. The zero contour is drawn with double thickness.

and 3.8 (top left panel). These quantities are defined:

$$APE = -\int_S \int_0^{p_r} \frac{p^{\kappa-1}\,\mathcal{R}}{2g\,{p_r}^{\kappa}} (\theta'')^2 \left(\frac{\partial\hat{\theta}}{\partial p}\right)^{-1} dp\,dA \tag{3.12}$$

$$EKE = \int_S \int_0^{p_r} \frac{1}{2g} \left[(u')^2 + (v')^2\right] dp\,dA\,, \tag{3.13}$$

where θ'' is the deviation of θ from its isobaric average $\hat{\theta}$, and the integrations are over the surface area A and pressure p. The baroclinic instability taps the APE to drive the eddy motions.

At $t \approx 5\ \tau$ a rapid non-linear development ensues in both fields. Note, for example, the scale change in the ζ field at $t = 6\ \tau$. A large amplitude wave can now also be clearly seen in the T field. In both fields, sharp frontal features form. These dynamically-significant sharp features require very high resolution to capture faithfully. This will be discussed more in detail in section 3.3.5. By $t = 8\ \tau$ sharp temperature gradients trail out around the anticyclonic region (large "clover-leaf" shaped area of negative vorticity, shaded in blue), forming curved baroclinic fronts. At this time, the EKE is well into its non-linear growth stage. Note the pools of

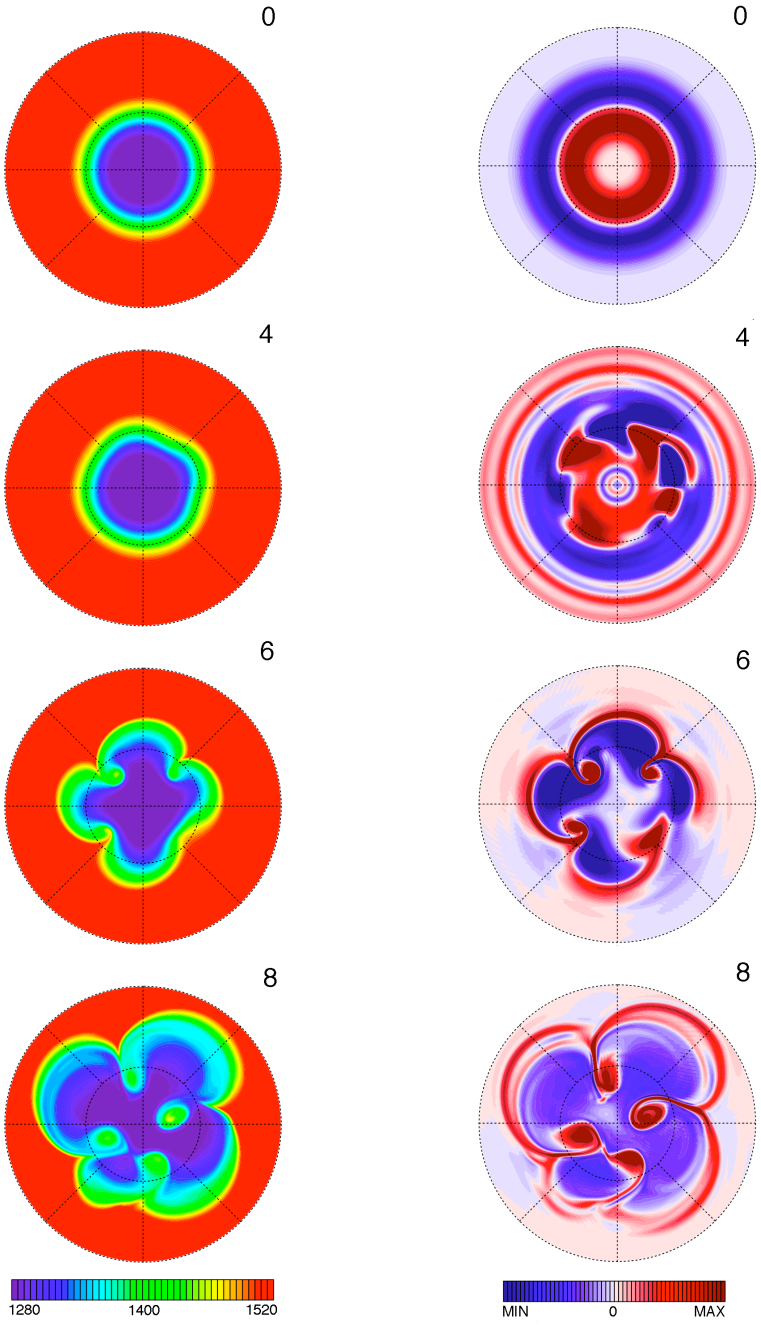

Figure 3.6: Temperature T (left) and relative vorticity ζ (right) from run E45N in polar stereographic view, centred on the north pole. The fields are shown at the 975 hPa pressure level for $t = 0\ \tau$ to $t = 8\ \tau$. Maximum and minimum values for T are 1280 K and 1520 K, respectively, with contour interval 6 K. For ζ, the maximum and minimum values are $\pm 5 \times 10^{-7}$ s^{-1} ($t = 0\ \tau$), $\pm 1 \times 10^{-6}$ s^{-1} ($t = 4\ \tau$), $\pm 1 \times 10^{-5}$ s^{-1} ($t = 6\ \tau$) and $\pm 4 \times 10^{-5}$ s^{-1} ($t = 8\ \tau$); the contour intervals are, respectively, 2×10^{-8} s^{-1}, 4×10^{-8} s^{-1}, 4×10^{-7} s^{-1} and 1.6×10^{-6} s^{-1}. The spectral resolution of this simulation is T170L20 (see text). Note the large, nearly two orders of magnitude, change in the magnitude of ζ during the evolution – as well as the formation of sharp fronts and coherent vortices, particularly at $t = 6\ \tau$ and $t = 8\ \tau$.

warm air that have been pinched off (cyclonic vortices embedded in the anticyclonic region), intruding into the high latitudes (i.e., downgradient heat transport). Simultaneously, broad regions of cool air spread into the tropical region from higher latitude (i.e., upgradient heat transport). Thus, the original equator–pole temperature gradient is significantly reduced by the instability.

The poleward heat transport can be checked against linear theory for eddy transport (see e.g., Holton, 1992; Vallis, 2006) by examining the zonal cross-sections of streamfunction, meridional velocity and temperature perturbations: ψ', v' and T', respectively. The cross-sections at midlatitude are shown in Figure 3.9. As can be seen, ψ' and v' tilt westward with height and T' tilts eastward with height, demonstrating that heat transport is taking place. Note that, in the case of the baroclinically unstable westward jet at the same latitude, the directions of the tilts are reversed. This is because gradient wind balance produces a temperature distribution that is warmer at the poles than at the equator, as can be seen in Figure 3.4b. This results in an equatorward transport of heat by the eddies (section 3.3.3 and Figure 3.13 (top right)).

The long-time evolution of the run presented in Figure 3.6 is illustrated in Figure 3.10 ($t = 10\ \tau$ and $t = 40\ \tau$). By $t \approx 40\ \tau$ the T and ζ fields have organised into essentially zonal structures and eddy activity has mostly ceased. The cyclones that have emerged from the baroclinic wave breaking, strongly interact ($t = 10\ \tau$) and ultimately merge into an unsteady cyclonic polar vortex ($t = 40\ \tau$). A similar "end-state", resulting from vortex mergers, has been observed in HD209458b simulations of Cho et al. (2003).

The long-range interaction of the like-signed vortices on hot-Jupiters is more pronounced than on the Earth (and other cool, rapidly-rotating planets). This can be explained by the much larger Rossby deformation length scale, $L_\mathrm{D}/R_p = \mathcal{O}(1)$, on the hot-Jupiter. Larger L_D means more robust mergers and a more dynamic final vortex (Cho et al., 2003, 2008; Cho and Polvani, 1996). Scott (2011) has recently quantified this behaviour: merger and poleward migration of cyclones ensues if the potential vorticity anomaly q' associated with a vortex exceeds the magnitude of the planetary vorticity 2Ω by ~ 12 per cent. In this case, $(q'/2\Omega) \geq 1.19$ – i.e., anomaly excess of 19 per cent – by $t = 6\ \tau$, consistent with Scott's finding.

The temporal evolution of the global average *EKE* (the dashed blue line for run E45N and solid black line for run EEQ in Figure 3.7) is typically described as a "baroclinic growth – barotropic decay" cycle (e.g., Simmons and Hoskins, 1979; Thorncroft et al., 1993). During the cycle, conversion of *APE* to *EKE* is impeded by a positive feedback between the horizontal shear in the flow and the eddy momen-

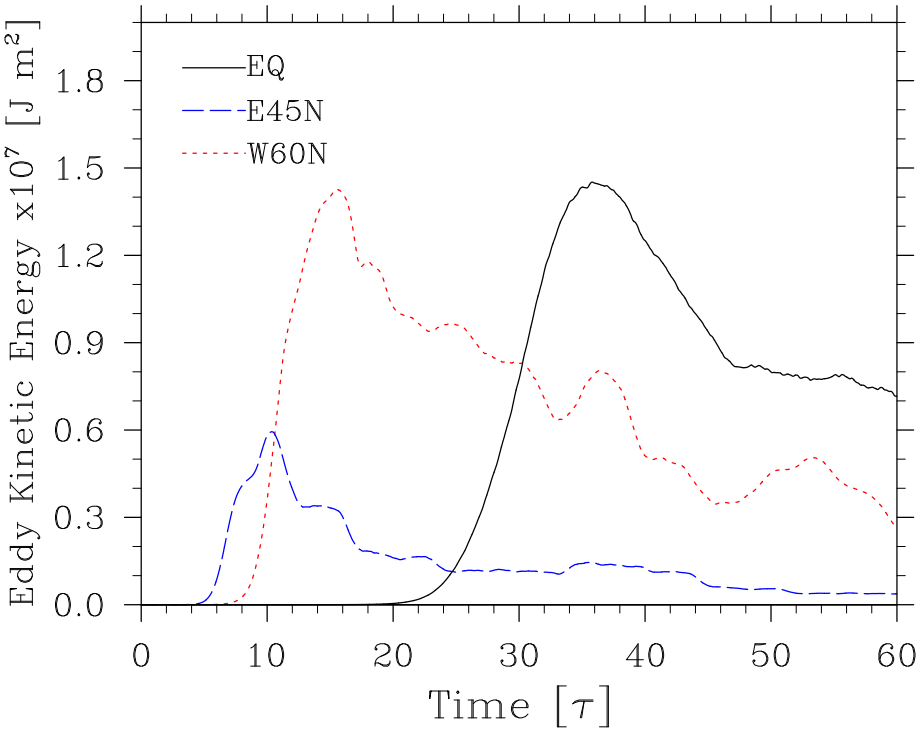

Figure 3.7: Evolution of globally-averaged eddy kinetic energy (per area) [J m^{-2}] for runs E45N (dashed blue line), W60N (dotted red line) and EEQ (solid black line). The eddy kinetic energy for EEQ has been multiplied by a factor of 40.

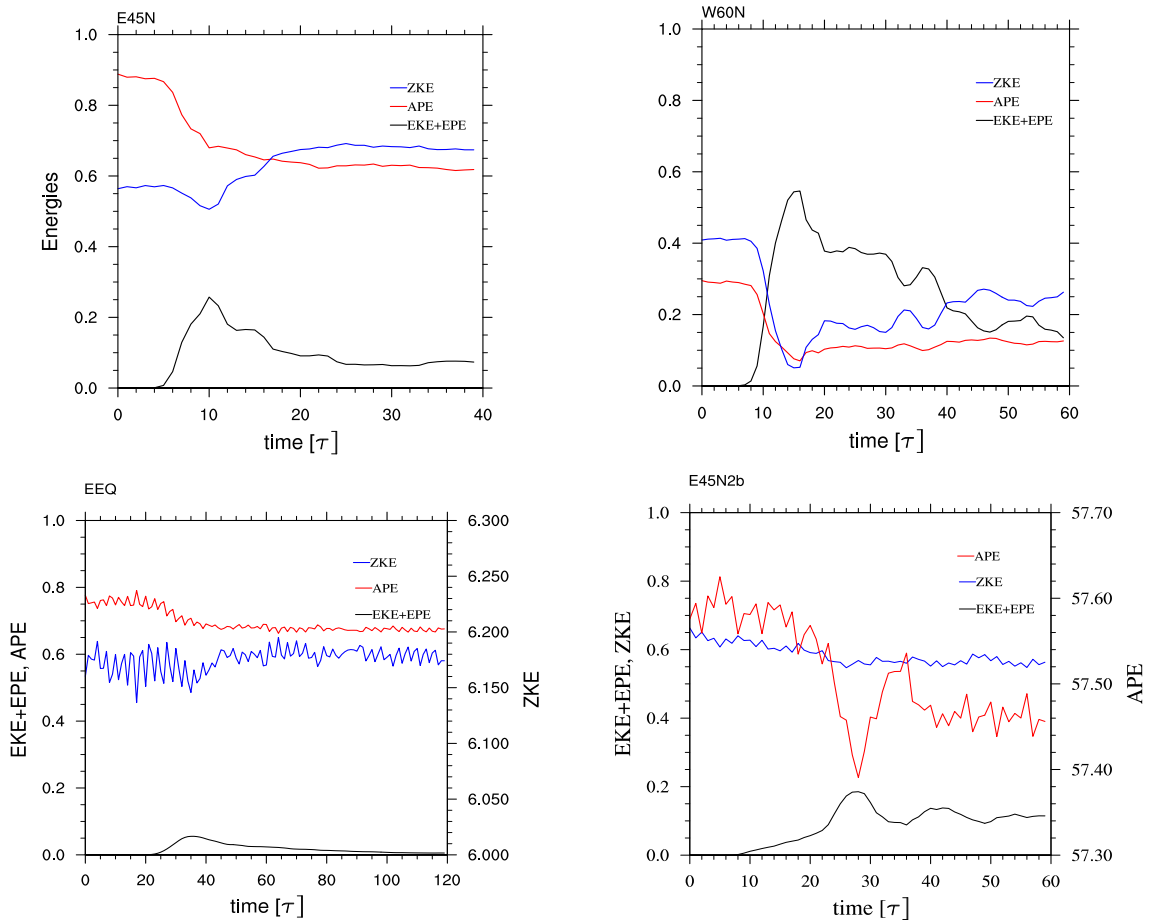

Figure 3.8: Time evolution of total eddy energy (EKE+EPE) [m^2 s^{-2}], zonal potential energy (APE) [m^2 s^{-2}] and zonal kinetic energy (ZKE) [m^2 s^{-2}] for E45N (top left), W60N (top right), EEQ (bottom left), and E45N2b (bottom right). For E45N and W60N all energies are scaled by 28000, and for EEQ and E45N2b by 8000. Note that ZKE for EEQ and APE for E45N2b is plotted on a separate y-axis. In all the simulations, APE is converted into eddy energy during the baroclinic growth stage. The eddy energy is subsequently returned to the mean flow (i.e., ZKE) during the barotropic decay stage in E45N and W60N. Note that for simulation W60N, conversion from ZKE into eddy energy is larger than conversion from APE into eddy kinetic energy.

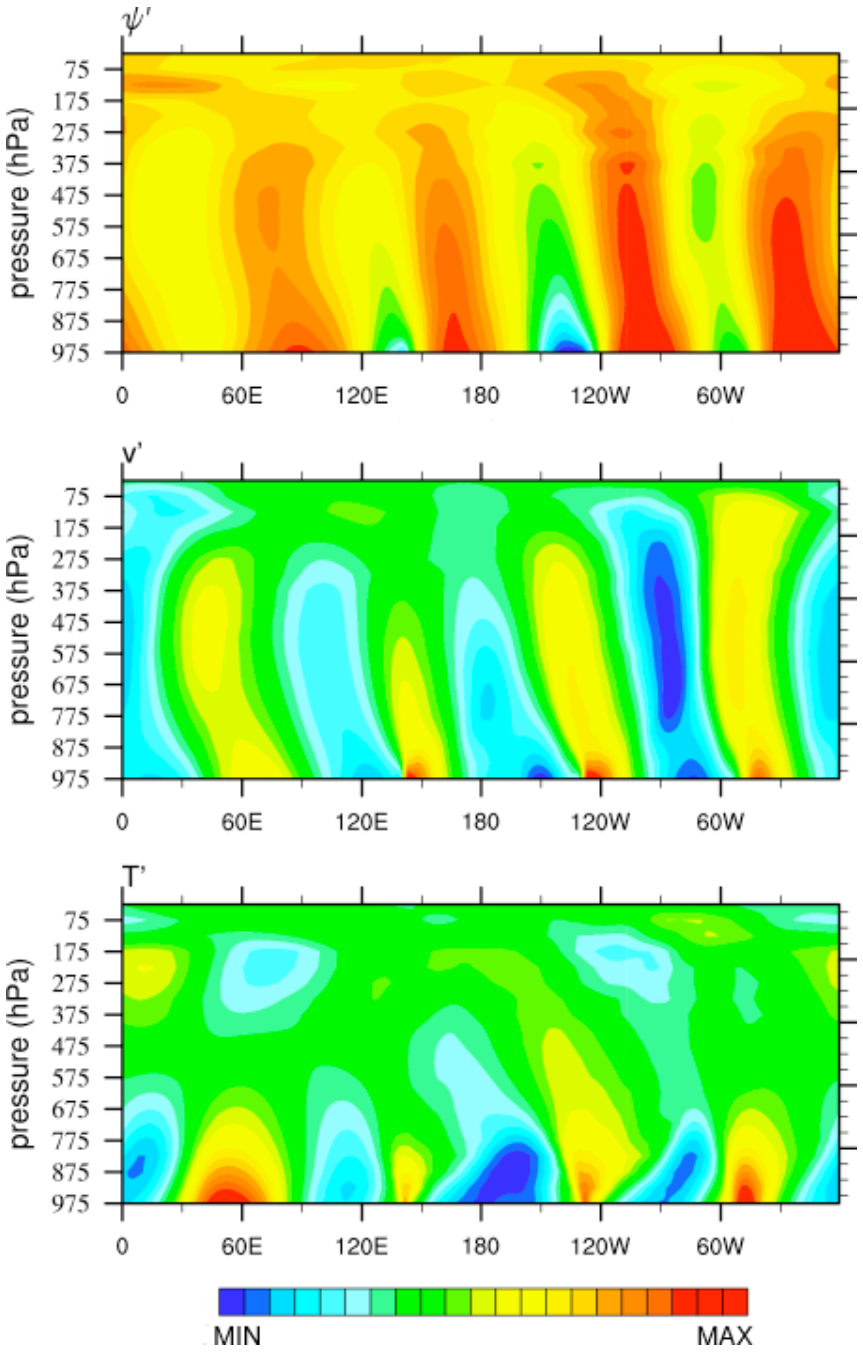

Figure 3.9: Perturbation streamfunction ψ' (top), perturbation meridional velocity v' (middle) and perturbation temperature T' (bottom) at midlatitude as a function of pressure and longitude at $t = 6\ \tau$ for run E45N. Contour intervals are: -24×10^8 m^2 s^{-1} to 11×10^8 m^2 s^{-1} in steps of 10^8 m^2 s^{-1}, -180 m s^{-1} to 320 m s^{-1} in steps of 20 m s^{-1} and -75 K to 125 K in steps of 5 K, respectively. Note, ψ' and v' tilt westward with height and T' tilts eastward with height, signifying meridional transport of heat and reduction of equator-pole temperature gradient.

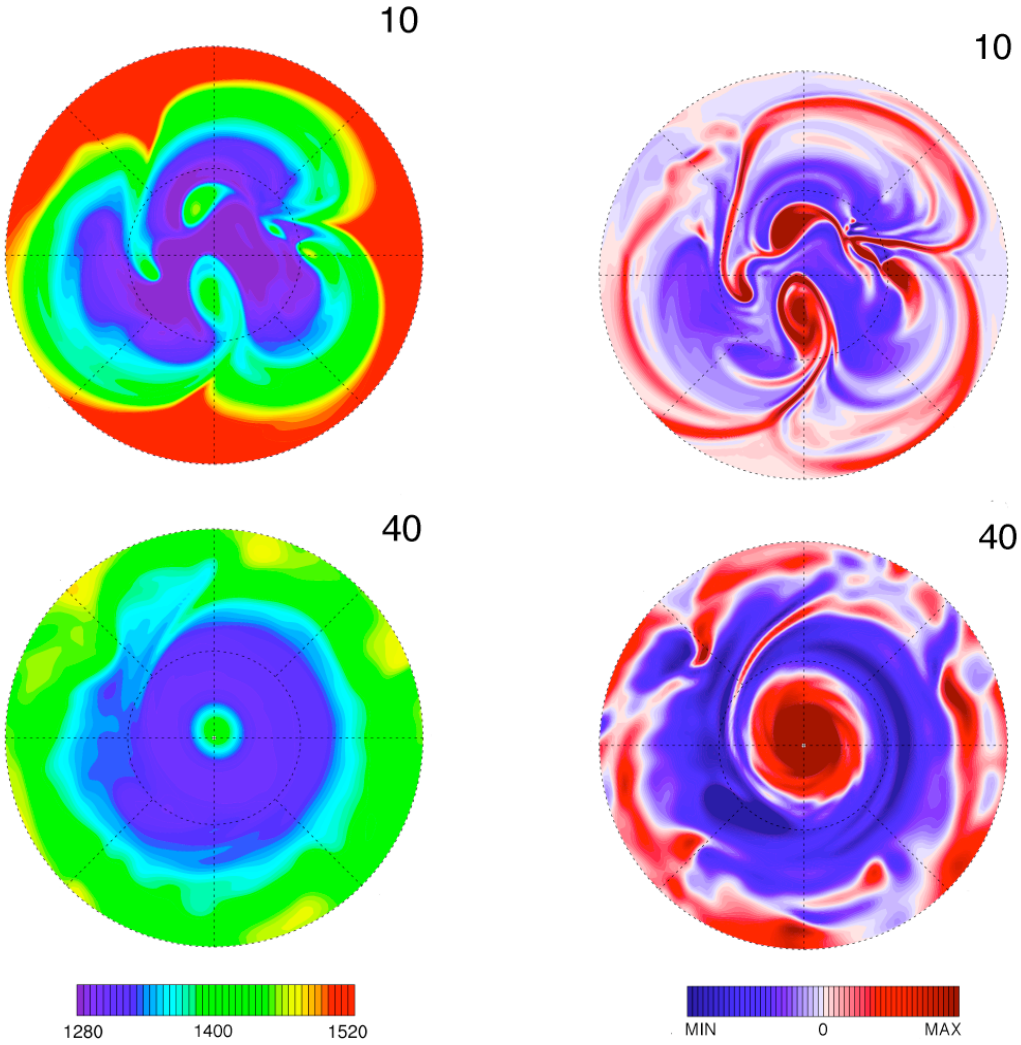

Figure 3.10: Same as Figure 3.6 but for $t = 10\ \tau$ and $t = 40\ \tau$. Contour interval for temperature is 6 K. The maximum and minimum contours for relative vorticity are $\pm 4 \times 10^{-5}$ s^{-1} at $t = 10\ \tau$ and $\pm 10^{-5}$ s^{-1} at $t = 40\ \tau$. The respective contour intervals are 1.6×10^{-6} s^{-1} and 4×10^{-7} s^{-1}.

tum flux. At $t \geq 10\ \tau$, the disturbances in run E45N are sheared out and *EKE* is lost to the mean flow through the Reynolds stresses more than it is gained through baroclinic conversion. In this process, eddy energy is returned to the zonal kinetic energy (henceforth ZKE) as can be seen in Figure 3.8 (top left). The feedback is the main component in the previously mentioned non-linear "barotropic governor effect", affected by the horizontal shear in the jet, spherical geometry and ageostrophy (see e.g., Nakamura, 1993b).

The zonal mean zonal wind $\bar{u}$ and zonal mean zonal potential temperature $\bar{\theta}$ at the end of the life-cycle is presented in Figure 3.11 (see panel *a* on the left for run E45N). The jet itself has becomes broader and more barotropic – much

like the "LC1 life cycle" reported in Thorncroft et al. (1993). Furthermore, the meridional entropy gradient $\mathrm{d}\bar{\theta}/\mathrm{d}\phi$ is significantly reduced compared to the initial state, particularly at the lower levels in the domain (cf. Figure 3.4a). Much of the *APE* is taken up by the kinetic energy of the zonal mean flow and the flow is accelerated there. To quantify the accelerations, consider the transformed Eulerian-mean zonal momentum equation (e.g., Andrews and McIntyre, 1978):

$$\frac{\partial\,\bar{u}}{\partial\,t} \;=\; -\left[\frac{1}{R_p\,\cos\phi}\frac{\partial}{\partial\,\phi}(\bar{u}\,\cos\phi) - f\right]\,\bar{v}^* \;-\; \frac{\partial\bar{u}}{\partial\,p}\,\bar{\omega}^* \;+\; \frac{1}{R_p\,\cos\phi}\,\nabla\cdot\mathbf{F}\,. \quad (3.14)$$

Here $\bar{v}^*$ and $\bar{\omega}^*$ represent the "residual" mean meridional circulation,

$$\bar{v}^* \;\equiv\; \bar{v} - \frac{\partial}{\partial p}\left(\frac{\overline{v'\theta'}}{\partial\bar{\theta}/\partial p}\right) \quad (3.15)$$

$$\bar{\omega}^* \;\equiv\; \bar{\omega} + \frac{1}{R_p\cos\phi}\frac{\partial}{\partial\phi}\left(\frac{\overline{v'\theta'}}{\partial\bar{\theta}/\partial p}\cos\phi\right)\,, \quad (3.16)$$

and $\mathbf{F}=(F_\phi, F_p)$ is the Eliassen-Palm (EP) flux vector with

$$F_\phi \;=\; R_p\cos\phi\left[-\overline{u'v'} + \left(\frac{\overline{v'\theta'}}{\overline{\partial\theta/\partial p}}\right)\left(\frac{\partial\overline{u}}{\partial p}\right)\right] \quad (3.17)$$

$$F_p \;=\; R_p\cos\phi\left[(\overline{\zeta}+f)\left(\frac{\overline{v'\theta'}}{\overline{\partial\theta/\partial p}}\right) - \overline{u'\omega'}\right]\,. \quad (3.18)$$

The influence of eddies on the mean flow is measured by the EP fluxes: a convergent flux ($\nabla\cdot\mathbf{F}<0$) corresponds to the deceleration of the eastward flow and a divergent flux ($\nabla\cdot\mathbf{F}>0$) corresponds to acceleration. Figure 3.12 depicts vertically and temporally averaged EP flux divergence for E45N (dashed line) over the life-cycle. The EP fluxes are divergent in the net on the poleward flank of the jet, where the flow is accelerated, and (more strongly) convergent in the net on the equatorial flank, where overall the flow speed is reduced from the initial value (cf. Figure 3.11a).

Figure 3.13 (top left) shows a more complete picture of the EP fluxes for the E45N simulation. In the figure the latitude-pressure cross sections of EP flux vector field and its divergence, $\nabla\cdot\mathbf{F}$ (contours) averaged over the life-cycle are shown. The EP flux and its divergence are reminiscent of the "LC1 life cycle" reported in Thorncroft et al. (1993) with Rossby waves, generated near the surface, propagating upward and equatorward, transporting momentum poleward (cf. the equatorward pointing

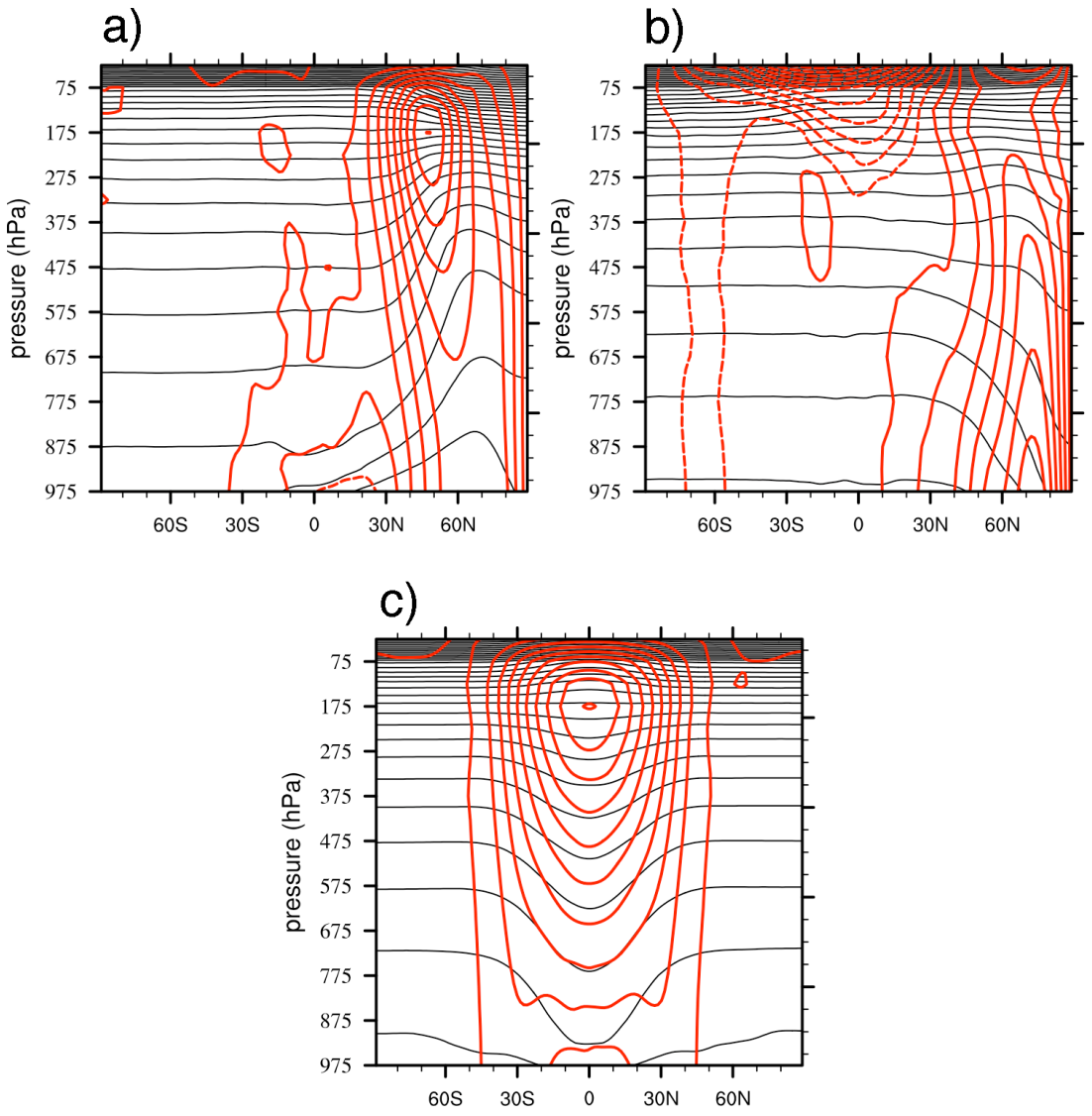

Figure 3.11: Zonal mean zonal wind $\bar{u}$ (red) and potential temperature $\bar{\theta}$ (black) contours for runs a) E45N at $t = 30\ \tau$, b) W60N at $t = 60\ \tau$ and c) EEQ at $t = 60\ \tau$. Wind contour interval for runs E45N and EEQ is 100 m s^{-1} and for run W60N is 50 m s^{-1}. Temperature contour interval is 100 K. Negative (westward) wind contours are dashed.

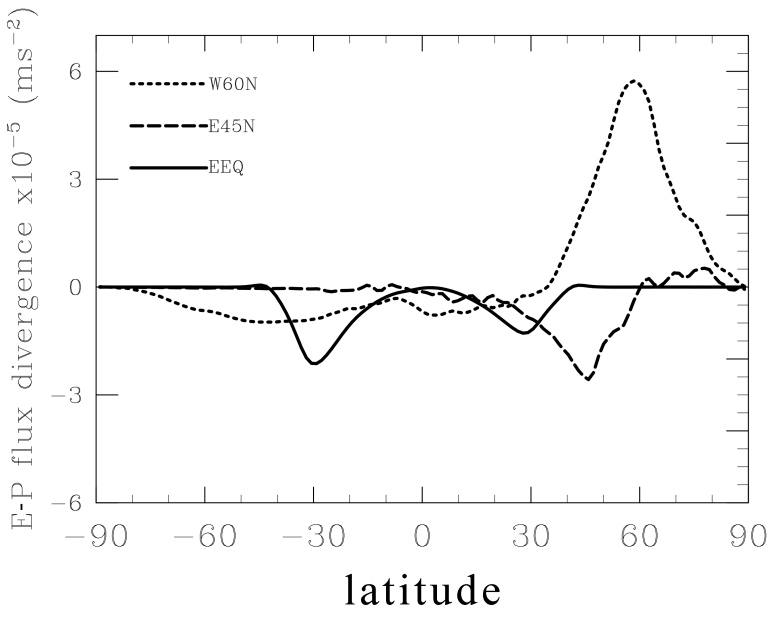

Figure 3.12: Vertically and temporally averaged divergence of Eliassen-Palm (EP) flux [m s^{-2}] for runs E45N (dashed line), W60N (dotted line) and EEQ (solid line) during the life-cycle in each run. The EEQ curve has been multiplied by a factor of 100.

F vectors) and heat upward and poleward (cf. the upward pointing **F** vectors). The vector field is divergent (positive) near the surface at mid- and high-latitudes and convergent (negative) throughout the vertical domain on the equatorward flank of the jet.

Finally, note that the most unstable mode for this simulation is ~ 4 (see Figure 3.6). As discussed earlier, the linear theory of section 3.2.3 underestimates this number to ~ 2. However, the full numerical simulation shows that the simple linear theory is successful, at least qualitatively, in capturing the behaviour of the instability in the following sense: the most unstable mode and the growth time for the baroclinic wave amplitude for HD209458b are smaller than the corresponding quantities for the Earth (cf., for example, Polvani et al., 2004).

Lower Boundary

As is well-known, boundary conditions are crucial in solving differential equations. Differences in the conditions, even in relatively simple physical situations, can alter the admitted solutions. For example, new or modified modes can be introduced or existing modes can be filtered by employing rigid boundary condition (i.e., $w = 0$).

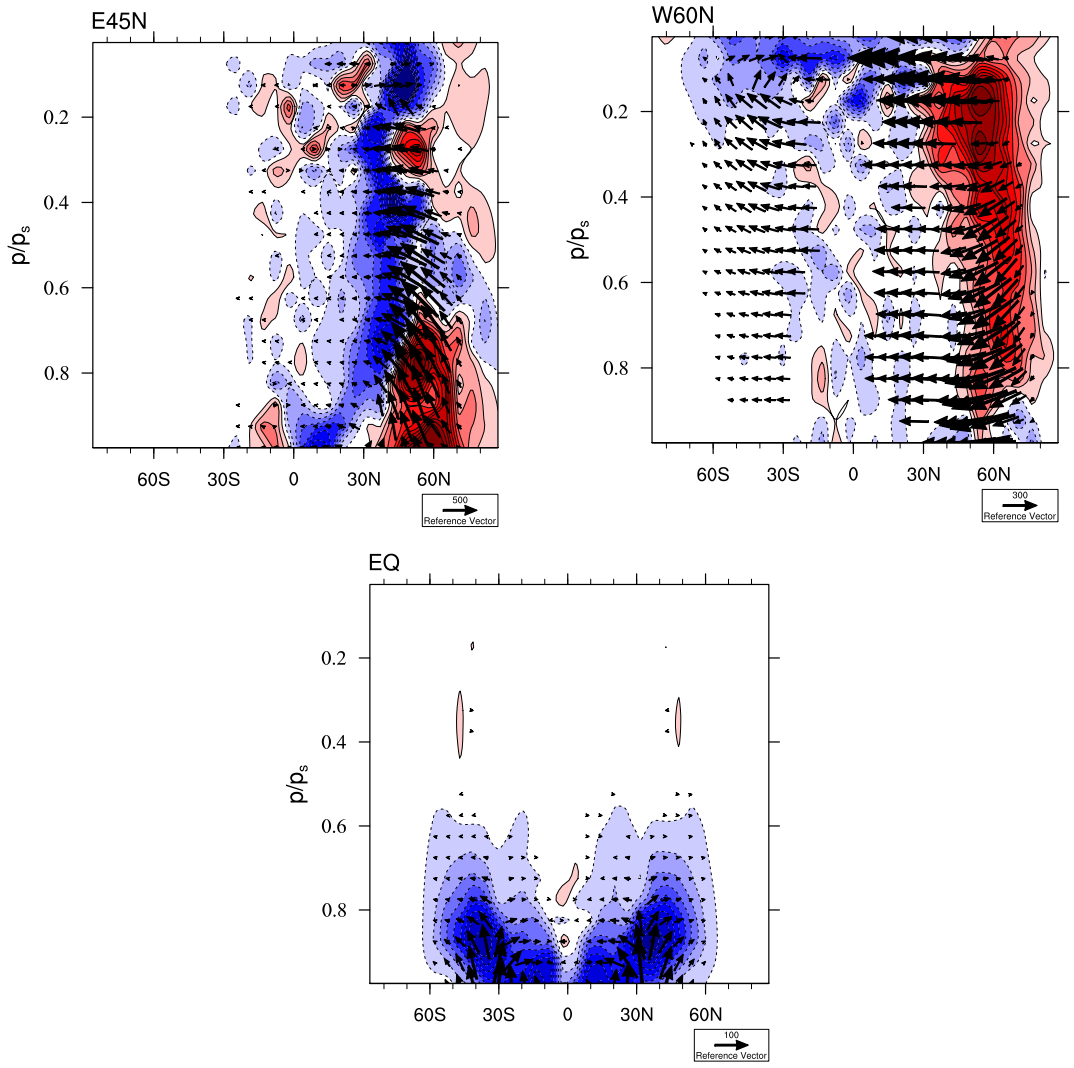

Figure 3.13: Eliassen-Palm flux vector, $\mathbf{F} = (F_\phi, F_p)$ [m^2 s^{-2}], and its divergence, $\nabla \cdot \mathbf{F}$ [m s^{-2}], fields for the E45N simulation (top left), the W60N simulation (top right), and the EEQ simulation averaged over the life-cycle. Negative $\nabla \cdot \mathbf{F}$ values are dashed (and in blue) and positive values are solid (and in red). Maximum and minimum $\nabla \cdot \mathbf{F}$ values are $\pm 10000\,\mathrm{m\,s^{-2}}$ in top panels and ± 2000 m s^{-2} in bottom panels. The reference vector has magnitude of 500 m^2 s^{-2} (top left), of 300 m^2 s^{-2} (top right), and 100 m^2 s^{-2} (bottom). F_ϕ and F_p are scaled by 1 radian of latitude and 1 Pa of pressure, respectively. In addition, F_p is scaled by a factor of 0.5 in all panels. The wave propagation is upward and equatorward in the E45N simulation; downward and equatorward on the Northern hemisphere and poleward on the Southern hemisphere in the W60N simulation; and, upward and equatorward and poleward in the EEQ simulation.

The lower boundary of the simulations discussed in this chapter is rigid and located at 1 bar for the most part. In this case, the vertical wind shear in the basic flow used is small, but non-zero, at the bottom boundary and baroclinically unstable modes can arise due to the presence of the boundary – via condition (ii) of the Charney-Stern-Pedlosky criteria. However, the stably-stratified radiative zone in hot-Jupiter atmospheres may extend down to perhaps as deep as 1000 bars (Guillot and Showman, 2002). Hence, the effects of lowering the bottom boundary and preventing flow shear there require careful consideration.

Figure 3.14 presents a run (E45N2b) that is very similar to the "paradigm case", but with the lower boundary of the simulation extended down to 2 bars. The jet is confined to pressures above the 1 bar level. In doing so the influence of the lower boundary is removed far enough away from the jet while still retaining an adequate vertical resolution. In the figure, u_0 and θ_0 are shown in the top panel. Note, the jet profile shown in the figure has a different vertical structure than the "paradigm case" jet. This is because balancing a jet with the vertical structure given by equation (3.8) to the isothermal reference state produces a convectively unstable region in the computational domain, causing the vertical coordinate to lose single-valuedness and the run to immediately crash. The shown profile does not suffer from this. Significantly, the Charney-Stern-Pedlosky criteria (iv) and (i) remain satisfied for this profile. It is crucial to understand here that, once these criteria are met, it does not matter whether the lower boundary is located at 10 or 1000 bars for the instability to occur.

The ζ field at $t = 10\ \tau$ is shown in the right panel of Figure 3.14. Although the evolution is now slightly altered from the "paradigm case" (i.e., mode-3 is dominant, rather than mode-4), the jet is still unstable, as expected. It has been verified that the evolution in run E45N2b is indeed a result of baroclinic instability: the perturbation fields tilt in the appropriate directions with height, as seen in Figure 3.9 for run E45N. Additionally, as can be seen in Figure 3.8 (bottom right) the available potential energy APE is converted into eddy energy — as is characteristic of baroclinic instability. The instability is, however, weaker and evolves differently than when there is an initial vertical wind shear and meridional entropy gradient at the lower boundary (see also Chapter 5). A simulation with the initial flow profile used in run E45N2b but with bottom raised to 1 bar, in which the shear and gradient is non-zero at the bottom has also been performed. The peak global eddy kinetic energy in this run is ~ 40 per cent greater and vorticity perturbations are up to six times stronger than in run E45N2b. Nevertheless, the point is, the instability is present regardless of vertical flow shear at the bottom boundary.

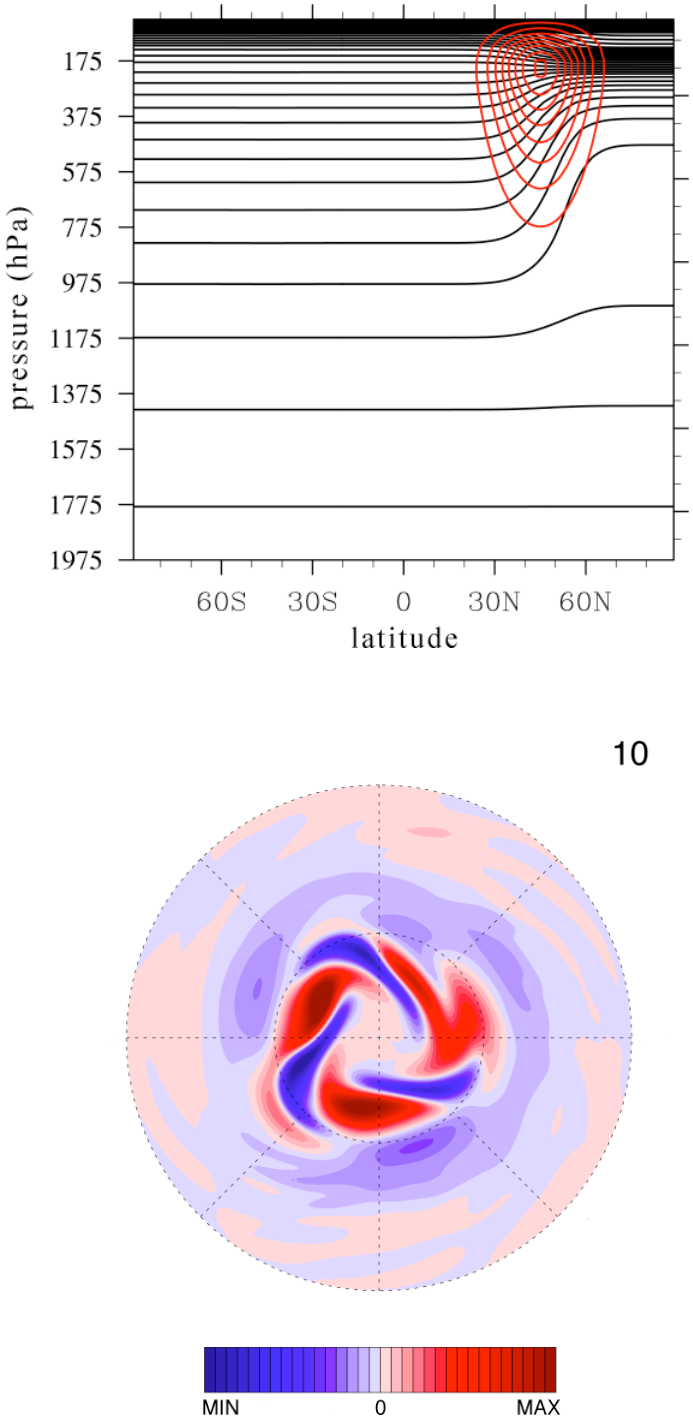

Figure 3.14: Top: Basic state zonal wind u_0 (red) and potential temperature θ_0 (black) for run E45N2b with the lower boundary extended to 2 bars. Contour interval for the zonal wind is 100 m s^{-1} and for the potential temperature 100 K. Bottom: Relative vorticity ζ from run E45N2b at $t = 10\ \tau$. The field is plotted at 975 hPa pressure level. Maximum and minimum values are $\pm 6 \times 10^{-6}$ s^{-1}, with contour intervals of 4×10^{-7} s^{-1}.

3.3.3 High Latitude Westward Jet

Having presented the evolution of the "paradigm case", the case of a baroclinically unstable high-speed westward jet at high latitude (run W60N) is now presented. The speed at the core of the jet is 1000 m s^{-1}. Such jets have been observed in recent GCM simulations (e.g., Showman et al., 2008; Menou and Rauscher, 2009; Thrastarson and Cho, 2010; Heng et al., 2011). In the above mentioned simulations, the high latitude jets are observed to be more narrow and shallow than the equatorial jets. Equatorial jets will be discussed in section 3.3.4. The T field from run W60N at $t = 9\ \tau$ (975 hPa pressure level) is shown in the left column of Figure 3.15. Polar stereographic view, centred on the north pole (top frame), and cylindrical-equidistant view, centred on the equator (bottom frame), are shown for latitudes poleward of 20°N. For comparison, the right column shows the corresponding projections of the T field from the E45N run at $t = 7\ \tau$, roughly at a similar stage of the evolution in run W60N.

In run W60N, baroclinic wave develops a significant northwest–southeast tilt. This is consistent with the predominantly negative momentum fluxes on the poleward side of the jet during the linear stage of the evolution (see also Figure 3.13 (top right panel)). Again, the flow is characterized by sharp cyclonic fronts, this time with the most unstable mode having 3 undulations at $\phi = 60°$. The reduction in the number of undulations is also consistent with linear theory developed in section 3.2.3. However, contrary to the predictions from the linear analysis, the growth rate of the instability is lower than for the E45N run (cf. the onset of growth between dashed blue and dotted red lines in Figure 3.7). As already discussed, this agrees with the analysis of the Charney model by Wang (1990) and extends that result to the more general, global primitive equations model.

Note that wave-breaking in the westward jet case occurs in the opposite direction to that in the "paradigm case" (see bottom row of Figure 3.15). The waves in run W60N (left) break eastward, whereas in run E45N (right) the waves break westward. "Blobs" of higher temperature fluid penetrate into the lower temperature region and cooler fluid subsides into the warm region. The situation is analogous to Rayleigh-Taylor or convective instability (e.g., Sharp, 1984), where a decrease of potential energy results under the interchange of two blobs at different heights. In baroclinic instability, this can occur despite the stable density stratification because the density surfaces are sloping more steeply than the line joining the two blobs. Indeed, for this reason baroclinic instability is sometimes refer to as "sloping convection" (e.g., Vallis, 2006).

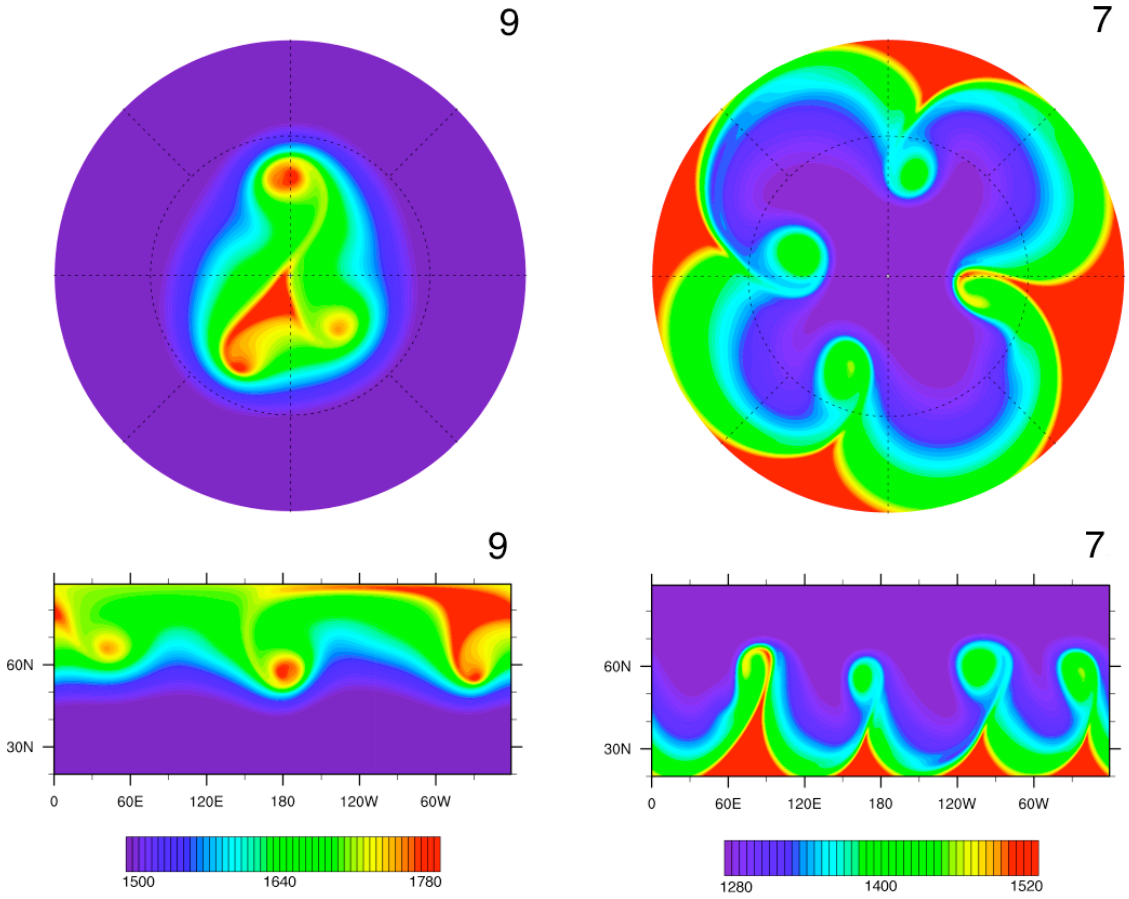

Figure 3.15: Temperature field T for run W60N at $t = 9\ \tau$ (left) and T for run E45N at $t = 7\ \tau$ (right). The fields are shown at 975 hPa pressure level. Top frame shows the field in polar stereographic view, centred on the north pole, and bottom frame shows the field in cylindrical-equidistant view, centred on the equator. In all frames area poleward of $\phi = 20°$ is shown. For run W60N the maximum and minimum values are 1500 K and 1780 K, respectively. For run E45N the maximum and minimum values are 1280 K and 1520 K, respectively. Contour interval is 6 K in both runs.

Note that the *EKE* for the westward jet case does not follow a simple "baroclinic growth – barotropic decay" cycle, as seen in the "paradigm case" (Figures 3.7 and 3.8). Instead, after the initial decay stage at $t \approx 15\,\tau$, the *EKE* for run W60N shows large vacillations, corresponding to a sequence of baroclinic–barotropic life cycles. Similar behaviour of energetics has been observed by Feldstein (1991) for the Earth case. In a two-layer QG β-plane model, he found westward jets to undergo a series of mixed, baroclinic–barotropic instability, caused by the reversal of sign in the jet curvature $\partial^2 u_0/\partial y^2$. Recall that $\beta \geq 0$. Hence, a barotropically unstable region, in which $\beta - \partial^2 u_0/\partial y^2 < 0$, forms at the core of the westward jet (as is the case in run W60N). The combined effects of vertical and horizontal shears reinforce each other to establish a mixed, baroclinic–barotropic unstable region. According to WKB analysis (e.g., Bender and Orszag, 1999), growing disturbances emanating from a westward jet are trapped (i.e., reflected) between two turning latitudes, initiating the sequence. Consistent with this, the meridional structure of the disturbance is able to remain close to the normal mode form. In contrast, disturbances emanating from the eastward jet are absorbed at or near the critical latitudes, resulting in a single cycle and meridional structure that changes with time. As shown in Figure 3.8 (top right) more zonal kinetic energy (ZKE) than *APE* is converted into eddy energy. Note also that the EP flux has a significant horizontal component (see Figure 3.13 (top right)). This suggests that barotropic instability plays a significant role in the W60N life-cycle.

Figure 3.11b shows the equilibrated $\bar{u}$ and $\bar{\theta}$ at the end of the simulation. The original westward jet has been completely disrupted, giving way to a fairly barotropic eastward jet centred at 60°. Predominantly westward flow is now situated in the subtropics, at the upper levels of atmosphere. The reversal of the flow direction is consistent with EP flux divergence shown in Figure 3.12 (dotted line) and Figure 3.13 (top right), which acts as a positive momentum source. Given that high-latitude westward jets appear to be a fairly common feature in GCM simulations of hot-Jupiters, the result here suggests external (e.g., stellar irradiation) or internal (e.g., wave) forcing may be required to maintain baroclinic westward jets. Note also from Figures 3.11b, 3.12 and 3.13 (top right), the negative zonal flow and EP flux convergence, especially in the equatorial region. Significantly, such negative EP flux divergences present a source of drag for equatorial jets. Finally, as in the "paradigm case", the potential vorticity anomalies exceed 2Ω by over 12 per cent and by $t = 35\,\tau$ a cyclonic polar vortex forms that is warmer than its surroundings (not shown).

3.3.4 Equatorial Jet

The evolution of a broad, high-speed equatorial jet (run EEQ) is presented in this section. The initial flow and potential temperature is shown in Figure 3.4c. Unlike the jets discussed in sections 3.3.2 and 3.3.3, the equatorial jet satisfies the Charney-Stern-Pedlosky instability criteria (iv) on its flanks (at $\sim 30°$ on both northern and southern hemispheres), rather than at the core. The stability of this jet's core is consistent with linear theory of section 3.2, which predicts no growth for a jet located equatorward of 28°.

Figure 3.16 shows temperature T and relative vorticity ζ fields at $t = 26\ \tau$. At this time the instability is well developed, with sharp fronts rolling up non-linearly into cyclones at $\phi \approx 35°$, where the instability criteria is met. A mode with ~ 7 undulations can clearly be seen at this stage of the evolution. The number of undulations is significantly higher and the growth rate is significantly lower for EEQ than for simulations where the same jet is placed at $\phi = 30°$. Evidently, since the vertical shear of the equatorial jet at its flanks is significantly lower than at its core, a value smaller than the peak core value for the characteristic flow speed should be used in interpreting the results from the linear analysis. As has already been seen, a weaker jet (shear) results in a smaller growth rate and wavelength of the most unstable mode at a given latitude (e.g., curves "HD45L" and "HD45" in Figure 3.2). Hence, these non-linear simulations appear to be in qualitative agreement with linear theory. Despite the instability at the flanks, the core of the jet in run EEQ remain stable throughout the integration (up to $t = 60\ \tau$), in very good agreement with linear theory.

The *EKE* evolution for run EEQ is shown in Figure 3.7 (solid black line). The equatorial jet instability is shallow and confined to a pressure range between 1 to 0.7 bar, unlike the high-latitude jet instability (cf. Figure 3.13); in those cases, the range of instability is much larger, extending up to 0.01 bar. Thus, only the lower pressure levels exhibit an increase in *EKE* during the linear stage. For this reason, the *EKE* values have been multiplied by a factor of 40 in the figure: the globally averaged *EKE* for run EEQ is much lower than for the "paradigm case" or run W60N. Note also that conversion of energy from *APE* into *EKE* is significantly smaller than for the E45N and W60N simulations (see Figure 3.8). Qualitatively, the non-linear evolution of run EEQ is similar to run E45N, with waves tilting and breaking in same directions. As can be seen in Figure 3.13, the vertical wave propagation in both E45N and EEQ simulations is upward (signifying poleward heat transport by the eddies). However, for EEQ the meridional wave propagation is both

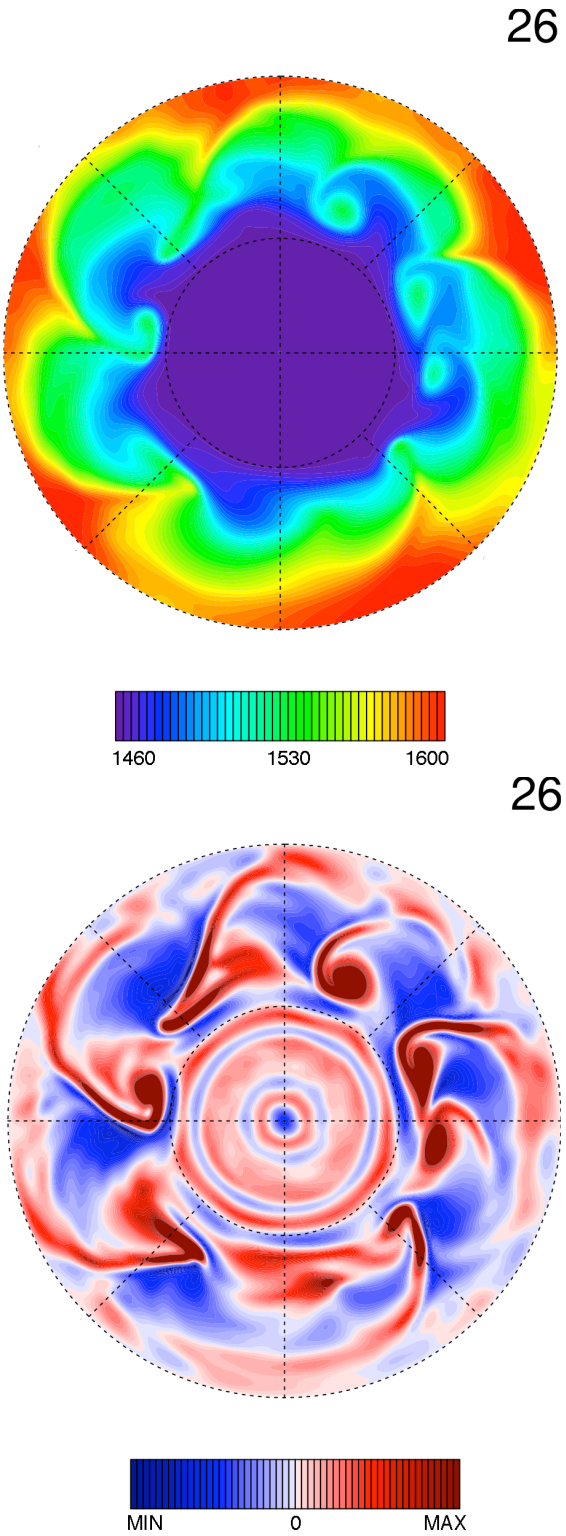

Figure 3.16: Temperature T (top) and relative vorticity ζ (bottom) for run EEQ in polar stereographic view, centred on the north pole. The fields are shown at 975 hPa pressure level for $t = 26\ \tau$. Maximum and minimum values for temperature are 1460 K and 1600 K, respectively, with contour interval 3.5 K. Values for ζ are in the range $\pm 1.5 \times 10^{-5}\mathrm{s}^{-1}$, with contour interval $6 \times 10^{-7}\mathrm{s}^{-1}$.

poleward *and* equatorward (signifying both poleward and equatorward momentum transport by the eddies) whereas the wave propagation is mostly equatorward for the paradigm case (signifying mostly poleward momentum transport). Additionally, potential vorticity anomaly only slightly exceeds the polar value and the cyclonic drift does not ensue. Therefore, a monolithic polar vortex does not form in this case.

Interestingly, the jet structure is only slightly altered by baroclinic instability from the basic state zonal flow. Mainly, the jet has become more barotropic at the flanks. This can be seen in Figure 3.11c, which shows $\bar{u}$ and $\bar{\theta}$ at $t = 60\ \tau$. Relatively small values of EP flux convergence equatorward of 50° (see the solid line in Figure 3.12 and the bottom panel in Figure 3.13) do not significantly contribute to the deceleration of the zonal mean zonal wind.

It is also worth noting that stability properties of the westward equatorial jet have been investigated. The jet is found to be stable to baroclinic instability, in good agreement with Wang (1990). A westward jet placed at the equator would have to exceed the sound speed, if the condition (3.7) of section 3.2 is to be fulfilled. However, note that a broad, "supersonic" westward jet does not appear to be unstable in full, non-linear GCM simulations (Thrastarson, private communication). But, the simulation is at T21 resolution (see section 3.3.5). Eastward equatorial jets have been found to be stable to baroclinic instability, if the width of the jet is 50° and smaller.

3.3.5 Numerical Convergence

Baroclinic instability in numerical simulations of hot-Jupiters is highly sensitive to numerical resolution (both horizontal and vertical) and to dissipation. High resolution is required to capture the instability accurately. In particular, for the jet profiles used, five or more layers are necessary to capture the instability, and good convergence is reached only with ~ 10 or more layers. In addition, high horizontal resolution ($\geq$ T85) is necessary to ensure accurate representation of the eddy fluxes, as well as convergence. Separately, artificial viscosity must not be too high, as it results in artificially-enhanced stabilization of the baroclinic modes. It is emphasized that resolution and dissipation requirements are dependent on the jet profile. Hence, the requirements should be carefully assessed for each profile employed. This "problem-dependence" conclusion has also been discussed by Thrastarson and Cho (2011) for "spin-up" experiments of hot-Jupiter circulations.

Before presenting the results, a brief discussion concerning the general approach

to convergence testing is in order. In general, for numerical stability reasons, the usual practice is to use a larger dissipation coefficient value when performing a simulation with lower resolution – or, alternatively, a smaller coefficient value when performing the same simulation at higher resolution – so that the damping time is same at the truncation scale. This results in a different damping time for a given mode at different resolutions. However, here the aim is to demonstrate convergence of the numerical model. Hence, the same value of the coefficient at all resolutions is employed so that each mode, up to the truncation, experiences same dissipation rate in all the runs. The employed value is: $\nu_4 = 6 \times 10^{19}$ m^4 s^{-1}. Similar methodology has been implemented in e.g., Polvani et al. (2004) to test convergence in the Earth case. Later, non-convergence is also demonstrated when the damping time is chosen such that it is same at the truncation scale for all resolutions, as in the usual practice.

The requirement of adequate resolution is demonstrated in Figure 3.17. The figure shows a set of four simulations with all parameters identical to run EEQ presented in section 3.3.4 – except the resolution. The resolutions are: T21 (a), T42 (b), T85 (c) and T170 (d). Note, panel (d) is run EEQ. All four runs use the same value of superviscosity coefficient, $\nu_4 = 6 \times 10^{19}$ m^4 s^{-1}, as already mentioned. Note also that the resolutions correspond, respectively, to 64×32, 128×64, 256×128 and 512×256 Gaussian grids in physical space. But, because of the exponential convergence property of the spectral method, they are equivalent in accuracy to finite difference grids $\mathcal{O}(10)$ times finer in resolution (e.g., Thrastarson and Cho, 2011). Polar stereographic projections of the relative vorticity field ζ at $t = 22\ \tau$ are shown, when the instability is in the early exponentially-growing stage (see Figure 3.7).

Visual inspection of the fields readily reveals that the T21 (a) and T42 (b) runs do not converge to the T170 (d) run. The T85 (c) run is marginally converged, though this may change after a long time (e.g., many hundreds of planetary rotations). In the figure, frames (a) and (b) are qualitatively different than frames (c) and (d), which clearly show mode-6 instability. The T85 run in frame (c) captures the basic structure present in the T170 run in frame (d). However, spurious small-scale oscillations are also clearly visible in frame (c); these are not present in frame (d). The small-scale oscillations contaminate the simulation – causing the simulation to blow up, depending on the numerical parameters used; see e.g., discussion in Thrastarson and Cho (2011).

The above behaviour can be quantified by computing the corresponding kinetic energy spectra for each run. The spectra for the fields shown in Figure 3.17 are presented in the top panel of Figure 3.18. Inspection of the T85 and T170 spectra

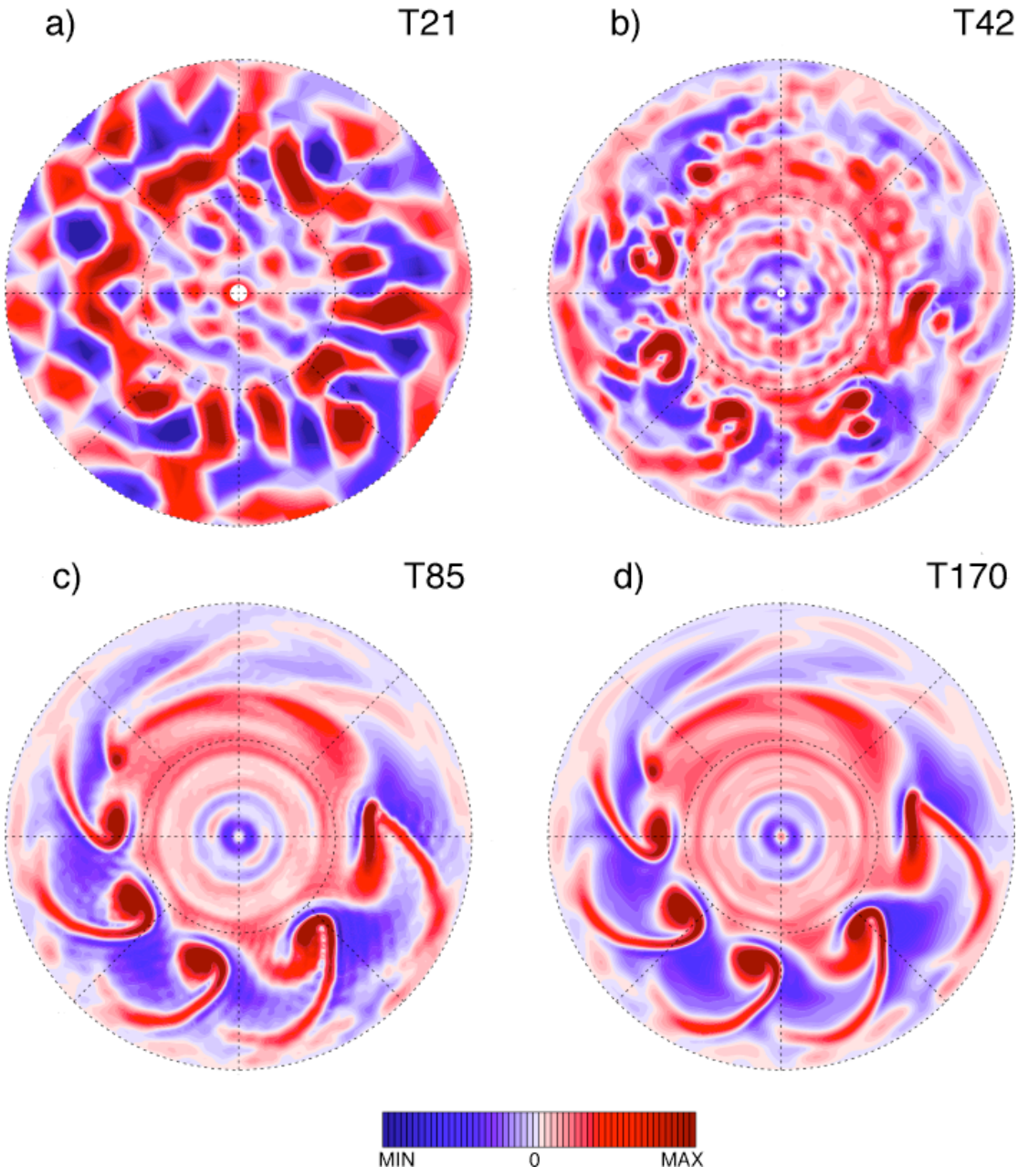

Figure 3.17: Polar stereographic view of the relative vorticity field ζ, centred on the north pole, for four runs with all parameters identical – except the horizontal resolution. The common parameters are as in run EEQ. The fields at $t = 22\ \tau$ are shown. The number at upper right in each panel indicates the resolution. Contour levels are the same to those in Figure 3.16.

(red and black lines, respectively) confirms the convergence of the simulations. Note the presence of a clear dissipation range in the T170 run. In contrast, the appearance of nearly grid-scale waves in physical space for T21 and T42 resolution runs corroborates the tendency of the spectrum (blue and pink lines for T21 and T42, respectively) in these runs to peel off and curl up considerably left of the aliasing limit (~ 21 for T21 and ~ 42 for T42). This is caused by discretization errors that are not adequately controlled by the applied explicit viscosity.

An analogous series of runs in which a much larger dissipation coefficient value, $\nu_4 = 10^{21}$ m^4 s^{-1} has been used have also been performed. This mimics "properly" dissipated runs at T21 and T42 resolutions (i.e., runs with well represented dissipation range in spectral space). However, in this series the high resolution simulations are significantly over-dissipated and the physical space picture is characterised by a severe reduction in eddy kinetic energy at all times. This is supported by the spectra for two T170 resolution simulations with the two coefficients (bottom frame of Figure 3.18). The spectrum for a run using $\nu_4 = 10^{21}$ m^4 s^{-1} (black line) is shown together with the spectrum of the previously presented T170 run with $\nu_4 = 6 \times 10^{19}$ m^4 s^{-1} (red line). With the larger ν_4, the spectrum is severely over-dissipated with only ~ 20 modes being resolved; the rest of the modes clearly lie in the dissipation range. In contrast, at least ~ 80 modes are well-resolved with the smaller ν_4 value.

It is important to understand that wavenumbers smaller than those located in the fiducial "dissipation range" (i.e., less than 20 and 80, respectively, in the runs discussed above) are still affected by a small amount of dissipation in practice: that is, dissipation affects the entire spectrum of wavenumbers continuously, rather than just the wavenumbers in the dissipation range. The amount, while small, can nevertheless be *dynamically* significant, as it can change the quantitative character of the instability, even suppress the instability altogether. Indeed, if the value of ν_4 is increased further, to 10^{22} m^4 s^{-1}, the baroclinic waves completely disappear.

As discussed above, a common practice in numerical studies which vary the resolution is to adjust the dissipation coefficient ν_4 so that the damping time τ_d is same at the truncation scale N:

$$\tau_\mathrm{d} = \frac{1}{\nu_4} \left[\frac{R_p^2}{N(N+1)} \right]^2 . \tag{3.19}$$

While the physical basis of this procedure is arguable, it is demonstrated here that

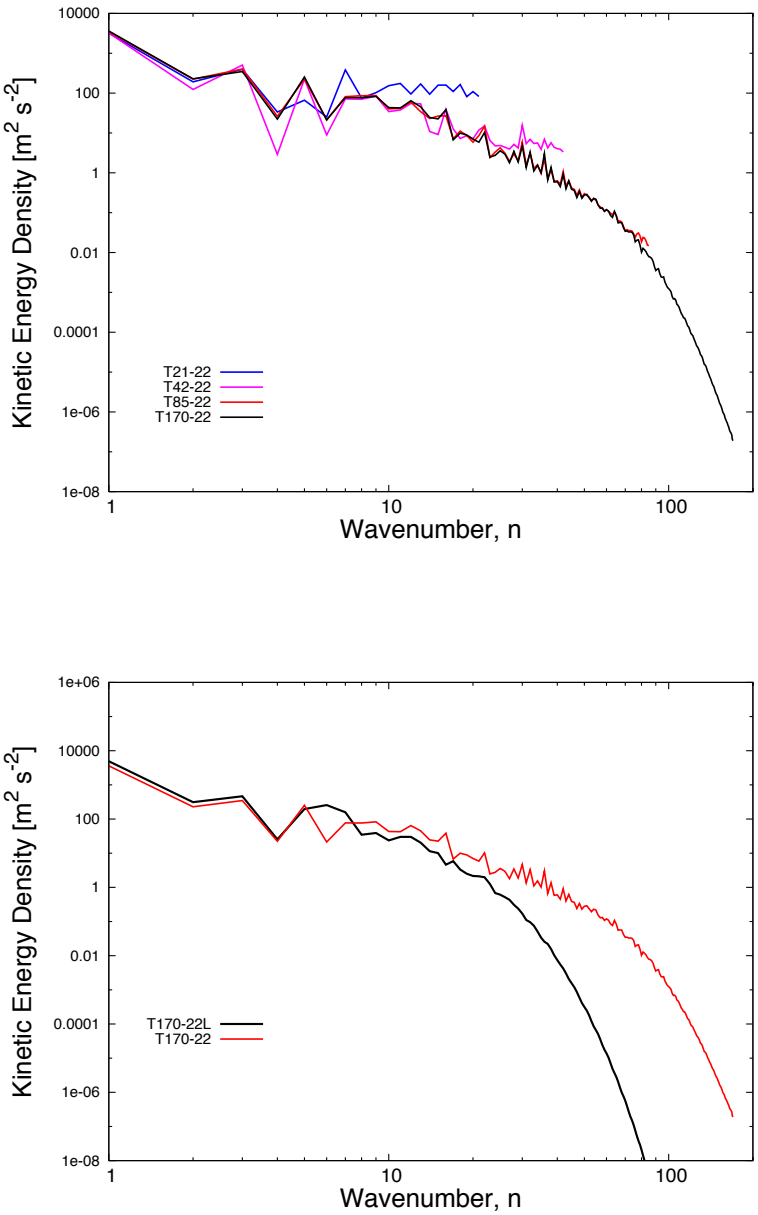

Figure 3.18: Kinetic energy density [m^2 s^{-2} (per wave number)] as a function of (total) wavenumber n. Spectra for the fields from the four runs shown in Figure 3.17 (top). The different lines refer to different horizontal resolutions, as indicated in the legend. The viscosity coefficient is same ($\nu_4 = 6 \times 10^{19}$ m^4 s^{-1}) in all four runs. Spectra for run EEQ at T170 resolution with different viscosity coefficients (bottom): $\nu_4 = 6 \times 10^{19}$ m^4 s^{-1} (red line) and $\nu_4 = 10^{21}$ m^4 s^{-1} (black line), respectively.

the practice still does not lead to convergence at low resolution[2]. Consider the value, $\nu_4 = 6 \times 10^{19}$ m^4 s^{-1}, used in the high resolution simulation discussed above. The dissipation rate at the truncation scale for HD209458b corresponding to this ν_4 value is $\tau_{\rm d}^{-1} = 5.07 \times 10^{-4}$ s^{-1}. Note that this damping rate is comparable to the rates used in current flow modeling studies of hot-Jupiter atmospheres at resolutions lower than T170 (e.g., Rauscher and Menou, 2010; Thrastarson and Cho, 2010, 2011; Heng et al., 2011). Its significance can be seen in Figure 3.19.

Figure 3.19 shows the effects of adjusting ν_4 so that the damping rate is constant at the truncation scale. The rate used is the one just discussed above: $\tau_{\rm d}^{-1} = 5.07 \times 10^{-4}$ s^{-1}. Relative vorticity field ζ at four resolutions for run EEQ at $t = 22\ \tau$ is shown. Two points are clear from the figure. First, the simulations in this series are not converged. The T21 and T42 resolution runs are completely over-dissipated and the momentum and heat transports are absent throughout the duration of the runs, up to $t = 60\ \tau$. Second, the ν values used in current GCM modelling studies of hot-Jupiters do not permit the instability. Note that, if the dissipation rate is chosen instead to be the one that "adequately" permits the instability in the low resolution run, the high resolution runs are severely under-dissipated and inundated with noise (not shown). Either way, convergence is not achieved by fixing the dissipation rate at the truncation scale.

Arguably, the two points above may not be significant for atmospheres characterized by a very short diabatic relaxation time (see also discussion in Chapter 4). For then the thermal damping would dominate and naturally short-circuit the above issues pertaining to the artificial viscosity and resolution. However, in some GCM simulations, the dynamically-relevant, intrinsic thermal relaxation time is not always short after quasi-equilibration is reached, even above the $\sim$1 bar level[3] (Thrastarson (private communication)). Moreover, the instabilities at higher latitudes possess short growth times and are much less affected by short relaxation times. Additionally, there is the issue of transient growth, which has not been discussed in this work. The non-normal modes, associated with such growth, may operate on a much shorter time scale than the growths described in this work.

It is stressed here that the high resolution runs described do not merely contain more fine-scale structures that presumably do not significantly affect the evolution. On the contrary, it has been found that high resolution fundamentally affects the

[2]A better practice would be to vary the dissipation coefficient in time (i.e., $\nu = \nu(t)$). For example, in Dritschel et al. (1999) ν was chosen to depend on the maximum vorticity in the system. This is physically more justifiable than keeping ν or $\tau_{\rm d}$ constant across horizontal resolutions.

[3]It is, in general, sufficiently long below this level.

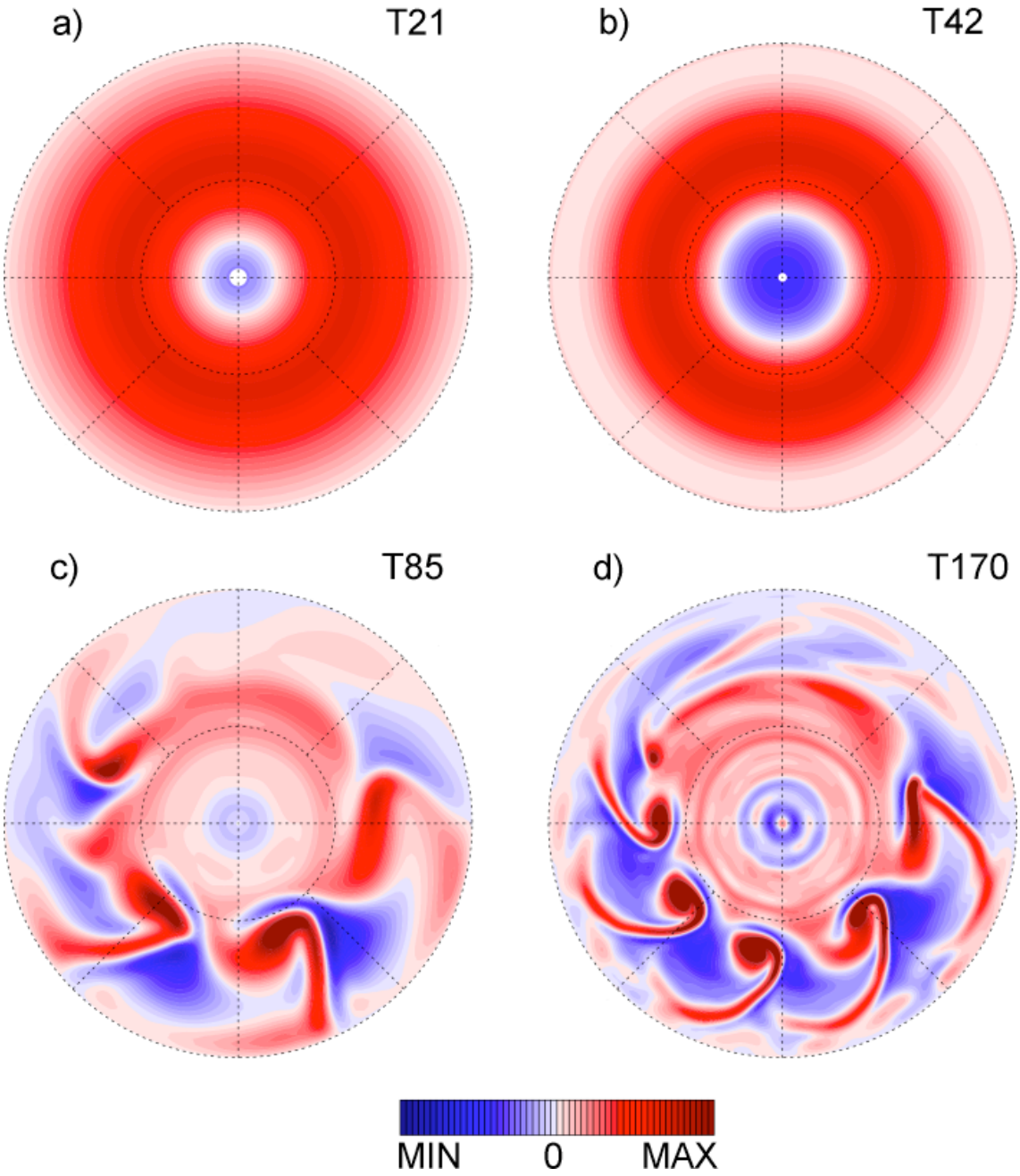

Figure 3.19: Same as Figure 3.17 but with $\tau_d^{-1} = 5.07 \times 10^{-4}$ s^{-1} in all runs. Maximum and minimum values for frames a) and b) are $\pm 3 \times 10^{-6}$ s^{-1} and for frames c) and d) $\pm 1.5 \times 10^{-5}$ s^{-1}; the contour intervals are, respectively, 1.4×10^{-7} s^{-1} and 6×10^{-7} s^{-1}.

evolution — much like in many ocean simulations (e.g., Kirtman et al., 2012). For example, bulk eddy heat- and momentum-fluxes differ significantly (up to an order of magnitude) in high- and low-resolution simulations. The reason for this is that vorticity anomalies (eddies) are much stronger, in addition to the filaments, in the high-resolution simulations; and, *EKE* growth is exponential in the stage of the evolution when these structures have emerged (Figure 3.7). Hence, heat and momentum are redistributed much more effectively.

3.4 Summary and Discussion

Baroclinic instability on extrasolar planets has not been studied thus far. In this chapter, an advanced pseudospectral GCM has been used to perform an extensive study of the stability and non-linear evolution of balanced jets on hot-Jupiters. These non-linear baroclinic instability simulations have been fully validated against previous similar simulations for the Earth (e.g., Polvani et al., 2004; Jablonowski and Williamson, 2006). For concreteness, results for a model planet with physical parameters corresponding to the close-in giant planet HD209458b have been presented here. The focus has been on the stability of high-speed (typically 1000 $\mathrm{m\,s^{-1}}$) eastward jets at the equator and westward jets at high latitudes. Broad jets of such magnitude are a common feature in current GCM simulations of tidally-synchronized giant planet atmospheres.

Linear growth rate and phase speed spectra have been derived, via standard normal mode analysis, and the results compared with full non-linear numerical simulations. According to the linear analysis of the two-layer primitive equations model on the β-plane, the growth rate of the instability is reduced for a jet located at low latitudes, compared with a jet located at high latitudes. Near the equator, where the deformation length scale L_D becomes too large to accommodate baroclinic waves, the linear theory predicts stability. In general, linear analysis agrees reasonably well with the full non-linear simulations at the early stage of the unstable evolution, during the transient phase. After a long time, in simulations with high values of initial potential vorticity anomaly (i.e., $|q'/2\Omega| \geq 1.2$, where q' is the anomaly), cyclones merge to form robust monolithic vortices at the poles. This is not captured by linear analysis.

As expected, full non-linear simulations show richer behaviour than that obtained through linear analysis. Non-linear simulations show that baroclinic instability occurs for all eastward jet profiles used in this study. In particular, broad equatorial

eastward jets are unstable (on a time scale of ~ 20 planetary rotations), despite stability suggested by the linear analysis. The instability takes place at the jet flanks, where there is still a significant vertical shear to satisfy the necessary condition for instability. The jet core is stable, unlike in the jets situated at higher latitudes; this is in accordance with linear theory. Westward jets near the equator, however, remain stable, both at the core and the flanks. This is the first time *non-linear* baroclinic instability has been studied with the traditional primitive equations in spherical geometry for broad eastward and westward equatorial jets in the atmosphere[4]. In general, westward jets are found to be more stable compared to their eastward counterparts (e.g., at midlatitude, instability timescale of ~ 6 planetary rotations for westward jets vs. ~ 3 planetary rotations for eastward jets), and to require much stronger vertical shear for instability in the full primitive equations system. Additionally, in this work it has been demonstrated that baroclinic instability does not require a solid boundary on planets, as long as there is a change of sign in the meridional potential vorticity gradient $\partial q_0/\partial\phi$ in the domain's interior.

By performing the simulations described above with a wide range of horizontal resolution (from T21 to T170), it has been found that the simulations do not converge for resolutions below T85. This is a somewhat stronger requirement than for Earth simulations and is primarily due to the much stronger jet amplitude on hot-Jupiters (~ 1000 m s^{-1}, compared to ~ 50 m s^{-1} for the Earth). Furthermore, it has been found that baroclinic instability does not occur at all if the artificial viscosity coefficient used in the simulation is too high. A high artificial viscosity is often used to stabilize numerical simulations against strong forcing in current studies of extrasolar planet atmospheres. Given this, baroclinic instability is unlikely to be represented in current simulations – even when necessary conditions for instability are satisfied. This may pose a serious issue in flow modelling studies of extrasolar planet atmospheres in which the natural diabatic relaxation time is not too short (i.e., greater than a few planetary rotations).

The more stringent numerical convergence requirements for baroclinic instability on a hot-Jupiter compared to that of the Earth motivates a closer look at the ability of a numerical model to fruitfully and consistently capture the dynamical behaviour in hot-Jupiter flow modeling studies. While GCMs are extensively developed, tested and validated for parameter regime of the Earth, their behaviour for markedly dif-

[4]The work in this chapter was published in Polichtchouk and Cho (2012). Recently, Ribstein et al. (2014) also investigated stability properties of westward equatorial jets with varying Rossby and Burger numbers on the equatorial β-plane in the shallow water model. Their analysis mainly consentrated on the linear stability of the jets that satisfy the necessary condition for intertial or barotropic instability *at* the equator unlike the jets studied here.

ferent and more "violent" conditions applicable to hot-Jupiters (i.e., $\sim$1000 m s^{-1} flow speeds, $\sim$1000 K temperature gradients, and, fast thermal relaxation times) is not well understood. In the next chapter, the results from a broad, detailed GCM intercomparison study for conditions relevant to hot-Jupiters are presented. In particular, the aim of the next chapter is to identify how well different numerical algorithms, employed by GCMs to solve the traditional hydrostatic primitive equations, cope under such extreme conditions.

Appendix 3.A Non-dimensional Analysis

Equations set (3.5) is made non-dimensional by introducing the "discretized deformation length scale", horizontal length scale, timescale, and height scale:

$$\begin{aligned}
\hat{L}_{\mathrm{D}} &= \frac{1}{f_0}\sqrt{h_2 \triangle p \sigma_0}\,, \\
L &= \frac{1}{\sqrt{2}}\,\hat{L}_{\mathrm{D}}\,, \\
T &= \frac{1}{\sqrt{2}}\left(\hat{L}_{\mathrm{D}}/U_0\right)\,, \\
H &= \frac{1}{\sqrt{2}}\left(U_0 f_0 \hat{L}_{\mathrm{D}}\right)\,,
\end{aligned}$$

respectively. Hence, the set of equations becomes characterised only by the Rossby number,

$$\hat{Ro} = \frac{U_0\sqrt{2}}{f_0 \hat{L}_{\mathrm{D}}}\,,$$

and the Charney-Green number,

$$\hat{\gamma} = \frac{\beta\,\hat{L}_{\mathrm{D}}^2}{2\,U_0}\,.$$

The Charney-Green number measures the relative importance of the planetary vorticity gradient to the relative vorticity gradient. Using these non-dimensionalised

scales and parameters, the equations now read:

$$\frac{\partial}{\partial\tilde{t}}\left(\frac{\partial^2\tilde{\Psi}}{\partial\tilde{x}^2}\right) = -\frac{\partial}{\partial\tilde{x}}\left(\frac{\partial^2\tilde{\Theta}}{\partial\tilde{x}^2}\right) - \hat{\gamma}\frac{\partial\tilde{\Psi}}{\partial\tilde{x}} \tag{3.20a}$$

$$\frac{\partial}{\partial\tilde{t}}\left(\frac{\partial^2\tilde{\Theta}}{\partial\tilde{x}^2}\right) = -\frac{\partial}{\partial\tilde{x}}\left(\frac{\partial^2\tilde{\Psi}}{\partial\tilde{x}^2}\right) - \frac{1}{\hat{Ro}}\frac{\partial^2\tilde{\chi}}{\partial\tilde{x}^2} - \hat{\gamma}\frac{\partial\tilde{\Theta}}{\partial\tilde{x}} \tag{3.20b}$$

$$\frac{\partial}{\partial\tilde{t}}\left(\frac{\partial^2\tilde{\chi}}{\partial\tilde{x}^2}\right) = \frac{1}{\hat{Ro}}\frac{\partial^2\tilde{\Theta}}{\partial\tilde{x}^2} - \frac{1}{\hat{Ro}}\frac{\partial^2\tilde{\Phi}}{\partial\tilde{x}^2} - \hat{\gamma}\frac{\partial\tilde{\chi}}{\partial\tilde{x}} \tag{3.20c}$$

$$\frac{\partial\tilde{\Phi}}{\partial\tilde{t}} = \frac{\partial\tilde{\Psi}}{\partial\tilde{x}} - \frac{1}{\hat{Ro}}\frac{\partial^2\tilde{\chi}}{\partial\tilde{x}^2}\,, \tag{3.20d}$$

where $(\tilde{\cdot})$ denotes non-dimensional variables. The variables, $(\tilde{\Psi},\, \tilde{\Theta},\, \tilde{\chi},\, \tilde{\Phi})$, are the non-dimensional counterparts of $(\psi'_+,\, \psi'_-,\, \chi'_-,\, \Phi'_-)$ in section 3.2.3.

Denoting disturbances by

$$\tilde{\mathbf{\Psi}} = \hat{\tilde{\mathbf{\Psi}}}\exp\{i\tilde{k}\,(\tilde{x}-\tilde{c}\tilde{t})\}\,,$$

where $\tilde{\mathbf{\Psi}} = (\tilde{\Psi},\tilde{\Theta},\tilde{\chi},\tilde{\Phi})^{\mathrm{T}}$, $\hat{\tilde{\mathbf{\Psi}}} = (\hat{\tilde{\Psi}},\hat{\tilde{\Theta}},\hat{\tilde{\chi}},\hat{\tilde{\Phi}})^{\mathrm{T}}$, and $\tilde{c}\in\mathbb{C}$, equations (3.20) reduce to

$$\tilde{\mathbf{M}}\,\hat{\tilde{\mathbf{\Psi}}} = 0\,,$$

where

$$\tilde{\mathbf{M}} = \begin{bmatrix} -\tilde{c}-\hat{\gamma}/\tilde{k}^2 & 1 & 0 & 0 \\ 1 & -\tilde{c}-\hat{\gamma}/\tilde{k}^2 & -i/(\tilde{k}\,\hat{Ro}) & 0 \\ 0 & i/(\tilde{k}\,\hat{Ro}) & -\tilde{c}-\hat{\gamma}/\tilde{k}^2 & -i/(\tilde{k}\,\hat{Ro}) \\ 1 & 0 & -i\,\tilde{k}/\hat{Ro} & \tilde{c} \end{bmatrix}.$$

This leads to a normal mode solution fulfilling the fourth order characteristic equation for $\tilde{c}$:

$$\begin{aligned} \tilde{c}^4 + \tilde{c}^3\left(\frac{3\hat{\gamma}}{\tilde{k}^2}\right) + \tilde{c}^2\left(\frac{3\hat{\gamma}^2}{\tilde{k}^4} - \frac{1}{\hat{Ro}^2} - \frac{1}{\tilde{k}^2\hat{Ro}^2} - 1\right) + \\ \tilde{c}\left(\frac{\hat{\gamma}^3}{\tilde{k}^6} - \frac{2\hat{\gamma}}{\tilde{k}^2\hat{Ro}^2} - \frac{\hat{\gamma}}{\tilde{k}^4\hat{Ro}^2} - \frac{\hat{\gamma}}{\tilde{k}^2}\right) + \\ \frac{1}{\hat{Ro}^2}\left(1 - \frac{1}{\tilde{k}^2} - \frac{\hat{\gamma}^2}{\tilde{k}^4}\right) = 0\,. \end{aligned} \tag{3.21}$$

Equation (3.21) is solved numerically for varying values of $\hat{Ro}$ and $\hat{\gamma}$. Figure 3.20 shows the results for HD209458b (cf. Figure 3.2).

Non-dimensional analysis is useful because it explicitly gives the dependence of stability properties on dynamically-significant non-dimensional numbers, such as $\hat{Ro}$ and $\hat{\gamma}$. Extensive exploration of the solutions for a continuum of $\hat{Ro}$ and $\hat{\gamma}$ values reveals that, as $\hat{Ro}$ and/or $\hat{\gamma}$ increase, the low wavenumber cutoff for instability increases while the high wavenumber cutoff for instability and growth rate decrease slightly (Figure 3.20). Figure 3.21 illustrates how the growth rates depend on $\hat{Ro}$ when $\hat{\gamma}$ is held fixed at a typical midlatitude value for HD209458b. As $\hat{Ro}$ increases from $\hat{Ro} << 1$ to $\hat{Ro} \sim 1$, the growth rate decreases linearly. However, the reduction in growth rate is exponential as the $\hat{Ro} \sim 1$ threshold is crossed and the two-layer linear analysis predicts stability for flows with $\hat{Ro} > 3.3$.

To obtain the *dimensional* values of the growth rate from Figure 3.20 and Figure 3.21, multiply the growth rate ($\tilde{k} \cdot \Im\mathfrak{m}\{\tilde{c}\}$), for example, by $U_0\sqrt{2}/\hat{L}_{\mathrm{D}}$ and the wavenumber ($\tilde{k}$) by $\sqrt{2}/\hat{L}_{\mathrm{D}}$. The result of Figure 3.20 is growth rates identical to those presented in Figure 3.2. The dimensional phase speed is obtained similarly.

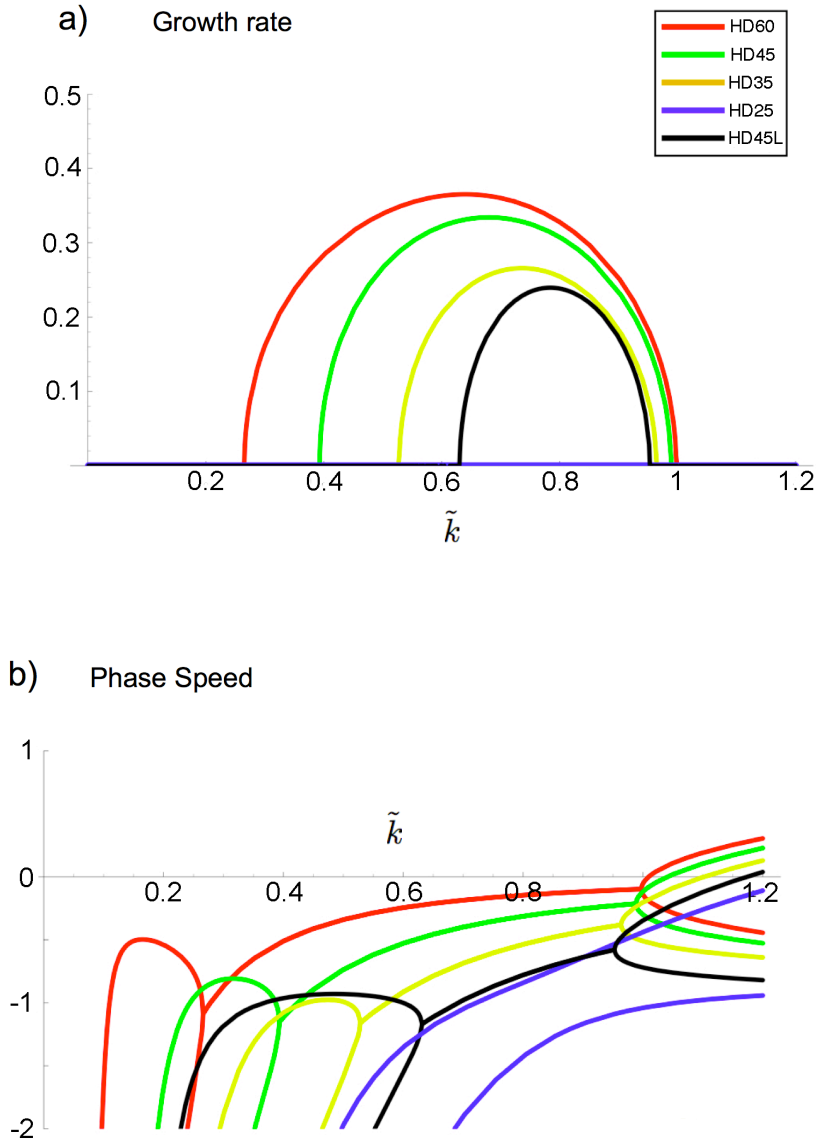

Figure 3.20: Non-dimensional growth rate $[\tilde{k} \cdot \Im\mathfrak{m}\{\tilde{c}\}]$ (top) and phase speed $[\Re\mathfrak{e}\{\tilde{c}\}]$ (bottom) for HD209458b, as a function of non-dimensional wavenumber $\tilde{k}$. Curves "HD60", "HD45", "HD35" and "HD25" represent growth rates and phase speeds at $\phi = (60°, 45°, 35°, 25°)$ computed with ($\hat{Ro}$= 0.76, $\hat{\gamma}$ = 0.14), ($\hat{Ro}$= 0.76, $\hat{\gamma}$ = 0.3), ($\hat{Ro}$= 0.76, $\hat{\gamma}$ = 0.51), ($\hat{Ro}$= 0.76, $\hat{\gamma}$ = 1.04). Curve "HD45L" has been computed for HD209458b parameters at $\phi = 45°$, but with $U_0 = 200$ m s^{-1} corresponding to ($\hat{Ro}$= 0.3, $\hat{\gamma} = 0.72$). To obtain dimensional values, multiply the growth rate by $U_0\sqrt{2}/\hat{L}_\mathrm{D}$ and wavenumber by $\sqrt{2}/\hat{L}_\mathrm{D}$.

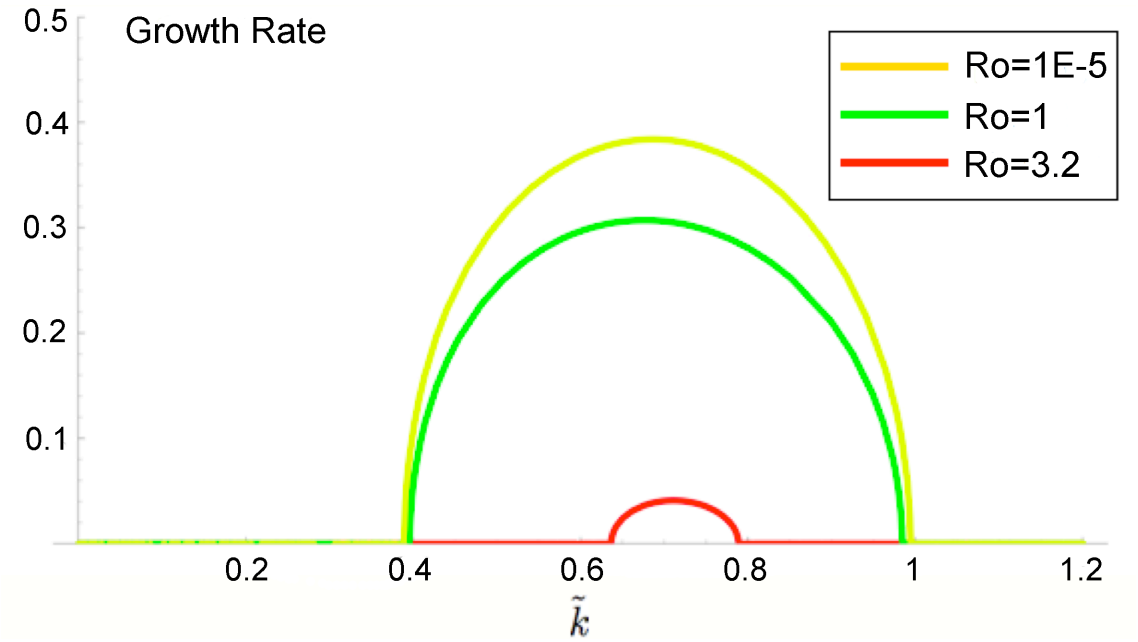

Figure 3.21: Non-dimensional growth rate $[\tilde{k} \cdot \Im\mathfrak{m}\{\tilde{c}\}]$ as a function of non-dimensional wavenumber $\tilde{k}$ for different values of $\hat{Ro}$. Yellow, green and red curves have been calculated with $\hat{Ro} = 10^{-5}$, $\hat{Ro} = 1$ and $\hat{Ro} = 3.2$, respectively. The value of $\hat{\gamma}$ is held constant at $\hat{\gamma} = 0.3$. To obtain dimensional values, multiply the growth rate by $U_0\sqrt{2}/\hat{L}_\mathrm{D}$ and wavenumber by $\sqrt{2}/\hat{L}_\mathrm{D}$.

4 Intercomparison of General Circulation Models for Hot-Jupiters

Five GCMs which have been recently used to study hot-Jupiter atmospheres (BOB, CAM, IGCM, MITgcm, and PEQMOD), are compared under three test cases useful for assessing model convergence and accuracy. Such a broad, detailed intercomparison has not been performed thus far for extrasolar planets study. The models considered all solve the traditional primitive equations, but employ different numerical algorithms or grids (e.g., pseudospectral and finite volume, with the latter separately in longitude-latitude and "cubed-sphere" grids). The test cases are chosen to cleanly address specific aspects of the behaviours typically reported in hot-Jupiter simulations: *1*) steady-state, *2*) non-linearly evolving baroclinic wave, and *3*) response to fast timescale thermal relaxation. When initialized with a steady jet, all models maintain the steadiness, as they should—except MITgcm in cubed-sphere grid. A very good agreement is obtained for a baroclinic wave evolving from an initial instability in pseudospectral models (only). However, exact numerical convergence is still not achieved across the pseudospectral models: amplitudes and phases are observably different. When subject to a typical "hot-Jupiter-like" forcing, all five models show quantitatively different behaviour—although qualitatively similar, time-variable, quadrupole-dominated flows are produced. Hence, as have been advocated in several past studies (e.g., Cho, 2008; Thrastarson and Cho, 2010, 2011), specific quantitative predictions (such as the location of large vortices and hot regions) by GCMs should be viewed with caution. Overall, in the tests considered here, pseudospectral models in pressure coordinate (PEBOB and PEQMOD) perform the best and MITgcm in cubed-sphere grid performs the worst.

4.1 Introduction

Carefully testing GCMs of extrasolar planets is important for understanding the physical properties of the atmospheres and for attaining confidence in the complex models themselves. Intercomparison of full GCMs, as well as benchmarking of dynamical cores and testbed models against "standard solutions", are common in Earth studies (e.g., Held and Suarez, 1994; Boer and Denis, 1997; Polvani et al., 2004; Jablonowski and Williamson, 2006). Intercomparisons are also becoming more common for circulation models of other Solar System planets (e.g., Lebonnois et al., 2013). However, similar intercomparisons have not been performed for models of hot-Jupiters. Given that the conditions of many extrasolar planets are markedly different than the Earth—and much more exacting on the circulation models—it is useful to subject the models to tests which are appropriate for extrasolar conditions (e.g., Thrastarson and Cho, 2011).

Thus far, only Rauscher and Menou (2010) and Heng et al. (2011) have explicitly attempted to intercompare simulations of hot-Jupiters performed with different GCMs. The former study attempts to compare their results using the Intermediate General Circulation Model (Blackburn, 1985) with those reported in Cooper and Showman (2005) using the ARIES/GEOS model (Suarez and Takacs, 1995). However, while qualitatively similar features were observed, the comparison was somewhat inconclusive because the model setup was not identical. In their studies using the Community Atmosphere Model (Collins et al., 2004), Thrastarson and Cho (2010, 2011) have shown sensitivity to initial condition, as well as thermal relaxation and explicit numerical dissipation specifications. A clearer comparison than in Rauscher and Menou (2010) has been presented in Heng et al. (2011). In the latter study, time-mean zonally-averaged fields are presented from simulations with the Flexible Modeling System (Gfdl Global Atmospheric Model Development Team:, 2004), using two different types of numerical algorithm (pseudospectral and finite volume). However, while zonal and temporal averaging is somewhat justifiable for rapidly rotating planets, the procedure is less useful for the more slowly rotating planets, such as those considered in the study: the averaging can destroy dynamically-significant flow structures, as well as conceal subtle numerical and coding errors. [1]

In addition to the setup not being same or systematic across different models, the

[1] During the preparation of this study another study, by Bending et al. (2013) appeared that compares their results with those of Menou and Rauscher (2009). The authors of the new study report that they are not able to reproduce precisely the results of the older study, although both studies use the same dynamical core (section 4.2.1).

inconclusiveness of the past comparisons and the general variability of the model results stem from the fact that the models employ different numerical algorithms, grids, and coordinates to solve the governing equations—as shall be shown in this chapter. Moreover, the numerical parameters of the model calculations are often not described explicitly in the literature, or even in the technical documentations of the models themselves. Thus, it has been difficult to ascertain which differences between model outputs are due to the model and which are due to the setup. Here, a careful comparison of five GCMs recently used to study hot-Jupiter atmospheres is performed. The GCMs are: BOB[2], CAM[3], IGCM[4], MITgcm[5], and PEQMOD[6]. They have been used, for example, in the following extrasolar planet circulation studies: BOB (Beaulieu et al., 2011; Polichtchouk and Cho, 2012), CAM (Thrastarson and Cho, 2010, 2011), IGCM (Menou and Rauscher, 2009; Rauscher and Menou, 2010), MITgcm (Showman et al., 2009; Lewis et al., 2010), and PEQMOD (Cho and Polichtchouk, in prep.).

The five GCMs are submitted to three tests which are useful for assessing model convergence and accuracy. The tests are chosen to specifically address three features that have been typically reported in hot-Jupiter atmospheric flow simulations: *1)* steady flow, *2)* non-linear baroclinic wave, and *3)* response to a fast timescale thermal relaxation. In addition to their good range and relevance, the tests are purposely chosen with reproducibility of the results in mind: the tests are not difficult to set up and full descriptions of the test cases (as well as the GCMs tested) are provided, along with all of the model parameter values used in the simulations (see Appendix). Note that the emphasis in this chapter is on models tested in their "default configuration" (i.e., essentially as they are unpacked), except minor modifications to facilitate equatable (as well as equitable)[7] comparisons.

The overall plan of this chapter is as follows. In section 4.2, the governing equations solved by the five GCMs and the discretization and dissipation schemes used in the models are reviewed and described. In section 4.3, the three test cases are carefully described and the results from the tests are presented in turn. Both *inter*-model and *intra*-model comparisons are presented in detail, where the former comparison refers to "between different models" and the latter comparison refers to "within a single model". The aim of this section—indeed, of this entire chapter—is to permit

[2] *Built on Beowolf* (Scott et al., 2003)
[3] *Community Atmosphere Model – version 3.0* (Collins et al., 2004)
[4] *Intermediate General Circulation Model* (Blackburn, 1985)
[5] *MIT general circulation model – checkpoint64d* (Adcroft et al., 2012)
[6] *Primitive Equations Model* (Saravanan, 1992)
[7] Equitable refers to "impartial" or "fair", and equatable refers to "equivalent" or "comparable".

one to go beyond broad-brush comparisons based on strongly dissipated/constrained or averaged fields. In section 4.4, summary and conclusions are given, along with some discussion of implications of this work.

4.2 Dynamical Cores and Test Cases

4.2.1 Dynamical Cores

The GCMs—or, more precisely, their "dynamical cores"—discussed in this chapter all solve the hydrostatic primitive equations for the "dry" atmosphere. In this chapter, "GCMs" and "dynamical cores" are referred to interchangeably, as the distinction is not particularly important here. As discussed in Chapter 2, none of the physical parameterizations are used in any of the models for the comparisons and only a Newtonian cooling scheme is used in one of the test cases. In general, it is prudent to test and characterize the core before moving onto the full GCM.[8].

The GCMs tested solve the equations (2.1) together with the boundary conditions (2.2) in different vertical coordinate systems (e.g., pressure, sigma, eta—see below). All the cores tested solve the equations in the Eulerian framework. Hence, for all of them, there is an associated grid for the computational domain—e.g., longitude-latitude (LL) and cubed-sphere (CS) grids for the MITgcm core and the Gaussian grid for the remaining four cores. The numerical integrations are directly performed on the LL and CS grids (see Figure 4.1) in MITgcm, while only the non-linear products are evaluated and initial conditions are specified on the Gaussian grid in the pseudospectral cores. More details on the cores are provided below, beginning with the pseudospectral ones. All cores use common parameter values characteristic of the planet HD209458b: the values are listed in Table 2.1.

Pseudospectral Cores

As in BOB core, equations (2.1) in the vorticity-divergence form are solved in CAM, IGCM, and PEQMOD cores, with triangular truncation (see section 2.3).[9] As described in Chapter 2, a standard second-order finite difference scheme is used in the vertical direction in the above four cores. For the time integration, the four cores use semi-implicit leap-frog scheme, and the dissipations, $\mathcal{D}_{\mathbf{v},\theta}$ in equations (2.1), are

[8]Note that, in comparisons of full GCMs for the Earth, model differences generally increase when physics parameterizations are included (e.g., Blackburn et al. (2013))

[9]IGCM uses the "jagged triangular truncation", in which $n \leq M-1$ for variables even about the equator and $n \leq M$ for variables odd about the equator. Here, n is the total wavenumber.

in the form of a "hyperdissipation" operator (i.e., equation (2.20)).

BOB and PEQMOD solve equations (2.1) in the p-coordinate and the exact form of the equations together with the boundary conditions solved by these two cores are given in Chapter (2.3).

IGCM is formulated in the σ-coordinate: $\sigma = p/p_{\rm s}$, where $p_{\rm s}$ is the surface pressure. This coordinate system is specifically designed to "follow the terrain" at the bottom. CAM is formulated in a more general, *hybrid* terrain-following vertical coordinate, η: this coordinate system allows the upper part of the model atmosphere to be represented by p-coordinates and the lower part of the model atmosphere by σ-coordinates. To ensure equitable model inter-comparison, η has been set so that $\eta = \sigma$ throughout the vertical domain in CAM. In the σ-coordinate the vorticity-divergence form of the primitive equations read:

$$\frac{\partial \zeta}{\partial t} = \mathbf{k}\cdot\boldsymbol{\nabla}\times\mathbf{n}_\sigma + \mathcal{D}_\zeta \tag{4.1a}$$

$$\frac{\partial \delta}{\partial t} = \boldsymbol{\nabla}\cdot\mathbf{n}_\sigma - \nabla^2\big(E+\Phi\big) + \mathcal{D}_\delta \tag{4.1b}$$

$$\frac{\partial \Phi}{\partial \sigma} = -\frac{\mathcal{R}T}{p}\frac{\partial p}{\partial \sigma} \tag{4.1c}$$

$$\frac{\partial p_{\rm s}}{\partial t} = \int_1^0 \boldsymbol{\nabla}\cdot\big(p_{\rm s}\mathbf{v}\big)\,{\rm d}\sigma' \tag{4.1d}$$

$$\frac{\partial T}{\partial t} = -\mathbf{v}\cdot\boldsymbol{\nabla}T - \dot\sigma\frac{\partial T}{\partial \sigma} + \frac{\kappa T\omega}{p} + \frac{\dot q}{c_p} + \mathcal{D}_{\mathcal{T}}\,, \tag{4.1e}$$

where

$$\mathbf{n}_\sigma = -\big(\zeta+f\big)\,\mathbf{k}\times\mathbf{v} - \dot\sigma\frac{\partial \mathbf{v}}{\partial\sigma} - \frac{\mathcal{R}T}{p}\boldsymbol{\nabla}p$$

with $\dot\sigma \equiv {\rm D}\sigma/{\rm D}t$ and ${\rm D}/{\rm D}t \equiv \partial/\partial t + \mathbf{v}\cdot\boldsymbol{\nabla} + \dot\sigma\partial/\partial\sigma$, the material derivative; $\mathcal{D}_\chi$, where $\chi = \{\zeta, \delta, T\}$, are given by

$$\mathcal{D}_\chi = \nu_{2\mathfrak{p}}[(-1)^{\mathfrak{p}+1}\nabla^{2\mathfrak{p}} + \mathcal{C}]\chi, \tag{4.2}$$

where the correction term $\mathcal{C} = (2/\mathcal{R}_{\rm p}^2)^{\mathfrak{p}}$ is added in CAM only; and, $\boldsymbol{\nabla}$ here acts on the constant σ surfaces. Note that these set of equations are slightly different than equations (2.19).

For example, the continuity equation (4.1d) comes in the form of a prognostic equation for surface pressure $p_{\rm s}$ and is obtained by integrating the continuity equation (2.1c) from the bottom ($\sigma = 1$) to the top ($\sigma = 0$) surfaces and using the boundary conditions,

$$\dot\sigma = 0 \qquad \text{at} \qquad \sigma = 0,\, 1. \tag{4.3}$$

The pressure vertical velocity, $\omega = \mathrm{D}p/\mathrm{D}t$, is computed diagnostically from the definition:

$$\omega \;=\; \sigma \mathbf{v}\cdot\boldsymbol{\nabla} p_\mathrm{s} - \int_0^\sigma \boldsymbol{\nabla}\cdot\big(p_\mathrm{s}\mathbf{v}\big)\,\mathrm{d}\sigma' \,. \tag{4.4}$$

Note, IGCM and CAM employ a vertical discretization scheme described by Simmons and Burridge (1981). This vertical finite difference scheme explicitly conserves mass, total energy and angular momentum.[10]

Finite Volume Core

The MITgcm core is widely employed by the Earth's atmospheric and oceanic communities. It is highly configurable and is also used in modeling flows on and in Solar System planets (e.g., Kaspi et al., 2009). MITgcm supports both the traditional hydrostatic and non-hydrostatic formulation of the primitive equations. The model, in its traditional formulation, has been applied in extrasolar planet circulation studies (e.g., Showman et al., 2009; Lewis et al., 2010). In this work, the traditional hydrostatic formulation is used to ensure equatable comparison.

The primitive equations (2.1) in equally-spaced p-coordinate, in spherical geometry, are solved on a staggered Arakawa C-grid (Arakawa and Lamb, 1977) with a second-order finite volume spatial discretization method (e.g., Durran, 1999) in the LL grid and an enstrophy-conserving[11] scheme (Sadourny, 1975) on the CS grid—the default configurations of the MITgcm core for the two grids, respectively.[12] On the LL grid, the grid size approaches zero near the poles; and, to maintain numerical stability given by the Courant-Friedrichs-Lewy (CFL) condition (e.g., Durran, 1999, and references therein), an infinitesimal timestep size is required. To avoid taking very small timesteps, a fast Fourier transform (FFT) filter, which smooths out the physically-insignificant grid-scale waves in the zonal direction, is applied polewards of 45° at each timestep. The problem of grid singularity at the poles in the LL grid is overcome by the CS grid (Figure 4.1), which has nearly uniform grid-spacing. This grid allows longer timesteps to be taken at a comparable resolution and eliminates

[10] However, the issue of "hard-wiring" in select conservation laws in a numerical scheme is a matter of current debate. For example, an adequately resolved simulation arguably does not require a scheme that explicitly enforces global energy conservation, which can sometimes lead to unphysical stabilization and erroneous results.

[11] Enstrophy is $\frac{1}{2}\zeta^2$. It is conserved in 2D Euler equation—a 2D, barotropic form of equations (2.1) with rigid lid and bottom, in the inviscid limit.

[12] Embedded in the code are two additional schemes, for solving the momentum equation on the CS grid, which are not described in the official documentation. These schemes are not invoked in the default setting, and results from detailed tests are presented in a follow-up study (Polichtchouk and Cho, in prep.)

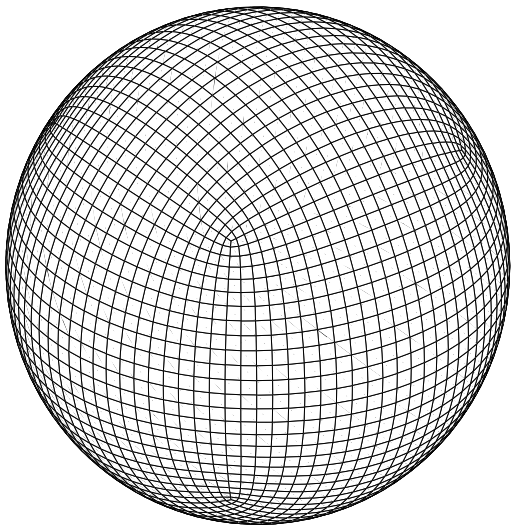

Figure 4.1: Cubed-sphere (CS) grid used in some simulations with MITgcm. The CS grid introduces eight special "corner points" (four in each hemisphere).

the need for a zonal filter. However, the CS grid introduces eight special "corner points" (four in each hemisphere), which lead to an intrinsic wavenumber-4 error in both the northern and southern hemispheres (see section 4.3.1).

For the timestepping, a third-order Adams-Bashforth scheme (e.g., Durran, 1999) is used.[13] The third-order Adams-Bashforth scheme is more stable, compared with its second-order counterpart, and does not require a stabilizing parameter to damp the computational mode. This scheme is superior to the second-order leapfrog scheme used in the pseudospectral cores, especially when the second-order scheme is used in conjunction with the Robert-Asselin filter—as is often the case.

MITgcm supports several dissipation schemes, including harmonic and biharmonic dissipations, as well as the Shapiro filter (Shapiro, 1970). Because ordinary harmonic dissipation is easy to implement in both pseudospectral and finite volume cores, Laplacian dissipation (corresponding to $\mathfrak{p} = 1$ in equations (2.20) and (4.2)), is applied to the thermodynamic and momentum equations to control the grid-scale noise in the baroclinic wave test case. This approach is similar to the one in Polvani et al. (2004), and Chapter 3, and ensures that all models solve the same equations, except the vertical coordinate.

Previous extrasolar planet studies with MITgcm have implemented the Shapiro

[13]Strictly speaking, this scheme is not "default" in MITgcm. However, by also testing the second-order default Adams-Bashforth scheme, it has been verified that there is no noticeable difference in the results between the two schemes.

filter (in CS grid) to control the grid scale oscillations (e.g., Showman et al., 2009; Lewis et al., 2010). Since the purpose of the diabatic test case is to facilitate clear interpretation of outputs from current hot-Jupiter studies, the Shapiro filter in the third test case is applied.[14]

The Shapiro filter is applied to prognostic variable χ, where $\chi = \{\mathbf{v}, \theta\}$, in the zonal and meridional directions. The discrete form of the Shapiro filter in MITgcm is:

$$\widetilde{\chi}_{i,j} \;=\; \left[1 - \frac{\Delta t}{\tau_{\rm shap}} \left\{\frac{1}{8}\Big(\mathsf{F}_\lambda + \mathsf{F}_\phi\Big)\right\}^{\mathfrak{n}}\right] \chi_{i,j}\,. \tag{4.5}$$

Here, $\chi_{i,j}$ is an arbitrary variable at the longitude and latitude grid points i and j, respectively, and is denoted with an overtilde (i.e., $\widetilde{\chi}_{i,j}$) when smoothed; $\mathsf{F}_\lambda(\cdot)$ and $\mathsf{F}_\phi(\cdot)$ are dimensionless operators operating on $\chi_{i,j}$ such that

$$\mathsf{F}_\lambda\big(\chi_{i,j}\big) \;=\; \chi_{i+1,j} - 2\chi_{i,j} + \chi_{i-1,j}\,,$$

$$\mathsf{F}_\phi\big(\chi_{i,j}\big) \;=\; \chi_{i,j+1} - 2\chi_{i,j} + \chi_{i,j-1}\,.$$

The integer $\mathfrak{n}$ (different from n, the total wavenumber) is the power of the Shapiro filter; Δt is the timestep size; and, $\tau_{\rm shap}$ is a parameter which defines the strength of the filter, given Δt. In Earth circulation studies, low power (i.e., $\mathfrak{n} = \{2, 4, 6\}$) Shapiro filters are generally avoided and are replaced either by highly scale-selective FFT filters or by less dissipative, $\mathfrak{n} = \{8, 16\}$, Shapiro filters. Higher power filters are chosen to avoid over-dissipating the mid-latitude and tropical waves (e.g., Lauritzen et al., 2011). However, the strong forcing used in hot-Jupiter studies generally necessitates the use of a more dissipative ($\mathfrak{n} \leq 6$) filter, for the model in its default configuration. For example, in the diabatic forcing test case, simulations with MITgcm core at C16 resolution in the CS grid crash for $\mathfrak{n} \geq 8$ Shapiro filters for all values of $\tau_{\rm shap} \geq \Delta t$, with Δt comparable to those used in pseudospectral core simulations at similar resolution.[15]

The form of the primitive equations (2.1) solved by MITgcm in the p-coordinate

[14] Note, the third test case with Laplacian dissipation, as well as with the full range of Shapiro filters, has also been performed for completeness (see section 4.3.3).

[15] At this resolution, timestep size of typically 5 times smaller than that used in pseudospectral cores is required to prevent blow-up in the MITgcm core in the default configuration.

is as follows:

$$\frac{\partial \mathbf{v}}{\partial t} = -\left(\mathbf{v}\cdot\boldsymbol{\nabla}\right)\mathbf{v} - \omega\frac{\partial \mathbf{v}}{\partial p} - \boldsymbol{\nabla}\Phi - f\mathbf{k}\times\mathbf{v} + \mathcal{D}_{\mathbf{v}} \tag{4.6a}$$

$$\frac{\partial \Phi}{\partial p} = -\frac{1}{\rho} \tag{4.6b}$$

$$\boldsymbol{\nabla}\cdot\mathbf{v} = -\frac{\partial \omega}{\partial p} \tag{4.6c}$$

$$\frac{\partial \theta}{\partial t} = -\mathbf{v}\cdot\boldsymbol{\nabla}\theta - \omega\frac{\partial \theta}{\partial p} + \frac{\theta}{c_p T}\,\dot{q}_{\text{net}} + \mathcal{D}_{\theta}\,, \tag{4.6d}$$

where $\mathcal{D}_{\mathbf{v}}$ and $\mathcal{D}_{\theta}$ represent diffusion. As discussed above, the diffusion is in the form of Laplacian dissipation (i.e., $\nu_2\nabla^2\chi$, where $\chi = \{u, v, \theta\}$ and ν_2 is the constant dissipation coefficient) in the baroclinic wave test case, while it is in the form of a ($\mathfrak{n} = 2$) Shapiro filter in the diabatic test case. Note that, in the latter test case, $\mathfrak{n} = 2$ gives the best performance in terms of angular momentum conservation in the default CS grid setting. Note also that, when solving the primitive equations in CS grid, a vector-invariant momentum equation must be used to avoid explicit representation of geometry-dependent metric terms. As in the pseudospectral model cores, the equation set is closed by the ideal gas law and boundary conditions (2.21):

4.2.2 Test Cases

The dynamical cores described in section 4.2.1 are subjected to three tests, which increase in physical complexity. The test cases are as follows:

1) Steady-State — assesses the ability of the core to maintain a steady-state. A steady-state is often observed in hot-Jupiter simulations in some parameter regimes. The state in this case is a zonally-symmetric jet in gradient wind balance with the specified temperature distribution. The balanced jet is stable in the absence of a perturbation and is an exact solution to the steady-state primitive equations. In theory, when initialized thus, the cores should maintain the state without any change for all times, in the absence of external perturbation. In practice, gravity waves and model truncation errors degrade the steady-state solution over time (Polichtchouk and Cho, 2012). A noticeable deviation from the initial condition implies the presence of numerical and/or programming errors. The reader is reminded that no explicit dissipation is applied in this test case.

2) Baroclinic Wave — assesses the ability of the core to faithfully capture the nonlinear evolution of a well-studied, three-dimensional flow structure of Chapter 3 (see also e.g., Simmons and Hoskins, 1979; Thorncroft et al., 1993; Polvani et al., 2004; Jablonowski and Williamson, 2006; Polichtchouk and Cho, 2012). In contrast to the steady-state case, a small perturbation is introduced to the neutrally-stable jet to trigger a baroclinic instability, and subsequent evolution over a finite duration (20 planetary rotations) is followed. The magnitude (but not the sense and precise location) of the jet is typical of that observed in hot-Jupiter simulations. The primary aim of this test is to clearly expose phase and amplitude errors, which can often be obscured by complicated flow evolutions that cannot be readily compared with analytic solutions. Note that, for this setup, analytic solutions do not exist.

3) "Tidally-locked" Diabatic Forcing — assesses the performance of the core in a setup similar to that used in many synchronized hot-Jupiter studies in the past (e.g., Showman et al., 2009; Rauscher and Menou, 2010; Thrastarson and Cho, 2010). In the setup, the effect of zonally asymmetric heating from the host star is idealized as a simple "Newtonian relaxation" to a prescribed temperature distribution in equation (2.1b). Subject to this applied diabatic forcing, the atmosphere is "spun-up" from an initial state of rest. The "strength" of the forcing is controlled by the specified day-night temperature gradient and characteristic relaxation time which varies in height. The purpose of the test is to elucidate large-scale flow and temperature distributions observed in current simulations of tidally synchronized extrasolar planets. In general, the established flow and temperature distributions can be variable, depending on the forcing and dissipation parameters used (e.g., Cho et al., 2008; Thrastarson and Cho, 2011).

Before presenting the test case results, a brief discussion concerning convergence is in order. Throughout the chapter the word, "convergence" is extensively used. A particular care is taken to distinguish three different types of convergence: *numerical*, *visual*, and *qualitative*. In this heuristic definition, numerical convergence is achieved when a model output is the same up to a specified decimal precision (e.g., two places), at least at two different spatial resolutions. This is the most stringent criterion for convergence and not easily achieved if the model parameters (e.g., dissipation coefficient) are different between two resolutions, even for the same

dynamical core. Visual convergence is less stringent than numerical convergence and is achieved when plots of the model solutions at two or more resolutions are nearly visually indistinguishable. Qualitative convergence is the least stringent definition and is achieved when the model results at two or more resolutions are similar in a qualitative sense. Solutions which differ in phase and amplitude at a given time, are qualitatively converged if they behave similarly over a finite time window. Qualitative convergence can be achieved within a single core (e.g., at different resolutions) and across different cores (despite different model parameters).

4.3 Results

4.3.1 Test Case 1 (TC1): Steady-State

TC1 Setup

In this test case, a non-linearly balanced, midlatitude eastward jet is specified as the initial condition. The jet is a neutrally-stable solution to equations (2.1), and is unstable in the presence of a perturbation. The setup is nearly-identical to the midlatitude jet setup of Chapter 3 (i.e., run E45N). The only difference is the jet amplitude, which in this work is taken as $U = 500$ m s^{-1} (compared to $U = 1000$ m s^{-1} in Chapter 3). A weaker jet amplitude is chosen here in order to achieve better numerical and visual convergence at lower resolutions. As was discussed in Chapter 3, higher resolution is required for convergence of high amplitude jets, due to the stronger ageostrophy associated with high speed jets. Note also that unlike in Chapter 3, no initial perturbation is applied to initiate baroclinic instability in this test case. The setup described in section 3.3.1 is in p-coordinates: in σ-coordinate the setup can be obtained by using the relation, $p = \sigma p_s$.

In Figure 4.2, the meridional cross-section of the zonally-symmetric basic state flow u_0 and potential temperature θ_0 (top), as well as the longitude-latitude map of the relative vorticity ζ_0 at 975 hPa level (bottom), are shown. It is emphasized that the initial condition is trivial to set up in all the models—except for the MITgcm in the CS grid configuration. To specify the initial zonal wind field in this grid, a MATLAB routine (supplied with MITgcm) is used to re-grid the wind from the LL grid to the CS grid. This re-gridding procedure involves changing the orientation of the wind velocity vector from the LL grid to the CS grid by rotating the vector components through grid orientation angles. As a result of the procedure, small values of meridional wind are artificially introduced in the initial wind field; hence,

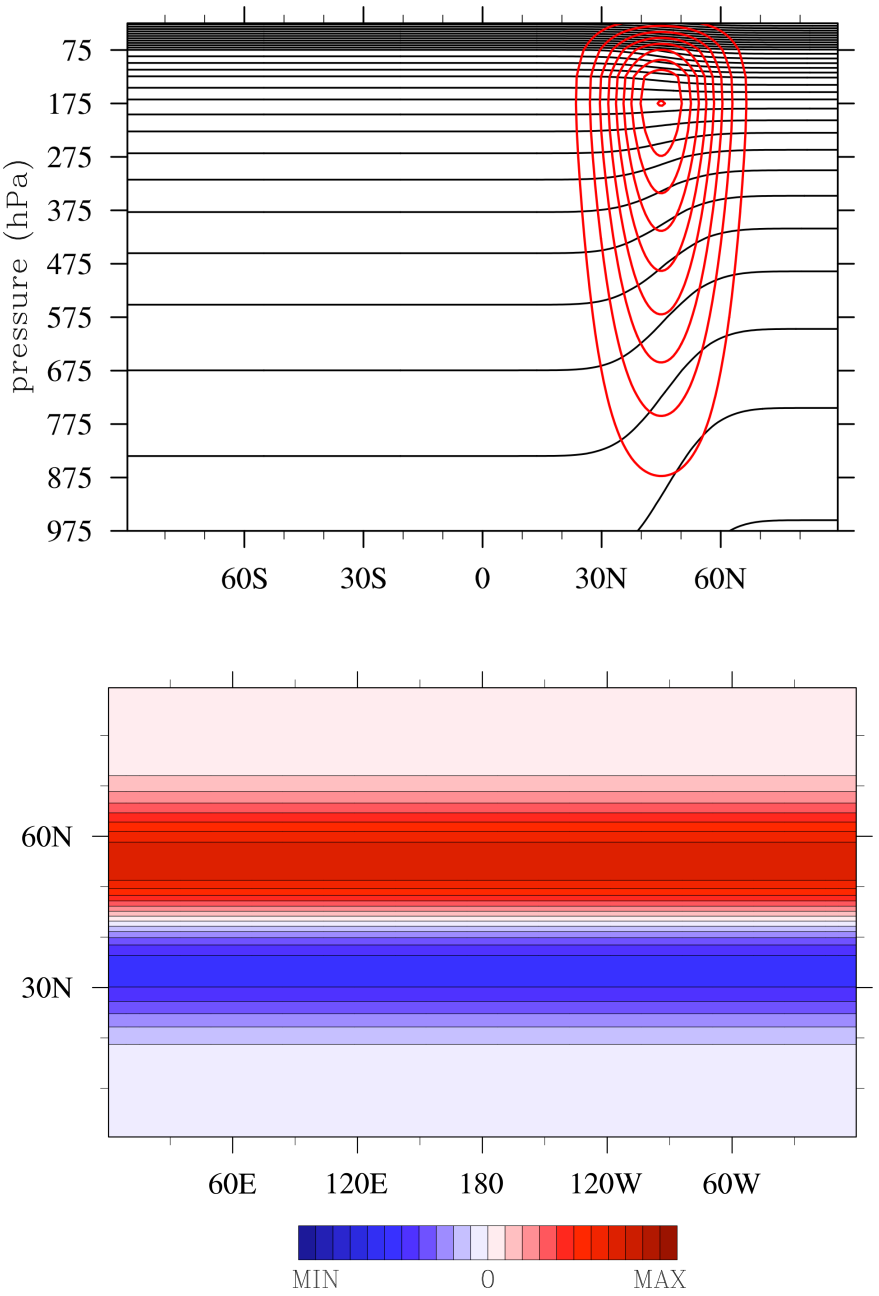

Figure 4.2: Top: The basic state zonal wind u_0 [m s^{-1}] (red) and potential temperature θ_0 [K] (black), as a function of latitude and pressure for test case 1, the steady-state test. The contour interval for zonal wind is from 50 m s^{-1} to 500 m s^{-1}, in steps of 50 m s^{-1}. The contour interval for potential temperature is from 1400 K to 4400 K, in steps of 100 K. The same setup is used as the initial condition in test case 2, the baroclinic wave test. Bottom: Basic state relative vorticity (ζ) field [s^{-1}] as a function of longitude and latitude in cylindrical-equidistant view, centered on the equator, at the 975 hPa ($\approx$ 975 mbar) pressure level. Maximum and minimum values are $+5 \times 10^{-7}$ s^{-1} and -5×10^{-7} s^{-1}, respectively, with contour interval of 5×10^{-8} s^{-1}.

the initial state becomes slightly less well balanced than that before the re-gridding. However, the re-gridding procedure itself does not cause the destabilization of the jet. This has been checked by re-gridding the field from the CS grid onto the Gaussian grid: the jet in the Gaussian grid is stable when the unbalancing effects from the corner points in the CS grid are removed.

The steady-state case (as well as the other test cases) have been performed mainly at three different horizontal resolutions. The vertical domain is resolved by 20 equally spaced p or σ levels such that the bottom level midpoint is placed at $p =$ 975 hPa ($\sigma = 0.975$) and top level midpoint is placed at $p = 25$ hPa ($\sigma = 0.025$)[16]. The pseudospectral resolution in the horizontal direction is up to T170 in BOB and up to T85 in other model cores. As in Chapter 3, the letter "T" refers to the triangular truncation and the number refers to the maximum total (as well as the zonal) wavenumber retained in the spherical harmonic expansion. The highest horizontal resolution in MITgcm for the LL grid is G128 and for the CS grid is C64.[17] The "G128" designation refers to 256×128 grid points covering the surface of the sphere. The "C64" designation refers to 64×64 points covering one of the six cube faces, for a total of $6 \times 64 \times 64$ points covering the entire surface of the sphere. All the other model specific parameters needed for reproducing the steady-state test case are listed in the Appendix, in Tables 4.1–4.3.

The dynamical cores are integrated for 20τ, (recall, τ is one planetary rotation i.e., $2\pi/\Omega$), with no forcing and dissipation. Hence, $\boldsymbol{\mathcal{F}}_{\mathbf{v}} = \boldsymbol{\mathcal{D}}_{\mathbf{v}} = \mathcal{D}_\theta = \dot{q}_{\text{net}} = 0$ in equations (2.1). Note that, in the absence of forcing and dissipation, all dynamical cores should conserve mass, total energy (TE), total angular momentum (AM) and potential temperature *exactly*. The TE and AM are defined as:

$$\text{TE} = \int_V \left(\frac{u^2 + v^2}{2} + c_p T + \Phi \right) \mathrm{d}M \tag{4.7}$$

$$\text{AM} = \int_V \left[\left(\Omega R_{\text{p}} \cos\phi + u \right) R_{\text{p}} \cos\phi \right] \mathrm{d}M \,, \tag{4.8}$$

where the integral is taken over the volume V of the atmosphere. Note also, AM is the total absolute angular momentum.

[16] Note, however, that the bottom interface is placed at $p = 10^3$ hPa ($\sigma = 1$) and the top interface at $p = 0$ hPa ($\sigma = 0$), respectively.

[17] The C64 and C16 CS grids have been generated by me with MATLAB routines provided by MITgcm support. However, the default C32 grid (also MATLAB generated) comes included with MITgcm.

TC1 Results

As discussed earlier, all models are expected to maintain the initial condition (Figure 4.2) because it is an exact solution to equations (2.1) in the steady state and there are no external perturbations. However, in practice the initial state degrades over time because balance is never perfectly achieved due to the slight numerical errors generated in the integration of equation (3.10), as well as in the inherent space and time discretizations. The numerical errors are quantified via two l_2 error norms: the "symmetry" norm and the "degradation" norm (see, e.g., Jablonowski and Williamson, 2006). In TC1, these norms are computed for the zonal wind field u.

The symmetry norm assesses the deviation from zonal symmetry (related to eddy kinetic energy) at each instant. It is defined:

$$l_2\big[u(t)-\overline{u}(t)\big] = \left\{ \frac{1}{4\pi}\int_{s_\mathrm{B}}^{s_\mathrm{T}}\int_{-\frac{\pi}{2}}^{\frac{\pi}{2}}\int_{0}^{2\pi}\Big[u(\lambda,\phi,s,t)-\overline{u}(\phi,s,t)\Big]^2\cos\phi\,\mathrm{d}\lambda\,\mathrm{d}\phi\,\mathrm{d}s \right\}^{1/2}$$
$$\approx \left\{ \frac{\sum_k\sum_j\sum_i\big[u(\lambda_i,\phi_j,s_k,t)-\overline{u}(\phi_j,s_k,t)\big]^2 w_j\,\Delta s_k}{\sum_k\sum_j\sum_i w_j\,\Delta s_k} \right\}^{1/2}. \tag{4.9}$$

Here, overbar $\overline{(\cdot)}$ denotes the zonal average; indices i, j, and k are for longitude, latitude, and height, respectively; s denotes generalized height (and is either p or σ in all the cores); w_j are the Gaussian weights (e.g., Canuto et al., 2007) for the pseudospectral cores or are defined as $w_j = |\sin\phi_{j+1/2} - \sin\phi_{j-1/2}|$ for MITgcm in LL grid, where the "half-indices" denote points half way between two neighboring grid points; and, Δs_k are the layer thicknesses. The degradation norm, on the other hand, assesses the deviation of zonal average from the zonally-symmetric *initial* flow. It is defined:

$$l_2\big[\overline{u}(t)-\overline{u}(0)\big] = \left\{ \frac{1}{2}\int_{s_\mathrm{B}}^{s_\mathrm{T}}\int_{-\frac{\pi}{2}}^{\frac{\pi}{2}}\Big[\overline{u}(\phi,s,t)-\overline{u}(\phi,s,0)\Big]^2\cos\phi\,\mathrm{d}\phi\,\mathrm{d}s \right\}^{1/2}$$
$$\approx \left\{ \frac{\sum_k\sum_j\big[\overline{u}(\phi_j,s_k,t)-\overline{u}(\phi_j,s_k,0)\big]^2 w_j\,\Delta s_k}{\sum_k\sum_j w_j\,\Delta s_k} \right\}^{1/2}. \tag{4.10}$$

Note, simulation results are interpolated onto a regular LL grid to compute both l_2 norms for MITgcm in CS grid.

In this work, all pseudospectral cores and MITgcm in LL grid maintain zonal symmetry to machine precision, at all resolutions. The results are not shown, since

they are identical to Figure 4.2. However, this is not the case for MITgcm in CS grid: eight special "corner points" (four in the northern hemisphere and four in the southern hemisphere), where the cube facets meet, introduce an artificial wavenumber-4 disturbance, quickly degrading the zonal and temporal symmetry. This is shown in Figure 4.3.

In the figure, the top panel shows the l_2 symmetry norm. The effect of the corners is more pronounced at higher horizontal resolution, as the grid size near the corners becomes smaller. The numerical noise introduced by the corner points causes the higher resolution simulations to crash earlier—at $t = 15.5\,\tau$ and $t = 4.5\,\tau$ at C32 and C64 resolutions, respectively. Recall that explicit diffusion is not used in these simulations; but with "enough" diffusion applied, crashing can be prevented (see, e.g., section 4.3.2). This is a simple example of when viscosity, filters, or "fixers" can unintentionally obscure issues in the numerics and when systematic model intercomparisons can be very fruitful. The bottom panel in Figure 4.3 shows the relative vorticity (ζ) field from the MITgcm CS simulation at C64 resolution. The field at the 975 hPa level is shown in the cylindrical-equidistant projection, centered on the equator; the time of the simulation is $t = 2.5\,\tau$. Only the northern hemisphere is shown. The numerical noise from the four special corner points in this hemisphere can clearly be seen.[18] It has been verified that the noise is not due to the slight imbalance of the flow field introduced by the vector component rotation, mentioned above (section 4.3.1). All other models, including MITgcm in LL grid, maintain the initial ζ distribution throughout the duration of simulation (20τ).

Figure 4.4 shows the l_2 degradation norm evolution over the 20τ duration for all models at varying horizontal resolutions. The degradation norm presents a more stringent quantification of the error growth and fluctuation, as well as the intra-core convergence with resolution, since the deviation is measured against the initial state. First the error growth and fluctuation characteristics are discussed. This is then followed by a discussion of the convergence characteristics.

In the figure, the error growths for the pseudospectral cores and the MITgcm core in LL grid cease, after an initial increase. The initial error growth is due to generation of gravity waves. The error growth characteristics are identical in

[18] Here, one could argue that this test case (and the next one) unfairly favors the Gaussian and LL grids because the jet is zonal and passes over the corner points. However, rotating the grid does not fully resolve the adverse effect of the corner points nor improves (or reduces the disparity in) the performance of the model over a finite duration (see, e.g., Lauritzen et al., 2010). Note that the default setting of the MITgcm in CS grid is the unrotated grid configuration. More importantly, the grid has not been rotated in past simulations of extrasolar planets using the MITgcm in CS grid. For these reasons, in this study the focus is on the unrotated grid configuration.

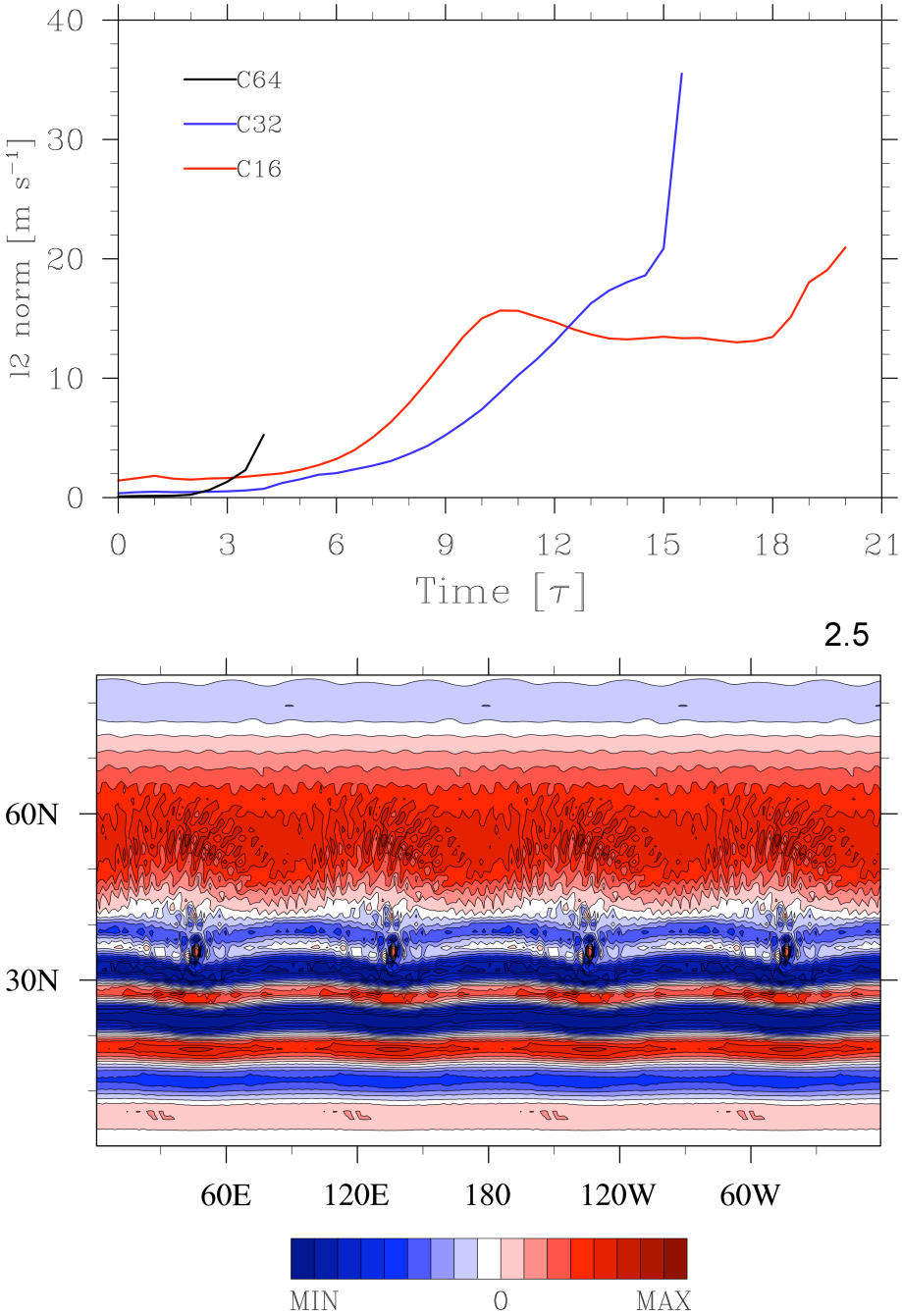

Figure 4.3: Top: Symmetry deviation l_2-norm of $\left[u(t) - \overline{u}(t)\right]$ [m s^{-1}] for MITgcm cubed-sphere (CS) steady-state case simulations in the default configuration. Three different resolutions (C16, C32, C64) are presented. Higher resolution simulation norms blow-up earlier. Bottom: ζ field at $t = 2.5\,\tau$, at the 975 hPa level, from the C64 resolution simulation in the top panel. Maximum and minimum values are $+6 \times 10^{-7}$ s^{-1} and -6×10^{-7} s^{-1}, respectively, with contour interval of 8×10^{-8} s^{-1}. The increase in the l_2-norms in the top panel are caused by the special corner points, seen in the bottom panel. Note, the norms are not exactly zero initially, especially at low resolution. This is due to the errors introduced by the re-gridding procedure of u from LL to CS grid.

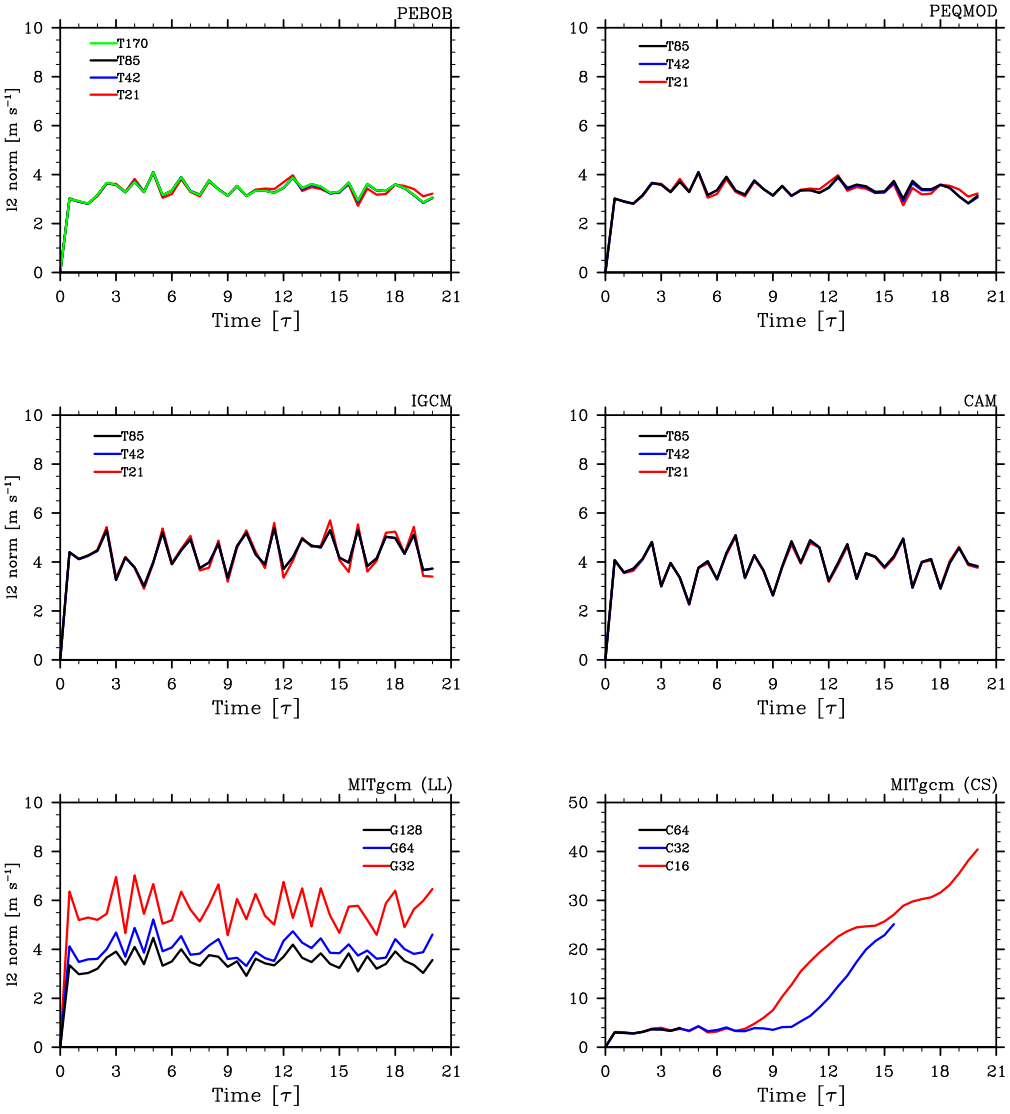

Figure 4.4: The degradation l_2-norm of $\left[\overline{u}(t) - \overline{u}(0)\right]$ [m s^{-1}] for all the dynamical cores with varying horizontal resolutions. Note that the vertical scale of the plot for the MITgcm in CS grid (bottom right) is five times that of the other panels. In this panel, the three simulations are indistinguishable from each other until just before the C64 simulation crashes, at $t \approx 4.5\,\tau$.

BOB and PEQMOD cores (top row in Figure 4.4), which employ the same vertical discretization scheme. The IGCM and CAM cores (middle row in Figure 4.4) exhibit similar error growth characteristics as BOB and PEQMOD, but follow much more closely between themselves. This is not surprising since IGCM and CAM both use the σ-coordinate vertical discretization.[19] Note that both IGCM and CAM show errors saturating at slightly higher levels and with larger deviations from the saturation level, compared to PEBOB and PEQMOD.

The MITgcm in the two grids tested, LL and CS grids, show interesting behaviour. In the LL grid, the core exhibits similar behaviour as the pseudospectral cores—particularly at the higher grid resolutions (see bottom left panel in Figure 4.4). At the low grid resolution (G32), the error saturation level and/or fluctuation magnitude are larger than in the pseudospectral cores. However, both the level and fluctuation magnitude decrease with higher resolution. In contrast, the core in CS grid exhibits error growth behaviour that is completely different from any of the cores tested (see bottom right panel in Figure 4.4). This is expected from the result already presented in Figure 4.3. The degradation error in the MITgcm in CS grid continues to grow with time—again, due to the wavenumber-4 noise from the corner points in the CS grid. This effect is probably not so important in simulations of hot-Jupiter atmospheres, which are strongly forced non-zonally as well as strongly dissipated. However, it could have a deleterious influence on steady state and instability simulations, as demonstrated here (and in the next test case).

Figure 4.4 also shows the convergence characteristics of the cores. As can be seen, the pseudospectral simulations are all visually converged. CAM simulations are particularly well converged: the norms for three resolutions tested show essentially no discernible differences. On the other hand, the simulations with the MITgcm in LL grid are not visually converged for resolutions lower than G128, and this is reflected in the figure (bottom left panel). Therefore, these particular simulations are not *intra*-model converged.

The above behaviour is consistent with the theoretical understanding of pseudospectral and finite difference and volume methods and past inter-method comparisons (see, e.g., Durran, 1999; Boyd, 2001, and references therein). The larger saturation and fluctuation of the lower grid resolution simulations are likely due to the second-order accurate finite volume method employed. For a smooth flow devoid of shocks or fronts, such as flow discussed in this test case, the resolution of a pseudospectral simulation is equivalent to an order of magnitude higher horizontal

[19] Note that the CAM core normally uses the more general η-coordinate (see, e.g., Thrastarson and Cho, 2010), but it has been run in the simpler σ-coordinate to facilitate equatable comparison.

resolution than in a finite volume/difference simulation with the same number of degrees of freedom[20] (e.g., Canuto et al., 2007; Durran, 1999; Boyd, 2001; Thrastarson and Cho, 2011); this is because the order of the pseudospectral method approaches infinity exponentially fast with increasing resolution. Note that the MITgcm CS grid simulations are neither *inter*- nor *intra*-converged, as the C16 and C32 simulations strongly diverge after $t \approx 7\,\tau$ and the C64 simulation crashes before this point at $t \approx 4\,\tau$.

Of all the cores tested, BOB and PEQMOD cores maintain the steady state solution the best: their norms level off with the smallest mean value as well as with the smallest root mean square fluctuation from the mean. This is partly due to the exclusion of the external gravity wave mode, a constraint imposed by the "zero vertically-integrated divergence over the atmosphere" algorithm employed by the two cores (see Section 4.2.1).

In terms of convergence, pseudospectral cores are all converged at T42 resolution for this test case. Differences in the norms, as the horizontal resolution is increased, is hardly noticeable in these cores: their solutions are visually converged. As already mentioned, the CAM solutions show remarkably little difference at different resolutions: they are numerically converged. *Numerical* convergence is achieved in BOB at T85 resolution; the norms for T85 and T170 resolutions match exactly up to the second decimal place. Again, this is expected, given the exponential convergence property of the pseudospectral method. In contrast, the MITgcm simulations are not visually converged in both LL and CS grid configurations.

In summary, apart from the MITgcm in CS grid, the steady-state condition is well maintained throughout the duration of the simulations by all of the cores. Hence, these simulations are qualitatively inter-model converged for this test case at the resolutions considered. As additional measures of convergence, these cores are found to conserve the total initial energy (equation (4.7)) and total angular momentum (equation (4.8)). The values of the two quantities are 2.3×10^{28} J and 1.8×10^{32} J s, respectively, for this test case. These values are maintained throughout the integration to within 0.02 percent (except, of course, for the MITgcm in CS grid). At this point, one may be tempted to down-play the differences between the model

[20] This also means that, in practice, a finite volume/difference grid should not be compared with a Gaussian grid of a pseudospectral method *with the same number of grid points*, as the latter grid is still equivalent to effectively at least three times the resolution of the former grid. The latter point is demonstrated in Figure 4.4 (cf. T21 and G32 simulations, for example). Note also that when shocks/fronts are present, *all* methods have difficulty representing the flow accurately, unless specialized treatments (available in both pseudospectral and finite difference methods) are implemented to specifically deal with the sharp flow structures.

cores reported here—particularly in the pseudospectral cores. However, even such small discrepancies can—and in practice do—lead to non-trivial differences in the model outputs, if the problem is more complex or requires high spatio-temporal accuracy (e.g., instability and transition to turbulence).

4.3.2 Test Case 2 (TC2): Baroclinic Wave

TC2 Setup

In this case, an instability is initiated in the neutrally-stable state of Section 4.3.1 to generate an non-linearly evolving baroclinic wave. As in Chapter 3, the instability is triggered by perturbing the initial temperature T_0 with a heat bump T' at all pressure levels, where

$$T'(\lambda, \phi) \;=\; \operatorname{sech}^2\big(3\,\lambda\big)\operatorname{sech}^2\left[6\left(\phi - \frac{\pi}{4}\right)\right]. \tag{4.11}$$

Once the instability ensues, the flow is allowed to evolve freely thereafter for $20\,\tau$. It is important that exactly this perturbation is used, when attempting to reproduce these results. This is because, while the flow is expected to asymptotically reach qualitatively the same state, the early-time evolution is different for a different perturbation. It is then difficult to delineate the source of the variations in the subsequent evolution—whether the variations are due to physically different modes being excited or to numerical inaccuracies.

As in the previous chapter, the instability leads to a rapid development of sharp fronts in few planetary rotations (i.e., few τ's), and purely inviscid equations (as in TC1) can no longer be integrated. This case is arguably more "realistic" than the steady-state case, in the sense that explicit viscosity must be used—as in most long-duration simulations involving complex flows.

To make the comparison easier, in this test case a Laplacian dissipation operator is implemented in all the cores even though in pseudospectral simulations, more scale-selective, higher order, hyperdiffusion operators (e.g., $\mathfrak{p} \geq 2$ in equation (2.20)) are almost always used (e.g., in Chapter 3, superviscosity corresponding to $\mathfrak{p} = 4$ is used). Although hyperdiffusion operators acting on vorticity and divergence fields are common in pseudospectral cores, they are less common in finite volume cores because they are more difficult to implement in the finite volume discretization scheme. In the latter type of cores, alternative strategies are used to effect high scale-selectivity. As discussed in section 4.2.1, in addition to the harmonic (second-order) and biharmonic (fourth-order) diffusion, the MITgcm also supports the Shapiro

filter.

As in Polvani et al. (2004) and in Chapter 3, the same value of dissipation coefficient ($\nu_2 = 2 \times 10^7$ m^2 s^{-1}) is used for all the resolutions in TC2. The usual practice is to adjust—or tune—the value for each resolution, problem and model (see, e.g., discussions in Thrastarson and Cho (2011) and Chapters 3 and 5). However, ν_2 is not adjusted in this case so that each mode, up to the truncation wavenumber, experiences the same amount of dissipation, regardless of the resolution. For example, the dissipation time at the T21 truncation scale for HD209458b corresponding to the above value of ν_2 is: $\tau_\mathrm{d} = 3.58\,\tau$. In comparison, current flow modeling studies of hot-Jupiters employ a much shorter damping time of $\tau_\mathrm{d} \sim 0.02\,\tau$ (e.g., Rauscher and Menou, 2010; Heng et al., 2011); hence, these simulations are more dissipative than the ones in this study. However, the damping time used is still generally shorter than that used in a similar study of Chapter 3—again, to allow a more equatable comparison between the different cores to be performed.

The highest horizontal resolutions investigated in this test case are the same as in the steady-state test case (TC1). The resolution specifications and other parameters needed for reproducing this test case are listed in the Appendix, Tables 4.4–4.6. Note, unlike in TC1, the true solution to the primitive equations is unknown for this test case.

TC2 Results

Figure 4.5 shows the evolution of ζ at the $p = 975$ hPa surface from a simulation with BOB at T170L20 (i.e., T170 horizontal resolution with 20 vertical levels) resolution, for $t = 6\,\tau$ to $t = 18\,\tau$. As in Chapter 3, the 975 hPa pressure surface is chosen because the maximum eddy activity of the unstable evolution occurs near the lower boundary. In the evolution, the perturbed jet undergoes a period of linear growth ($t \ll 9\,\tau$), when the most unstable mode (mode 3–4) emerges. By $t \approx 14\,\tau$ the evolution is well into its non-linear stage, characterized by the exponential growth of eddy kinetic energy and wave breaking. As in the paradigm case of Chapter 3, the ζ perturbation exhibits a distinct northwest-southeast tilt on the poleward side of the jet and southwest-northeast tilt on the equatorward side of the jet. Near $t = 18\,\tau$, the eddy kinetic energy reaches the maximum value of the simulation and the barotropic decay cycle, in which eddy kinetic energy is returned back to the mean flow, ensues for $t \gtrsim 20\,\tau$. In this period, the cyclones (areas of positive ζ anomalies, shown in red in the figure) that have emerged from the wave breaking, start interacting and advance poleward—as was observed in Chapter 3.

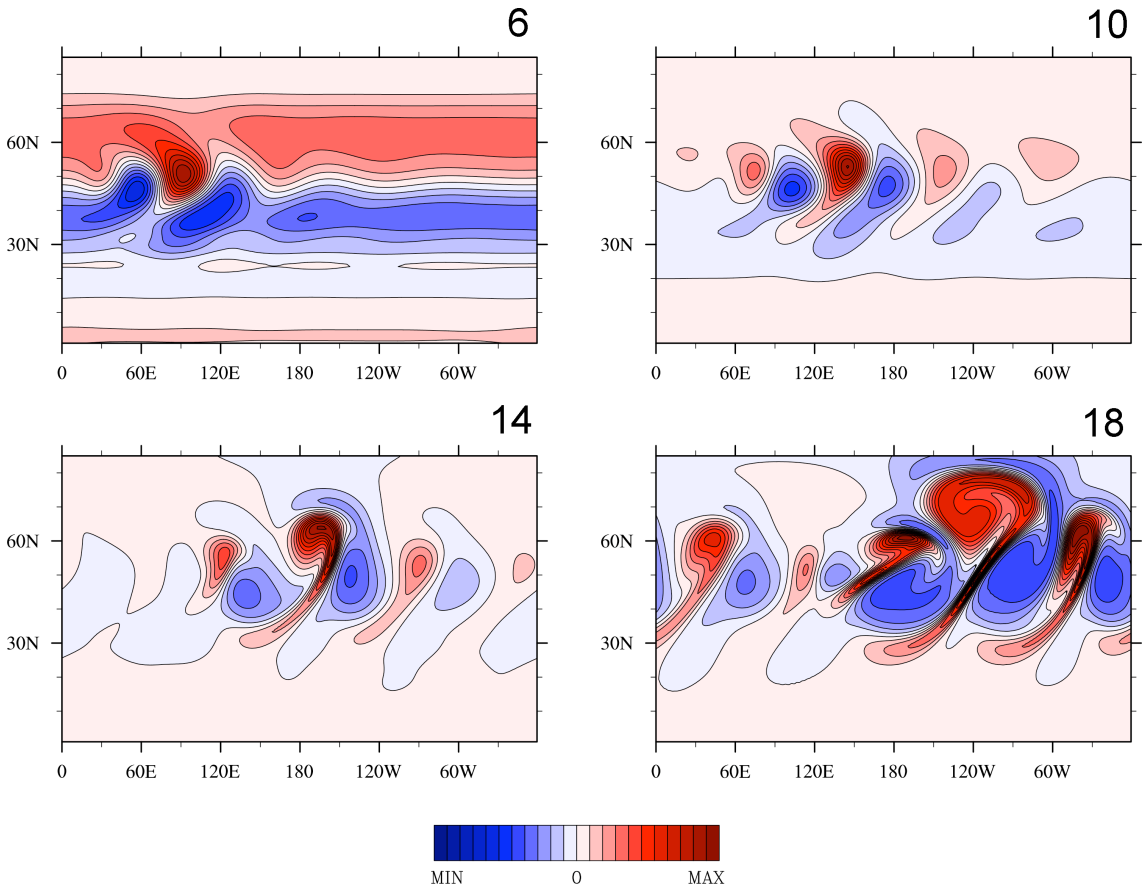

Figure 4.5: Relative vorticity (ζ) field from T170L20 simulation with BOB in cylindrical-equidistant view, centered on the equator. The fields are shown at the 975 hPa pressure level for $t = 6\,\tau$ to $t = 18\,\tau$. Maximum and minimum values are: $\pm 1 \times 10^{-6}$ s^{-1} ($t = 6\,\tau$); $\pm 5 \times 10^{-6}$ s^{-1} ($t = 10\,\tau$); and, $\pm 2 \times 10^{-5}$ s^{-1} ($t = 14\,\tau$ and $t = 18\,\tau$). The contour intervals are, respectively, 1×10^{-7} s^{-1}, 5×10^{-7} s^{-1} and 2×10^{-6} s^{-1}. Note the large, an order of magnitude, change in the amplitude of ζ during the evolution—as well as the formation of sharp fronts and coherent vortices, particularly at $t = 14\,\tau$ and $t = 18\,\tau$.

The evolution presented in Figure 4.5 is the high resolution "reference solution" for the BOB core. For the other pseudospectral cores and the MITgcm core in LL and CS grids, the reference solution is computed at T85L20, G128L20, and C64L20 resolutions, respectively. In addition to these solutions, the outputs from the other model cores may be compared with the T170L20 reference solution obtained with the BOB core. In principle, since all cores solve the same equations (and boundary conditions), the high resolution reference solution computed with one of the cores should serve as a reference solution for all the models. However, in practice, there is a danger in using a single model core to determine the reference solution in problems involving unstable states, as noted by Jablonowski and Williamson (2006). This is due to the differences in how various model cores handle geostrophic adjustment.

Figure 4.6 compares the solutions of all the dynamical cores at the T85L20, G128L20, and C64L20 resolutions at $t = 10\,\tau$ (cf. upper right frame in Figure 4.5). As in TC1, the simulations with IGCM and CAM look nearly identical. The same is true for BOB and PEQMOD simulations, although the amplitude of vorticity anomalies in PEQMOD is somewhat stronger than in BOB. Comparing with IGCM and CAM, the amplitude in PEQMOD is noticeably stronger. In general, it is found that the vorticity anomalies are stronger in the p-coordinate pseudospectral cores than in σ-coordinate pseudospectral cores. In contrast, the phases are impressively similar among all the pseudospectral cores.

There are, however, considerable differences in both amplitude and phase between solutions with MITgcm and pseudospectral cores. Compare the overall vorticity fields, and especially the magnitude of the ζ anomalies in the fields. This is partly caused by ζ not being a prognostic variable in the MITgcm core: u and v fields are evolved, and the calculation of ζ from these fields introduces some errors. If the potential temperature (θ) field is compared instead of the ζ field, the MITgcm LL grid solution resembles the corresponding PEQMOD solution more closely (not shown). However, even using the θ field, the MITgcm CS grid solution differs significantly from the pseudospectral core solutions. This difference—between the two MITgcm solutions, in LL and CS grids—is revealing (cf. two bottom panels in Figure 4.6). Note that the only difference between the two simulations is the grid (and the use of a high-wavenumber zonal filter in the LL grid simulation).

The solution from MITgcm in CS grid clearly exhibits a different unstable mode structure than that of the LL grid solution at $t = 10\,\tau$ (i.e., wavenumber ~ 5 for the CS grid compared with wavenumber ~ 4 for the LL grid). The difference is due to the corners in the CS grid, which provide an additional source of perturbation (i.e., in addition to the applied heat bump) for the fully non-linear flow. This has

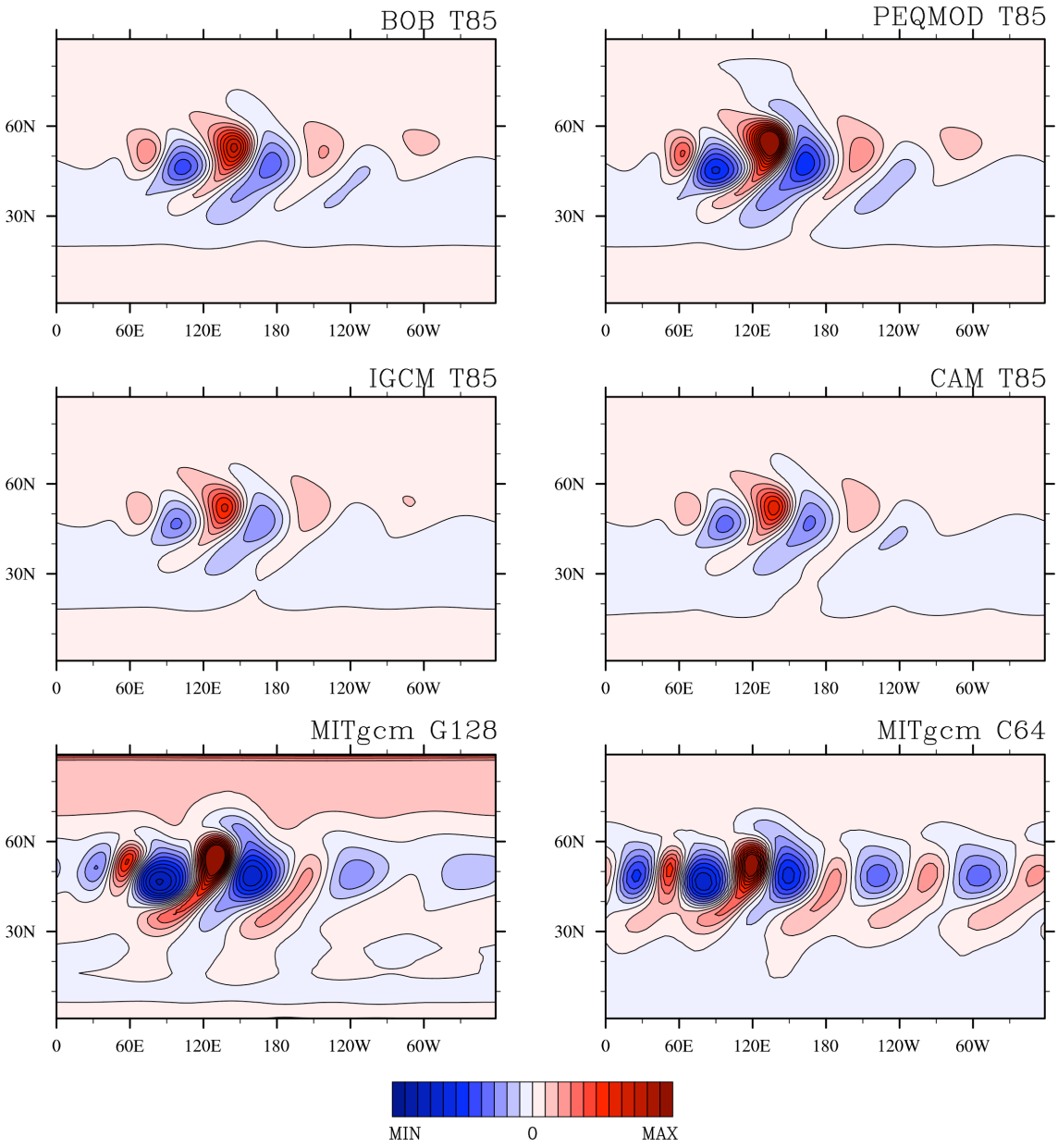

Figure 4.6: Cylindrical equidistant view, centered on the equator, of ζ field at $t = 10\,\tau$ from different model cores. The resolution is the highest tested in all the cores, except in BOB; it is the second highest. The fields shown are from the bottom vertical level ($\sim$ 975 hPa). Maximum and minimum values for all the cores are $\pm 5 \times 10^{-6}$ s^{-1}, with contour interval 5×10^{-7} s^{-1}. These fields are to be compared with each other, as well as with that at $t = 10\,\tau$ in Figure 4.5.

been verified by running a MITgcm in CS grid baroclinic wave simulation without perturbing the background temperature T_0 by T' (see equation 4.11). In this case a clear mode-4 structure associated with the corner points (different from those produced in pseudospectral core simulations shown in Figure 4.6) dominates the evolution throughout.

To assess the convergence (with resolution) characteristics of a model, the l_2 relative vorticity norm is computed at the lowest model layer (i.e., the ∼975 hPa pressure surface). The norm is defined as follows:

$$
\begin{aligned}
l_2\big[\zeta(s_{20})\big] &= \left\{ \frac{1}{4\pi} \int_0^{2\pi} \int_{-\frac{\pi}{2}}^{\frac{\pi}{2}} \Big[\zeta(\lambda, \phi, s_{20}, t)\Big]^2 \cos\phi \, \mathrm{d}\phi \, \mathrm{d}\lambda \right\}^{1/2} \\
&\approx \left\{ \frac{\sum_i \sum_j \big[u(\lambda_i, \phi_j, s_{20}, t)\big]^2 w_j}{\sum_i \sum_j w_j} \right\}^{1/2}, \qquad (4.12)
\end{aligned}
$$

where s_{20} is the lowest model layer in p- or σ-coordinate and the sums are taken over all (λ_i, ϕ_j) points on the sphere. The integration weights are defined as in equation (4.9). After calculating the $l_2[\zeta(s_{20})]$-norm for each resolution, the highest resolution l_2-norm is subtracted from lower resolution l_2-norms within the same model to assess model core convergence.

The differences between $l_2[\zeta(s_{20})]$-norms within the same core are shown in Figure 4.7. It is clear that none of the cores are (numerically or visually) converged at the second lowest resolution—T42, G64 and C32: the curves all deviate from zero (cf. in the upper left panel the "T85−T170" curve, which shows visual convergence). The non-convergence is particularly apparent after the baroclinic instability enters the fully non-linear growth stage ($t \gtrsim 10\,\tau$). Even at T85 resolution, BOB is only visually (not numerically) converged. This can be verified by comparing the top right panel of Figure 4.5 to the top left panel of Figure 4.6: the plots in the two panels are very close to each other but not identical.

Note that the y-scale in the MITgcm plots in Figure 4.7 (as well as in Figure 4.8) is an order of magnitude larger than in the corresponding pseudospectral core plots. This suggests that the apparent qualitative inter-convergence of the MITgcm core in LL grid at G128L20 resolution (seen in Figure 4.6) is suspect. It has been verified that large differences in the l_2-norm in MITgcm are not caused by the errors introduced in the calculation of ζ. For example, the l_2-norm of the surface u-field behaves in a similar way and visual convergence is clearly not achieved in the MITgcm core at the highest resolution tested in this work.

Figure 4.8 shows the differences between $l_2[\zeta(s_{20})]$-norms of a given core and the

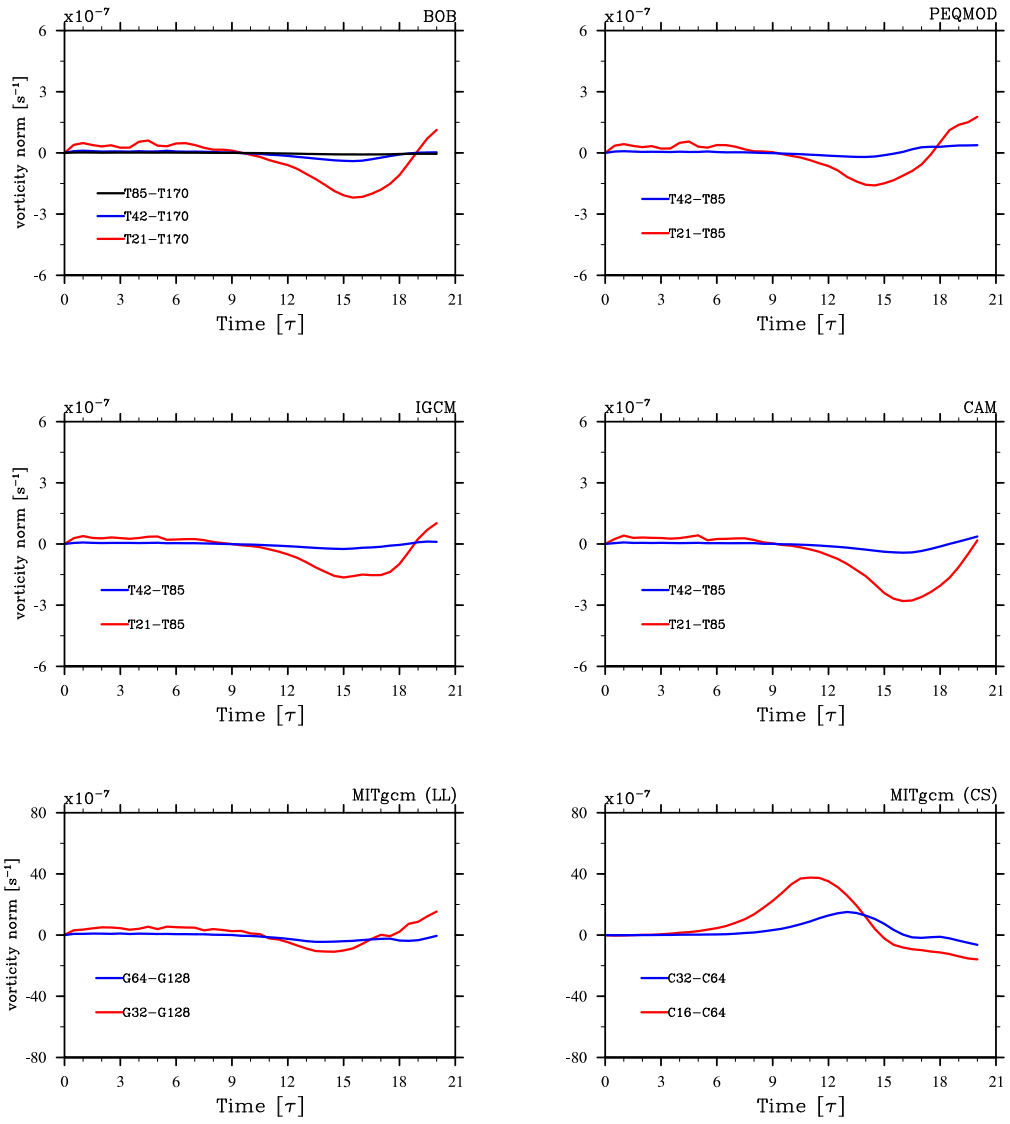

Figure 4.7: Differences of the root mean square l_2 vorticity norm [s^{-1}] between high resolution reference solution and lower resolution solutions within the same model core. The T85 BOB simulation is well converged. No other cores are "intra-model" converged. Note, the y-scale in the two plots of the bottom row for the MITgcm core is nearly an order of magnitude larger than in the other plots.

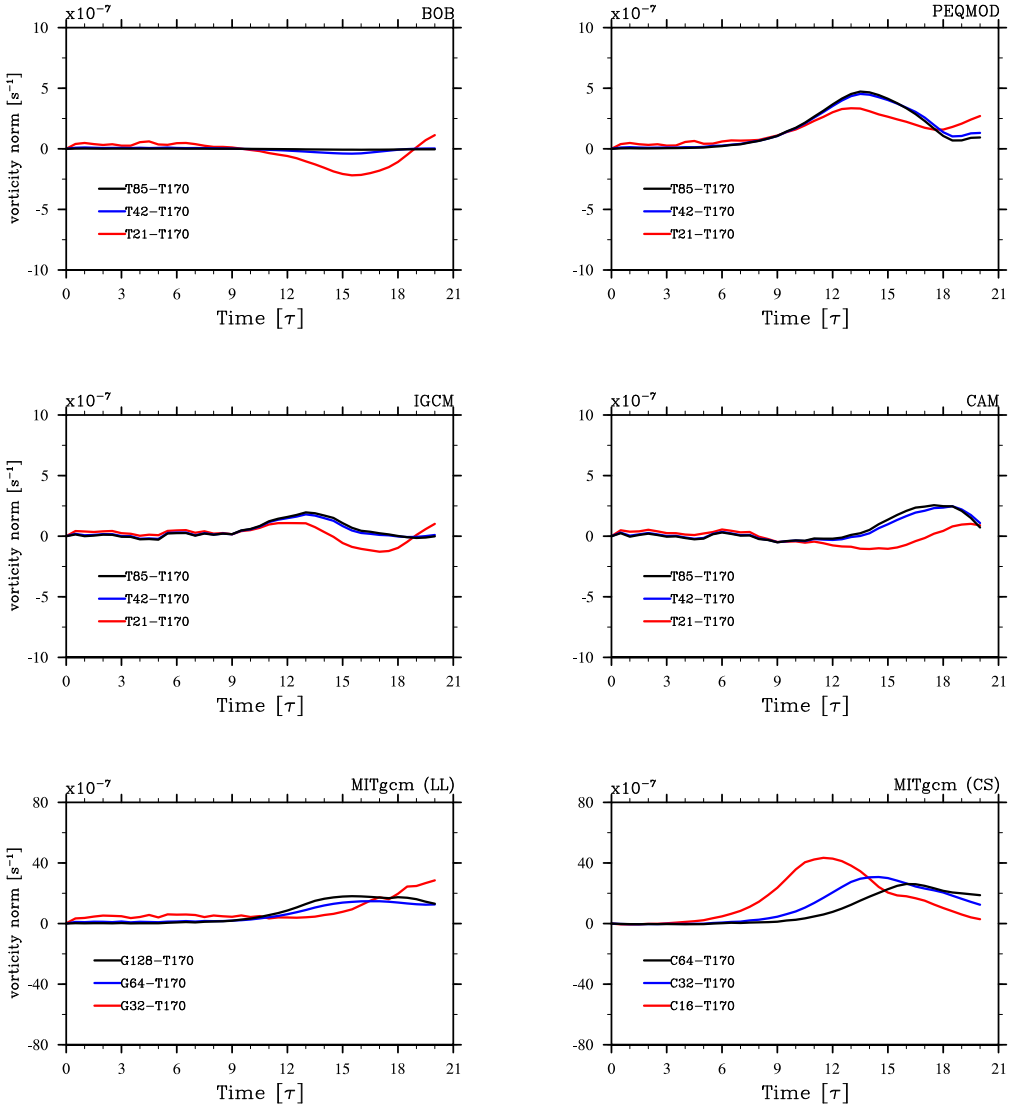

Figure 4.8: Differences of the root mean square l_2 vorticity norm [s^{-1}] between T170L20 reference solution for BOB and solutions with other dynamical cores at various resolutions. The scales are same as in Figure 4.7. The T42 simulations in all the pseudospectral cores appears to be marginally "intra-converged". MITgcm core in both LL and CS grids are not converged, particularly in the latter grid.

T170 $l_2[\zeta(s_{20})]$-norm of BOB. Hence, here the T170 simulation is treated as a "reference solution"—as if it were the "correct solution". Recall that ideally simulations by each core should be compared with T170 (or higher) resolution simulation of the same core. For technical reasons, this is not feasible in all the cores. However, this comparison is still useful and provides some insights. The figure clearly demonstrates that solutions of other model cores are not visually converged to BOB's high-resolution solution. In all model solutions, the norms are small until $t \sim 9\,\tau$, but then increase markedly once the evolution enters the fully non-linear stage, when the wave begins to develop sharp fronts. This is expected, given the behaviour of baroclinically unstable evolution reported in the previous chapter.

Note that the evolution of the baroclinic wave growth in this set of simulations is considerably retarded by the stronger explicit dissipation, compared to that in Chapter 3 (recall that Laplacian dissipation, rather than superdissipation, is employed here). Moreover, the initial jet's maximum speed is weaker here than that in Chapter 3, leading to a smaller growth rate for the baroclinic instability. Recall that in Chapter 3, it was demonstrated that baroclinic instability in a similar situation is only marginally captured with T85 resolution for a 1000 m s^{-1} jet. Consistent with those results, all pseudospectral cores are visually converged at resolution T85 here, as expected for a 500 m s^{-1} jet. The more stringent resolution criterion for convergence in Chapter 3 is due to the stronger ageostrophy present in a faster jet, as already discussed in section 4.3.1. Similarly, if the initial jet amplitude had been greater than 1000 m s^{-1}, the resolution at which convergence would be achieved is expected to be correspondingly higher.[21]

Interestingly, even with the application of Laplacian dissipation, which is a strong dissipation, the global energy is conserved to within 0.1 percent in all the model cores throughout the integration ($t = 20\,\tau$). Global angular momentum is conserved to within 0.02 percent in all the model cores throughout the integration. Note that this is for Laplacian dissipation only, as only this dissipation is used in TC2. These conservation properties should be compared with the corresponding ones in the next test case.

[21] Note, speeds greater than 2000 m s^{-1} are often produced in many hot-Jupiter simulations. Some simulations produce speeds which are much greater than this (e.g., Cooper and Showman, 2005; Showman et al., 2008; Liu and Showman, 2013).

4.3.3 Test Case 3 (TC3): Diabatic Forcing

TC3 Setup

No "physical processes" (e.g., net heating, wave drag, convection) were specified in the setup of TC1 and TC2, if explicit dissipation is not considered to be representing "turbulent viscosity" in the latter test case. Most of these processes are as yet poorly constrained by observations or unobtainable from first principles for extrasolar planets (see, e.g., discussion in Cho et al., 2008; Cho, 2008; Showman et al., 2011). Two such processes are irradiation from the host star and radiative cooling in the atmosphere of the planet. These processes are currently represented essentially in all extrasolar planet atmosphere simulations in a highly idealized way. For example, Newtonian relaxation parameterization to a prescribed "equilibrium temperature" is often used to crudely represent the combined thermal forcing (see, e.g., Cooper and Showman, 2005; Showman et al., 2008; Menou and Rauscher, 2009; Rauscher and Menou, 2010; Thrastarson and Cho, 2010, 2011; Heng et al., 2011). Despite the crudeness, the parameterization is also used here due to its simplicity and common usage in past works. The idea is to be reasonably close to past simulations, while facilitating reproducibility of the present work and clean comparisons with future work.

In the Newtonian relaxation parameterization, the source term ($\dot{q}/c_p$) in the thermodynamic equation (equations (2.19e), (4.1e) or (4.6d)) is specified as

$$\frac{\dot{q}}{c_p} \;=\; -\frac{1}{\tau_{\rm th}}\big(T - T_e\big)\,. \tag{4.13}$$

Here, in its general form, $T_e = T_e(\lambda, \phi, s, t)$ is the equilibrium temperature and $\tau_{\rm th} = \tau_{\rm th}(\lambda, \phi, s, t)$ is the thermal relaxation time. Both T_e and $\tau_{\rm th}$ distributions are currently not well known, both in space and in time. In many studies, very short relaxation times ($\ll$1 hour) and large equilibrium temperature gradients across the day-night terminator ($\approx$1000 K) are specified (e.g., Showman et al., 2008; Rauscher and Menou, 2010; Thrastarson and Cho, 2010). Such a condition constitutes an "extreme forcing" on the dynamics—especially in simulations started from rest state and spun up to a strongly "unbalanced" state (Cho et al., 2008; Thrastarson and Cho, 2011; Polichtchouk and Cho, 2012). Here "unbalanced" state refers to flow and temperature distribution inundated with fast phase speed gravity waves. The Solar System planets, in comparison, are characterized by comparatively much longer $\tau_{\rm th}$ and much smaller T_e gradient.

In this test case, T_e is height-independent (i.e., $\partial T_e/\partial s = 0$) and both T_e and $\tau_{\rm th}$

are steady (i.e., $\partial \{T_e, \tau_{\rm th}\}/\partial t = 0$). In general, both T_e and $\tau_{\rm th}$ are complicated functions of space and time (Cho et al., 2008; Showman et al., 2009). However, in keeping with the overall aim of this work, a setup which is at once easily describable and easily implementable in all models is chosen. Here, T_e is chosen to be as in Thrastarson and Cho (2011):

$$T_e \;=\; T_m + \Delta T_e \cos\phi \cos\lambda \;\;, \tag{4.14}$$

where $T_m = (T_D + T_N)/2$ and $\Delta T_e = (T_D - T_N)/2$ with $T_D = 1900$ K and $T_N = 900$ K the maximum and minimum temperatures at the day and night sides, respectively. $\tau_{\rm th}$ is set to vary linearly with pressure (or σ) such that, at the $p = 975$ hPa ($\sigma = 0.975$) level, $\tau_{\rm th} = 3.6 \times 10^5$ s and, at the $p = 25$ hPa ($\sigma = 0.025$) level, $\tau_{\rm th} = 3.6 \times 10^4$ s. The relaxation time is just slightly longer than in some recent studies of hot-Jupiters, making the forcing slightly less "violent". The basic state temperature is isothermal and set to $T = 1400$ K; and, in all simulations, initial wind $\mathbf{v}_0$ is zero everywhere in the computational domain. The vertical domain in all the simulations in this test case, as in the previous test cases, extends from 975 hPa to 25 hPa (again, $\approx$ 975 mbar to $\approx$ 25 mbar, respectively). Similarly, horizontal resolutions are the same as in TC1 and TC2 and listed with other model parameters in the Appendix, in Tables 4.7–4.9. The simulations are run for 100τ, much longer than the maximum $\tau_{\rm th}$ ($\approx$1.2 τ).

To control the small-scale noise inherent in all simulations, superdissipation (see equation (2.20)) is applied in pseudospectral simulations (in each layer) to prevent accumulation of energy at the small scales. Note that this is the "least common denominator" dissipation, since not all of the tested pseudospectral cores come with higher order (hyper)viscosity as the default. Superviscosity is also more equatably compared to explicit viscosity used in finite volume cores, which in general cannot dissipate as scale-selectively as cores using the pseudospectral algorithm. The value of superdissipation coefficient $\nu_4 = 10^{22}$ m^4 s^{-1} at T85 horizontal resolution (corresponding to a damping time of 190 s for the smallest resolved scale) is chosen based on the study of Thrastarson and Cho (2011): they have found this value to produce a well-behaved kinetic energy spectrum with the $0.1 \leq (\tau_{\rm th}/\tau) \leq 3$ vertical distribution.

In this test case, unlike in TC2 above, the value of $\nu_{2\mathfrak{p}}$ is increased/decreased with decreasing/increasing resolution for a given $\mathfrak{p}$ in pseudospectral simulations (see Table 4.7); this practice is common in simulation studies. The procedure will definitely preclude numerical convergence especially at later times after the peak

in enstrophy dissipation. However, since the simulations in this chapter are not numerically converged in general in the simpler test cases (particularly in TC2), numerical convergence in the more extreme conditions of TC3 is not expected. Hence, attention is focused on visual and qualitative convergences in this test case.

In past extrasolar planet simulations performed with MITgcm, it has been customary to use the Shapiro filter (e.g., Showman et al., 2009; Lewis et al., 2010). Hence, the power-two ($\mathfrak{n} = 2$ in equation (4.5)) Shapiro filter is used here to control oscillations near the grid-scale. Note that the above mentioned studies have used $\mathfrak{n} = 4$ Shapiro filter (Showman, private communication). Recall that the strength of the filter is controlled by $\tau_{\rm shap}$, for a given Δt and $\mathfrak{n}$. In this work, the value of $\tau_{\rm shap}$ is chosen so that $\Delta t/\tau_{\rm shap} = 1/6$ for all resolutions. By experimenting with different values, this value has been found to give flow and temperature structures that are qualitatively in good agreement with the the pseudospectral cores across different resolutions: in general, simulations with $\Delta t/\tau_{\rm shap} = 1/12$ are found to be under-dissipated and $\Delta t/\tau_{\rm shap} = 1/3$ to be over-dissipated with the model in its default setting.

As discussed in section 4.1, past simulations of diabatically-forced, hot-Jupiters using different models produce different results—even for fairly similar (but not identical) setup. In many cases, the results are qualitatively different, and the origin of the difference is not obvious. Quite often, this is because all the details of the models, model parameters, and model setup are not reported in the literature—and sometimes not even described in the original model documentation. Hence, truly "clean", unambiguous comparisons have not been possible thus far. In TC3, the physical setup in all the model simulations is identical. The aim here is to identify whether variation in recent model results is merely due to the differences in physical setup, or whether variation is also attributed to differences in the numerical formulation of a model (e.g., dissipation scheme, spatial grid, discretization method, etc.).

TC3 Results

Figure 4.9 shows longitude-latitude maps of the temperature (T) field, with horizontal wind vectors ($\mathbf{v}$) overlaid, from simulations with different model cores. The resolutions for the pseudospectral cores and the MITgcm in LL and CS grids are: T85L20, G128L20, and C64L20, respectively. The instantaneous fields at the $p \approx$ 475 hPa level at $t = (5\,\tau,\, 20\,\tau,\, 100\,\tau)$ are shown. The figure illustrates the main result of this comparison: when subject to strong "hot-Jupiter-like" forcing, differ-

ent model cores produce solutions which are visually different among them. This is caused by spatiotemporal variability in the computed fields and renders specific predictions, such as the precise location of hot and cold regions, difficult (see right column of Figure 4.9).

Qualitatively, there *are* some notable common features. For example, most models produce a "quadrupolar-flow" structure, with two large cyclonic and anti-cyclonic vortex-pairs straddling the equator. The flow in all the simulations is time variable with vortices appearing nearly stationary at times or moving longitudinally eastward or westward at other times, disappearing and reforming on a time scale of 5–7 τ. The temperature in all cases is strongly linked to the flow and varies on corresponding timescales. Consequently, the minimum-to-maximum temperature ranges vary from $\sim$600 K to $\sim$200 K, at the shown pressure level (e.g., compare middle and right panel in the third row of Figure 4.9). Despite the qualitative similarity, model results are quantitatively very different and can diverge more markedly when integrated for longer durations than shown in the figure.

At the beginning, during the first few planetary rotations, the flow in all models resembles a linear, "Matsuno-Gill-type" solution (Matsuno, 1966; Gill, 1980). In the solution, westward-propagating Rossby waves and eastward-propagating Kelvin waves are generated as a response to the specified mode-1 zonal heating. At high pressure (lower altitude) levels, there is a convergent flow near the substellar point, accompanied by rising motion; concurrently, there is a divergent flow near the anti-stellar point, accompanied by sinking motion (not shown). At low pressure (higher altitude) levels, there is a divergent flow near the substellar point and a convergent flow near the antistellar point. In the classic Matsuno-Gill setup, strong linear (momentum and thermal) drags balance the forcing. However, in the absence of strong momentum drag, as in this test case, non-linear interactions quickly degrade the Matsuno-Gill-type solution, and the model solutions start to deviate strongly from the Matsuno-Gill solution—and, importantly, from each other. The latter is due to how different model cores handle adjustment, as discussed earlier.

At early times ($t < 10\,\tau$), all core solutions are still similar but a small phase difference is already clearly evident between BOB and PEQMOD (which are nearly identical to each other at this point) and the other model cores (see left column in Figure 4.9). At later times ($t \geq 10\,\tau$), all solutions start to visibly diverge from each other and significantly differ quantitatively. For example, the north-south flow symmetry is broken in CAM and PEQMOD simulations (at $t = 14\,\tau$) and in MITgcm in both LL and CS grids (at $t = 10\,\tau$). In contrast, the symmetry is not broken in BOB and IGCM cores even at $t = 100\,\tau$. It should be noted that in more

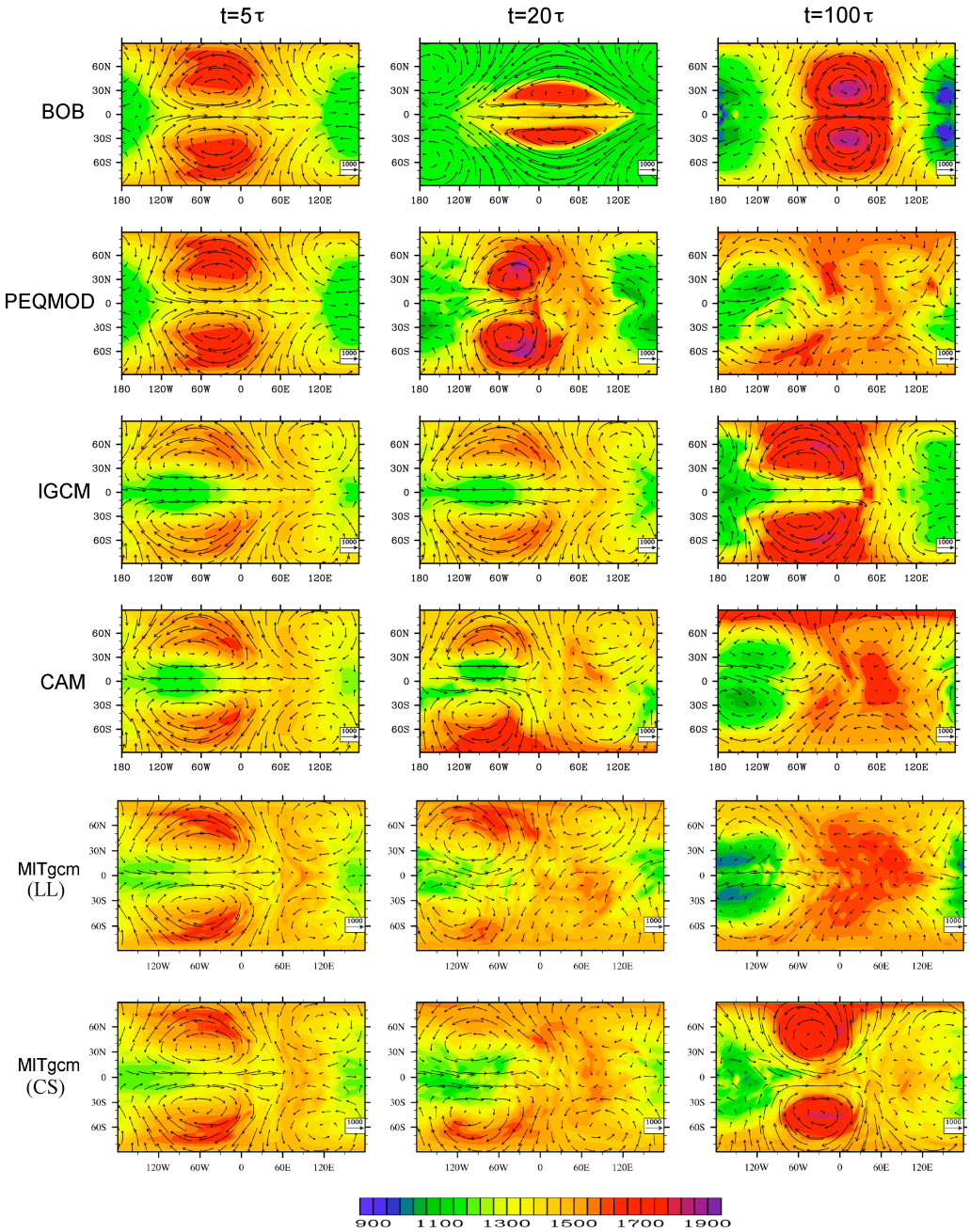

Figure 4.9: Temperature (color coded in K) with wind vectors overlaid, for the diabatic forcing test case (TC3) with different model cores, at three times at the 475 hPa level. Form left to right, the snapshots are taken at $t = (5\,\tau, 20\,\tau, 100\,\tau)$. The (top, second, third, fourth, fifth, bottom) row is, respectively, from a simulation with (BOB, PEQMOD, IGCM, CAM, MITgcm in LL grid, MITgcm in CS grid). The resolution for pseudospectral codes is T85L20 and for MITgcm in LL and CS grids is G128L20 and C64L20, respectively. The flow and temperature distributions are qualitatively similar (e.g., quadrupolar flow) but quantitatively different (e.g., time-variable).

realistic situations the T_e profile is unlikely to be exactly hemispherically-symmetric (the asymmetry could stem from e.g., libration or small but non-zero eccentricity) and the symmetry *should* be broken. However, here the objective is to compare the accuracy of the models; therefore imposing a hemispherically symmetric T_e profile is more appropriate and provides a more stringent test for the models.

It is important to understand that the temporal variability observed here is *not* due to large-scale baroclinic instability stemming from the location and thermal forcing of the lower boundary. Visual and quantitative check (i.e., of eddy production, wave propagation, and heat and momentum fluxes) has verified that large-scale baroclinic instability is not present in this setup and that similar variability is exhibited even with the lower boundary placed much deeper (e.g., 10 and 100 bars) with the forcing limited down to only 1 bar. However, small-scale waves are produced through the adjustment process.

The flow structure remains either quasi-symmetric about the equator throughout the integration (see panels for BOB and IGCM in Figure 4.9) or the equatorial flow symmetry is broken at an early time (see panels for PEQMOD, CAM, and MITgcm in Figure 4.9). Detailed analyses of the computed fields show that the symmetry breaking is associated with emergence of a large equatorial Rossby wave at $t \approx 10\,\tau$, which is not as prominent in simulations with BOB or IGCM. The north-south symmetry in these simulations is not an artifact of a short integration time. It remains even at the end of a 2000τ simulation with BOB at T21L20 resolution (not shown). However, when the simulation with BOB is initialized with a small, random perturbation in the flow, the north-south symmetry does break at an early time and the flow and temperature evolution closely match simulations with PEQMOD. A likely explanation of the equatorial symmetry breaking is errors introduced by insufficient precision. By repeating this test case with PEQMOD at single, double and quadruple precisions, it is found that the onset time of equatorial symmetry breaking roughly doubles every time the precision is doubled.

Since the flow and temperature structure is strongly time variable in all the simulations, snapshots in time may give an incomplete—possibly even misleading—picture, since large differences in Figure 4.9 could simply be due to "phasing" (simple translation of the flow structure in time). To quantify variability and the behaviour with resolution, a time series of global average temperature is shown in Figure 4.10. The first thing to note is that essentially all the simulations are equilibrated in temperature: there are no secular growth or decay—hence, the difference in the fields is not due to failure to achieve "statistical equilibration". The qualitative evolution of global average temperature is similar in all models after the initial adjustment pe-

riod (i.e., for $t \geq 20\,\tau$), with the globally averaged temperature exhibiting periodic fluctuations of amplitude ∼10–20 K on a timescale of 5–7 τ (due to the vortex life cycle discussed above) in all the models. The exception to this is the simulations with IGCM: in these simulations, temperature fluctuates with a clear 10–50 τ period, depending on the resolution, and the amplitude of the fluctuations is much larger (~ 40 K) than in simulations with other cores. Note, the temperature fluctuations in simulations with CAM are also large at early times ($t \leq 20\,\tau$) but subsequently reduce, as discussed more in detail below.

Remarkably, the behaviour of global average temperature in BOB and PEQMOD is nearly identical, up to the point when the equatorial symmetry is broken in PEQMOD (e.g., $t \sim 30\,\tau$ in T21L20 resolution simulation). The clear periodicity present in the T21L20 and T42L20 BOB simulations disappears with increasing horizontal resolution (cf. red curve with green curve in top left panel of Figure 4.10, for example). Note that, in all simulations, the global average temperature decreases by 10–20 K from the initial value of 1400K. The initial dip is related to the short timescale on which the large T_e gradient is relaxed. For example, if the relaxation time is increased by 1 τ everywhere in a BOB core simulation, the global average temperature decreases by less than 1 K (not shown). The adjustment demanded by the fast relaxation produces violent flows. Such a representation of thermal forcing is not physical—certainly its resulting flow is difficult to model accurately in current GCMs. Nevertheless, since primary concern here is to compare the model cores, the representation is used here—for heuristic purposes.

Large amplitude fluctuations in the global average temperatures of IGCM and CAM simulations (particularly at early times in the latter) are associated with atmospheric thickness variations, caused by fluctuations in the surface pressure (recall that both cores use the σ-coordinate). This "flapping" of the bottom boundary is absent in p-coordinate models with rigid top and bottom boundaries, in which surface pressure remains constant throughout the integration. By removing the bottom boundary away from the forcing region, it has been found that the atmospheric thickness variation is greatly reduced in σ-coordinate models. Interestingly, as already mentioned, the fluctuations in the CAM core subside at $t \gtrsim 30\,\tau$. This is likely due to the η-coordinate employed by the core.

Note that the flapping is not necessarily unphysical, and could be used to represent a physical phenomena at the 1 bar level if a hot-Jupiter happens to have a natural, non-rigid boundary (e.g., jump in stratification, composition etc.) there.[22] It is also

[22]Such a setup is common in Earth's middle atmosphere and climate studies to represent thermal and mechanical forcing.

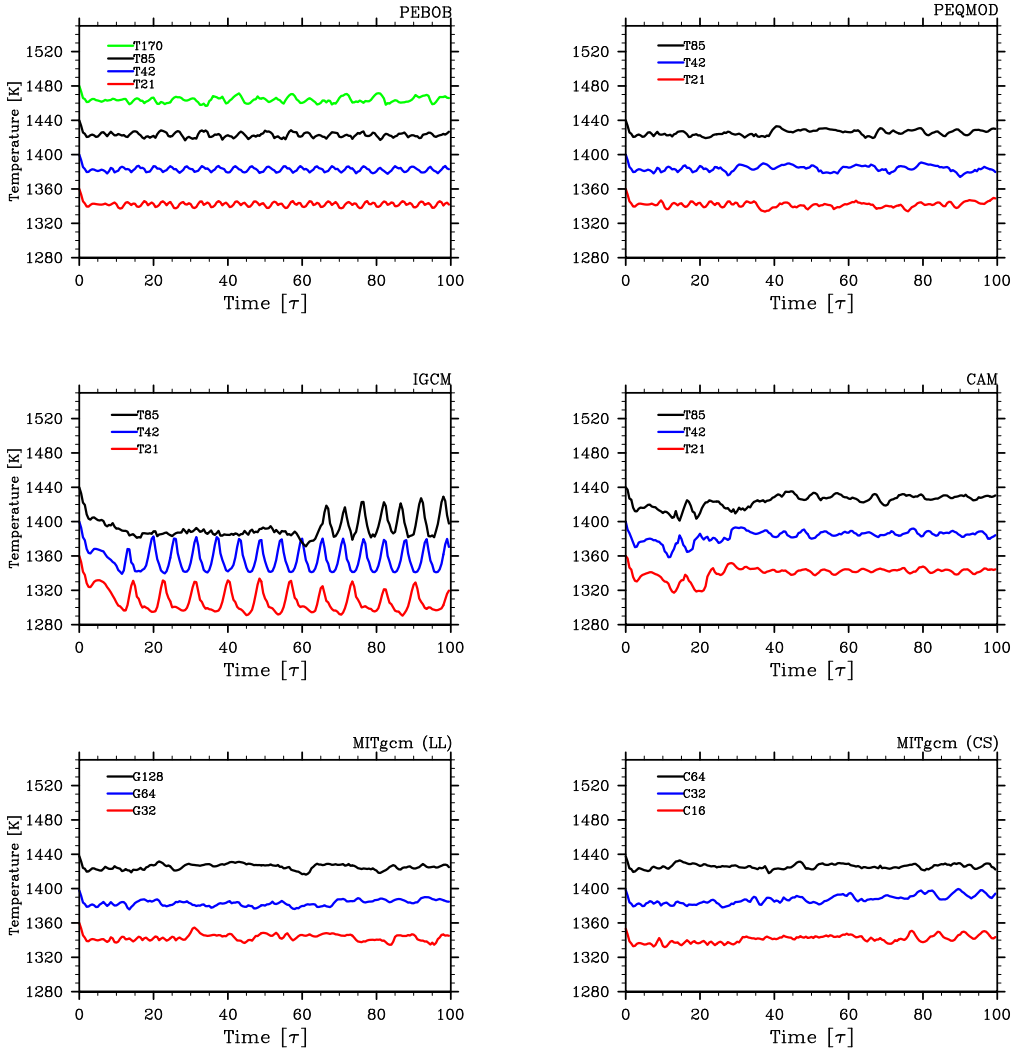

Figure 4.10: Time series of globally averaged temperature for the diabatic test case with different model cores at various horizontal resolutions. The top left panel is from simulations with BOB, the top right panel is from simulations with PEQMOD, the middle left panel is from simulations with IGCM, the middle right panel is from simulations with CAM, the bottom left panel is from simulations with MITgcm in LL grid and the bottom right panel is from simulations with MITgcm in CS grid. The curves have been offset from each other by 40K, with the temperature of the blue color having the correct scale. The panels show that all the simulations are equilibrated in temperature. They also show that qualitatively similar behaviour in all the model simulations is not due to simple "phasing" of the flow/temperature structures. For IGCM, there is a large, non-secular oscillatory behaviour.

possible to specify a free-surface boundary condition at the bottom in MITgcm. The specification replaces the condition, $\omega = 0$ at $p = p_{\rm r}$, with $\omega = {\rm D}p_s/{\rm D}t$ at $p = p_{\rm r}$. With this boundary condition an additional prognostic equation for free surface pressure anomaly, called $\hat{\eta}$ in MITgcm (not to be confused with the η associated with the CAM), is solved. However, given the strong forcing and violent flow that ensues, MITgcm in the default setting crashes with the boundary at 1 bar with the free-surface condition. This is due to the large undulation of the pressure surface, which can cause two or more pressure surfaces to intersect somewhere in the domain. Loss of single-valuedness such as this is not an issue in σ-coordinate model cores because surface pressure is not a coordinate surface.

It is clear from Figure 4.10 that the cores are not numerically or visually converged, for $t > 10\tau$. This is not surprising, especially for the pseudospectral cores, given that the superdissipation coefficient is decreased with increasing horizontal resolution. However, qualitative convergence in TC3 appears to be achieved at the lowest horizontal resolutions (i.e., T21, G32 and C16) in all the cores: at least, the qualitative behaviour of flow and temperature appears to be the same at all resolutions. Given the behaviour observed in TC2, however, it cannot completely be ruled out that this conclusion may need to be revised when simulations of substantially higher resolution (than those in this work) are carried out. In any case, the conclusion depends on the field or quantity considered, as shall be show later. For example, qualitative convergence is not achieved when the vorticity field is considered instead (Thrastarson and Cho, 2011).

In TC3, the total global energy is not conserved because $\dot{q}/c_p \neq 0$ in the thermodynamic equation. However, in the absence of momentum forcing, the global integral of absolute angular momentum is still conserved. While the angular momentum conservation has been almost exact in TC1 and TC2 (up to ~ 0.02 percent), in this test case the conservation property is strongly violated in some model cores—particularly in their default configurations. This is shown in Figure 4.11, which presents time series of globally integrated absolute angular momentum (equation (4.8)). Each time series is normalized by its initial value of 1.77×10^{32} kg m^2 s^{-1}.

As can be seen from Figure 4.11, only BOB and PEQMOD conserve angular momentum exactly—*and they do so at all resolutions* (see top row of the figure). The conservation property of CAM and MITgcm in LL grid becomes better with increasing resolution. The periodic "spinning" and "de-spinning" of the atmosphere in IGCM by $\sim$10 percent (see middle left panel of Figure 4.11) is caused by variation in the atmospheric mass, due to large surface pressure variations. Clearly, angular momentum is poorly conserved in the simulations with the MITgcm in the CS grid,

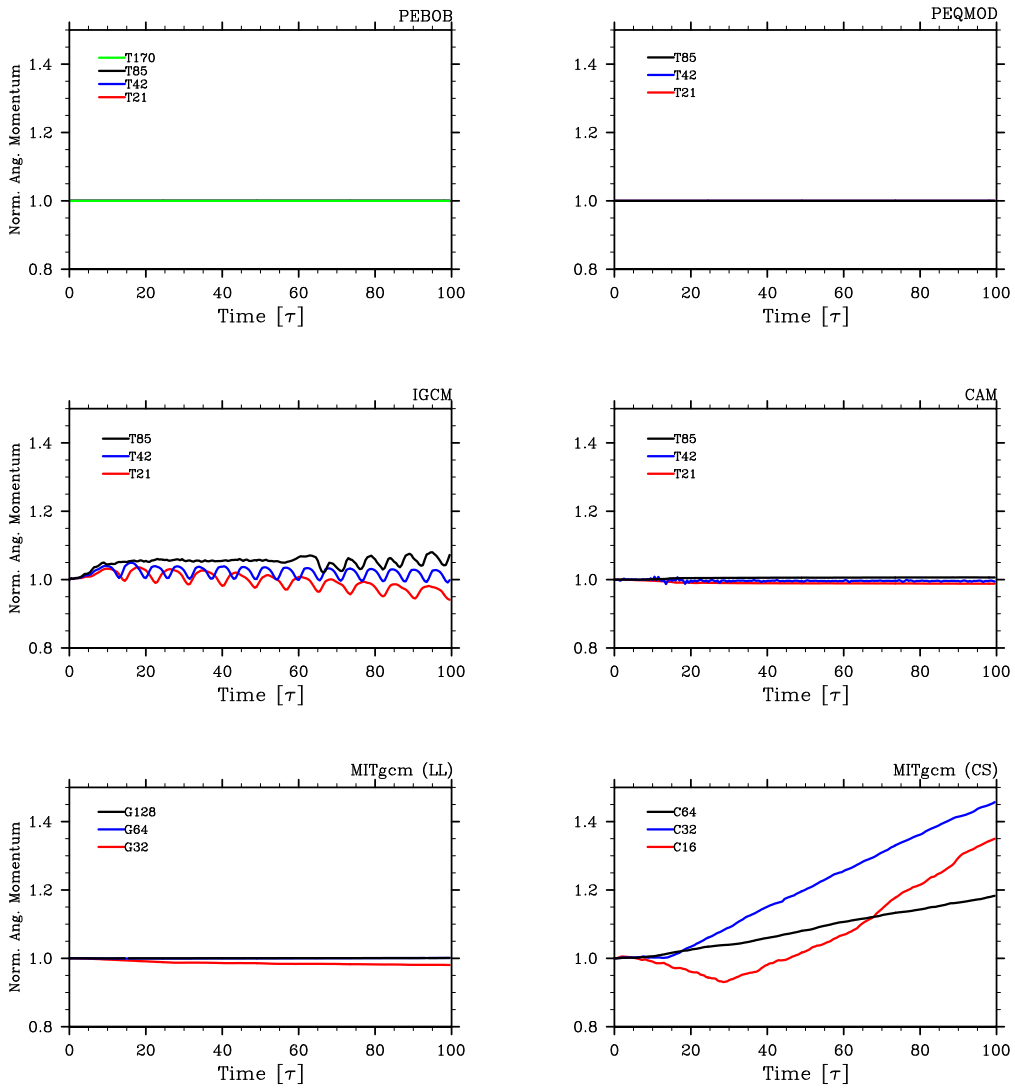

Figure 4.11: Time series of global angular momentum (normalized by initial value of 1.77×10^{32} kg m^2 s^{-1}) for the diabatic test case with different model cores at various horizontal resolutions. The panel placements are as in Figure 4.10 (i.e., BOB core at upper left, etc.). The total absolute angular momentum is exactly conserved at all resolutions in PEBOB and PEQMOD and at high resolutions in CAM and in MITgcm in LL grid. It is somewhat poorly conserved in IGCM and not at all in MITgcm in CS grid.

especially at C32 resolution: the total angular momentum increases by more than 45 percent at the end of the $100\,\tau$ simulation. The conservation is actually better at the lower, C16 resolution, in terms of the time series at $t = 100\,\tau$. When these simulations are integrated for longer than $100\,\tau$, the runaway angular momentum is associated with a zonally-averaged zonal flow which is *strongly* superrotating[23] over a broad range of latitudes. For example, the transition to such a superrotating state occurs by $t \approx 200\,\tau$ in C16 and C32 simulations.

The angular momentum runaway behaviour in the MITgcm in CS grid simulations is caused by an instability associated with the Shapiro filter used in the simulations. When the strength of the filter is doubled (i.e., $\Delta t/\tau_{\text{shap}} = 1/3$), angular momentum decreases over time leading to unphysical *subrotation* (i.e., westward flow of the atmosphere everywhere). This occurs by $t = 100\,\tau$. When the strength is halved (i.e., $\Delta t/\tau_{\text{shap}} = 1/12$), not enough dissipation is supplied to the flow and the runaway still occurs and is more severe at an earlier time. Indeed, through an extensive study, it is found that a suitable strength of the Shapiro filter (which would conserve angular momentum exactly on the cubed sphere) does not exist for TC3. Note that this behaviour is not just limited to the $\mathfrak{n} = 2$ Shapiro filter. It occurs for higher power filters (e.g., $\mathfrak{n} = 4$ and $\mathfrak{n} = 6$) as well. Note also that, for this test case, the MITgcm in CS grid at C16 resolution (in the default setting) always crashes with $\mathfrak{n} = 8$ Shapiro filter, independent of $\Delta t/\tau_{\text{shap}}$.

For completeness, TC3 with the MITgcm core in both LL and CS grids (at G32 and C16 resolutions, respectively) with ordinary, Laplacian dissipation (i.e., ∇^2 in MITgcm and $\mathfrak{p} = 1$ in equations (2.20) and (4.2)) is also performed. The damping time in these simulations is chosen to be the same as in the simulations performed with the pseudospectral cores. The use of ordinary dissipation considerably improves the angular momentum conservation of MITgcm in CS grid (a monotonic increase of only $\sim$0.5 percent at $t = 100\,\tau$). However, there is now a significant ($\sim$40 percent) loss of angular momentum in the LL grid simulation using the same dissipation. In other words, the CS grid simulation is severely overdissipated compared to the LL grid simulation. From this it is concluded that the dissipation is compensating the runaway in the CS grid. Therefore, the grid itself appears to be a significant source of the runaway behaviour, with the Shapiro filter amplifying the behaviour—at least in the model's default CS grid configuration.

As already discussed, the total energy with the applied forcing in TC3 is not expected to be conserved by any of the models. However, as shown below, the

[23] i.e., $\overline{u} > (\Omega\, R_{\text{p}}\, \sin^2\phi/\cos\phi)$, where $\overline{u} = \overline{u}(\phi, s, t)$ is the zonally-averaged wind. Here, "strongly" means $\overline{u}$ close to, or even exceeding, 3000 m s^{-1}.

inclusion of Newtonian relaxation does not alter the total atmospheric energy budget by more than 5 percent. Figure 4.12 shows a global integral of total energy as a function of time, normalized by the initial value of 2.2×10^{28} J. In all but the IGCM and CAM simulations the total energy steadily increases at the beginning by $\sim$2.5 percent. Thereafter, BOB maintains the total energy at a nearly constant level (see top left panel of the figure). With the other cores, the total energy fluctuates by up to 5 percent, with largest fluctuations observed in IGCM simulations; at $t = 100\,\tau$ the total energy for IGCM increases by 2–3 percent, on the average. The energy in the MITgcm simulations in CS grid also increases noticeably over time (particularly in the lower resolution simulations), consistent with the runaway angular momentum and transition to a superrotating state for $t \gtrsim 200\,\tau$, discussed above. The total energy for CAM shows a slight increases, by $\sim$1 percent, over the initial value, after settling from large initial fluctuations; but, PEQMOD and MITgcm LL grid simulations show the energy decrease slightly by $\sim$1.5 percent, after the initial rise of $\sim$2.5 percent mentioned above.

In the process of thoroughly verifying these results, two additional advection schemes for the vector invariant momentum equation have been discovered for the MITgcm CS grid. Of the two undocumented schemes, one explicitly conserves energy (Sadourny, 1975) and the other conserves energy *and* enstrophy (Burridge and Haseler, 1977). Note that the angular momentum conservation is noticeably improved in TC3, particularly with the energy conserving scheme. For example, with the use of the energy conserving scheme the angular momentum in TC3 *decreases* by 33 percent at C16 resolution, by 6 percent at C32 resolution and by 2 percent at C64 resolution at the end of the $100\,\tau$ simulation. Because these decreases are monotonic with time, longer time integrations would result in a more significant violation of angular momentum conservation in TC3. Also note that the two undocumented schemes do not improve the performance in TC1 and TC2, compared to the default enstrophy conserving scheme.

As a closing remark, somewhat disconcertingly, the model cores appear to be perceptibly sensitive to small, perhaps uncontrollable, changes in input parameters when subject to the strong forcing, as in TC3. It has already been shown that the simulation results are different 1) between different model cores at the same or comparable resolution and 2) between different resolutions with the same model core. However, the simulation results can also differ with the same core at the same resolution. For example, simulations with PEQMOD at T42L20 resolution with single, double and quadruple precision produce quantitatively unconverged results (although they may be qualitatively converged). In addition to the onset

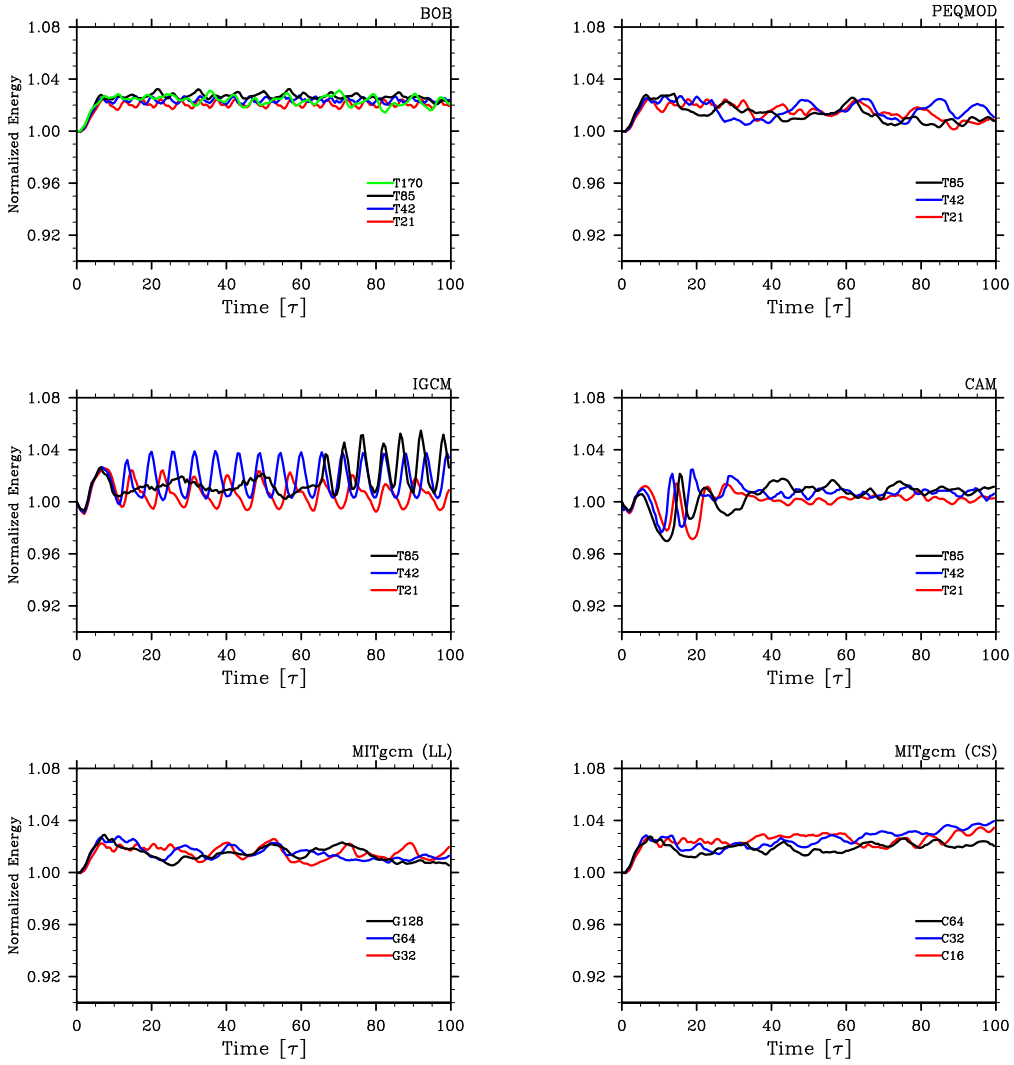

Figure 4.12: Time series of global total energy (normalized by initial value of 2.2×10^{28} J) for test case 3 with different model cores at varying horizontal resolutions. The panel placements are as in Figure 4.10 (i.e., BOB core at upper left, etc.). All the simulations appear to be well or roughly equilibrated, with the possible exception of the lower resolution simulations with the MITgcm core in CS grid. The total energy fluctuations are correlated with the temperature fluctuations (cf. Figure 4.10).

of the north-south symmetry breaking, a noticeable phase difference between the solutions are seen. Such phase differences are significant for predicting precise flow and temperature patterns. Moreover, the phase differences occurred in a model core with identical setup and precision when the core was simply compiled with a different compiler or the same compiler on a different computing platform. It is important to note that the above issues did not play significant roles in TC1 and TC2 because "violent" (i.e., strongly unbalanced) flows are not involved. Given this, it is not expected that the results presented in TC3 are *exactly* reproducible when a different compiler is used and/or on different platforms: slight phase variations are nominally expected.

4.4 Summary and Discussion

Intercomparison and benchmarking of GCMs, and in particular their cores, are necessary for assessing the efficacy of models and for understanding the physical properties of atmospheres. While such testing is common practice in Earth and some Solar System planet studies, only three tests (e.g., Rauscher and Menou, 2010; Heng et al., 2011; Bending et al., 2013) have been attempted for hot-Jupiter GCMs. Here, five GCMs currently used in the hot-Jupiter studies are subjected to three benchmark tests. The tested GCMs are: BOB, PEQMOD, IGCM, CAM, and MITgcm. These models employ a range of numerical algorithms for the spatial discretization and explicit viscosity: respectively, pseudospectral with pseudospectral filtering (BOB, PEQMOD, IGCM, and CAM) and finite volume with differenced, pole (zonal), and Shapiro filtering (MITgcm). All the GCMs solve the dry, hydrostatic primitive equations and are subjected to identical tests. From least to most stringent, these tests are: 1) the steady-state test case (TC1); 2) the baroclinic wave test case (TC2); and, 3) the diabatic test case (TC3). In all three test cases, all of the models are tested at varying horizontal resolutions to assess numerical convergence. Both inter- and intra-comparisons are carried out.

TC1 assesses how a model is able to maintain a balanced initial condition in the form of a midlatitude eastward jet with no applied dissipation, before gravity waves and numerical noise degrade the jet. With the exception of MITgcm employing the CS grid, all models maintain the true, steady-state solution very well throughout the time of integration ($t = 20\,\tau$). The special corners in the CS mesh quickly degrade the balanced state; and, in the absence of any dissipation, the imbalance causes the

model simulations to crash at early time when using the default advection scheme[24]: for example, the simulation at C64 resolution crashes at $t = 4.5\,\tau$. Of all the models, BOB and PEQMOD maintain the true solution the best (see, e.g., Figure 4.4).

In TC2, a temperature perturbation applied to the steady-state initial condition of TC1 triggers a non-linear evolution of a baroclinic wave. The emergence of sharp fronts from baroclinic instability necessitates the use of flow viscosity, unlike in TC1. Ordinary Laplacian (i.e., ∇^2 in MITgcm and $\mathfrak{p} = 1$ in equations (2.20) and (4.2)) dissipation is chosen. While all model simulations permit baroclinic instability, only pseudospectral ones appear to be visually converged, and this occurs at a horizontal resolution of T85 (corresponding to 85 total and zonal modes each in the spherical harmonic expansion—a resolution above most current extrasolar planet simulations). Solutions with MITgcm are not converged at the highest resolutions investigated here (i.e., G128 and C64). While the most unstable mode of the unstable jet is approximately 3–4 (see Figure 4.5 and Figure 4.6), the presence of the special corner points on the cubed-sphere grid produces an unstable wave field with mode greater than 3–4 (see Figure 4.6 bottom right panel). This behaviour is significant for model predictions and observational confirmations.

While the first two test cases are adiabatic, the third case is diabatic. For some regions of the planet atmosphere, diabatic forcing is necessary. In this work, as in most hot-Jupiter studies thus far, a simple Newtonian relaxation parameterization is applied to represent the heating and cooling in the modeled atmosphere. Here, the atmosphere is "spun-up" from an initial isothermal condition at rest. Note that, although many past studies have employed a similar setup, there is no general agreement on the robustness of the flow and temperature distributions produced by the simulations. By employing an identical setup in all the models, the aim of TC3 has been to clearly assess whether (and how much) the non-robustness of the results is intrinsic to the numerical model employed. It is again emphasized that without such tests, the simulation community—indeed the extrasolar planet community as a whole—would not have a baseline for any consensus. For this reason, a biharmonic (∇^4) superviscosity in pseudospectral models and a power-two ($\mathfrak{n} = 2$) Shapiro filter in MITgcm is employed so that the comparisons are equatable among the models tested in this study and shed some light on the results of past studies. [25]

Unlike in the first two test cases, the extreme forcing condition of the third test

[24] Note that the steady-state simulations with energy and energy *and* enstrophy conserving schemes do not crash before $t = 20\,\tau$. However, the physical space fields are inundated with grid-scale noise at early time and the simulations are clearly unbalanced.

[25] The reader is reminded that here the MITgcm in this default CS grid configuration possesses the least amount of angular momentum runaway at $t = 100\,\tau$ with $\mathfrak{n} = 2$.

case produces a range of behaviours in the model simulations. While there are some qualitatively similar features (e.g., a time-variable quadrupole flow structure), the location and magnitude of the hottest and coldest regions are not same in the model simulations. In large part, this is due to significant phase differences in the computed fields. Moreover, apart from BOB and IGCM, all models break the flow symmetry about the equator relatively early on, before $t = 100\,\tau$ (see Figure 4.9). This behaviour may be somewhat surprising as the forcing is north-south symmetric and no initial noise is present to break the symmetry, but machine precision or coding inexactitude eventually break the symmetry in all the cores tested.

Throughout this work a careful attention was paid to the conservation properties of the numerical models. In TC1 and TC2, the angular momentum and total energy conservations are well fulfilled by all the models. In TC3, however, it was found that—apart from BOB and PEQMOD—no other model conserves angular momentum exactly. The MITgcm in CS grid with Shapiro filter perform the poorest in this case, with the total absolute angular momentum increasing by as much as 45 percent at the end of the integration ($t = 100\,\tau$). As pointed out in Thrastarson and Cho (2011) and in Chapter 3, the normally "relatively harmless" small non-conservation in Earth-like conditions, for which the GCMs have been constructed and tested, could be exacerbated in the hot-Jupiter condition. This is because of the exacting requirements the condition places on the numerics. Such model behaviours should be carefully taken into account, when performing hot-Jupiter simulations. This point is emphasized in this work because runaway (or decaying) angular momentum is not necessarily apparent from looking at the flow pattern alone (see Figure 4.9 bottom row). Long-time integration of such a simulation leads to an atmosphere that superrotates in a manner similar to those reported in previous studies.

GCMs are complex. Getting them to run properly and verifying their results is not trivial. Trade-offs between accuracy, speed and algorithmic/coding simplicity are always made; and, even when such things are well-understood theoretically, the actual behaviour of the model is not always "stable" or uniform across problems. This then also raises the complexity of interpreting the results. In this work, an endeavour to fairly assess the performance of a number of GCMs—covering a good cross-section of algorithms, grids and treatment of explicit viscosity—has been carried out. For the most part, the tested models behave well and similarly to each other, but with some unexpected results. Although the simulations have been extensively checked here and despite the best effort to provide all the details of the simulations, it is still possible—especially given some of the findings presented in TC3—that other studies may obtain different results.

Finally, the results presented in TC3 suggest that when subject to the typical "hot-Jupiter-like" zonally asymmetric thermal forcing all the codes robustly produce equatorial superrotation — at least when initialized from an isothermal rest state. Identification of the exact dynamical mechanism producing such superrotating jet on a tidally-synchronized hot-Jupiter most definitely warrants further study. Given that the generation of equatorial superrotation involves local angular momentum transfer by waves and eddies, isolating and quantifying such mechanism in current models of hot-Jupiters is made difficult due to: 1) the violation of exact global axial angular momentum conservation in all but two models, and 2) the high horizontal resolution requirements for accurate wave-mean flow interaction representation (Thrastarson & Cho, in prep). Thus, before attempting to identify mechanisms responsible for equatorial superrotation on tidally-synchronized hot-Jupiters, it is fruitful to investigate generation of equatorial superrotation in a well-studied parameter regime of the Earth. Therefore, transition to superrotation in Earth-like planet atmospheres, subject to zonally-symmetric thermal forcing, is investigated in the next chapter.

Appendix 4.A Tables of Values for Test Cases

Table 4.1: Table of vertical and horizontal grid resolutions as well as other parameters needed for reproduction of steady-state case with pseudospectral cores. Note, PEQMOD has an additional equatorial latitude point (i.e., T21 pseudospectral resolution corresponds to 33×64 grid points, T42 to 65×128 grid points etc.). BOB only has been integrated at resolution T170L20.

Horizontal Resolution	Vertical Resolution	Gaussian Grid (lon $\times$ lat)	Timestep (Δt) [s]	Hyperdissipation	Robert-Asselin Coefficient (ϵ)
T21	L20	64×32	120	No	0.001
T42	L20	128×64	60	No	0.001
T85	L20	256×128	30	No	0.001
T170	L20	512×256	15	No	0.001

Table 4.2: As in Table 4.1, but for MITgcm in longitude-latitude (LL) grid. Note, the computational grid size below should not be compared directly with the Gaussian grid size in Table 4.1, as the pseudospectral evolves the fields in spectral space: the Gaussian grid is used only to evaluate the non-linear products and de-alias the fields.

Horizontal Resolution	Vertical Resolution	Computational Grid (lon $\times$ lat)	Timestep (Δt) [s]	Harmonic Dissipation	Zonal (FFT) Filter	Shapiro Filter
G32	L20	64×32	120	No	Yes	No
G64	L20	128×64	60	No	Yes	No
G128	L20	256×128	30	No	Yes	No

Table 4.3: Same as Table 4.1, but for MITgcm in cubed-sphere (CS) grid. N.B., the C16 and C64 CS grids have been generated by us with MATLAB routines provided by MITgcm support; but, the MATLAB generated C32 grid comes included with the MITgcm.

Horizontal Resolution	Vertical Resolution	Computational Grid (irregular)	Timestep (Δt) [s]	Harmonic Dissipation	Zonal (FFT) Filter	Shapiro Filter
C16	L20	$6 \times 16 \times 16$	120	No	No	No
C32	L20	$6 \times 32 \times 32$	60	No	No	No
C64	L20	$6 \times 64 \times 64$	30	No	No	No

Table 4.4: Table of vertical and horizontal grid resolutions as well as other parameters needed for reproduction of baroclinic wave test case with pseudospectral cores. Note, as above, PEQMOD has an additional equatorial latitude point (i.e., T21 pseudospectral resolution corresponds to 33×64 grid points, T42 to 65×128 grid points etc.). Also, note, only BOB has been integrated at resolution T170L20.

Horizontal Resolution	Vertical Resolution	Guassian Grid (lon $\times$ lat)	Timestep (Δt) [s]	Hyperdissipation	Dissipation Order ($\mathfrak{p}$)	Dissipation Coefficient (ν_2) [m^2 s^{-1}]	Robert-Asselin Coefficient (ϵ)
T21	L20	64×32	120	Yes	1	2×10^7	0.001
T42	L20	128×64	60	Yes	1	2×10^7	0.001
T85	L20	256×128	30	Yes	1	2×10^7	0.001
T170	L20	512×256	15	Yes	1	2×10^7	0.001

Table 4.5: Same as Table 4.4, but for MITgcm in LL grid.

Horizontal Resolution	Vertical Resolution	Computational Grid (lon $\times$ lat)	Timestep (Δt) [s]	Harmonic Dissipation	Dissipation Coefficient (ν_2) [m^2 s^{-1}]	Zonal (FFT) Filter	Shapiro Filter
G32	L20	64×32	120	Yes	2×10^7	Yes	No
G64	L20	128×64	60	Yes	2×10^7	Yes	No
G128	L20	256×128	30	Yes	2×10^7	Yes	No

Table 4.6: Same as Table 4.4 but for MITgcm in cubed-sphere grid.

Horizontal Resolution	Vertical Resolution	Computational Grid (irregular)	Timestep (Δt) [s]	Harmonic Dissipation	Dissipation Coefficient (ν_2) [m^2 s^{-1}]	Zonal (FFT) Filter	Shapiro Filter
C16	L20	$6 \times 16 \times 16$	120	Yes	2×10^7	No	No
C32	L20	$6 \times 32 \times 32$	60	Yes	2×10^7	No	No
C64	L20	$6 \times 64 \times 64$	30	Yes	2×10^7	No	No

Table 4.7: Table of vertical and horizontal grid resolutions as well as other parameters needed for reproduction of diabatic forcing test case with pseudospectral cores. Note, as above, PEQMOD has an additional equatorial latitude point (i.e., T21 pseudospectral resolution corresponds to 33×64 grid points, T42 to 65×128 grid points etc.). Here also, only BOB has been integrated at resolution T170L20.

Horizontal Resolution	Vertical Resolution	Gaussian Grid (lon × lat)	Timestep (Δt) [s]	Hyperdissipation	Dissipation Order ($\mathfrak{p}$)	Dissipation Coefficient ν_4 [m^4 s^{-1}]	Robert-Asselin Coefficient (ϵ)
T21	L20	64×32	240	Yes	2	1×10^{23}	0.01
T42	L20	128×64	120	Yes	2	5×10^{22}	0.01
T85	L20	256×128	60	Yes	2	1×10^{22}	0.01
T170	L20	512×256	30	Yes	2	5×10^{21}	0.01

Table 4.8: Same as Table 4.7 but for MITgcm in LL grid.

Horizontal Resolution	Vertical Resolution	Computational Grid (lon × lat)	Timestep (Δt) [s]	Harmonic Dissipation	Zonal (FFT) Filter	Shapiro Filter	Filter Power ($\mathfrak{n}$)	Filter Parameter (τ_{shap}) [s]
G32	L20	64×32	240	No	Yes	Yes	2	1440
G64	L20	128×64	120	No	Yes	Yes	2	720
G128	L20	256×128	60	No	Yes	Yes	2	360

Table 4.9: Same as Table 4.7 but for MITgcm in CS grid.

Horizontal Resolution	Vertical Resolution	Computational Grid (irregular)	Timestep (Δt) [s]	Harmonic Dissipation	Zonal (FFT) Filter	Shapiro Filter	Filter Power ($\mathfrak{n}$)	Filter Parameter (τ_{shap}) [s]
C16	L20	$6 \times 16 \times 16$	240	No	No	Yes	2	1440
C32	L20	$6 \times 32 \times 32$	120	No	No	Yes	2	720
C64	L20	$6 \times 64 \times 64$	60	No	No	Yes	2	360

5 Superrotation in Held & Suarez-like Flows With Weak Surface Temperature Gradient

Atmospheric superrotation in Earth-like planetary atmospheres is investigated under axisymmetric thermal forcing in a setup close to the classic, Held and Suarez (1994) setup. With the Held and Suarez setup, transition to equatorial superrotation occurs when the equator-to-pole surface equilibrium entropy gradient is weak. Two factors contribute to the transition in this situation: 1) reduction of breaking Rossby waves from the mid-latitude that decelerate the equatorial flow, and 2) presence of barotropic instability in the equatorial region that provides stirring to accelerate equatorial flow. The instability also excites Kelvin waves important for generation and maintenance of superrotation. In addition, the produced superrotation is weaker in simulations with high resolution or weak dissipation.

5.1 Introduction

Superrotation is an important phenomenon in atmospheric flows. It is defined as zonal-mean, zonal wind with axial angular momentum – $M(\phi)$, where ϕ is latitude – greater than the solid body angular momentum at the equator, $M_0 = M(0)$. Hence, a superrotating atmosphere has prograde (eastward) flow at the equator. For a "shallow" atmosphere, $M = R_\mathrm{p} \cos\phi (U + \Omega R_\mathrm{p} \cos\phi)$ and $M_0 = \Omega R_\mathrm{p}^2$, where R_p is planetary radius, U is zonal-mean zonal flow and Ω is planetary rotation rate. In the absence of sources and sinks, a zonally-symmetric mean meridional circulation conserves M such that $M \leq M_0$ at all latitudes. However, given a source which provides eddy angular momentum flux, for example, superrotation can be generated and maintained if the flux is directed up the meridional gradient of the mean angular momentum, $R_\mathrm{p}^{-1} \partial M / \partial \phi$ (Hide, 1969, and see also Read 1986).

Although transient superrotation is present in the present-day Earth's atmosphere

(e.g., the quasi-biennial oscillation), it is not superrotating in general. The current explanation for this is that Rossby waves generated by a baroclinically unstable subtropical jet propagate upwards, refract equatorward and break or saturate before reaching the equatorial region: in this process, because the waves deposit prograde momentum in the source region and retrograde momentum in the breaking/saturation region (e.g., Held and Hoskins, 1985), equatorial superrotation does not occur. On the other hand, superrotation does occur more robustly on other planets – and in idealized general circulation model (GCM) experiments. For example, in the latter, superrotation occurs under a variety of forcing conditions: zonally-*a*symmetric tropical heating (e.g., Suarez and Duffy, 1992; Saravanan, 1993; Hoskins et al., 1999) and zonally-symmetric heating with Ω or R_p smaller than those of the Earth (e.g., Williams, 1988, 2003; Mitchell and Vallis, 2010). In the zonally-symmetric case, the increase in the global scale Rossby number — effected by reducing Ω or R_p — results in weakening of the mid-latitude baroclinic instability and strengthening of the barotropic instability. In this case, Williams (2003) and Mitchell and Vallis (2010) attributed barotropic instability to be the mechanism for superrotation.

Williams (2003) has also shown that superrotation can occur on a zonally-symmetrically heated planet with Earth's Ω and R_p, when the center of maximum baroclinicity is shifted to a lower latitude than in the classic setup of Held and Suarez (1994) [hereafter HS]. In his study, the shift is effected by narrowing the meridional width of the radiative heating profile compared to that used in HS. There he proposes that barotropic instability (accompanying the baroclinic instability) at the equatorward flank of the subtropical jet provides the mechanism for producing superrotation. Williams (2006) extends this work by showing that high tropospheric static stability enhances superrotation. Recently, the barotropic instability mechanism has been challenged in Potter et al. (2014), who suggest thinking of equatorial jet dynamics independently from the higher-latitude eddy-driven jet dynamics. They propose that equatorial Kelvin wave-like disturbances drive and maintain superrotation in small Ω or R_p flows and in the setup of Williams (2003) just discussed. However, they do not identify the origin of the Kelvin waves.

The present study can be regarded as an extension of Williams (2003, 2006); Mitchell and Vallis (2010) and Potter et al. (2014). Here transition to superrotation is also investigated under zonally-symmetric thermal forcing in a model *with* Earth's Ω and R_p. However, it is shown in this study that superrotation also occurs with Earth's Ω and R_p if the equator-to-pole equilibrium temperature gradient near the surface (from 1000 hPa to 700 hPa) is weakened, compared to the gradient in the

HS setup. Further, it is shown that the magnitude of superrotation produced in this way is sensitive to numerical resolution and dissipation. Throughout this chapter, the reduced temperature gradient region is denoted as the "RTG" region. Such a region is not necessarily meant to address the present-day Earth; however, it may be relevant for "Earth-like" exoplanets, or past and future climates of the Earth, or other 'Earth-like' planets in the Solar and extrasolar systems. For example, such thermal forcing can be applicable to the runaway greenhouse state characterized by homogeneous surface temperatures (e.g., Leconte et al., 2013).

The overall plan of the chapter is as follows. In section 5.2 the setup used in this study is briefly discussed. In section 5.3 results from the model simulations with a RTG region are presented and compared with the classic HS-like simulations. This section also discusses in detail non-convergence of simulations when they are under-resolved or over-dissipated. Finally, conclusions are given in section 5.4.

5.2 Setup

Because the pseudospectral model BOB (see description in Chapter 2.3) was found to perform the best in the GCM intercomparison study of Chapter 4, the model is also used in this study. To control the grid-scale oscillations, a fourth-order hyperdissipation operator (i.e., $\mathfrak{p}$=4 in equation (2.20)), with constant ν_8, is applied to the prognostic variables: (relative) vorticity ζ, divergence δ and potential temperature θ. The Robert-Asselin filter (Robert, 1966; Asselin, 1972) with a small filter coefficient (0.02) is applied at each timestep.

The physical setup is essentially that of HS and Williams (2003) (his case *A*). A simple Newtonian relaxation scheme (as used in TC3 in Chapter 4) for the net heating,

$$\mathcal{Q} = -\frac{1}{\tau_{\rm th}}\Big(T - T_{\rm e}\Big), \tag{5.1}$$

is applied in the temperature tendency equation; here $\tau_{\rm th}$ is characteristic relaxation time, T is temperature and $T_{\rm e} = T_{\rm e}(\phi, p)$ is a specified equilibrium temperature distribution with p the pressure. The "boundary layer" is represented as a linear Rayleigh drag in the momentum equation:

$$\mathcal{D} \;=\; -\frac{\mathbf{v}}{\tau_{\rm R}}\;\max\!\left\{0,\,\frac{p-p_{\rm b}}{p_{\rm s}-p_{\rm b}}\right\}, \tag{5.2}$$

where $\mathbf{v}$ is flow on an isobaric surface, $\tau_{\rm R}$ is characteristic damping time and $p_{\rm b}$ and $p_{\rm s}$ are pressures at the top of the boundary layer (700 hPa) and at the bottom

surface (1000 hPa), respectively. The only important physical difference, relevant for superrotation, in this setup from that of HS is $T_{\rm e}(\phi, p)$ in some of the simulations. This is discussed more in detail below.

The physical parameters used in all the simulations presented in this study are listed in Tables 2.1 and 5.1. The simulations are started from an isothermal state of rest with a small amount of Gaussian white noise (10^{-7} s^{-1} standard deviation) introduced to the ζ field to break symmetry. Note that the results in this chapter are somewhat sensitive to the form of the initial perturbation. In particular, hemispherically symmetric perturbations such as those consisting of pure zonal wavenumbers, produce quantitatively different results. The sensitivity is discussed more in detail in section (5.3.3). The equilibrium temperature specified is

$$T_{\rm e}(p,\phi) = \max\left\{T_{\rm s}, \left[T_0 + \Delta T\, \cos^{\mathfrak{b}}\phi\, F(p) - \Delta\theta \log\left(\frac{p}{p_s}\right)\cos^2\phi\right]\left(\frac{p}{p_{\rm s}}\right)^{\kappa}\right\}. \quad (5.3)$$

Here $T_{\rm s}$ and T_0 are the stratospheric and upper tropospheric reference temperatures, respectively; ΔT is the equator-to-pole temperature difference; $\Delta\theta$ is the vertical potential temperature difference; and, $\kappa \equiv R/c_p = 2/7$.

In equation (5.3), $\mathfrak{b}$ and $F(p)$ control the meridional width of the equilibrium temperature and the equator-to-pole temperature gradient near the surface (i.e., in the RTG region), respectively. More precisely, the masking function F is defined

$$F(p) \;=\; \exp\left\{-\frac{(p/p_{\rm s})^{12}}{\gamma^2}\right\}, \quad (5.4)$$

where γ is a thickness parameter and is used to smoothly specify the vertical 'e-folding' extent of the RTG region. The masking function for varying γ values is shown in Figure 5.1. With $\mathfrak{b} = 4$ and $F(p) = 1$ (i.e., $\gamma \to \infty$), $T_{\rm e}$ reduces to the HS case, which roughly captures the statistical mean state of the Earth's troposphere. The resulting $T_{\rm e}$ distribution is shown in Figure 5.2a; here, the magnitude of the equator-to-pole equilibrium temperature gradient in the lower troposphere is $\sim\Delta T$. In section 5.3, simulations with $\gamma = 0.045$ are mainly discussed and $T_{\rm e}$ for this γ is shown in Figure 5.2b for comparison. Note that a surface temperature of 255 K is produced in this case. Such surface temperature is too cold to represent $T_{\rm e}$ of the runaway greenhouse regime as surface temperatures exceeding 340 K are required for runaway water evaporation (e.g., Kasting, 1988). However, this difference in surface temperatures is not pertinent to the results presented in this study: qualitatively the same results are obtained even with T_0 set to 350 K (provided the equatorial

Table 5.1: Parameter values used in the simulations: g is surface gravity; R_p is radius; Ω is rotation rate; $\mathcal{R}$ is gas constant; c_p is specific heat at constant pressure; p_s is surface pressure; p_b is the top of the boundary layer pressure; τ_th is radiative relaxation time; τ_R is Rayleigh drag time; T_s and T_0 are stratospheric and upper tropospheric reference temperatures, respectively; ΔT is equator-to-pole temperature difference; and, $\Delta\theta$ is vertical potential temperature difference.

Parameter	Value	Units
g	9.8	m s^{-2}
R_p	6.4×10^{6}	m
Ω	7.3×10^{-5}	s^{-1}
$\mathcal{R}$	287	J kg^{-1} K^{-1}
c_p	1004	J kg^{-1} K^{-1}
p_s	1000	hPa
p_b	700	hPa
τ_th	20	days
τ_R	1	day
T_s	200	K
T_0	255	K
ΔT	60	K
$\Delta\theta$	10	K

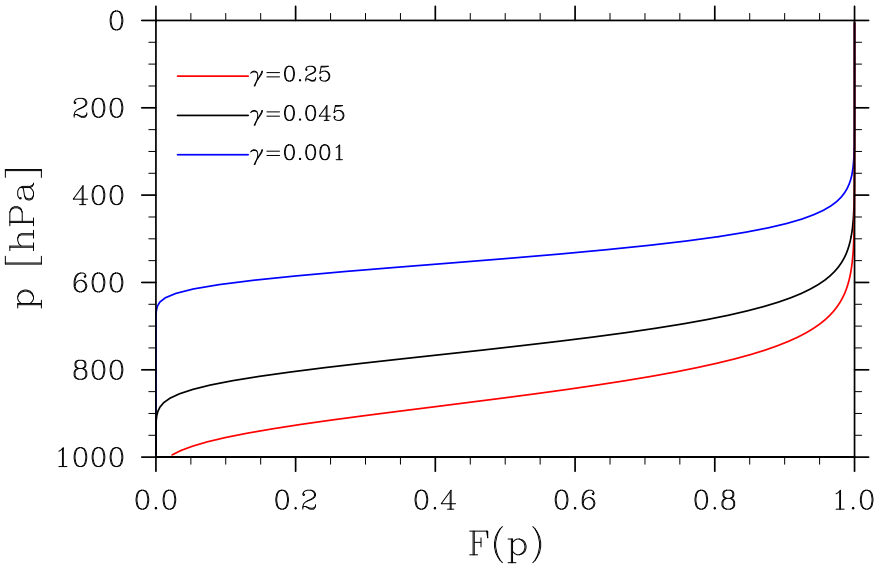

Figure 5.1: $F(p)$ given by equation (5.4) for different values of γ. Parameter γ controls the vertical extent of the lower atmospheric layer in which the surface temperature gradient is reduced. For the most simulations in this chapter $\gamma = 0.045$ (black curve).

stratosphere is kept at the same height, at $p = 200$ hPa). In the present study, the focus is on the influence of γ on superrotation. However, it is noted here that the generation and strength of superrotation are highly sensitive to all of $(\gamma, \mathfrak{b}, \Delta T)$, in general. This broad sensitivity on the physical parameters is briefly discussed in section 5.3.3.

Note that, apart from the masking function F, there are minor differences in the setup of HS, Williams (2003) and the present study – none of which affect the results presented here qualitatively. For example, in Williams (2003) $\Delta\theta$ in equation (5.3) is not modulated by $\cos^2\phi$, so that small-scale convection at all ϕ is eliminated. In addition, $\tau_{\text{th}} = 20$ days everywhere in this study – different than in HS, but same as in Williams (2003).

The vertical domain, which extends from $p = 10^3$ hPa to 0 hPa, is resolved by 30 levels equally spaced in p[1]. Simulations are performed at (T42, T85, T170, T341) horizontal resolutions. "Control (i.e., essentially HS) simulations" (with T_e shown in Figure 5.2*a*) are integrated for $t = 1200$ days, and "RTG simulations" (with T_e shown in Figure 5.2*b*) are integrated for up to $t = 7000$ days. In the latter simulations, equilibration takes longer at lower horizontal resolutions and/or with

[1] Setting vertical levels equally spaced in p or $\sigma = p/p_s$ is common in idealized tropospheric (e.g., Held and Suarez, 1994; Williams, 2003, 2006; Potter et al., 2014).

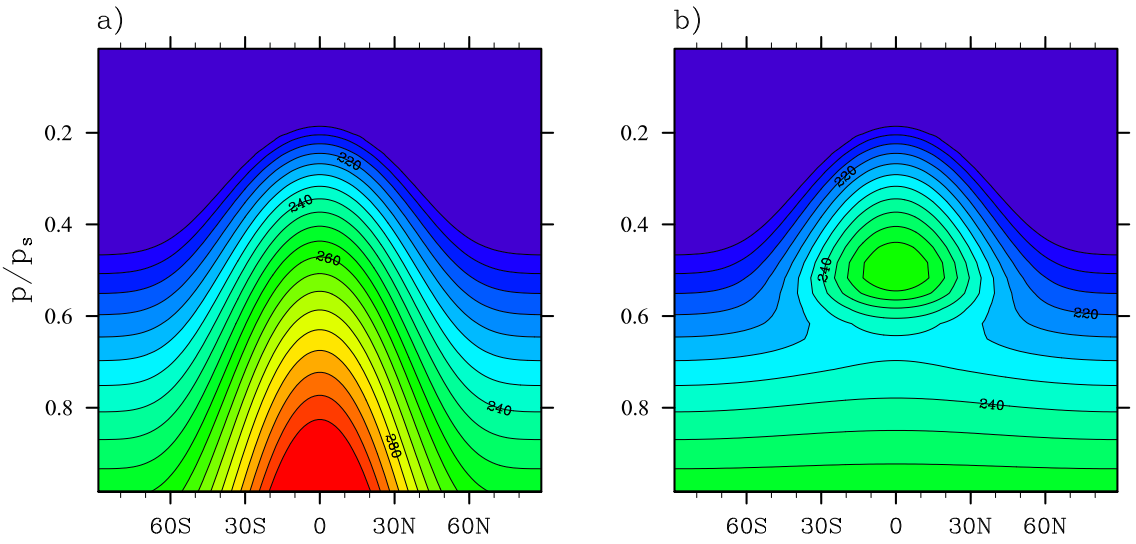

Figure 5.2: Prescribed radiative equilibrium temperature distributions T_e [K], pressure vs. latitude, for the Held and Suarez (HS) case (a) and the reduced temperature gradient (RTG) case (b). Maximum and minimum values are 200 K and 300 K, respectively, with contour interval of 5 K.

stronger dissipation, as is shown in section 5.3.2. The timestep size Δt (in seconds) is $(600, 300, 150, 75)$ for the resolutions given above, respectively. The hyperdiffusion coefficient ν_8 is chosen such that the e-folding time τ_d (in days) for the smallest scale in the system is (0.1, 0.01, 0.001, 0.0001), respectively. Assuming

$$\tau_{\rm d} \sim \frac{1}{\nu_8} \left[\frac{R_{\rm p}^2}{n_t(n_t+1)} \right]^4 , \tag{5.5}$$

where n_t is the spectral truncation wavenumber, the above $\tau_{\rm d}$ correspond to ν_8 (in $10^{37}\,{\rm m}^8\,{\rm s}^{-1}$) of (3.0, 0.1, 0.004, 0.0002), respectively. Sensitivity of the results to horizontal resolution and/or hyperdissipation specifications is discussed in section 5.3.2.

5.3 Results

Before describing turbulent three-dimensional simulations, it is insightful to examine the zonally-symmetric, eddy-free circulation in balance with the prescribed heating T_e shown in Figure 5.2. Figure 5.3 shows the zonally-symmetric zonal-mean zonal wind and mass streamfunction ($\overline{u}$ and $\overline{\psi}$, respectively) from the control (a) and the RTG (b) simulations at T170L30 resolution (i.e., T170 horizontal resolution with 30 vertical levels). The zonally-symmetric circulation is obtained by running the BOB

model with no initial perturbation and no hyperdiffusion (i.e. $\nu_8 = 0$). In both simulations, a weak Hadley cell is produced and the balanced zonal flow consists of weak subrotation at the equator and eastward jets centred at $\phi \sim \pm 25°$.

Figure 5.4 shows the time- and zonal-mean temperature, zonal wind, and mass streamfunction meridional cross-sections ($\overline{T}^*$, $\overline{u}^*$, and $\overline{\psi}^*$ respectively) from the fully turbulent, three-dimensional control (*a* and *c*) and RTG (*b* and *d*) simulations at T170L30 resolution. Time-averaging is performed over 25 τ_{th}'s after the simulations have reached statistically equilibrated state, over the intervals $t = [700, 1200]$ days for the control simulation and $t = [4500, 5000]$ days for the RTG simulation.

In the control simulation, initially zonally-symmetric eastward jets become baroclinically unstable and nonlinear, zonally-asymmetric nonlinear flow develops. Following the onset of baroclinic instability, the jets move poleward and equilibrate at $\phi \sim \pm 45°$ (Figure 5.4*b*). The exact mechanism for the poleward migration is currently not well understood, but all of the proposed mechanisms involve some form of eddy-mean flow interaction (see e.g. Chen et al., 2007; Kidston and Vallis, 2010). Crucially, at the equator the flow remains weakly westward at all heights in the control simulation. Baroclinic eddies transport heat from low to high latitudes. As a result, the equator-to-pole temperature gradients are weaker in the equilibrated $\overline{T}^*$ distribution than in the prescribed T_{e} distribution (cf. Figure 5.4*a* with Figure 5.2*a*). Note that the Hadley circulation in the full non-linear simulation is considerably stronger than in the zonally-symmetric eddy-free simulation (cf. Figures 5.3*a* and 5.4*c*).

In contrast, the equilibrated flow in the RTG simulation is superrotating at the equator – and there at all altitudes, except at the top (Figure 5.4*d*). By comparing Figure 5.4*d* to Figure 5.3*b* it is clear that the generation of superrotation requires either the presence of non-axisymmetric eddies or diffusion. The Hadley circulation is also stronger in the RTG simulation in the presence of eddies. Note that in this simulation the $\overline{T}^*$ distribution changes only slightly from the prescribed T_{e} distribution (cf. Figure 5.4*b* with Figure 5.2*b*). This is consistent with the marked reduction in baroclinic instability. The equilibrated subtropical jets remain close to their initial latitude – i.e., at $\phi \approx \pm 25°$ – and takes much longer time to equilibrate, compared to the control simulation. In the simulation presented, the total (column-mean) equatorial zonal wind $\langle u_{\text{eq}} \rangle$ undergoes rapid acceleration over $t = [200, 1000]$ days, reaching statistical equilibration thereafter. In this study, the early stage shall be referred to as the "acceleration stage" and the latter stage as the "equilibrated stage".

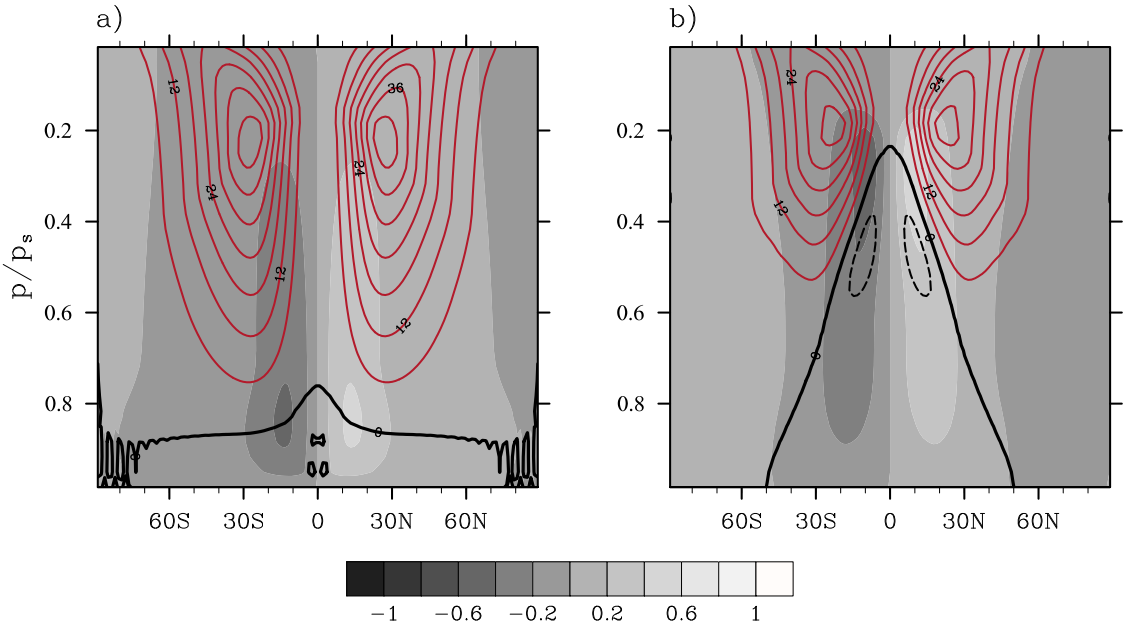

Figure 5.3: The zonally-symmetric zonal-mean zonal wind $\overline{u}$ [m s^{-1}] (contours) and mass streamfunction $\overline{\psi}$ [kg s^{-1}] (in greyscale) for the control (HS-like) simulation (a) and the RTG simulation (b) at T170L30 resolution, with corresponding T_e from Figure 5.2. Maximum and minimum values for $\overline{u}$ are $\pm$ 60 m s^{-1}, with contour interval 6 m s^{-1}. Negative $\overline{u}$ values are dashed (and in black) and positive are solid (and in red). The zero contour is drawn with double thickness. The mass streamfunction in panel (a) has been divided by 10^{-10} and in panel (b) by 5×10^{-11}, respectively. No superrotation is present in the zonally-symmetric, eddy-free case with no applied hyperdissipation (i.e., $\nu_8 = 0$).

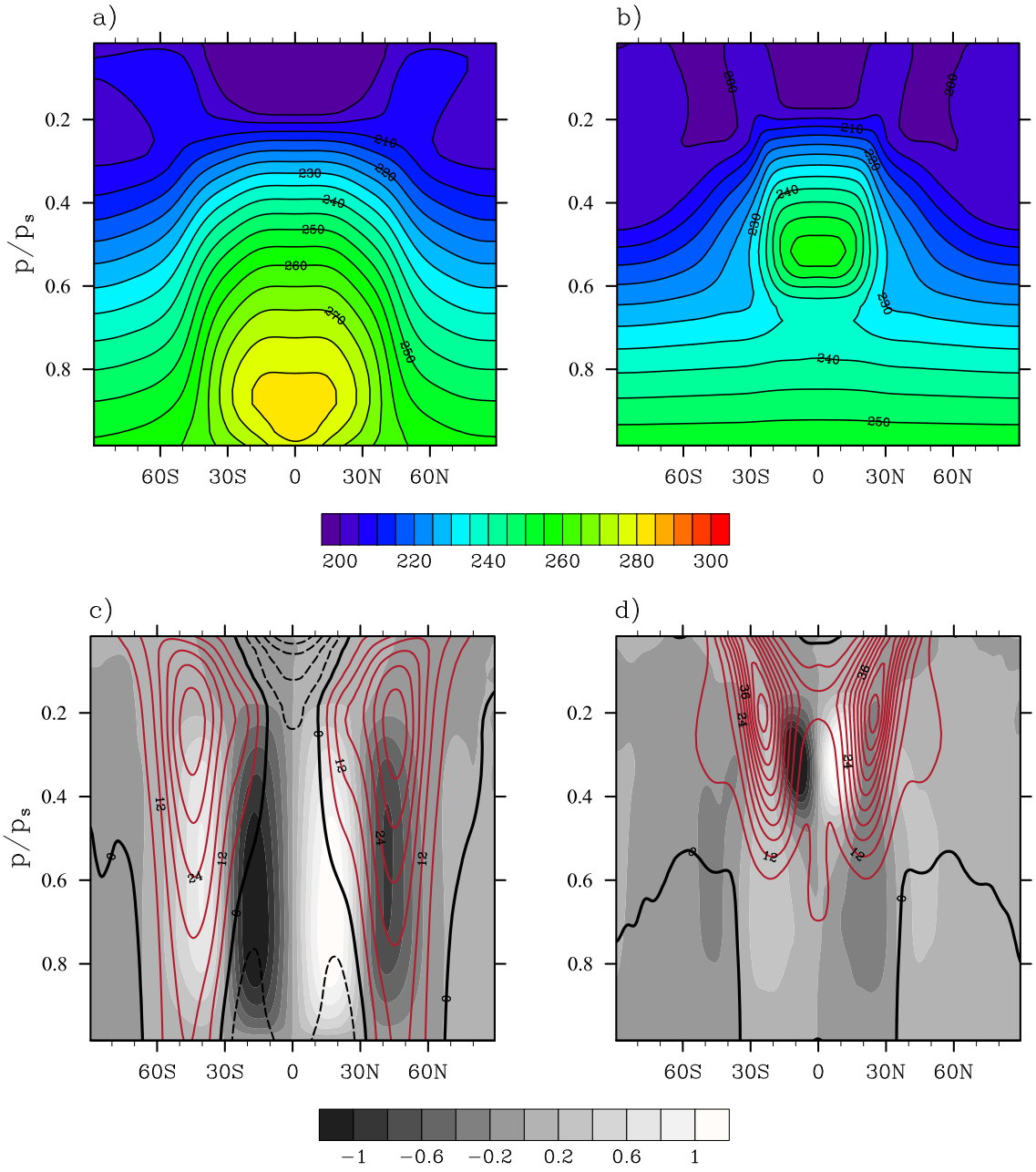

Figure 5.4: The time- and zonal-mean temperature $\overline{T}^*$ [K], zonal wind $\overline{u}^*$ [m s^{-1}], and mass stream function $\overline{\psi}^*$ [kg s^{-1}] for the fully turbulent three-dimensional control (HS-like) simulation (a and c) and the RTG simulation (b and d) at T170L30 resolution, with corresponding T_e from Figure 5.2. The time averages are taken over $t = [700, 1200]$ days (a and c), and over $t = [4500, 5000]$ days (b and d). Contour values for $\overline{T}^*$ are same as in Figure 5.2 and for $\overline{u}^*$ and $\overline{\psi}^*$ same as in Figure 5.3. Clear superrotation is generated at the equator (at all altitudes) in the fully turbulent RTG simulation.

5.3.1 Wave-mean Flow Analysis

Accelerations of the zonal-mean zonal flow and directions of wave propagation can be assessed via the Eliassen-Palm (EP) flux vector, $\mathbf{F} = (F_\phi, F_p)$ (equations (3.17) and (3.18)) and its divergence $\mathcal{E} = \nabla \cdot \mathbf{F}$ (e.g., Andrews and McIntyre, 1978). Recall that zonal flow is accelerated (decelerated) in regions of positive (negative) $\mathcal{E}$: this can be readily inferred from the *transformed Eulerian mean* (TEM) zonal momentum equation (3.14) in which $\mathcal{E}$ represents wave forcing.

Figure 5.5 shows the EP flux vector field and its divergence, $\mathcal{E} = \nabla \cdot \mathbf{F}$ (contours), for the control simulation (a) and RTG simulation, during the acceleration and equilibrated stages (b and c, respectively). The fields at T170L30 resolution are shown. While the ageostrophic terms (i.e., the second term in equation (3.17) and the first and third terms in equation (3.18)) are small compared to the geostrophic terms, the ageostrophic EP diagnostics are calculated here for completeness. Note that qualitatively the EP flux diagnostics are similar at all horizontal resolutions investigated in this study.

In the control simulation, the EP flux and its divergence (Figure 5.5a) follow the classic scenario: Rossby waves, generated near the surface by mid-latitude baroclinic instability, propagate upward in the troposphere and equatorward at mid-height, transporting momentum poleward and heat upward *and* poleward. According to equation (3.17), $F_\phi < 0$ implies $\overline{u'v'} > 0$, leading to a poleward (equatorward) eddy momentum flux in the northern (southern) hemisphere; and, according to equation (3.18), $F_p > 0$ implies $\overline{v'\theta'} > 0$, leading to a poleward (equatorward) eddy heat flux in the northern (southern) hemisphere. The vector field is divergent (positive) near the surface at mid- and high-latitudes and convergent (negative) in the upper troposphere and lower stratosphere, as well as in the equatorial region near the surface. According to the TEM equations (e.g., Andrews and McIntyre, 1978), zonal flow is accelerated (decelerated) in regions of positive (negative) $\mathcal{E}$; hence, the jet becomes increasingly barotropic.

In the RTG simulation, the wave propagation is upward and, unlike in the control simulation, mainly poleward (see Figures 5.5b and 5.5c). The poleward heat flux is considerably weaker (n.b. the smaller reference vectors for Figures 5.5b and c, compared with that for Figures 5.5a) and the flux activity is clearly dominant at higher altitudes (above $p \sim 600$ hPa level). The eddy momentum flux is mostly equatorward in both the northern and southern hemispheres. The $\mathcal{E}$ field is also weaker than in the control simulation, but below the $p \sim 600$ hPa level both the control and RTG simulations exhibit similar $\mathcal{E}$ distributions. Above that level,

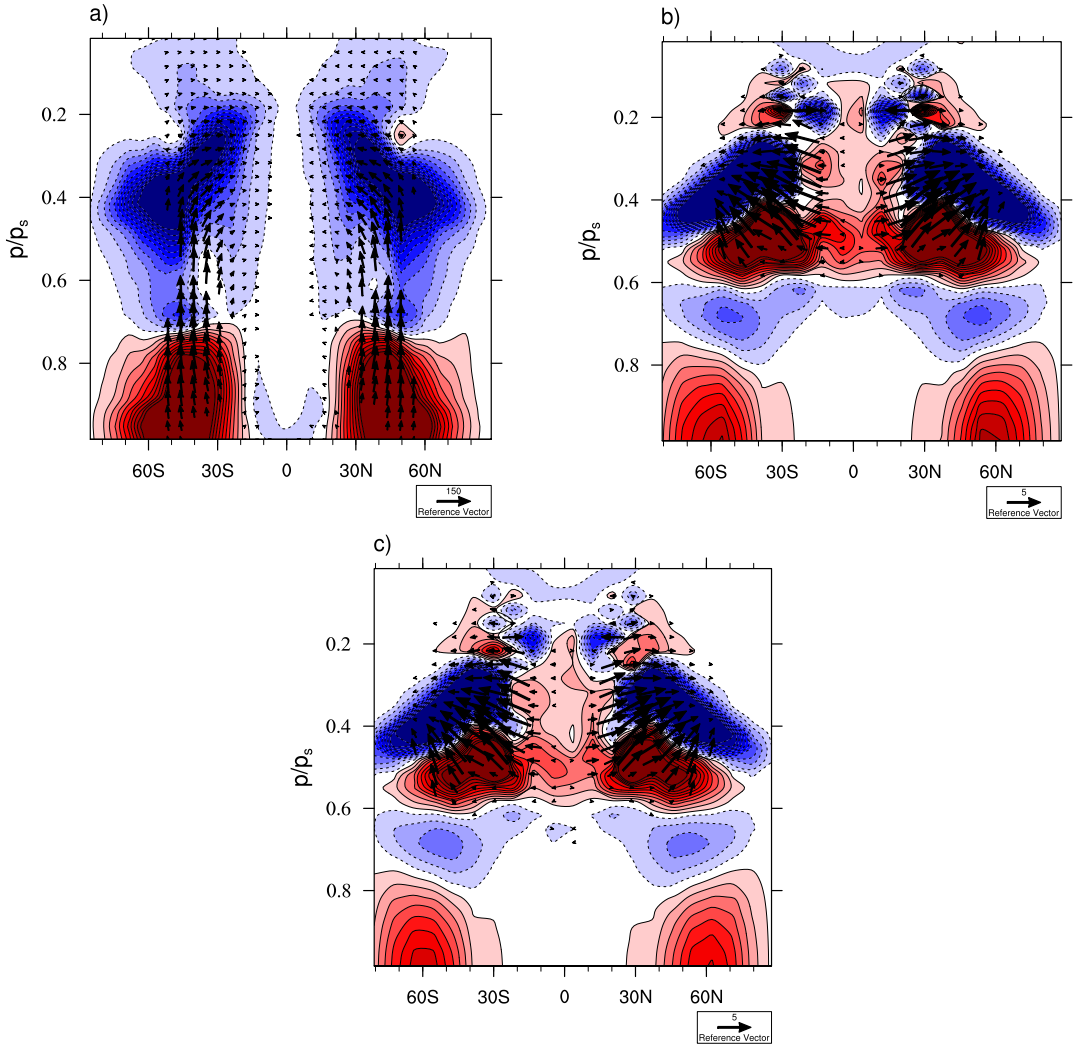

Figure 5.5: Eliassen-Palm flux vector, $\mathbf{F} = (F_\phi, F_p)$ [m^2 s^{-2}], and its divergence, $\mathcal{E} = \nabla \cdot \mathbf{F}$ [m s^{-2}], fields for the control simulation (a) and the RTG simulation (b and c) at T170L30 resolution. a): time-average during a statistically steady state, over $t = [700, 1200]$ days. b) and c): RTG simulation time-average during the acceleration stage, over $t = [200, 700]$ days and during a statistically steady state, over $t = [4500, 5000]$ days, respectively. Negative $\mathcal{E}$ values are dashed (and in blue) and positive values are solid (and in red). Maximum and minimum $\mathcal{E}$ values are $\pm 700\,\mathrm{m\,s^{-2}}$ in (a) and ± 100 m s^{-2} in (b and c). The reference vector in a) has magnitude of 150 m^2 s^{-2} and in b) and c) of 5 m^2 s^{-2}. F_ϕ and F_p are scaled by 1 radian of latitude and 1 Pa of pressure, respectively. In addition, F_p is scaled by a factor of 0.5 in b) and c). The wave propagation is upward and equatorward in the control simulation, and upward and mainly *poleward* in the RTG simulation. The wave activity is changed little between the acceleration and the equilibrated stages in the RTG simulation: the largest differences occur at $p \approx 500\,\mathrm{hPa}$ level in the equatorial region, where the zonal flow acceleration is stronger during the acceleration stage.

the $\mathcal{E}$ field displays a more complicated structure than in the control simulation. Significantly, an eastward zonal flow acceleration ($\mathcal{E} > 0$) is present in the tropics ($\phi \lesssim \pm 20°$), in the $p \approx [250, 600]$ hPa region. Note also that at $p = 200$ hPa, the the zonal flow is accelerated at the equator and decelerated in the subtropics, in the $10° < |\phi| < 30°$ region, where the wave propagation is equatorward. In addition, the poleward flanks of the subtropical jets are decelerated at higher altitudes ($p \approx [200, 450]$ hPa) and accelerated at lower altitudes ($p \approx [450, 600]$ hPa). While the $\mathbf{F}$ and $\mathcal{E}$ distributions are similar during the acceleration and the equilibrated stages, there is a notable difference in the equatorial region at $p \approx 500$ hPa level: the acceleration of zonal wind is stronger during the acceleration stage than during the equilibrated stage.

It is also useful to examine the spectral characteristics of the eddy momentum flux convergence, $\mathfrak{C} \equiv -1/(R_\mathrm{p} \cos^2\phi)\partial/\partial\phi(\overline{u'v'}^* \cos^2\phi)$. The eddy momentum flux at each ϕ is first spectrally decomposed among the zonal wavenumbers $\{m\}$ to obtain the m–ϕ covariance spectrum, before computing divergence (e.g. Hayashi, 1971; Randel and Held, 1991). Similarly, the phase speed, $c\,(m, \phi) = \varpi R_\mathrm{p} \cos\phi/m$ with $\varpi = \varpi(m)$ the frequency, is computed to obtain the c–ϕ $\mathfrak{C}$ spectrum. Note that positive (negative) $\mathfrak{C}$ spectra is associated with momentum source (sink). Both spectra from the control simulation and the RTG simulation are shown in Figure 5.6. The spectra are taken from the $p = 500$ hPa level, the level of maximum zonal wind acceleration in the RTG simulation (see Figure 5.5*b* and *c*); recall that there is no superrotation in the control case.

First the m–ϕ spectra is discussed. Figure 5.6*a* shows the m–ϕ spectrum calculated for 5 consecutive 50 day windows over $t = [950, 1200]$ days from the control simulation after reaching equilibration. The spectrum for $m \leq 10$ is shown because larger wavenumbers (i.e. $m > 11$) have insignificant power. The $\mathfrak{C}$ spectrum shows that $m \sim 6$ modes, which are centered on the jets, dominate at mid-latitudes. Figures 3.5*b* and *c* show the m–ϕ spectrum from the RTG simulation over the acceleration stage ($t = [250, 500]$ days), and the equilibrated stage ($t = [4750, 5000]$ days), respectively. The spectrum in the RTG simulation is also dominated by $m \sim 6$ modes, but the waves are excited on both flanks of the subtropical jets at $\phi \approx \pm 5°$ and $\phi \approx \pm 35°$. These modes stir the flow and converge eastward momentum into their source region and westward momentum into their breaking or saturation region. In addition, low wavenumber (i.e. $m \sim 2$) modes converge eastward momentum at the equator. In what follows, it will be shown that the $m \sim 2$ modes have a distinct Kelvin wave-like behaviour as also found in Potter et al. (2014).

There are other distinguishing features in the RTG simulations, in general. For

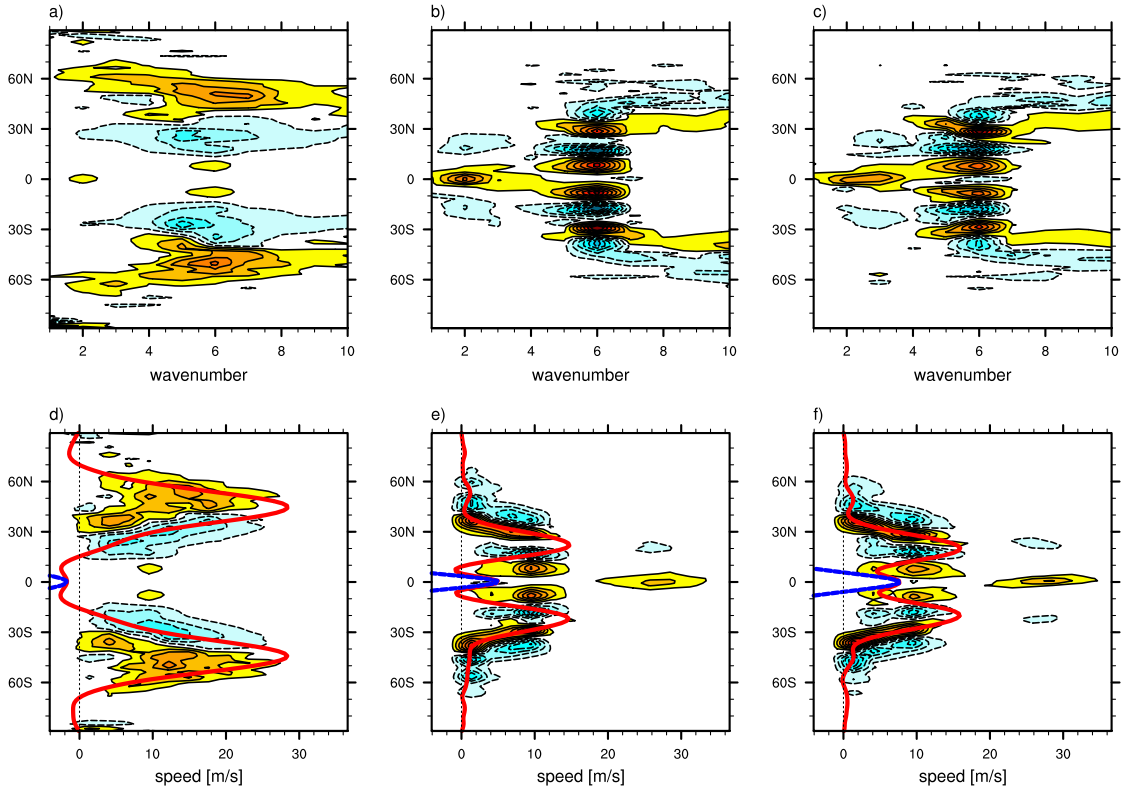

Figure 5.6: $\mathfrak{C}$ spectra [m s^{-2}] at $p = 500$ hPa for the control simulation and RTG simulation at T170L30 resolution. $a-c$): the m–ϕ spectrum. $d-f$): the c–ϕ spectrum (contours), $\overline{u}/\cos\phi$ (red curve) and $\overline{u} - \Omega R_{\rm p}\sin^2\phi/\cos\phi$ (blue curve). The spectra are computed for 5 50-day windows over $t = [950, 1200]$ days for the control simulation (a and d) and over $t = [250, 500]$ days (b and e) and $t = [4750, 5000]$ days (c and f) for the RTG simulation, respectively. Negative contours are dashed and positive contours are solid. Maximum and minimum values are $\pm 5 \times 10^{-11}$ m s^{-2} (a and d) and $\pm 2 \times 10^{-11}$ m s^{-2} (b-c and e-f). Notice the dominance of zonal wavenumbers $m \sim 6$ in both simulations. The phase speeds in the control simulation have values less than or comparable to $\overline{u}$ whereas $c > \overline{u}$ in the RTG simulation at the equator. Critical layers are located at latitudes where $c \approx \overline{u}$. Note the role of high phase speed, zonal wavenumber $m \sim 2$ modes in zonal mean zonal flow acceleration at the equator in the RTG simulation.

example, the $\mathfrak{C}$ spectra in the RTG simulations are qualitatively same at lower model resolutions. However, there are significant *quantitative* differences. For example, at lower resolutions the power in $m \sim 6$ modes, which are still located at the flanks of the subtropical jet, is significantly smaller (by ∼10 times): the power in these modes is comparable to those of $m \sim 2$ modes. Moreover, the $m \sim 6$ modes on the equatorward flanks of the subtropical jets disappear completely after the acceleration stage (recall the modes persist well into the equilibrated stage in the simulation presented in Figure 5.6). As we shall show in section 5.3.2, this is due to inadequate horizontal resolution.

Now the c–ϕ spectra are discussed. The lower panels of Figure 5.6 present the c–ϕ spectra at the $p = 500$ hPa level for the control (panel d) and RTG (panels e and f) simulations, respectively. Note that the spectrum has insignificant power for $c \lesssim 0$ m s^{-1} and for $c \geq 40$ m s^{-1}. The calculation is performed over the same time windows as in the corresponding upper panels of Figure 5.6. In each panel, the superimposed red curve shows $\overline{u}$ (divided by $\cos\phi$) and the superimposed blue curve shows the difference between $\overline{u}$ and the angular momentum conserving wind U_m (i.e., $\overline{u} - U_m$), where

$$U_m \equiv \frac{\Omega R_\mathrm{p} \sin^2\phi}{\cos\phi}. \tag{5.6}$$

Superrotation, $M > M_0$, is associated with $(\overline{u} - U_m) > 0$.

The mean flow acceleration will tend to push $\overline{u}$ towards c. Because in Figure 5.6d $c \lesssim \overline{u}$ everywhere, the equatorward propagating Rossby waves can not accelerate the zonal flow in the control simulation. The waves, which are generated at the cores of the jets, propagate equatorward until they encounter a critical layer on the equatorward flanks of the jets. In the critical layer, Rossby waves break and deposit westward momentum; hence, no superrotation is present in the control simulation. In contrast, in the RTG simulation (Figures 5.6e and f), the $m \sim 6$ modes that propagate poleward from their source region at $\phi \sim \pm 5°$ deposit eastward momentum near the equator where $c \gtrsim \overline{u}$. These waves break at $\phi \sim \pm 15$–$20°$ and decelerate the flow there. Additionally, the $m \sim 2$ disturbance, with $c \sim 30$ m s^{-1}, accelerates the zonal flow at the equator by pushing $\overline{u}$ towards c and converging eastward momentum at the equator throughout the RTG simulation (Figures 5.6e and f).

For a more detailed view of the flow field, a snapshot of Ertel potential vorticity, $q = [(\zeta + f)\cdot\nabla\theta] \,/\, \rho$ is shown in Figure 5.7; here ρ is density, and the projection shown is cylindrical-equidistant centered on the equator. Figure 5.7a shows q for the control simulation on the $\theta = 315$ K isentrope and Figure 5.7c shows q for the RTG simulation on the $\theta = 300$ K isentrope at T170L30 resolution, at $t = 600$ days.

These isentropic surfaces lie approximately on the $p = 500$ hPa surface in the tropics. To illustrate how the PV distribution changes in time the zonal-mean PV ($\overline{q}$) for the two simulations at $t = 40$ days (red curve), $t = 200$ days (black curve), and $t = 600$ days (blue curve) is shown in panels b and d for $|\phi| \leq \pm 15°$. Note that at $t = 40$ days the unaveraged flow in both simulations is nearly zonally-symmetric.

The $m \sim 6$ structure can clearly be seen in panels a and c, but mixing of q occurs closer to the equator in the RTG simulation than in the control simulation. This is consistent with the diagnostics in Figure 5.6 just discussed above. In the control simulation no mixing is taking place in the equatorial region as the zonal-mean PV changes little from the zonally-symmetric PV at $t = 40$ days (see Figure 5.7b). Crucially, in the RTG simulation, mixing results in a band of sharp q-gradient pushed to the equator; a corresponding band is not present in the control simulation. The band is not zonally-symmetric and often appears with a blob of q that appears to have broken off from large-amplitude undulations of the high-gradient band. In addition to inducing a q-jump *at* the equator, the undulations and concentrations of PV at the equator act as sources of enhanced superrotation. The blobs of q at the equator translate longitudinally faster than the zonal mean zonal wind and show up in the spectrum as the $m \sim 2$ features.

While the $m \sim 2$ features lack a coherent wave-like structure in the q field, the wave-like behaviour can be seen more clearly by examining the perturbation geopotential height Φ' in the RTG simulation in the equatorial region. Figure 5.8 shows Φ' with wind vectors overlaid on the $p = 500$ hPa surface, at $t = 600$ days. In panel (a) the whole fields are shown and in panel (b) the fields have been filtered in Fourier space such that only the $m = 2$ signal remains. The filtered fields, in particular, resemble the classic Kelvin wave solution of the equatorial beta-plane shallow water model (e.g., Matsuno, 1966). The Kelvin wave mechanism was proposed as an explanation for equatorial superrotation under axisymmetric thermal forcing in Potter et al. (2014). Note that Kelvin waves and Rossby-Kelvin modes excited in the presence of non-uniform mean flow have also been discussed in e.g., Iga and Matsuda (2005) as a possible mechanism for superrotation on Venus.

Kelvin waves in the RTG simulation can be identified by Fourier transforming equatorial geopotential height field Φ in space and time and depicting the resulting spectra in Wheeler-Kiladis diagrams as a function of ϖ and m (Wheeler and Kiladis, 1999). Here, 10 96-day time windows are taken to obtain the Φ spectrum. Both symmetric and antisymmetric Wheeler-Kiladis diagrams for the control (panels a and c) and the RTG simulations (panels b and d) are shown in Figure 5.9 at T170L30 resolution at the $p = 500$ hPa level. Overlaid on the symmetric diagrams are

the theoretical dispersion curves for the Kelvin waves and on the antisymmetric diagrams the theoretical dispersion curves for the mixed Rossby-gravity waves for equivalent depths of $h_0 = 12, 40$, and 100 m.

For the control simulation, only a weak Kelvin wave signal is present at the equator (panel *a*) and the spectrum is dominated by the westward propagating mixed Rossby-gravity waves with $h_0 = 100$ m (panel *c*). For the RTG simulation, a clear $h_0 = 100$ m Kelvin wave signal dominates the spectrum (panel *b*) with little or no westward propagating wave activity. The above diagnostics suggest that Kelvin waves, together with mixing of q by the $m \sim 6$ modes on the equatorward flanks of the subtropical jets, play a significant role in driving and maintaining the equatorial superrotation in the RTG simulations. Note that the equatorial Φ spectra is both quantitatively and qualitatively the same for all horizontal resolutions investigated in this study.

Detailed diagnostics of the flow field reveal that the meridional gradient of zonal mean q, $R_{\rm p}^{-1}\partial\overline{q}/\partial\phi$, changes sign at both flanks of the subtropical jets, at $\phi = \pm 4^\circ$ and at $\phi = \pm 10^\circ$ in the $p = 600 - 300$ hPa region, throughout the RTG simulation (not shown). Because a necessary (but not sufficient) Rayleigh-Kuo condition for barotropic instability is that $R_{\rm p}^{-1}\partial\overline{q}/\partial\phi$ changes sign somewhere in the domain, this suggests that the source of the $m \sim 6$ at the flanks of the jets and the equatorial $m \sim 2$ Kelvin wave-like features is barotropic instability. The latitudinal scale L_ϕ of an equatorially trapped Kelvin wave can be estimated to be of the order of the equatorial Rossby deformation length scale $L_\phi = \sqrt{c/\beta}$ where $\beta = 2\Omega/R_p$. For the wave with $c \sim 30$ m s^{-1} (cf. Figures 5.6 and 5.9*b*), $L_\phi \sim 1500$ km or $\phi = 10^\circ$. Therefore to excite equatorially trapped Kelvin waves stirring must occur within the $\phi \sim 10^\circ$ band from the equator. For the control simulation neither the necessary condition for barotropic nor baroclinic instability is satisfied in this region. This might explain the absence of equatorial Kelvin waves from the control simulation in Figure 5.9.

To elucidate the role of the instabilities in generating superrotation, adiabatic initial value simulations are also carried out with the shallow water model SWBOB (Scott et al., 2003), which employs the same numerical algorithms as BOB. Equilibration of subtropical eastward jets is studied in two setups: SW1 and SW2. In SW1, the initial jets are centred close to the equator, at $\phi = \pm 20^\circ$, and satisfy both the Rayleigh-Kuo criterion for barotropic instability on the equatorward flank, at $\phi \sim \pm 5^\circ$. In SW2, the initial jets are centred at $\phi \sim \pm 35^\circ$ and also satisfy the Rayleigh-Kuo instability criterion on both flanks, but further from the equator than in SW1. Note that the amplitude of the initial jets is same in both setups. After an

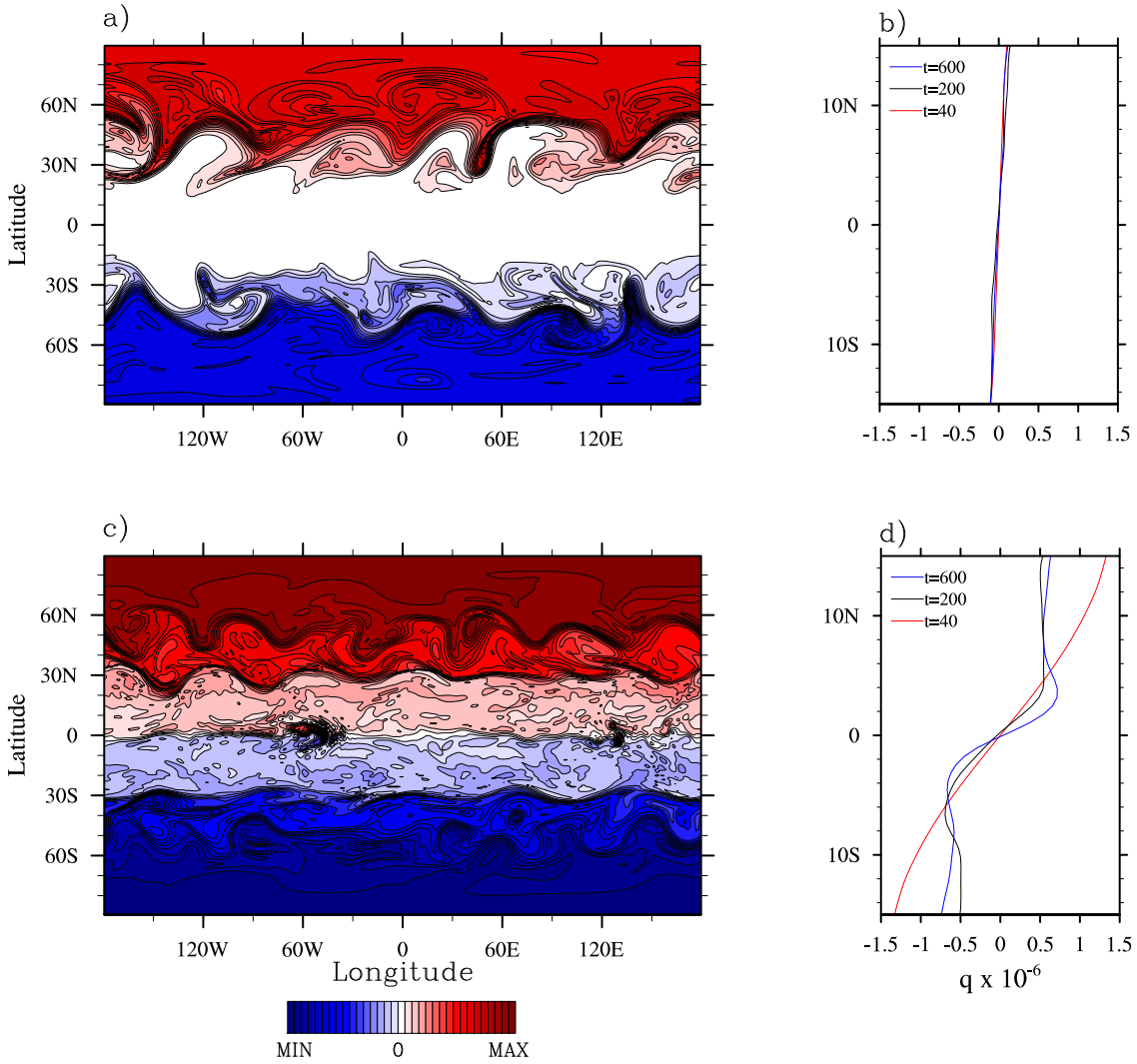

Figure 5.7: Snapshot of Ertel potential vorticity q [$\mathrm{K\,m^2\,kg^{-1}\,s^{-1}}$] and its zonal-mean $\overline{q}$ for the control simulation (a and b, respectively) and RTG simulation (c and d, respectively) at T170L30 resolution. The q fields are shown at $t = 600$ days in cylindrical-equidistant projection on the $\Theta = 315\,\mathrm{K}$ and $\Theta = 300\,\mathrm{K}$ isentropes, respectively (these surfaces lie approximately at $p = 500\,\mathrm{hPa}$ in the tropics). Maximum and minimum contour values are $\pm 10^{-5}\,\mathrm{K\,m^2\,kg^{-1}\,s^{-1}}$ and $\pm 5 \times 10^{-6}\,\mathrm{K\,m^2\,kg^{-1}\,s^{-1}}$, respectively. The $m \sim 6$ mode can be seen in both a) and c), as well as the presence of equatorial q-gradients and blobs in c) (only). Panels b) and d) show $\overline{q}$ on same isentropes as in a) and c). The equatorial region at $t = 40$ days (red), $t = 200$ days (black) and $t = 600$ days (blue) is shown. Superrotation is generated in the RTG simulation as a consequence of extrusion of high q from higher latitudes to the equator via mixing. In contrast, notice the absence of q-mixing at the equator in the control simulation.

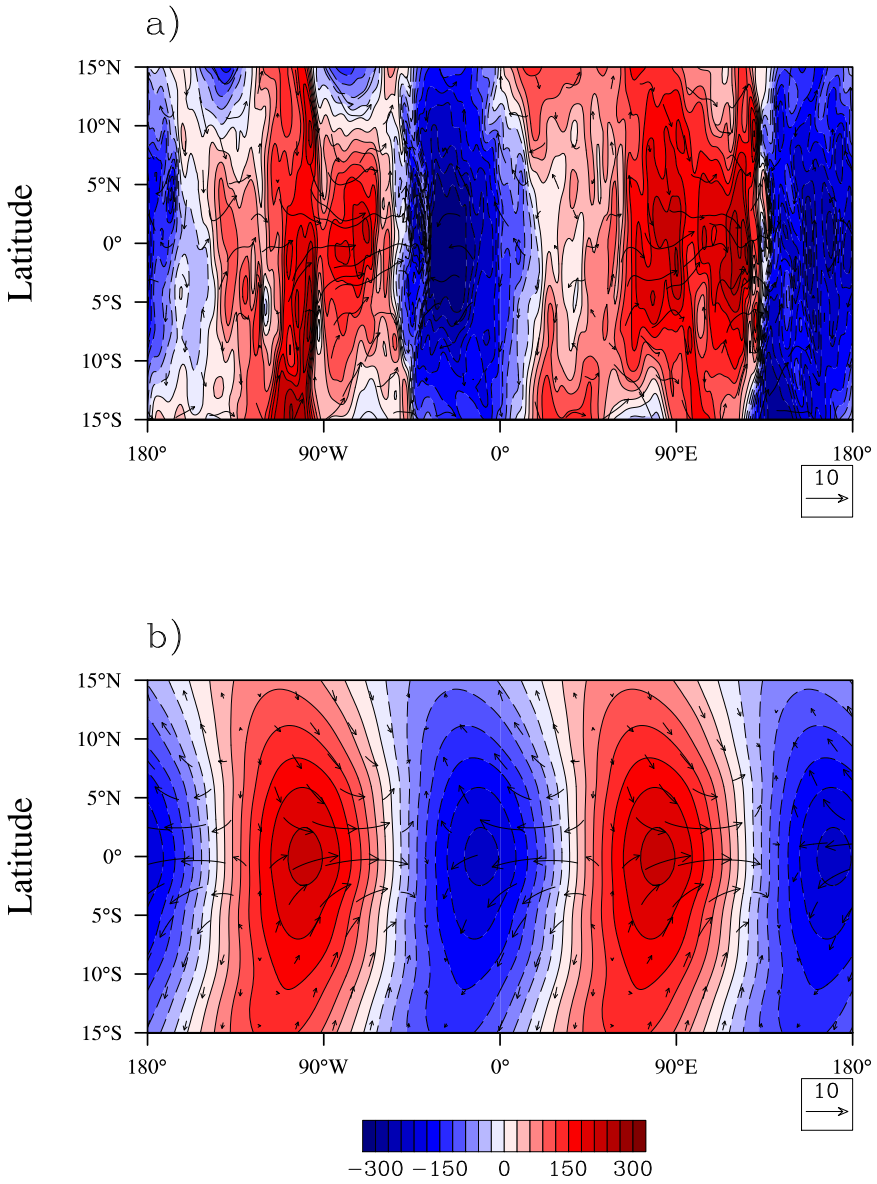

Figure 5.8: Snapshot of perturbation geopotential Φ' [$m^2\ s^{-2}$] with horizontal wind vectors overlaid for the RTG simulation at T170L30 resolution. The fields are shown at $t = 600$ days in cylindrical-equidistant projection in the equatorial region at the $p = 500$ hPa level. Panel (a) shows the unfiltered fields and panel (b) shows the fields filtered so that only $m = 2$ signal remains. Maximum and minimum contour values are $\pm 300\ m^2\ s^{-2}$. Note the resemblance of the filtered fields with the classic Kelvin wave solution.

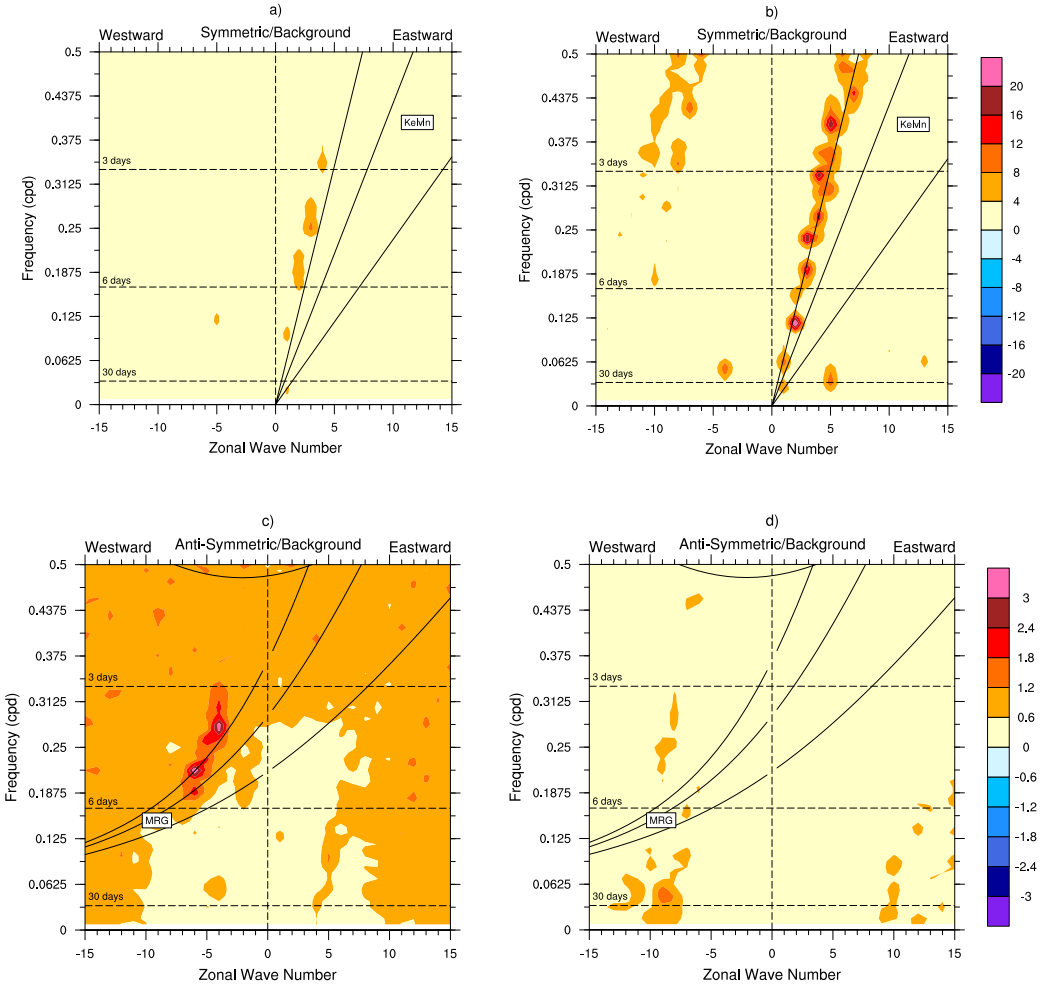

Figure 5.9: Symmetric and antisymmetric mode Wheeler-Kiladis diagrams of the geopotential height field in the equatorial region ($|\phi| < 10°$) for the control (panels a and c) and the RTG (panels b and d) simulations at $p = 500$ hPa. The theoretical dispersion curves for Kelvin and mixed Rossby-gravity waves for equivalent depths $h_0 = 12, 40$, and 100 m are overlaid on the diagrams. Notice the presence of $h_0 = 100$ m Kelvin waves in the RTG simulation.

applied initial perturbation, the jets are allowed to evolve freely in both setups until an equilibrated state is reached (as in Chapter 3). In setup SW1, the flow equilibrates to a superrotating state whereas in setup SW2, the flow remains subrotating at the equator. This can be seen in Figure 5.10, which shows the initial zonal wind $u_0(\phi)$ (red curve) and the equilibrated zonal mean zonal wind $\overline{u}$ for setup SW1 (a) and setup SW2 (b), respectively. The fields at T170 (blue curve) and T42 (black curve) horizontal resolutions are shown.

In Figure 5.11, a snapshots of shallow-water potential vorticity, $q_{\rm sw} = (f + \zeta)/h$ with h the fluid depth, are presented for setup SW1 (Figure 5.11a) and setup SW2 (Figure 5.11b) in cylindrical-equidistant view. The fields at T170 horizontal resolution, during the non-linear stage of the instability at $t = 16$ days, are shown. In Figure 5.11a, barotropic instability provides the necessary stirring mechanisms in the equatorial region, required for flow acceleration and generation of superrotation. In Figure 5.11b, the stirring is located too far from the equator to influence the equatorial flow; hence, no superrotation is generated. Moreover, the magnitude of equatorial superrotation in SW1 setup is stronger for larger initial jet amplitudes, when barotropic instability criterion is more strongly satisfied. In addition, the magnitude of superrotation in SW1 setup is larger at lower horizontal resolution for the same initial jet amplitude (see Figure 5.10a). Note also that as in the RTG simulation the peak flow amplitude is off the equator. As in the setup SW1, stronger superrotation is also produced at lower horizontal resolution in the RTG setup. Therefore, in what follows, the role of the horizontal resolution as well as the numerical dissipation on the simulated flow is clarified in both the control and the RTG simulations.

5.3.2 Resolution and Dissipation

In general, the strength of superrotation depends on the horizontal resolution or dissipation. For the full primitive equations, it is found that relatively high horizontal resolution ($\gtrsim$T170) is required for numerical convergence – particularly for the RTG case. The high resolution ensures accurate representation of the eddy fluxes, for example. In this work, simulations are defined to be *converged* if both of the following criteria on the total (column-averaged) equatorial zonal wind $\langle u_{\rm eq} \rangle$ are met:

i) At equilibration, $\langle u_{\rm eq} \rangle$ is statistically same at least at two different horizontal resolutions, for any viscosity coefficient ν_8.

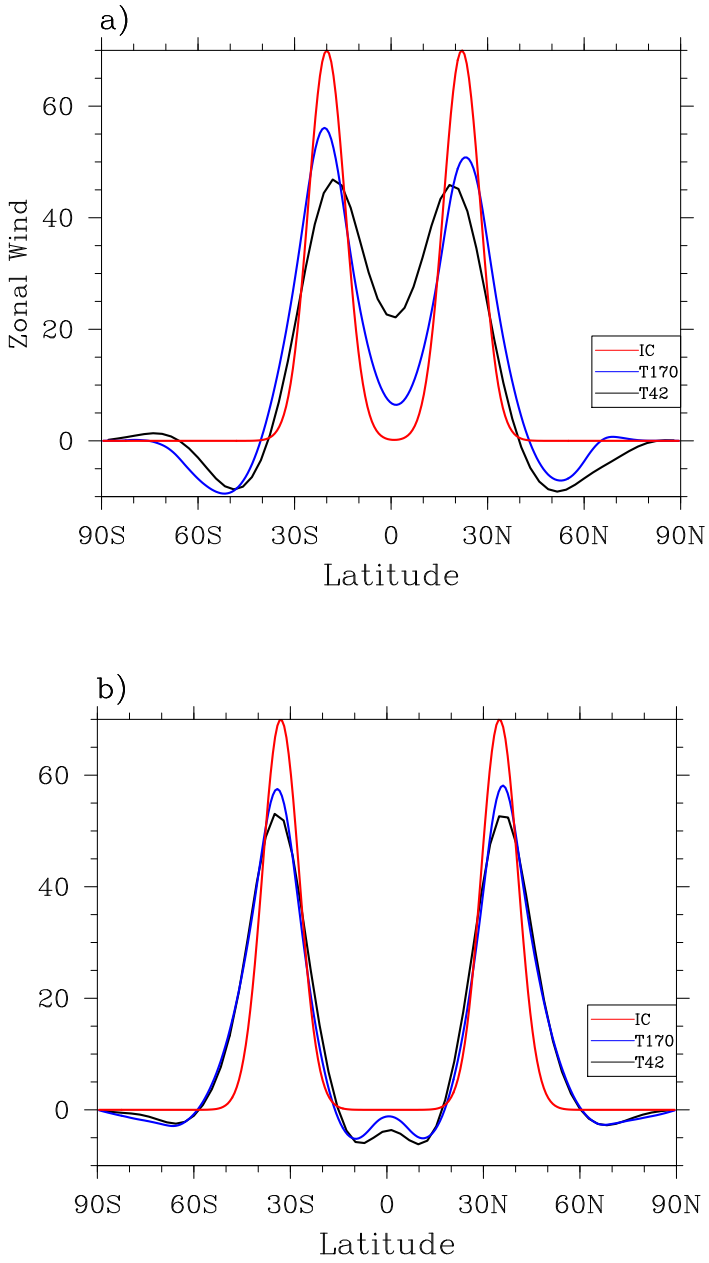

Figure 5.10: Initial zonal wind $u_0(\phi)$ [$\mathrm{m\,s^{-1}}$] (red curve) and equilibrated zonal-mean zonal wind ($\overline{u}$) [$\mathrm{m\,s^{-1}}$] at T170 (blue curve) and T42 (black curve) horizontal resolutions from initial value calculations with the shallow-water model. In *a*) u_0 satisfies the necessary condition for barotropic instability at $\phi \sim \pm 5°$. In *b*) u_0 satisfies the necessary condition for barotropic instability – but further from the equator than in *a*). In *a*) superrotation is produced as a result of mixing at the equator whereas in *b*) mixing is located further away from the equator and superrotation is not produced. Note also stronger superrotation in T42 simulation in *a*).

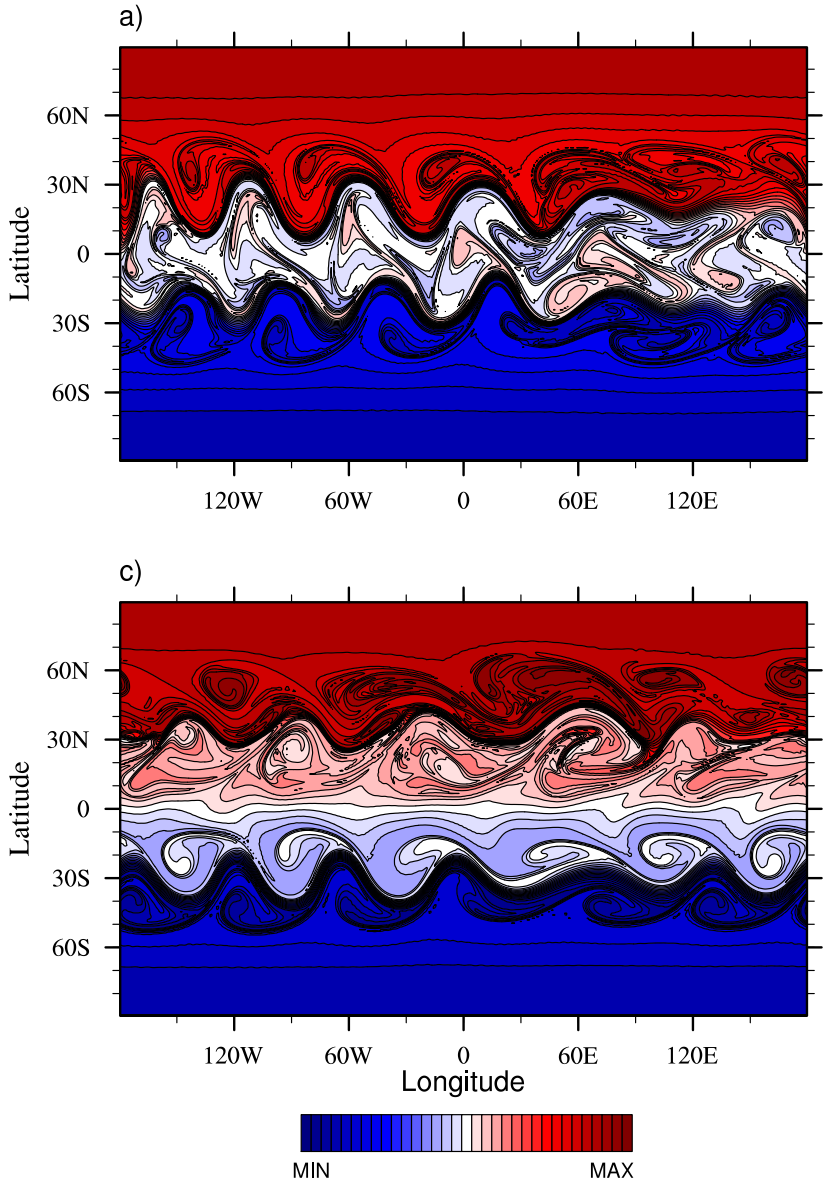

Figure 5.11: Shallow-water potential vorticity q_{sw} [$\mathrm{m}^{-1}\,\mathrm{s}^{-1}$] in cylindrical-equidistant view for setup SW1 (a) and setup SW2 (b) at $t = 16$ days. The horizontal resolution is T170. In a) instabilities located closer to the equator provide the necessary stirring for generation of superrotation. In b) stirring is located too far from the equator. Maximum and minimum contour values are $\pm 1.68 \times 10^{-8}$ m^{-1} s^{-1}, with contour interval 10^{-9} m^{-1} s^{-1}.

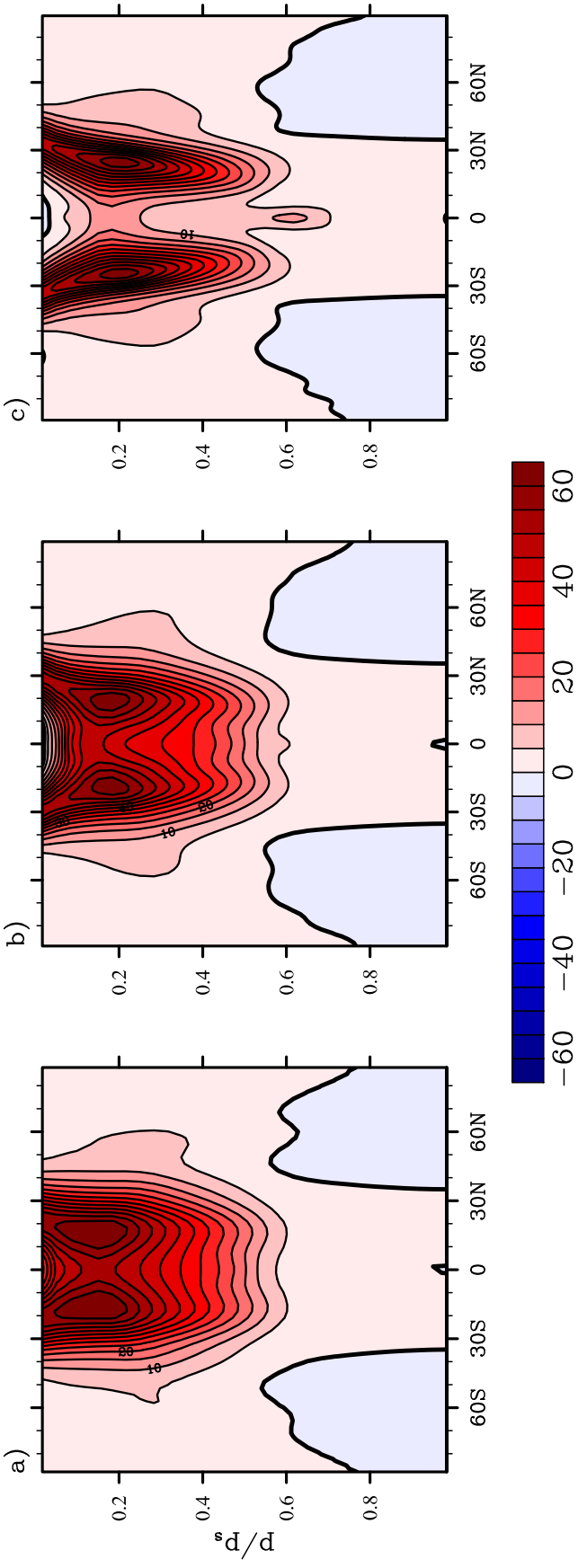

Figure 5.12: The time- and zonal-mean zonal wind $\overline{u}$ [m s^{-1}] for the RTG simulation at T42L30 (*a*), T85L30 (*b*) and T170L30 (*c*) resolutions. Contour intervals are same as in Figure 5.4*d*. Note how the subtropical jets have diffused together at low resolution.

ii) At equilibration, $\langle u_{\rm eq} \rangle$ is not sensitive to the choice of viscosity coefficient ν_8, at a given horizontal resolution.

For the latter criterion, ν_8 values are heuristically chosen from a "credible" range, which refers to those values that permit the vorticity field to be neither under-dissipated (i.e., inundated with grid-scale noise — e.g., the fields shown in Figures $3.17a-b$ in Chapter 3) nor over-dissipated (i.e., devoid of any strong coherent structures, such as vortices and sharp gradients — e.g., the fields shown in Figures $3.19a-b$ in Chapter 3). Experience has shown that certain amount of tuning is always necessary and that there always exists a finite range of values that is reasonably free from gross subjectivity and satisfy the credible condition on the vorticity field.[2]

Before the $\langle u_{\rm eq} \rangle$ is discussed, in Figure 5.12 the equilibrated $\overline{u}^*$ from the RTG simulations at T42L30 (a), T85L30 (b) and T170L30 (c) resolutions is presented. The figure clearly shows that RTG simulations are not converged at resolutions lower than T170L30, as it does not satisfy criterion *i*); the T170 and T341 results are very similar (not shown, but see discussion below). In contrast, the equilibrated $\overline{u}^*$ for the control simulations can exhibit qualitatively same behaviour at the same three horizontal resolutions presented (although they are still not converged, as is also discussed below). Interestingly, superrotation is considerably stronger at lower horizontal resolution in the RTG simulations.

Figure 5.13 now shows the time series of $\langle u_{\rm eq} \rangle$ from the control simulations (Figure 5.13a) and the RTG simulations (Figure 5.13b). For reference purpose, the time series from the T341L30 RTG simulation is also shown in Figure 5.13b. Note that, with exceptions as noted in the discussion below, the value of ν_8 for all the simulations in the figure is chosen so that the e-folding time for the truncation scale is nominally $(0.1,\, 0.01,\, 0.001,\, 0.0001)$ days at $(\mathrm{T42}, \mathrm{T85}, \mathrm{T170}, \mathrm{T341})$ resolutions, respectively. The chosen times correspond to $\nu_8 = (3.0,\, 0.1,\, 0.0044,\, 0.00017) \times 10^{37}\,\mathrm{m^8\,s^{-1}}$, respectively. In Figure 5.13a, the convergence criterion *i*) is fulfilled for the control simulation at T42 resolution. However, the control simulation does not fulfill criterion *ii*) at resolutions lower than T85. For example, a T42 resolution simulation employing the ν_8 value from the T21 resolution simulation (i.e. 25 times greater value) leads to a significantly different time series behaviour (cf. black and green lines); the behaviour does not persist into T85 resolution simulations, as is shown below. Convergence criterion *i*) is also fulfilled by the RTG simulation – but at the

[2]Experience has also shown that each new problem and setup necessitate a thorough characterization of accuracy and convergence, for confidence in the obtained results.

higher, T170 resolution. Moreover, the value of $\langle u_{\rm eq} \rangle$ at equilibration for the converged RTG simulations is much lower than for the un-converged, lower-resolution simulations – by as much as $17\,{\rm m\,s^{-1}}$ (cf. black and blue curves in Figure 5.13*b*). In addition, RTG simulations at T42 and T85 resolutions take considerably longer time to reach equilibration than that at T170 resolution. In the latter case, equilibration is reached at $t \sim 1000$ days, compared with $t \sim 7000$ days for the former cases.

Throughout this work, a larger value of ν_8 is used when performing a given simulation at a lower horizontal resolution – as is commonly practiced; alternatively, a smaller value of ν_8 is used when performing a given simulation at a higher horizontal resolution. The practice is primarily carried out for numerical stability and/or "spectrum tuning" reasons, and it results in different damping times for a given wavenumber at the different resolutions. However, as advocated in Polvani et al. (2004) and in Chapter 3, the same value of ν_8 should be used for all resolutions in order to "cleanly" assess numerical convergence: each wavenumber, up to the truncation, then experiences the same dissipation rate in all the simulations. This philosophy is closely related to the convergence criterion *ii*). Both imply that, once the wavenumbers required for convergence is adequately resolved, including additional wavenumbers in such a simulation would not affect the large-scale flow. Of course, this assumes weak or absence of non-locality in the flow, which may not be the case in practice because of physical and/or numerical reasons.

Indeed, consider the green and red curves in Figure 5.13*b*, showing two RTG simulations at different horizontal resolutions (T85 and T170) using the same ν_8 value (cf. green and red curves). It is clear that the RTG simulation is not converged at T85 resolution; it has been checked that the curves for T170 and T341 resolutions, subjected to the same test, do match very closely. In fact, the disagreement is much stronger, compared with the similar test in the control case, which is in fact performed at much lower resolutions (cf. green and black curves in Figure 5.13*a*). Clearly, the "extra modes" included in the T170 resolution in the RTG simulations affect $\langle u_{\rm eq} \rangle$ quantitatively.

Figure 5.14 illustrates the above points more lucidly with simulations at T85L30 resolution, for the control case (Figure 5.14*a*) and RTG case (Figure 5.15*b*). Criterion *i*) is met for the control case at T85 resolution, and has already been discussed above. Figure 5.14*a* demonstrates that criterion *ii*) is also met: the simulations are not sensitive to variations in ν_8, suggesting the control case is converged at T85 resolution. In contrast, Figure 5.14*b* demonstrates that criterion *ii*) is not met for the RTG case: the simulations are acutely sensitive to variations in ν_8. Moreover, superimposing the time series from the T170 resolution simulation illustrates that it

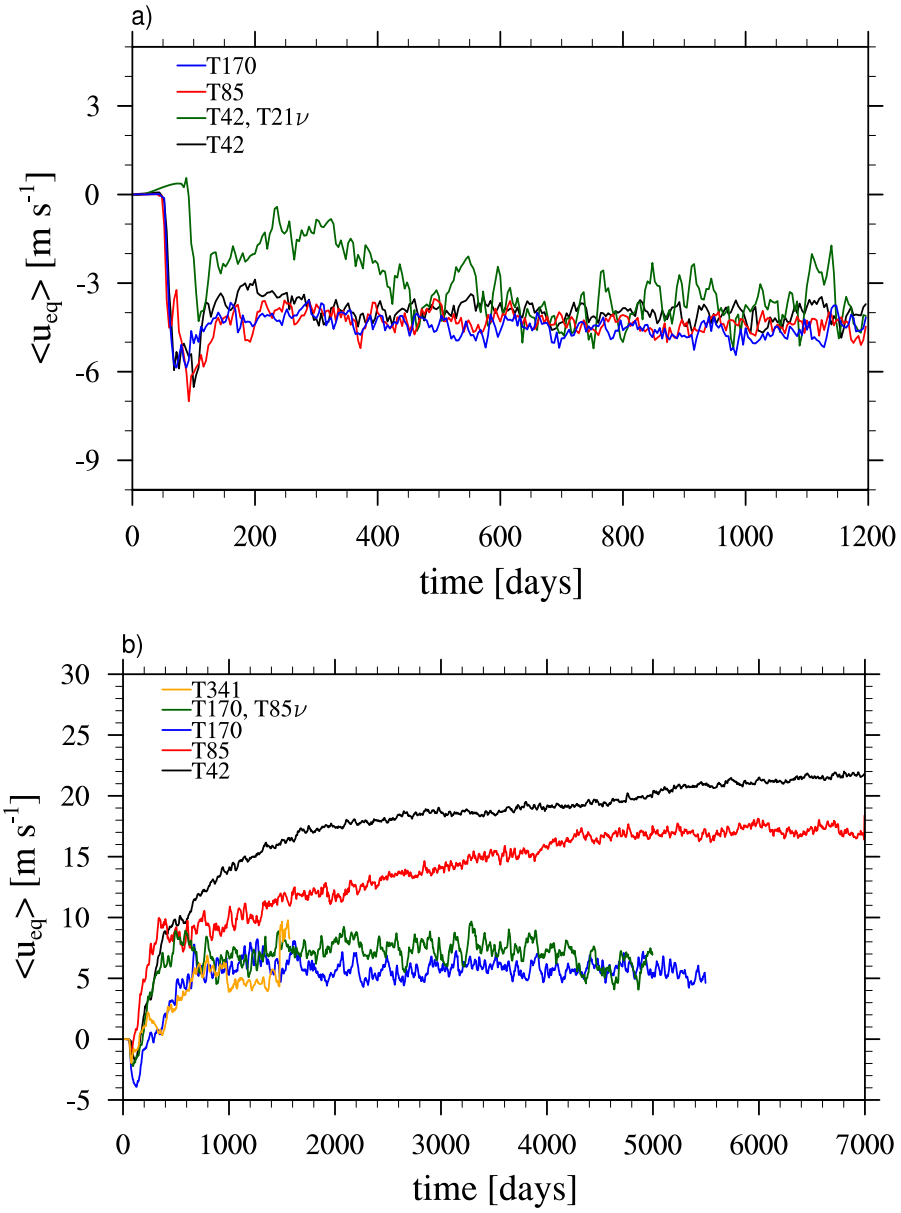

Figure 5.13: Time series of column-averaged zonal wind at the equator $\langle u_{\rm eq}\rangle$ [m s^{-1}] at varying horizontal resolutions for the control simulations (a) and the RTG simulations (b): $\langle u_{\rm eq}\rangle$ for {T42L30, T85L30, T170L30, T341L30} resolutions are shown in {black, red, blue, yellow}, respectively. The green curve in a) shows the control simulation performed at T42 horizontal resolution with ν_8 from a T21 resolution simulation, which is 25 times larger than in the "nominal" T42 simulation (black curve). The green curve in b) shows the RTG simulation performed at T170 horizontal resolution with ν_8 same as in the T85 resolution simulation (red curve). The magnitude of $\langle u_{\rm eq}\rangle$ is insensitive to horizontal resolution in the control simulations – *when properly tuned*, whereas $\langle u_{\rm eq}\rangle$ decreases with increasing resolution in the RTG simulations. In the latter simulations, T170L30 simulations with different ν_8 produce nearly-identical results.

is possible to erroneously conclude that criterion *i*) is met (see the blue and purple curves), if ν_8 were not varied at the T85 resolution. The equatorial superrotation is surprisingly weaker at the higher resolution. It is important to reiterate at this point that the "correct" ν_8 at T85 resolution cannot be determined a priori: it is only after performing the RTG simulation at T170L30 resolution and establishing that the converged simulations have $\langle u_{\rm eq} \rangle \approx 5\,{\rm m\,s^{-1}}$ that it is possible to tune ν_8 for an "optimal" simulation.

Extensive diagnostics of the simulations show that the stronger superrotation in the lower-resolution and/or stronger-dissipation simulation is due to the mitigation of nonlinear mixing of q at $\phi \approx \pm 15°$–$20°$. The $m \sim 6$ eddies at $\phi \approx \pm 15°$–$20°$ (Figure 5.6; see also Figures 5.7 and 5.13) are much weaker (or altogether absent) in the low-resolution/high-dissipation simulations. Because high-resolution/low-dissipation simulations permit stronger eddies, which mix q more efficiently, these simulations have a much more pronounced mixed zone at $\phi \approx \pm 10°$–$20°$ (as well as sharper "q-jumps" bounding the zone), compared to the low-resolution/high-dissipation simulations.[3] Note that the jumps would produce an eastward jet at that location and a weaker eastward, or even westward, flow in the mixed zone. Note however, that the equatorial Kelvin waves signal is independent of the horizontal resolution.

In addition to the reduction in q-mixing, diagnostics also show that the superrotation is enhanced in the lower-resolution and/or stronger-dissipation simulation, due to linear diffusion of q. In those simulations, the unmixed region at the equator is narrower and the jumps bounding the region are more diffused. Hence, the resulting jets at the subtropics are less sharp on the equatorward flanks and the flow is more strongly superrotating at the equator (cf. Figures 5.12*a*–*c*). The mechanism can be clearly seen in Figures 5.15 and 5.16, which show the q distributions on the $\theta = 330\,{\rm K}$ isentrope from two RTG simulations (one at T42 resolution and another at T170 resolution) at $t = 5000\,{\rm days}$. The q-gradients are clearly sharper at $\phi \approx \pm 25°$ and the equatorial step is wider in the T170 resolution calculation – i.e., the jets across the equator are much less "fused" into each other. It is important to understand that this is an entirely different mechanism than the Kelvin wave mechanism or the nonlinear mixing just discussed.

[3]Note, $\overline{q} = \overline{q}(\phi)$ forms a "staircase-like" structure, with "steps" and "jumps" (see e.g., Dritschel and McIntyre, 2008, and references therein).

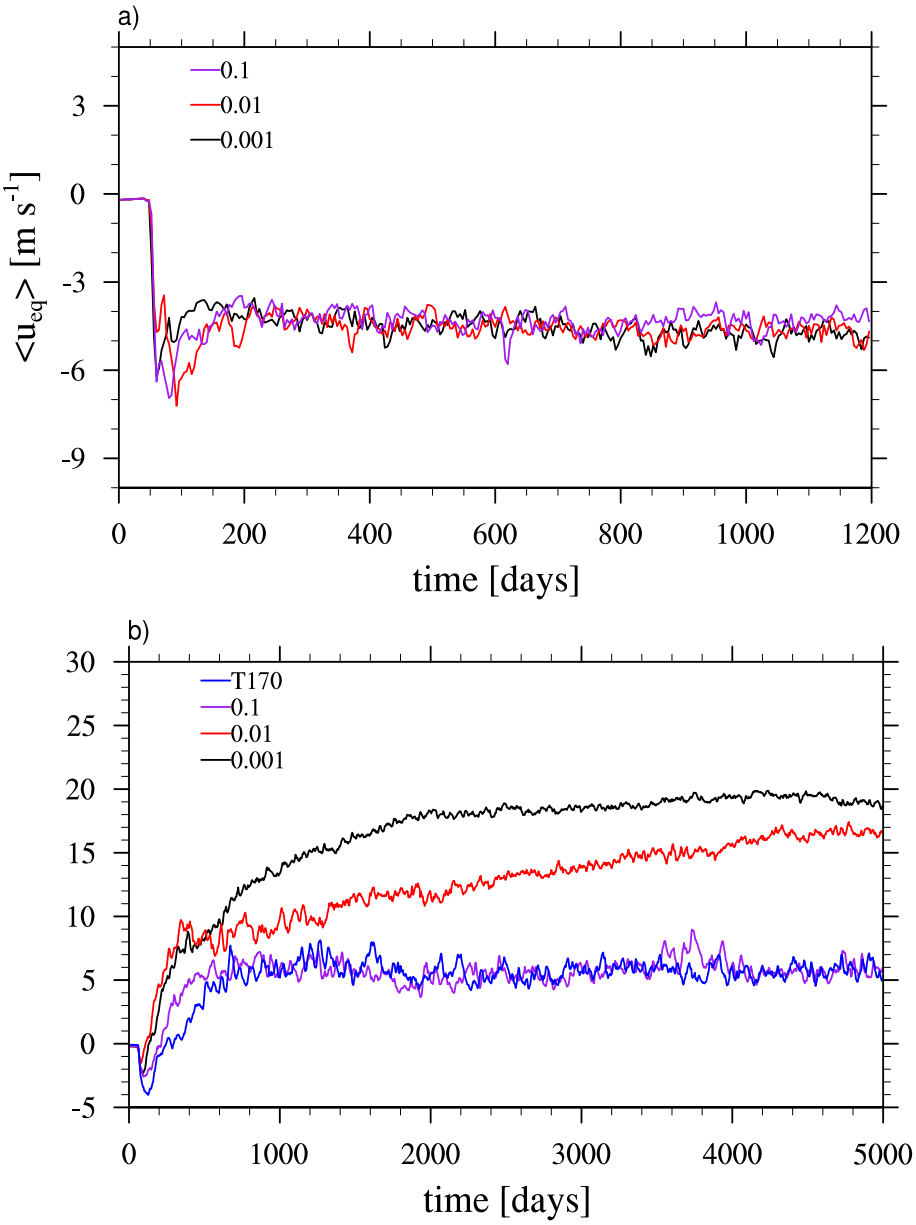

Figure 5.14: Time series of $\langle u_{\rm eq} \rangle$ [m s^{-1}] at T85L30 resolution with varying ν_8 for the control simulation (a) and the RTG simulation (b). The dissipation coefficient ν_8 is chosen such that $\tau_{\rm d}$ is 0.001 days (black curve); 0.01 days (red curve); and, 0.1 days (blue curve), respectively. In addition, $\langle u_{\rm eq} \rangle$ from the nominal T170L30 resolution simulation is plotted in panel b). Note the insensitivity of the control simulations to ν_8 but the reduction of $\langle u_{\rm eq} \rangle$ with decreasing ν_8 in the RTG simulations. Note also that T170L30 results are same as T85L30 results with $\tau_{\rm d} = 0.1$ days.

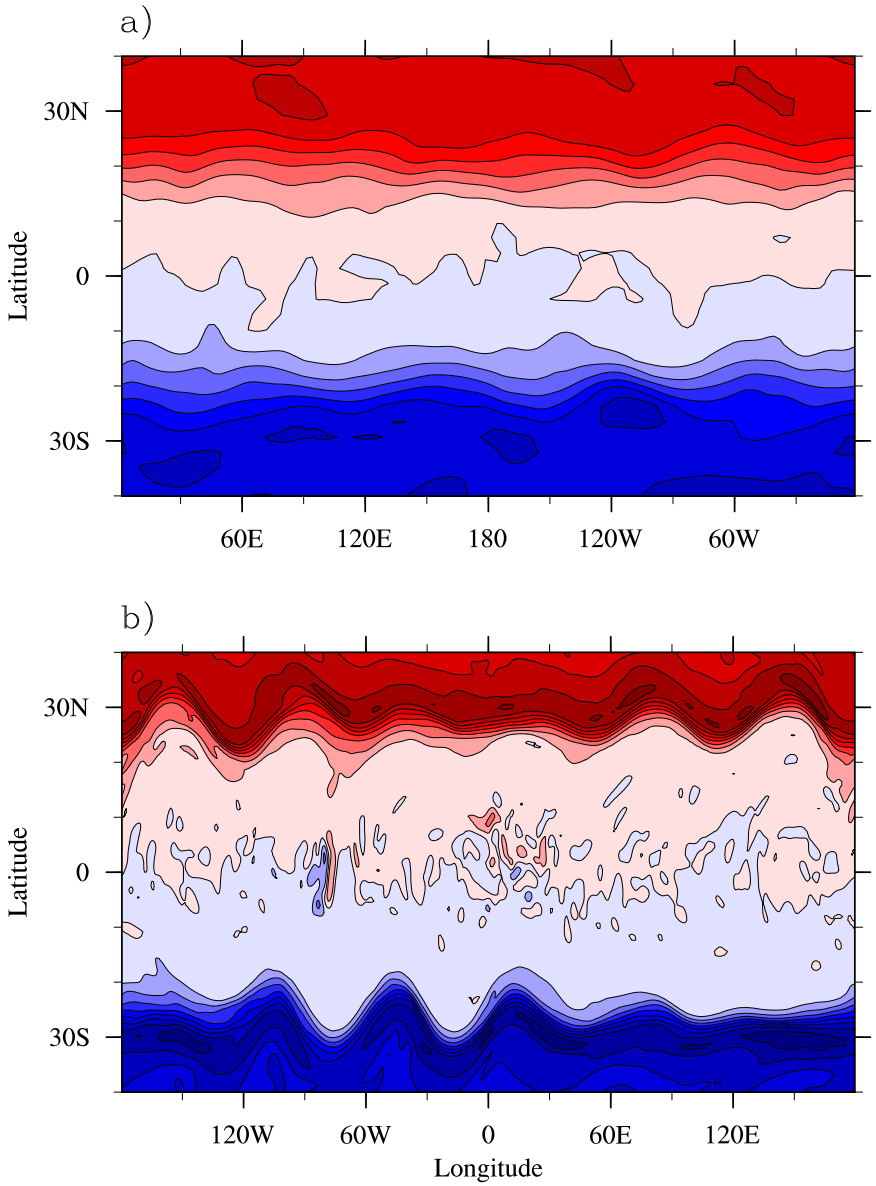

Figure 5.15: Ertel potential vorticity, q [K m^2 kg^{-1} s^{-1}] for the RTG simulation at T42L30 (a) and T170L30 (b) resolutions. The fields in cylindrical-equidistant view, for $-40° < \phi < 40°$, on the $\Theta = 330$ K isentropic surface (approximately at the $p = 200$ hPa level in the tropics), at $t = 5000$ days are shown. Maximum and minimum values are $\pm 8 \times 10^{-6}$ K m^2 kg^{-1} s^{-1}, with contour interval 10^{-7} K m^2 kg^{-1} s^{-1}. Note more spread out q contours at T42L30 resolution.

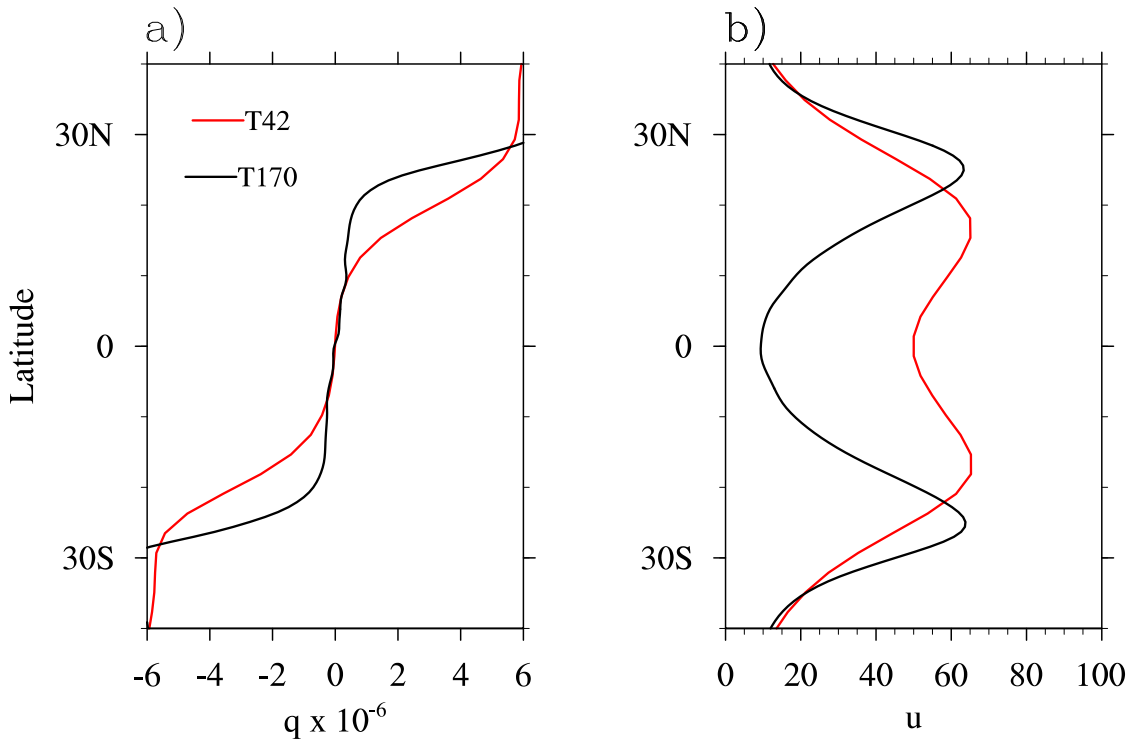

Figure 5.16: *a*): Zonal-mean Ertel potential vorticity, $\overline{q}$ [K m^2 kg^{-1} s^{-1}], on the $\Theta = 330$ K isentropic surface, at $t = 5000$ days for the RTG simulation at T42L30 (red) and T170L30 (black) resolution, respectively. *b*): Same as *a*) but zonal-mean zonal wind. The fields for $-40° < \phi < 40°$ are shown. As a result of enhanced PV diffusion at T42L30 resolution, the $\overline{q}$ gradients are larger poleward of $\phi = \pm 5°$: hence the subtropical jets are broader and their flanks extend more over the equator than at T170L30 resolution.

5.3.3 Other Sensitivities/Insensitivities

It is also important to note that the results discussed above apply for the specified forcing parameters only. In addition to resolution/dissipation, the magnitude of superrotation in the RTG simulation is sensitive to other parameters, such as $\{\gamma, \mathfrak{b}, \Delta T, T_s\}$ in equation (5.3). For example, for $\gamma \geq 0.05$ (with $\mathfrak{b} = 4$), the transition to superrotation – especially at high horizontal-resolution and/or low-dissipation – does not occur. However, transition to superrotation is still possible for $\gamma > 0.05$ – if baroclinic instability is allowed to occur at lower latitudes by setting $\mathfrak{b} > 4$, in agreement with Williams (2003). Setting $\Delta T > 60$ K (and keeping all other parameters fixed) also produces stronger superrotation because stronger meridional shear on the equatorward flanks of the subtropical jets is associated with stronger violation of the necessary criterion for barotropic instability than in the nominal RTG case.

The magnitude of superrotation in the RTG simulation is also somewhat sensitive to the form of the initial perturbation. A north-south symmetric perturbation—such as a small amplitude localized bump at $(\pm\phi_0, \lambda_0)$ or a pure spherical harmonic mode perturbation—produces north-south symmetric circulation and considerably stronger superrotation than in the simulations initialized with north-south asymmetric perturbation—such as Gaussian white noise. In such north-south symmetric simulations, the equatorial flow is purely zonal (i.e., does not meander) and as a result the superrotation is stronger. It is also worth noting that superrotation is generated in the RTG simulation even in the absence of the Rayleigh drag. Hence, superrotation can occur on planets with no solid surface as long as the equator-to-pole equilibrium temperature gradient is weakened in the region below. Finally, it is worth re-iterating that *subrotation* is even produced in a zonally-symmetric RTG simulation (i.e., with no initial perturbation applied to initiate three-dimensional turbulent flow). Hence, superrotation in the RTG simulation requires the presence of non-axisymmetric eddies.

5.4 Summary and Conclusions

In this study, it has been shown that equatorial superrotation can be easily generated, even under axisymmetric thermal forcing – if the equator-to-pole surface temperature gradient is weaker than in the classic HS test case. Superrotation does not easily arise under axisymmetric forcing. However, superrotation can be generated and maintained even under this situation via barotropic instability.

When the equator-to-pole surface temperature gradient is reduced, the role of Rossby waves – produced by mid-latitude baroclinic instability – in converging westward momentum in the equatorial region is diminished. Also, if a wave "source" exists at the equator, superrotation can develop if the eddy angular momentum fluxes out of the region are strong enough and directed up the mean angular momentum gradient. As in Williams (2003), it is also observed here that barotropic instability provides the necessary stirring in the equatorial region. The instabilities push sharp gradients toward the equator and also excite large-scale, Kelvin waves that accelerate the zonal-mean zonal wind at the equator. In the control simulation the necessary criterion for barotropic or baroclinic instability are not satisfied in the equatorial region; hence, no mechanisms to provide stirring or excite Kelvin waves exist. It is possible that barotropic instability is the source of Kelvin waves in Mitchell and Vallis (2010) and Potter et al. (2014). For a fixed phase speed, the meridional width of the Kelvin waves increases with decreasing $R_{\rm p}$ (and Ω). Thus the stirring does not need to be located as close to the equator as in the RTG simulation discussed here with Earth's Ω and R_p. Hence, unlike advocated in Potter et al. (2014) it is not possible to separate barotropic instability mechanism from the Kelvin wave mechanism in simulations with axisymmetric forcing.

To adequately resolve the dynamics of angular momentum fluxes near the equator, large horizontal resolution is required ($\gtrsim$T170). In low resolution or strongly dissipated simulations, potential vorticity mixing by the $m\sim6$ modes equatorward of $\phi \approx \pm 25^\circ$ is weaker and potential vorticity is more spread out by diffusion than in the high resolution or low dissipation simulations. Therefore, in the under-resolved case the superrotation is stronger and the subtropical jets are less sharp on their equatorward flanks. The stronger resolution requirement for the RTG simulation, compared to the control simulation (which is converged at T85 horizontal resolution), is due to the near-equatorial location of the mixing region in the former case. When the subtropical jets (and hence the mixing zone and the source of Kelvin waves) are located further poleward, low resolution therefore could still induce superrotation.

One could debate about whether such a mechanism is physically realistic, but perhaps argument could be made for the large variety of planets currently being discovered (see e.g., http://exoplanet.eu). Certainly, the choice of the RTG heating profile is not realistic for the present-day climate. However, such heating arrangement can be relevant to the runaway greenhouse Earth or other terrestrial planets characterized by thick cloud cover, as just discussed.

6 Conclusion

Baroclinic jet dynamics on both synchronized and unsynchronized hot-Jupiters and Earth-like planets has been the focus of this thesis. Hot-Jupiters are characterized by moderate rotation rates (∼few days), fast flow speeds (∼1000 m s^{-1}), hot equilibrium temperatures (∼2000 K), and, if spin-orbit synchronization is assumed, large (∼1000 K) equilibrium day-night temperature differences. These properties place hot-Jupiters in a dynamical parameter regime that has thus far received little attention in the area of classic geophysical fluid dynamics. In the astrophysical context, understanding jet dynamics on hot-Jupiters is important because it affects the temperature distribution and therefore, the observed signal. The Earth-like planets are also beginning to be accessible to characterization, making the study of their atmospheres extremely important and forefront research. Thus, there is a great opportunity to extend and challenge our current knowledge of atmospheric dynamics in conditions other than those of the present-day Earth or other Solar System bodies.

6.1 Summary

In this thesis general circulation models (GCMs) that solve the traditional primitive equations in spherical geometry have been used to study baroclinic jet dynamics on hot-Jupiters and Earth-like planets. Because of the extensive testing, validation and tuning, GCMs have been successful in studies of the Earth and some Solar System planets. However, performance and predictive capabilities of a GCM can be stretched beyond the limit under markedly different dynamical regime and forcing conditions. Full GCMs are complex and require a number of physical parameters and assumptions about fundamental physical processes (e.g., convection, radiation, wave-drag, etc.), which are as yet unconstrained or unobtainable from the first principles for an extrasolar planet. Hence, the overall approach taken in this thesis is to strive for minimal complexity and minimal reliance on unknown constraints and to set up idealized scenarios where dynamical mechanisms and model performance

can be studied in a "clean" way.

Baroclinic instability is one such dynamical mechanism, which has thus far not been studied on exoplanets. It is important for transporting and mixing heat, as well as for influencing large-scale variability. In Chapter 3, baroclinic instability under conditions relevant to unsynchronized hot-Jupiters was studied using both linear normal mode analysis and non-linear initial value simulations in adiabatic condition. In particular, stability properties of large-scale, high-speed ($\sim$ 1000 m s^{-1}) jets similar to those observed in diabatic simulations of hot-Jupiters (e.g., Showman et al., 2008; Rauscher and Menou, 2010; Thrastarson and Cho, 2010) were assessed. The focus has been on broad, eastward equatorial jets and westward, high-latitude jets. Such jets were shown to be baroclinically unstable on timescales of few to few tens of planetary rotations—despite the planetary size of the Rossby deformation scale. It was also shown that due to changes in sign of the jet curvature, unstable jets evolved differently depending on their sign (eastward or westward): westward jets are more stable than their eastward counterparts and require larger vertical shear to satisfy the necessary condition for baroclinic instability.

Throughout this thesis, particular attention was paid to model convergence with resolution and numerical dissipation. By performing baroclinic instability simulations in Chapter 3 with a range of horizontal resolutions (from T21 to T170) and hyperdissipation coefficients, it was shown that the instability is poorly (or not at all) captured at horizontal resolutions below T85 and/or for high numerical viscosity coefficients. Because large numerical viscosities are often used to balance strong thermal forcing in diabatic hot-Jupiter simulations, the implication is that baroclinic instability is unlikely to be represented in current simulations—even if necessary instability criteria are satisfied. Moreover, large-scale baroclinic instability is not likely to be important in diabatic simulations with thermal relaxation times shorter than the instability timescales (few to few tens of planetary rotations).

In the relatively untested area of extrasolar planet atmospheric modelling, it is important to ask if the results of a numerical simulation are of physical or numerical origin. The GCMs can easily be stretched to their limits—especially in an attempt to model extreme hot-Jupiter conditions (i.e., fast flow speeds, large equilibrium temperature gradients, and short $\sim 10 - 100$ h thermal relaxation times). Motivated by the variability in published hot-Jupiter simulation results by others and the findings in Chapter 3, a thorough and systematic intercomparison of five GCMs (BOB, CAM, IGCM, MITgcm and PEQMOD) for hot-Jupiter conditions was performed in Chapter 4. All tested GCMs have recently been used to study hot-Jupiter atmospheres and they all solve the traditional primitive equations, but employ a

range of algorithms for the spatial discretization (pseudospectral or finite volume) and numerical dissipation (hyperdissipation and Shapiro filter). The GCMs were tested under three tests which assessed: I) an ability of a truly inviscid model to maintain a balanced steady state; II) the ability of a model to faithfully capture the non-linear evolution of a baroclinic wave studied in Chapter 3; and, III) the performance of a model subject to a typical "hot-Jupiter-like" strong, zonally-asymmetric, mode-1 thermal forcing. In the first two test cases all models performed as expected apart from MITgcm in cubed sphere (CS) grid. In test case I), the eight special corner points inherent in the CS mesh quickly degraded the balanced state and caused the simulation to blow up. In test case II), the special corner points provided an additional perturbation and caused the unstable wave field to evolve differently in MITgcm in CS grid than in the other tested models. In contrast to test cases I) and II), the extreme forcing conditions (i.e., thermal relaxation times of $\sim$ 10-100 h, and 1000 K day-night equilibrium temperature differences) in test case III) produced a broad range of behaviour in the model circulations. While all models produced time-variable quadrupole flow structures with a superrotating jet at the equator, significant phase and amplitude differences were present in the prognostic fields. In contrast with many published studies, the implication of these results is that specific quantitative predictions (such as the location of large vortices and hottest regions) by GCMs should be viewed with caution.

Throughout Chapter 4, a careful attention was paid to the conservation properties of GCMs. In particular, it was shown that extreme forcing conditions in test case III), can lead to a severe violation of globally integrated absolute angular momentum conservation. For example, in simulations with MITgcm in CS grid the globally integrated angular momentum increased by as much as 45% at the end of the integration ($t = 100\,\tau$, where τ is planet day). Hence, the normally "harmless" small non-conservation in Earth-like conditions, for which the GCMs have been constructed and tested, could be exacerbated under hot-Jupiter-like forcing conditions. Severe non-conservation of globally integrated angular momentum can lead to unrealistic simulated jet magnitudes: for example, supersonic flows that are not permitted by the hydrostatic primitive equations with free slip boundary conditions, can be produced. However, as demonstrated in Chapter 4, globally integrated angular momentum non-conservation is not always apparent by looking at the flow fields alone. Therefore, diagnosing globally integrated angular momentum conservation in GCMs should be standard practice—especially when the GCMs are used in new and untested parameter regime.

Many diabatic simulations of hot-Jupiter atmospheres, including those presented

in test case III) in Chapter 4, produce a high-speed, superrotating jet at the equator when forced with zonally-asymmetric thermal forcing. However, equatorial superrotation is not a climate mode generally encountered in the atmospheres of zonally-symmetrically forced, rapidly rotating, Earth-size planets. For example, in the zonal mean the Earth's atmosphere subrotates weakly at the equator. However, in Chapter 5, it was shown that transition to equatorial superrotation in the atmospheres of Earth-like planets is possible—even under zonally-symmetric thermal forcing—if the equator-to-pole surface equilibrium temperature gradient is weakened near the surface. The main factors that contributed to the generation of superrotation under weakened temperature gradient are: 1) suppression of breaking Rossby waves (generated by midlatitude baroclinic instability), that decelerate the equatorial flow; and, 2) generation of inertial and barotropic instabilities in the equatorial region, that provide stirring to accelerate equatorial flow. As has been common practice throughout this thesis, a careful attention was paid to the convergence of model solutions with resolution. It was shown that the magnitude of superrotation is sensitive to the horizontal resolution and dissipation specifications. Simulations with low horizontal resolution and/or strong dissipation produced considerably stronger (by 4 times) superrotation and convergence of model results was not achieved at horizontal resolution lower than T170. In low resolution and/or strong dissipation simulations, it was found that the enhanced diffusion of potential vorticity and the reduced potential vorticity mixing on the equatorward flanks of the subtropical jets cause the jets to merge together at the equator. As a result, stronger superrotation is produced. The T170 resolution requirement for the reduced temperature gradient regime is somewhat stronger than for the classic, non-superrotating regime (i.e., Held and Suarez (1994)), for which convergence is achieved at T85 horizontal resolution. Therefore, as has been advocated throughout this thesis, numerical convergence must be carefully assessed in GCM simulations for each problem and setup considered.

6.2 Outlook and Future Work

The results presented in Chapter 3 showed that baroclinic instability is likely to play a role in weather, general circulation and large-scale variability on hot gas giant planets on time-scales of a few to few tens of planetary rotation periods. However, given that many typical hot-Jupiter simulations employ thermal relaxation times significantly shorter than the baroclinic instability time-scales, the instability is not likely

to play a significant role in current strongly forced hot-Jupiter simulations. Despite this, adiabatic simulations studied in Chapter 3 are important to cleanly delineate many subtle effects in rotating-stratified fluid that could obscure baroclinic instability. More importantly, adiabatic simulations are essential as a foundation for the instability under forced conditions. The role of forcing on the instability and the background flow itself remains to be elucidated and warrants further study as at present, it is unclear how realistic the often used short (2–100 h) thermal relaxation times and large day-night equilibrium temperature gradients are. Preliminary simulations of diabatically forced hot-Jupiter atmospheres indicate that baroclinic instability plays an important part when the thermal relaxation times are longer (i.e., few to few tens of τ) and the day-night equilibrium temperature differences are smaller ($\lesssim$100 K) than in many published "shallow atmosphere" hot-Jupiter simulations[1] to date (e.g., TC3 in Chapter 4, and Menou and Rauscher (2009); Thrastarson and Cho (2010, 2011); Bending et al. (2013)). The stably stratified radiative zone on hot-Jupiters may extend to as deep as 1000 bars and, if equation (2.10) is appropriate for estimating radiative time-scales, such "weak" forcing conditions might be relevant below $p \sim 1$ bar level. However, baroclinic instability is not likely to be captured in the current "deep atmosphere" simulations[2] either (e.g., Cooper and Showman (2005); Rauscher and Menou (2010); Liu and Showman (2013)). This is because the use of large numerical dissipation coefficients is required to prevent a model from crashing at high altitudes where strong thermal forcing generates fast flow speeds. As a result, lower altitude regions, characterized by weaker thermal forcing, are over-dissipated since the current practice is to employ a constant (vertically-independent) dissipation in the modelled domain.

If present, baroclinic instability could generate large, long-lived storms that could be observed remotely. Sharp fronts produced in baroclinic instability life-cycles can also act as a gravity wave source (e.g., O'Sullivan and Dunkerton, 1995; Plougonven and Snyder, 2007). Gravity waves are expected to play an important role in stably stratified atmospheres of hot-Jupiters: they can modify the circulation through exerting accelerations (positive and negative) on the mean flow, as well as transporting heat vertically from deep regions to regions above and laterally from day side to night side (Watkins and Cho, 2010). Thus, studying the role of baroclinic instability in generation of gravity waves on an extrasolar planet is an interesting

[1]Here, "shallow atmosphere" simulations are those which aim to characterize hot-Jupiter general circulation above $p = 1$ bar region.

[2]Here, "deep atmosphere" simulations are those which aim to characterize hot-Jupiter general circulation in $10^{-5} < p < 1000$ bar region.

problem. The effect of concomitant eddies on the background flow was also only lightly touched on in Chapter 3, in which the main focus was on the instability and subsequent evolution of jets in isolation. Therefore, the full effect of baroclinic instability on the mean flow in hot-Jupiter conditions remains to be carefully studied and elucidated.

The new and relatively untested forcing and dynamical parameter regime relevant to hot-Jupiters presents challenges to GCMs. Claims of predictions or even attempts to fruitfully model mechanisms, important instabilities and wave types are moot if GCM results are of numerical origin. As was identified in Chapter 4, conservation of global angular momentum is severely violated in MITgcm in CS grid when short thermal relaxation times and large equilibrium temperature gradients are used to force the flow. As alluded to in Chapter 4, using an alternative vorticity advection scheme in MITgcm in CS grid improves global angular momentum conservation. In diabatic hot-Jupiter simulations especially, it is found that the choice of the advection scheme (potential enstrophy conserving, energy conserving, or, energy-enstrophy conserving scheme) has a profound effect on global angular momentum conservation in MITgcm in CS grid. With the use of the non-default, energy conserving advection scheme global angular momentum conservation is substantially improved over the default enstrophy conserving scheme in moderate-time integration problems ($t \sim 100\,\tau$) started from an initial rest state. However, in long-time integration problems ($t \geq 1000\,\tau$), globally integrated angular momentum is poorly or not at all conserved with all schemes—especially at low and intermediate horizontal resolutions (C16 and C32). It should be emphasized that low resolution, long-time integration simulations are common in current hot-Jupiter studies (e.g., Cooper and Showman, 2005; Rauscher and Menou, 2010). In addition, it is found that the choice of the "optimal" advection scheme for MITgcm in CS grid is not always obvious and depends on the initial condition, resolution and dissipation specifications. Moreover, the global angular momentum non-conservation in MITgcm in CS grid is not limited to extreme forcing conditions only. For example, MITgcm simulations in CS grid experience runaway of globally integrated angular momentum in the well-studied Held and Suarez (1994) test case when the bottom Rayleigh drag is not applied. Interestingly, globally integrated angular momentum is conserved almost exactly in MITgcm when Rayleigh drag is applied—this is despite the globally integrated angular momentum not being conserved by the primitive equations in the presence of momentum sinks. It is therefore possible that large enough momentum sources and sinks arising from the inclusion of physical parametrizations will mask the inability of a GCM to conserve globally integrated angular momentum.

Therefore, assessing the impact of physical parametrizations on not only global but also local angular momentum conservation, would be advantageous to the whole atmospheric modelling community.

Somewhat disconcertingly, it is also found that in long-time integrations (i.e., $t \geq 1000\,\tau$) of strongly forced hot-Jupiter atmospheres, the errors associated with globally integrated angular momentum conservation are significant not only in MITgcm in non-uniform CS grid, but also in pseudospectral models—IGCM and CAM—and in MITgcm in uniform LL grid. The runaway of globally integrated angular momentum appears to be tied in with the insufficient numerical dissipation and/or resolution in a model and unphysical accumulation of energy in low wavenumber modes. Hence, carefully isolating the interplay between dissipation and/or resolution and angular momentum conservation would be an interesting problem to address. Also, the most obvious difference between the pseudospectral models that almost exactly conserve globally integrated angular momentum (BOB and PEQMOD) and those that do not (IGCM and CAM) is the lower boundary condition: in the former models rigid lower boundary condition (i.e., zero vertical velocity) with zero vertically integrated divergence over the whole atmosphere is implemented whereas in the latter models the surface pressure surface is "free" (i.e., non-zero vertical velocity). Therefore, it is possible that fast speed flows produced near the lower boundary in the diabatically forced hot-Jupiter simulations in Chapter 4 cause the models employing the free surface boundary condition to be less stable.

Given that the codes are pushed to their limits under typical hot-Jupiter setup, it seems obvious to ask whether setting up simulations in this way is realistic. Could some of the "bad" numerical behaviour be eliminated if the simulations were started from a more balanced state than rest? What is the appropriate way to force the simulations? Is choosing the equilibrium temperature based purely on the geometric arguments rather than climatological temperatures in balance with the flow appropriate? Is the extension of the lower boundary to $p = 100 - 1000$ bars, as has become more common in recent hot-Jupiter studies (e.g., Cooper and Showman, 2005; Showman et al., 2008, 2009; Rauscher and Menou, 2010), realistic given that the setup produces supersonic winds in hydrostatic primitive equation models? These are just some of the important questions to address in future studies before embarking on increasing the complexity of a model itself. When more complex physical parametrizations are included, the differences between models are likely to be amplified. Carefully assessing the role of physical parametrizations on model results is, in itself, a challenge that needs to be addressed in the future.

Characterization of Earth-like planet atmospheres will become more important

not only because of the advancements in exoplanet measurement and detection techniques but also because of the increased efforts to understand future and past climate on the Earth. As demonstrated in Chapter 5, the general circulation on Earth-like planets can be markedly different from the present-day Earth if only one parameter—the magnitude of the equator-to-pole temperature gradient—is changed. However, even under relatively well-studied forcing conditions and dynamical parameter regimes, erroneous conclusions can easily be drawn if the results are not meticulously checked for convergence and accuracy.

In particular, equatorial dynamics warrants further study since it appears that the resolution requirements are much higher for adequate representation of eddies and vortices in the equatorial region. In addition, the role of parametrised dissipation on equatorial superrotation needs to be investigated further. It is possible that models employing different discretization techniques and dissipation schemes are not as sensitive to the choice of the dissipation coefficient and/or horizontal resolution as the pseudospectral model employing hyperviscosity. For example, the use of a less dissipative contour-advective algorithm (e.g., Dritschel et al., 1999) would likely lead to much better convergence of the reduced equator-to-pole surface temperature gradient simulations in Chapter 5. It is also possible that stronger superrotation is generated as a result of too much dissipation being applied to the mean flow. However, preliminary calculations with the pseudospectral model show that applying hyperdissipation on the eddies only does not lead to better convergence.

Another interesting problem to address is how inclusion of more physical processes such as convection, clouds, sub-grid scale parametrizations etc. affect the equatorial superrotation and the resolution requirements. Superrotation is likely to feed back on the climate in complex ways. Therefore, its influence on climate should also be studied using full-complexity GCMs. Thus, the lessons learned from this thesis can be applied and extended not only by the exoplanet community but also by the climate community.

Bibliography

Adcroft et al. (2012). MITgcm User Manual.

Andrews, D. G. and McIntyre, M. E. (1978). On wave-action and its relatives. *Journal of Fluid Mechanics*, 89:647–664.

Arakawa, A. and Lamb, V. R. (1977). Computational design of the basic dynamical processes of the ucla general circulation model. *Methods in computational physics*, 17:173–265.

Arakawa, A. and Moorthi, S. (1988). Baroclinic Instability in Vertically Discrete Systems. *Journal of Atmospheric Sciences*, 45:1688–1708.

Asselin, R. (1972). Frequency Filter for Time Integrations. *Monthly Weather Review*, 100:487.

Beaulieu, J.-P., Tinetti, G., Kipping, D. M., Ribas, I., Barber, R. J., Cho, J. Y.-K., Polichtchouk, I., Tennyson, J., Yurchenko, S. N., Griffith, C. A., Batista, V., Waldmann, I., Miller, S., Carey, S., Mousis, O., Fossey, S. J., and Aylward, A. (2011). Methane in the Atmosphere of the Transiting Hot Neptune GJ436B? *The Astrophysical Journal*, 731:16.

Bender, C. M. and Orszag, S. A. (1999). *Advanced mathematical methods for scientists and engineers I: Asymptotic methods and perturbation theory*, volume 1. Springer.

Bending, V., Lewis, S., and Kolb, U. (2013). Benchmark experiments with global climate models applicable to extrasolar gas giant planets in the shallow atmosphere approximation. *Monthly Notices of the Royal Astronomical Society*, 428(4):2874–2884.

Blackburn, M. (1985). Program description for the multi-level global spectral model.

Blackburn, M., Williamson, D. L., Nakajima, K., Ohfuchi, W., Takahashi, Y. O., Hayashi, Y.-Y., Nakamura, H., Ishiwatari, M., McGregor, J. L., Borth, H., et al. (2013). The aqua-planet experiment (ape): Control sst simulation. *Journal of the Meteorological Society of Japan*, 91:17–56.

Boer, G. J. and Denis, B. (1997). Numerical convergence of the dynamics of a GCM. *Climate Dynamics*, 13:359–374.

Boyd, J. P. (2001). *Chebyshev and Fourier spectral methods*. Courier Dover Publications.

Burridge, D. M. and Haseler, J. (1977). A model for medium range weather forecast—adiabatic formulation. *ECMWF Tech. Rep.*, 4.

Canuto, C. G., Hussaini, M. Y., and Quarteroni, A. (2007). *Spectral methods: evolution to complex geometries and applications to fluid dynamics*. Springer.

Charbonneau, D., Allen, L. E., Megeath, S. T., Torres, G., Alonso, R., Brown, T. M., Gilliland, R. L., Latham, D. W., Mandushev, G., ODonovan, F. T., et al. (2005). Detection of thermal emission from an extrasolar planet. *The Astrophysical Journal*, 626(1):523.

Charney, J. G. (1947). The Dynamics of Long Waves in a Baroclinic Westerly Current. *Journal of Atmospheric Sciences*, 4:136–162.

Charney, J. G. and Stern, M. E. (1962). On the Stability of Internal Baroclinic Jets in a Rotating Atmosphere. *Journal of Atmospheric Sciences*, 19:159–172.

Chen, G., Held, I. M., and Robinson, W. A. (2007). Sensitivity of the latitude of the surface westerlies to surface friction. *Journal of the atmospheric sciences*, 64(8).

Cho, J. Y., Menou, K., Hansen, B. M., and Seager, S. (2008). Atmospheric circulation of close-in extrasolar giant planets. i. global, barotropic, adiabatic simulations. *The Astrophysical Journal*, 675(1):817.

Cho, J. Y.-K. (2008). Atmospheric dynamics of tidally synchronized extrasolar planets. *Philosophical Transactions of the Royal Society A: Mathematical, Physical and Engineering Sciences*, 366(1884):4477–4488.

Cho, J. Y.-K., Menou, K., Hansen, B. M., and Seager, S. (2003). The changing face of the extrasolar giant planet hd 209458b. *The Astrophysical Journal Letters*, 587(2):L117.

Cho, J. Y.-K., Polichtchouk, I., and Thrastarson, H. T. (2014). Sensitivity and variability redux in hot-jupiter flow simulations. *MNRAS*, submitted.

Cho, J. Y.-K. and Polvani, L. M. (1996). The emergence of jets and vortices in freely evolving, shallow-water turbulence on a sphere. *Physics of Fluids (1994-present)*, 8(6):1531–1552.

Collins, W. D., Rasch, P. J., Boville, B. A., Hack, J. J., McCaa, J. R., Williamson, D. L., Kiehl, J. T., Briegleb, B., Bitz, C., Lin, S., et al. (2004). Description of the ncar community atmosphere model (cam 3.0). *NCAR Tech. Note NCAR/TN-464+ STR*.

Cooper, C. S. and Showman, A. P. (2005). Dynamic meteorology at the photosphere of hd 209458b. *The Astrophysical Journal Letters*, 629(1):L45.

Cooper, C. S. and Showman, A. P. (2006). Dynamics and Disequilibrium Carbon Chemistry in Hot Jupiter Atmospheres, with Application to HD 209458b. *The Astrophysical Journal*, 649:1048–1063.

Cowan, N., Agol, E., and Charbonneau, D. (2007). Hot nights on extrasolar planets: mid-infrared phase variations of hot jupiters. *Monthly Notices of the Royal Astronomical Society*, 379(2):641–646.

Crossfield, I. J., Knutson, H., Fortney, J., Showman, A. P., Cowan, N. B., and Deming, D. (2012). Spitzer/mips 24 μm observations of hd 209458b: Three eclipses, two and a half transits, and a phase curve corrupted by instrumental sensitivity variations. *The Astrophysical Journal*, 752(2):81.

Daley, R. (1988). The normal modes of the spherical non-hydrostatic equations with applications to the filtering of acoustic modes. *Tellus A*, 40(2):96–106.

Dobbs-Dixon, I., Cumming, A., and Lin, D. (2010). Radiative hydrodynamic simulations of hd209458b: Temporal variability. *The Astrophysical Journal*, 710(2):1395.

Dobbs-Dixon, I. and Lin, D. (2008). Atmospheric dynamics of short-period extrasolar gas giant planets. i. dependence of nightside temperature on opacity. *The Astrophysical Journal*, 673(1):513.

Dritschel, D. and McIntyre, M. (2008). Multiple jets as pv staircases: The phillips effect and the resilience of eddy-transport barriers. *Journal of the Atmospheric Sciences*, 65(3).

Dritschel, D. G., Polvani, L. M., and Mohebalhojeh, A. R. (1999). The contour-advective semi-lagrangian algorithm for the shallow water equations. *Monthly Weather Review*, 127(7):1551–1565.

Durran, D. R. (1999). *Numerical Methods for Wave Equations in Geophisical Fluid Dynamics/c Dale R. Durran.* Number 32. Springer.

Eady, E. (1949). Long waves and cyclone waves. *Tellus*, 1(3):33–52.

Eliasen, E., Machenhauer, B., and Rasmussen, E. (1970). *On a numerical method for integration of the hydrodynamical equations with a spectral representation of the horizontal fields.* Kobenhavns Universitet, Institut for Teoretisk Meteorologi.

Feldstein, S. B. (1991). A Comparison of the Weakly Nonlinear Instability of Westerly and Easterly Jets in a Two-Layer Beta-Plane Model. *Journal of Atmospheric Sciences*, 48:1701–1717.

Fraedrich, K. and Frisius, T. (2001). Two-level primitive-equation baroclinic instability on an f-plane. *Quarterly Journal of the Royal Meteorological Society*, 127(576):2053–2068.

Gall, R. (1976). Structural changes of growing baroclinic waves. *Journal of Atmospheric Sciences*, 33:374–390.

Gfdl Global Atmospheric Model Development Team: (2004). The New GFDL Global Atmosphere and Land Model AM2 LM2: Evaluation with Prescribed SST Simulations. *Journal of Climate*, 17:4641–4673.

Gill, A. E. (1980). Some simple solutions for heat-induced tropical circulation. *Quarterly Journal of the Royal Meteorological Society*, 106:447–462.

Goldreich, P. and Soter, S. (1966). Q in the solar system. *Icarus*, 5(1):375–389.

Green, J. (1960). A problem in baroclinic stability. *Quarterly Journal of the Royal Meteorological Society*, 86(368):237–251.

Grillmair, C. J., Burrows, A., Charbonneau, D., Armus, L., Stauffer, J., Meadows, V., van Cleve, J., von Braun, K., and Levine, D. (2008). Strong water absorption in the dayside emission spectrum of the planet hd 189733b. *Nature*, 456(7223):767–769.

Guillot, T. and Showman, A. (2002). Evolution of "51 pegasus b-like" planets. *Astronomy and Astrophysics*, 385(1):156–165.

Hayashi, Y. (1971). A generalized method of resolving disturbances into progressive and retrogressive waves by space fourier and time cross-spectral analyses. *J. Meteor. Soc. Japan*, 49:125–128.

Held, I. M. and Hoskins, B. J. (1985). Large-scale eddies and the general circulation of the troposphere. *Advances in geophysics.*, 28:3–31.

Held, I. M. and Suarez, M. J. (1994). A Proposal for the Intercomparison of the Dynamical Cores of Atmospheric General Circulation Models. *Bulletin of the American Meteorological Society*, 75:1825–1830.

Heng, K., Menou, K., and Phillipps, P. J. (2011). Atmospheric circulation of tidally locked exoplanets: a suite of benchmark tests for dynamical solvers. *Monthly Notices of the Royal Astronomical Society*, 413(4):2380–2402.

Heng, K. and Vogt, S. S. (2011). Gliese 581g as a scaled-up version of earth: atmospheric circulation simulations. *Monthly Notices of the Royal Astronomical Society*, 415(3):2145–2157.

Hide, R. (1969). Dynamics of the atmospheres of the major planets with an appendix on the viscous boundary layer at the rigid bounding surface of an electrically-conducting rotating fluid in the presence of a magnetic field. *Journal of the Atmospheric Sciences*, 26(5):841–853.

Holton, J. (1992). *An introduction to dynamic meteorology (International geophysics series, San Diego, New York*. Academic Press.

Hoskins, B., McIntyre, M., and Robertson, A. W. (1985). On the use and significance of isentropic potential vorticity maps. *Quarterly Journal of the Royal Meteorological Society*, 111(470):877–946.

Hoskins, B., Neale, R., Rodwell, M., and YANG, G.-Y. (1999). Aspects of the large-scale tropical atmospheric circulation. *Tellus B*, 51(1):33–44.

Iga, S.-i. and Matsuda, Y. (2005). Shear instability in a shallow water model with implications for the venus atmosphere. *Journal of the atmospheric sciences*, 62(7):2514–2527.

Iro, N., Bezard, B., and Guillot, T. (2004). A time-dependent radiative model of hd209458b. *arXiv preprint astro-ph/0409468*.

Jablonowski, C. and Williamson, D. L. (2006). A baroclinic instability test case for atmospheric model dynamical cores. *Quarterly Journal of the Royal Meteorological Society*, 132(621C):2943–2975.

James, I. (1987). Suppression of baroclinic instability in horizontally sheared flows. *Journal of the atmospheric sciences*, 44(24):3710–3720.

James, I. N. (1995). *Introduction to circulating atmospheres*. Cambridge University Press.

Kasahara, A. (1974). Various vertical coordinate systems used for numerical weather prediction. *Monthly Weather Review*, 102(7):509–522.

Kaspi, Y., Flierl, G. R., and Showman, A. P. (2009). The deep wind structure of the giant planets: Results from an anelastic general circulation model. *Icarus*, 202(2):525–542.

Kasting, J. F. (1988). Runaway and moist greenhouse atmospheres and the evolution of earth and venus. *Icarus*, 74(3):472–494.

Kataria, T., Showman, A. P., Lewis, N. K., Fortney, J. J., Marley, M. S., and Freedman, R. S. (2013). Three-dimensional atmospheric circulation of hot jupiters on highly eccentric orbits. *The Astrophysical Journal*, 767(1):76.

Kidston, J. and Vallis, G. (2010). Relationship between eddy-driven jet latitude and width. *Geophysical Research Letters*, 37(21).

Kirtman, B. P., Bitz, C., Bryan, F., Collins, W., Dennis, J., Hearn, N., Kinter III, J. L., Loft, R., Rousset, C., Siqueira, L., et al. (2012). Impact of ocean model resolution on ccsm climate simulations. *Climate dynamics*, 39(6):1303–1328.

Knutson, H. A., Charbonneau, D., Allen, L. E., Fortney, J. J., Agol, E., Cowan, N. B., Showman, A. P., Cooper, C. S., and Megeath, S. T. (2007). A map of the day–night contrast of the extrasolar planet hd 189733b. *Nature*, 447(7141):183–186.

Knutson, H. A., Charbonneau, D., Cowan, N. B., Fortney, J. J., Showman, A. P., Agol, E., Henry, G. W., Everett, M. E., and Allen, L. E. (2009). Multiwavelength constraints on the day-night circulation patterns of hd 189733b. *The Astrophysical Journal*, 690(1):822.

Kuo, H. (1979). Baroclinic instabilities of linear and jet profiles in the atmosphere. *Journal of Atmospheric Sciences*, 36:2360–2378.

Langton, J. and Laughlin, G. (2007). Observational consequences of hydrodynamic flows on hot jupiters. *The Astrophysical Journal Letters*, 657(2):L113.

Lauritzen, P. H., Jablonowski, C., and Taylor, M. (2011). *Numerical techniques for global atmospheric models*. Springer.

Lauritzen, P. H., Jablonowski, C., Taylor, M. A., and Nair, R. D. (2010). Rotated versions of the jablonowski steady-state and baroclinic wave test cases: A dynamical core intercomparison. *Journal of Advances in Modeling Earth Systems*, 2(4).

Lebonnois, S., Lee, C., Yamamoto, M., Dawson, J., Lewis, S. R., Mendonca, J., Read, P., Parish, H. F., Schubert, G., Bengtsson, L., Grinspoon, D., Limaye, S. S., Schmidt, H., Svedhem, H., and Titov, D. V. (2013). *Models of Venus Atmosphere*, page 129.

Leconte, J., Forget, F., Charnay, B., Wordsworth, R., and Pottier, A. (2013). Increased insolation threshold for runaway greenhouse processes on earth-like planets. *Nature*, 504(7479):268–271.

Lee, C., Lewis, S., and Read, P. (2007). Superrotation in a venus general circulation model. *Journal of Geophysical Research: Planets (1991–2012)*, 112(E4).

Lewis, N. K., Showman, A. P., Fortney, J. J., Marley, M. S., Freedman, R. S., and Lodders, K. (2010). Atmospheric circulation of eccentric hot neptune gj436b. *The Astrophysical Journal*, 720(1):344.

Lissauer, J. J., Marcy, G. W., Bryson, S. T., Rowe, J. F., Jontof-Hutter, D., Agol, E., Borucki, W. J., Carter, J. A., Ford, E. B., Gilliland, R. L., et al. (2014). Validation of kepler's multiple planet candidates. ii. refined statistical framework and descriptions of systems of special interest. *The Astrophysical Journal*, 784(1):44.

Liu, B. and Showman, A. P. (2013). Atmospheric circulation of hot jupiters: insensitivity to initial conditions. *The Astrophysical Journal*, 770(1):42.

Lorenz, E. N. (1960). Energy and numerical weather prediction. *Tellus*, 12(4):364–373.

Matsuno, T. (1966). Quasi-geostrophic motions in the equatorial area. *J. Meteor. Soc. Japan*, 44(1):25–43.

Mayor, M. and Queloz, D. (1995). A jupiter-mass companion to a solar-type star. *Nature*, 378(6555):355–359.

Menou, K. and Rauscher, E. (2009). Atmospheric circulation of hot jupiters: a shallow three-dimensional model. *The Astrophysical Journal*, 700(1):887.

Merlis, T. M. and Schneider, T. (2010). Atmospheric dynamics of earth-like tidally locked aquaplanets. *Journal of Advances in Modeling Earth Systems*, 2(12).

Mitchell, J. L. and Vallis, G. K. (2010). The transition to superrotation in terrestrial atmospheres. *Journal of Geophysical Research: Planets (1991–2012)*, 115(E12).

Nakamura, N. (1993a). An illustrative model of instabilities in meridionally and vertically sheared flows. *Journal of the atmospheric sciences*, 50(3).

Nakamura, N. (1993b). Momentum flux, flow symmetry, and the nonlinear barotropic governor. *Journal of the atmospheric sciences*, 50(14).

Orszag, S. A. (1970). Transform method for the calculation of vector-coupled sums: Application to the spectral form of the vorticity equation. *Journal of the Atmospheric Sciences*, 27(6):890–895.

O'Sullivan, D. and Dunkerton, T. J. (1995). Generation of inertia-gravity waves in a simulated life cycle of baroclinic instability. *Journal of the atmospheric sciences*, 52(21):3695–3716.

Pedlosky, J. (1964). The Stability of Currents in the Atmosphere and the Ocean: Part II. *Journal of Atmospheric Sciences*, 21:342–353.

Pedlosky, J. (1986). *Geophysical fluid dynamics*. Springer-Verlag New York Inc., New York, NY.

Phillips, N. A. (1951). *A simple three-dimensional model for the study of large-scale extratropical flow patterns*. PhD thesis, University of Chicago, Department of Meteorology.

Plougonven, R. and Snyder, C. (2007). Inertia Gravity Waves Spontaneously Generated by Jets and Fronts. Part I: Different Baroclinic Life Cycles. *Journal of Atmospheric Sciences*, 64:2502.

Polichtchouk, I. and Cho, J. Y.-K. (2012). Baroclinic instability on hot extrasolar planets. *Monthly Notices of the Royal Astronomical Society*, 424(2):1307–1326.

Polichtchouk, I., Cho, J. Y.-K., Watkins, C., Thrastarson, H. T., Umurhan, O. M., and de la Torre Juarez, M. (2014). Intercomparison of general circulation models for hot extrasolar planets. *Icarus*, 229:355–377.

Polvani, L., Scott, R., and Thomas, S. (2004). Numerically converged solutions of the global primitive equations for testing the dynamical core of atmospheric gcms. *Monthly weather review*, 132(11):2539–2552.

Potter, S. F., Vallis, G. K., and Mitchell, J. L. (2014). Spontaneous superrotation and the role of kelvin waves in an idealized dry gcm. *Journal of the Atmospheric Sciences*, 71(2):596–614.

Randel, W. J. and Held, I. M. (1991). Phase speed spectra of transient eddy fluxes and critical layer absorption. *Journal of the atmospheric sciences*, 48(5):688–697.

Rauscher, E. and Menou, K. (2010). Three-dimensional modeling of hot jupiter atmospheric flows. *The Astrophysical Journal*, 714(2):1334.

Rhines, P. B. (1975). Waves and turbulence on a beta-plane. *Journal of Fluid Mechanics*, 69(03):417–443.

Ribstein, B., Zeitlin, V., and Tissier, A.-S. (2014). Barotropic, baroclinic, and inertial instabilities of the easterly gaussian jet on the equatorial β-plane in rotating shallow water model. *Physics of Fluids (1994-present)*, 26(5):056605.

Robert, A. (1966). The integration of a low order spectral form of the primitive meteorological equations. *J. Met. Soc. Japan*, 44:237–245.

Rowe, J. F., Bryson, S. T., Marcy, G. W., Lissauer, J. J., Jontof-Hutter, D., Mullally, F., Gilliland, R. L., Issacson, H., Ford, E., Howell, S. B., et al. (2014). Validation of kepler's multiple planet candidates. iii. light curve analysis and announcement of hundreds of new multi-planet systems. *The Astrophysical Journal*, 784(1):45.

Rowe, J. F., Matthews, J. M., Seager, S., Kuschnig, R., Guenther, D. B., Moffat, A. F., Rucinski, S. M., Sasselov, D., Walker, G. A., and Weiss, W. W. (2006). An upper limit on the albedo of hd 209458b: direct imaging photometry with the most satellite. *The Astrophysical Journal*, 646(2):1241.

Sadourny, R. (1975). The dynamics of finite-difference models of the shallow-water equations. *Journal of the Atmospheric Sciences*, 32(4):680–689.

Saravanan, R. (1992). A Mechanistic Spectral Primitive Equation Model using Pressure Coordinates. *Tech. Rep.*

Saravanan, R. (1993). Equatorial superrotation and maintenance of the general circulation in two-level models. *Journal of the atmospheric sciences*, 50(9):1211–1227.

Scott, R. (2011). Polar accumulation of cyclonic vorticity. *Geophysical & Astrophysical Fluid Dynamics*, 105(4-5):409–420.

Scott, R., Rivier, L., Loft, R., and Polvani, L. (2003). BOB: Model Description and User's Guide. *NCAR Tech. Rep.*

Shapiro, R. (1970). Smoothing, filtering, and boundary effects. *Reviews of geophysics*, 8(2):359–387.

Sharp, D. H. (1984). An overview of rayleigh-taylor instability. *Physica D: Nonlinear Phenomena*, 12(1):3–18.

Showman, A. P., Cho, J. Y.-K., and Menou, K. (2011). *Atmospheric Circulation of Exoplanets*, pages 471–516.

Showman, A. P., Cooper, C. S., Fortney, J. J., and Marley, M. S. (2008). Atmospheric circulation of hot jupiters: Three-dimensional circulation models of hd 209458b and hd 189733b with simplified forcing. *The Astrophysical Journal*, 682(1):559.

Showman, A. P., Fortney, J. J., Lian, Y., Marley, M. S., Freedman, R. S., Knutson, H. A., and Charbonneau, D. (2009). Atmospheric circulation of hot jupiters: Coupled radiative-dynamical general circulation model simulations of hd 189733b and hd 209458b. *The Astrophysical Journal*, 699(1):564.

Showman, A. P. and Polvani, L. M. (2011). Equatorial superrotation on tidally locked exoplanets. *The Astrophysical Journal*, 738(1):71.

Simmons, A. J. and Burridge, D. M. (1981). An energy and angular-momentum conserving vertical finite-difference scheme and hybrid vertical coordinates. *Monthly Weather Review*, 109(4):758–766.

Simmons, A. J. and Hoskins, B. J. (1979). The downstream and upstream development of unstable baroclinic waves. *Journal of the Atmospheric Sciences*, 36(7):1239–1254.

Simons, T. J. (1972). The nonlinear dynamics of cyclone waves. *Journal of Atmospheric Sciences*, 29:38–52.

Suarez, M. J. and Duffy, D. G. (1992). Terrestrial superrotation: A bifurcation of the general circulation. *Journal of the atmospheric sciences*, 49(16):1541–1554.

Suarez, M. J. and Takacs, L. L. (1995). Technical report series on global modeling and data assimilation. volume 5: Documentation of the aires/geos dynamical core, version 2. In *Unknown*, volume 5.

Swain, M. R., Vasisht, G., and Tinetti, G. (2008). The presence of methane in the atmosphere of an extrasolar planet. *Nature*, 452(7185):329–331.

Thorncroft, C., Hoskins, B., and McIntyre, M. (1993). Two paradigms of baroclinic-wave life-cycle behaviour. *Quarterly Journal of the Royal Meteorological Society*, 119(509):17–55.

Thrastarson, H. T. and Cho, J. Y. (2010). Effects of initial flow on close-in planet atmospheric circulation. *The Astrophysical Journal*, 716(1):144.

Thrastarson, H. T. and Cho, J. Y. (2011). Relaxation time and dissipation interaction in hot planet atmospheric flow simulations. *The Astrophysical Journal*, 729(2):117.

Tinetti, G., Vidal-Madjar, A., Liang, M.-C., Beaulieu, J.-P., Yung, Y., Carey, S., Barber, R. J., Tennyson, J., Ribas, I., Allard, N., et al. (2007). Water vapour in the atmosphere of a transiting extrasolar planet. *Nature*, 448(7150):169–171.

Vallis, G. K. (2006). *Atmospheric and oceanic fluid dynamics: fundamentals and large-scale circulation*. Cambridge University Press.

Wang, B. (1990). On the asymmetry of baroclinic instability between easterly and westerly shear. *Tellus A*, 42(4):463–468.

Watkins, C. and Cho, J. Y. (2010). Gravity waves on hot extrasolar planets. i. propagation and interaction with the background. *The Astrophysical Journal*, 714(1):904.

Wheeler, M. and Kiladis, G. N. (1999). Convectively coupled equatorial waves: Analysis of clouds and temperature in the wavenumber-frequency domain. *Journal of the Atmospheric Sciences*, 56(3):374–399.

Wiin-Nielsen, A. (1963). On baroclinic instability in filtered and non-filtered numerical prediction models. *Tellus*, 15(1):1–19.

Williams, G. P. (1978). Planetary circulations: 1. barotropic representation of jovian and terrestrial turbulence. *Journal of the Atmospheric Sciences*, 35(8):1399–1426.

Williams, G. P. (1988). The dynamical range of global circulationsi. *Climate Dynamics*, 2(4):205–260.

Williams, G. P. (2003). Barotropic instability and equatorial superrotation. *Journal of the atmospheric sciences*, 60(17).

Williams, G. P. (2006). Equatorial superrotation and barotropic instability: Static stability variants. *Journal of the atmospheric sciences*, 63(5).

Wolszczan, A. and Frail, D. A. (1992). A planetary system around the millisecond pulsar psr 1257+ 12. *Nature*, 355(6356):145–147.